Delft University of Technology

Document Version
Final published version

Licence
CC BY-NC-ND

Citation (APA)
Leerhoff, P. (2026). *Reduction mechanisms of goethite-rich iron ore fines under suspension smelting conditions: Influence of H_2-enrichment, ore mineralogy and morphology*. [Dissertation (TU Delft), Delft University of Technology].

Important note
To cite this publication, please use the final published version (if applicable).
Please check the document version above.

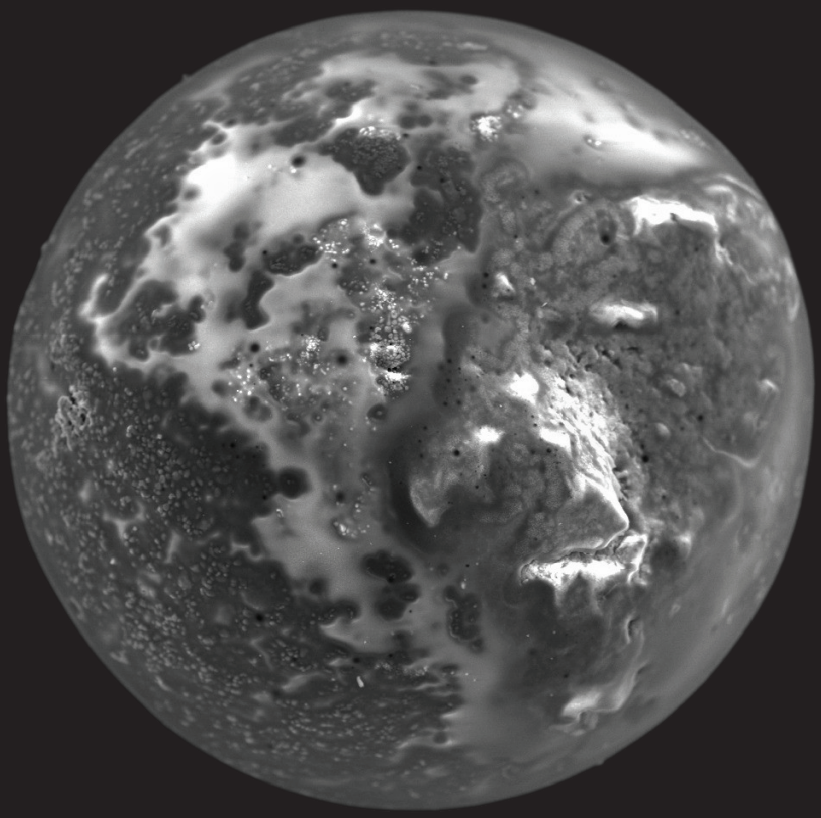
Copyright
In case the licence states “Dutch Copyright Act (Article 25fa)”, this publication was made available Green Open Access via the TU Delft Institutional Repository pursuant to Dutch Copyright Act (Article 25fa, the Taverne amendment). This provision does not affect copyright ownership.
Unless copyright is transferred by contract or statute, it remains with the copyright holder.

Sharing and reuse
Other than for strictly personal use, it is not permitted to download, forward or distribute the text or part of it, without the consent of the author(s) and/or copyright holder(s), unless the work is under an open content license such as Creative Commons.

Takedown policy
Please contact us and provide details if you believe this document breaches copyrights.
We will remove access to the work immediately and investigate your claim.

This work is downloaded from Delft University of Technology.

Reduction Mechanisms of Goethite-rich Iron Ore Fines under Suspension Smelting Conditions



Influence of H_2-enrichment, Ore Mineralogy and Morphology

Philipp Leerhoff

REDUCTION MECHANISMS OF GOETHITE-RICH IRON ORE FINES UNDER SUSPENSION SMELTING CONDITIONS

INFLUENCE OF H_2-ENRICHMENT, ORE MINERALOGY AND MORPHOLOGY

REDUCTION MECHANISMS OF GOETHITE-RICH IRON ORE FINES UNDER SUSPENSION SMELTING CONDITIONS

INFLUENCE OF H_2-ENRICHMENT, ORE MINERALOGY AND MORPHOLOGY

Dissertation

for the purpose of obtaining the degree of doctor
at Delft University of Technology,
by the authority of the Rector Magnificus,
Prof. dr. ir. H. Bijl,
chair of the Board of Doctorates
to be defended publicly on
Friday, September 11th 2026, at 10:00

by

Philipp LEERHOFF

This dissertation has been approved by the promotors and the copromotor.

Composition of the doctoral committee:

Rector Magnificus,	chairperson
Dr. Y. Yang,	Delft University of Technology, promotor
Dr. N.D. Dogan,	Delft University of Technology, promotor
Dr. ir S.T. Abrahami,	Delft University of Technology, copromotor

Independent members:

Prof. dr. M.J. Santofimia Navarro,	Delft University of Technology
Prof. dr. T. Fabritius,	University of Oulu, Finland
Prof. dr. L. Sundqvist-Öqvist,	Luleå University of Technology, Sweden
Prof. Dr.-Ing. K.B. Friedrich,	RWTH Aachen University, Germany
Prof. dr. J. Dik,	Delft University of Technology, reserve member

Other Member:

Dr. ir. C. Zeilstra,	Tata Steel

The research carried out in this dissertation was part of the CHIRON project (Towards a carbon-lean HIsarna ironmaking process) under the project number T20009 in the framework of the Research Program of the Materials innovation institute (M2i) (www.m2i.nl) supported by the Dutch government.







Keywords: suspension smelting, HIsarna® ironmaking, fine iron ores, goethite, hydrogen enrichment, thermal decomposition, pre-reduction, water-gas shift reaction, reaction kinetics

Printed by: Ridderprint | https://www.ridderprint.nl/

Cover by: Philipp Leerhoff

Copyright © 2026 by P. Leerhoff

ISBN 978-94-6518-396-1

An electronic version of this dissertation is available at
http://repository.tudelft.nl/.

To us
...

CONTENTS

Summary xi

Samenvatting xv

1 Introduction 1
- 1.1 Background . . . 2
- 1.2 Research objectives . . . 5
- 1.3 Thesis outline . . . 5
- References . . . 8

2 H_2 Adaptation in ironmaking 13
- 2.1 Introduction . . . 14
- 2.2 Hydrogen in DRI processes . . . 15
  - 2.2.1 DRI in shaft furnace . . . 15
  - 2.2.2 DRI in fluidized bed reactor . . . 16
- 2.3 Smelting reduction ironmaking . . . 17
- 2.4 Suspension smelting ironmaking . . . 19
- 2.5 Reaction mechanisms in suspension smelting . . . 24
  - 2.5.1 Thermal decomposition of goethite . . . 24
  - 2.5.2 Thermal decomposition of hematite . . . 26
  - 2.5.3 Gas reduction of iron oxides . . . 28
  - 2.5.4 Water-gas shift reaction . . . 36
- 2.6 Conclusions . . . 39
- References . . . 41

3 Characterisation and thermal decomposition 51
- 3.1 Introduction . . . 52
- 3.2 Material analysis . . . 53
  - 3.2.1 Composition analysis . . . 54
  - 3.2.2 Morphological analysis . . . 55
  - 3.2.3 Phase distribution . . . 56
- 3.3 Methods . . . 60
  - 3.3.1 TGA experiments . . . 60
  - 3.3.2 Assessment of reaction kinetics of thermal decomposition . . . 60
- 3.4 Results and discussion . . . 61
  - 3.4.1 Thermal decomposition . . . 62
  - 3.4.2 Kinetics of goethite decomposition . . . 65
  - 3.4.3 Kinetics of hematite decomposition . . . 70
- 3.5 Conclusions . . . 75
- References . . . 77

4 Thermal decomposition and pre-reduction **79**
4.1 Introduction . . . 80
4.2 Methodology . . . 82
4.2.1 Materials - Ore characterization . . . 82
4.2.2 Drop tube furnace experiments . . . 84
4.2.3 TGA experiments . . . 86
4.3 Results and discussion . . . 87
4.3.1 Particle morphology after flash thermal decomposition . . . 87
4.3.2 Evolution of particle size and density during flash reduction . . . 88
4.3.3 Phase evolution during flash pre-reduction . . . 90
4.3.4 Effect of residence time on the pre-reduction degree . . . 91
4.3.5 Evaluation of single particle reduction and heating behavior . . . 94
4.3.6 Microscopical and kinetic analysis of flash reduced particles . . . 97
4.4 Conclusions . . . 102
References . . . 105

5 H_2-enrichment and ore mineralogy **109**
5.1 Introduction . . . 110
5.2 Method . . . 113
5.2.1 Materials . . . 113
5.2.2 Experimental approach . . . 113
5.3 Results and discussion . . . 115
5.3.1 Isothermal reduction . . . 115
5.3.2 Isothermal reduction kinetics . . . 115
5.3.3 Non-isothermal reduction . . . 124
5.3.4 The influence of water-gas shift reaction . . . 125
5.3.5 Non-isothermal iron ore conversion . . . 129
5.4 Conclusions . . . 131
References . . . 133

6 In-flight reduction of iron ore fines **137**
6.1 Introduction . . . 138
6.2 Methods . . . 139
6.2.1 Materials . . . 139
6.2.2 Experimental approach . . . 141
6.3 Results and discussion . . . 143
6.3.1 Morphological analyses . . . 143
6.3.2 Mineralogical analyses . . . 143
6.3.3 Redox-titration analyses for PRD determination . . . 147
6.3.4 Phase distribution . . . 149
6.3.5 The water-gas shift reaction . . . 151
6.3.6 TGA gas reduction experiments . . . 153
6.3.7 Mechanisms of particulate fraction reduction . . . 154
6.3.8 Influence of reduction atmosphere . . . 159
6.3.9 Extent of reduction under isothermal and non-isothermal conditions . . . 160

6.4 Conclusions . . . 161
References . . . 163

7 Conclusions and recommendations **167**
7.1 Conclusions . . . 168
7.2 Recommendations . . . 172
References . . . 178

Acknowledgements **181**

A Appendix to chapter 3 **183**

B Appendix to chapter 4 **187**

C Appendix to chapter 5 **195**

D Appendix to chapter 6 **201**

Curriculum Vitæ **209**

List of Publications **211**

SUMMARY

The steel industry is one of the major contributors to anthropogenic CO_2-emissions, necessitating significant changes to achieve carbon neutrality in the future. Considerable efforts in recent years have focused on developing alternatives to the traditional blast furnace (BF) process, aiming for more sustainable ironmaking pathways. Within the framework of the ULCOS initiative in the early 2000s, the HIsarna® process was developed as a promising alternative ironmaking process. HIsarna produces liquid hot metal and slag, similar to the blast furnace, but enables rapid pre-reduction of fine iron ores in a suspension environment, often referred to as flash reduction due to the short reaction times and high temperatures, followed by a final smelting reduction step. Owing to its design, HIsarna offers several process advantages compared to the conventional BF. These are, for example, the elimination of material pre-treatment steps like ore agglomeration and coking, as well as the ability to use low-grade iron ores and secondary Fe-bearing materials.

This PhD project investigated the fundamental mechanisms of suspension smelting (flash ironmaking) in the pre-reduction stage of the HIsarna process, with a particular focus on the influence of ore mineralogy and H_2-enriched reducing atmospheres. The primary objective was to understand how these factors affect the pre-reduction kinetics and particle behaviour, providing relevant insights for optimizing the HIsarna process. To achieve this, a combination of thermogravimetric analysis (TGA) and high-temperature drop tube furnace (HTDF) experiments was carried out. TGA enables a detailed kinetic analysis under controlled non-isothermal or isothermal conditions and long residence times, while the HTDF simulates isothermal in-flight particle reduction at very short residence times (hundreds of milliseconds), which is much closer to the actual conditions in the upper part of the HIsarna furnace. Incorporation of both techniques provides a comprehensive understanding of the in-flight single particle reduction behaviour, and of molten particle films, which undergo longer reduction times.

The study begins with a comprehensive characterization of three potential iron ore fines for HIsarna ironmaking (OreA, OreB, OreC) using SEM-EDS, XRD, XRF for compositional analysis, Raman spectroscopy for Fe-phase distribution, light scattering for particle size distribution, He-pycnometer for true particle density, and BET analysis to assess specific surface area and porosity. Throughout the thesis, different size fractions were investigated. For OreA, the < 63 and (63-125) μm fractions were studied, for OreB < 63, (63-125) and (125-250) μm fractions, and for OreC the < 63 and (63-125) μm fractions. The primary mineralogical difference among the three types of iron ores is the goethite content, which is absent in OreA, intermediate in OreB, and high in OreC, influencing physical properties such as porosity, true particle density, specific surface area, and reactivity. Due to the lower iron content in goethite compared to hematite, OreB (58.80-61.60 total-Fe) and OreC (56.80-58.00 total-Fe) are considered low-grade ores, whereas OreA (60.10-64.00 total-Fe) can still be classified as a medium-grade ore. For all ores, SiO_2 and

Al_2O_3 are the main gangue components. Additional mineralogical differences between the ores are the dolomite phase present in OreA and kaolinite phase in OreB.

Thermal decomposition of the ores in the TGA revealed that goethite decomposition occurs in a two-stage process. The initial stage is the chemically reaction-controlled decomposition of nearly pure goethite particles within the ore. The following second stage is the decomposition of goethite-hematite intertwined phases, which is diffusion controlled . Hematite thermal decomposition in the TGA is consistently chemical reaction controlled for all ores. Higher goethite content leads to higher reduction degrees during thermal decomposition, highlighting the mineralogical impact on the pre-reduction behaviour. Hence, at the end of the non-isothermal heating zone at 1773 K OreC reached the highest reduction degrees (11.91-13.81 %), followed by OreB (11.90-12.90 %), and OreA reached the lowest reduction degrees (9.48-10.75 %). While OreB and OreC were completely converted to magnetite during the heating period, OreA required additional holding times at 1773 K to fully convert to magnetite. HTDF experiments indicated that under in-flight conditions, thermal decomposition alone resulted in much lower pre-reduction due to extremely short particle residence times. Goethite-containing ores exhibited significant cracking, followed by fragmentation, altering particle size and density, which then influenced the extent of pre-reduction and its kinetics. OreC, with the highest goethite content, showed more extensive fragmentation, whereas OreB primarily expanded before fragmentation. Reducing gas enrichment (at low CO or H_2 levels) slightly enhanced pre-reduction under flash conditions, but its effect was more pronounced in the TGA experiments, where small amounts of wustite have formed. EBSD analysis confirmed that reduction under both rapid thermal decomposition and low reducing gas-enriched atmospheres proceeded via a mixed mechanism of product-layer and internal pore diffusion.

Further isothermal TGA studies of OreB with varying H_2-levels (7.5-37.5 %) demonstrated that increasing H_2 in the atmosphere significantly accelerates reduction rates, reducing the overall reduction time even though the total reduction extent is only moderately affected. For example, at a post-combustion ratio (PCR) of 60 % and at a temperature of 1773 K, the reduction in 7.5 % H_2 took 502 s to achieve a PRD (pre-reduction degree) of 24.2 %. When the H_2-content in the atmosphere was increased to 22.5 %, the reaction took only 375 s to achieve a PRD of 25.0 %. By further decreasing the PCR to 40 % and, therefore, increasing the H_2-content to 37.5 %, the reaction only needed 206 s to reach a PRD of 27.1 %. SEM-EDS analysis indicated that the reduction was controlled by the diffusion of the reducing gas through a developing product layer. Within the same PCR, the activation energy decreased from 77.60 kJ/mol to 69.12 kJ/mol by increasing the H_2 content, but increased to 79.91 kJ/mol at a lower PCR. Non-isothermal experiments confirmed that mineralogy, especially the goethite content, enhances hematite to wustite reduction, while under isothermal conditions these effects were limited after initial magnetite formation. The water-gas shift reaction was observed at higher temperatures, impacting the extent of available H_2 during in-flight reduction. In HTDF experiments with 7.5 % H_2, OreA exhibited higher pre-reduction at the particle surface, whereas OreB showed more bulk reduction, indicating surface-controlled interfacial reaction for OreA and a likely more mixed control of nucleation and surface control for OreB. Testing higher H_2 levels under flash conditions was limited by rapid water-vapour formation via the

water-gas shift reaction, which caused excessive condensation in the quenching zone. This condensation prevented reliable sample collection after the experiments.

Overall, this thesis provides a comprehensive understanding of how ore mineralogy and H_2-enrichment influence reaction fundamentals under in-flight suspension smelting conditions. The findings highlight that under in-flight flash pre-reduction, goethite-containing ores perform better compared to ores containing only hematite due to favorable physical and morphological properties. H_2-enrichment offers a promising approach to accelerate reduction, potentially decreasing the amounts of coal injection needed in the HIsarna smelting stage. However, its application must consider issues arising from the water-gas shift reaction, which consumes H_2 and generates large amounts of water-vapour. This work establishes critical mechanistic insights for optimizing the HIsarna ironmaking process, demonstrating that control of ore selection and gas composition can enhance pre-reduction efficiency and support the development of more sustainable iron production processes.

SAMENVATTING

De staalindustrie is een van de grootste bijdragers aan antropogene CO_2-emissies, wat ingrijpende veranderingen noodzakelijk maakt om in de toekomst koolstofneutraliteit te bereiken. In de afgelopen jaren zijn aanzienlijke inspanningen geleverd om alternatieven voor het traditionele hoogovenproces (BF) te ontwikkelen, met als doel duurzamere ijzerproductie. In het kader van het ULCOS-initiatief begin jaren 2000 werd het HIsarna®-proces ontwikkeld als een veelbelovend alternatief voor ijzerproductie. HIsarna produceert vloeibaar ruwijzer en slak, vergelijkbaar met de hoogoven, maar maakt snelle voorreduktie van fijne ijzerertsdeeltjes in een suspensieomgeving mogelijk, vaak aangeduid als flashreductie vanwege de korte reactietijden en hoge temperaturen, gevolgd door een definitieve smeltreductiestap. Dankzij het ontwerp biedt HIsarna verschillende procesvoordelen ten opzichte van de conventionele hoogoven, zoals het elimineren van materiaalvoorbehandelingsstappen zoals ertsbundeling en coking, evenals de mogelijkheid om laagwaardige ijzerertssoorten en secundaire Fe-bevattende materialen te gebruiken.

Dit promotieonderzoek onderzocht de fundamentele mechanismen van suspensiesmelten (flash-ijzerproductie) in de voorreduktiefase van het HIsarna-proces, met bijzondere aandacht voor de invloed van ertsmijnalogie en H_2-verrijkte reducerende atmosferen. Het primaire doel was te begrijpen hoe deze factoren de voorreduktiekinetiek en het deeltjesgedrag beïnvloeden, en relevante inzichten te bieden voor het optimaliseren van het HIsarna-proces. Hiertoe werd een combinatie van thermogravimetrische analyse (TGA) en hoogtemperatuur drop tube furnace (HTDF)-experimenten uitgevoerd. TGA maakt gedetailleerde kinetische analyses onder gecontroleerde niet-isotherme of isotherme condities en lange verblijftijden mogelijk, terwijl de HTDF isotherme reductie van deeltjes in vlucht simuleert bij zeer korte verblijftijden (enkele honderden milliseconden), wat veel dichter bij de werkelijke omstandigheden in het bovenste deel van de HIsarna-oven ligt. Door beide technieken te combineren, ontstaat een uitgebreid inzicht in het reductiegedrag van individuele deeltjes in vlucht en van gesmolten deeltjesfilms, die langere reductietijden ondergaan.

De studie begint met een uitgebreide karakterisering van drie potentiële ijzererfslijpen voor HIsarna-ijzerproductie (OreA, OreB, OreC) met behulp van SEM-EDS, XRD, XRF voor samenstellingsanalyse, Raman-spectroscopie voor Fe-fasedistributie, lichtverstrooiing voor deeltjesgrootteverdeling, He-pycnometer voor ware deeltjesdichtheid en BET-analyse om het specifieke oppervlak en de porositeit te beoordelen. Gedurende het proefschrift werden verschillende deeltjesgroottes onderzocht. Voor OreA werden de fracties < 63 en (63-125) μm bestudeerd, voor OreB < 63, (63-125) en (125-250) μm, en voor OreC de < 63 en (63-125) μm fracties. Het belangrijkste mineralogische verschil tussen de drie ijzerertssoorten is het goethietgehalte, dat afwezig is in OreA, gemiddeld in OreB en hoog in OreC, wat de fysische eigenschappen zoals porositeit, ware deeltjesdichtheid, specifiek oppervlak en reactiviteit beïnvloedt. Vanwege het lagere ijzergehalte in goethiet

ten opzichte van hematiet, worden OreB (58,80–61,60 totaal-Fe) en OreC (56,80–58,00 totaal-Fe) beschouwd als laagwaardige ertsen, terwijl OreA (60,10–64,00 totaal-Fe) nog steeds als middelhoogwaardige ertsen kan worden geclassificeerd. Voor alle ertsen zijn SiO_2 en Al_2O_3 de belangrijkste gangue-componenten. Extra mineralogische verschillen tussen de ertsen zijn de dolomietfase in OreA en de kaolienfase in OreB.

Thermische ontleding van de ertsen in de TGA toonde aan dat goethietontleding in twee fasen verloopt. De eerste fase is de chemisch reactie-gestuurde ontleding van bijna pure goethietdeeltjes binnen het erts. De tweede fase betreft de ontleding van goethiet-hematiet verweven fasen, die diffusie-gestuurd is. Hematietthermische ontleding in de TGA is consequent chemisch reactie-gestuurd voor alle ertsen. Een hoger goethietgehalte leidt tot hogere reductiegraden tijdens thermische ontleding, wat het effect van mineralogie op het voorreductiegedrag benadrukt. Aan het einde van de niet-isotherme verwarmingszone bij 1773 K bereikte OreC de hoogste reductiegraden (11,91-13,81 %), gevolgd door OreB (11,90-12,90 %), terwijl OreA de laagste reductiegraden bereikte (9,48-10,75 %). Terwijl OreB en OreC volledig werden omgezet in magnetiet tijdens de verwarmingsperiode, vereiste OreA extra verblijftijden bij 1773 K om volledig in magnetiet te worden omgezet. HTDF-experimenten gaven aan dat onder in-flight condities thermische ontleding alleen resulteerde in veel lagere voorreduktie vanwege de extreem korte verblijftijden van deeltjes. Goethiethoudende ertsen vertoonden aanzienlijke scheuring, gevolgd door fragmentatie, waardoor de deeltjesgrootte en dichtheid veranderden, wat vervolgens de mate van voorreduktie en de kinetiek beïnvloedde. OreC, met het hoogste goethietgehalte, vertoonde meer uitgebreide fragmentatie, terwijl OreB voornamelijk uitzetting vertoonde voorafgaand aan fragmentatie. Verrijking van reducerend gas (bij lage CO- of H_2-niveaus) verbeterde de voorreduktie onder flashcondities enigszins, maar het effect was meer uitgesproken in de TGA-experimenten, waar kleine hoeveelheden wüstiet werden gevormd. EBSD-analyse bevestigde dat reductie onder zowel snelle thermische ontleding als lage reducerende gasverrijkte atmosferen plaatsvond via een gemengd mechanisme van productlaag- en interne pore-diffusie.

Verdere isotherme TGA-studies van OreB met variërende H_2-niveaus (7,5-37,5 %) toonden aan dat het verhogen van H_2 in de atmosfeer de reductiesnelheden aanzienlijk versnelt, waardoor de totale reductietijd wordt verkort, ook al wordt de totale reductieomvang slechts matig beïnvloed. Bijvoorbeeld, bij een naverbrandingsratio (PCR) van 60 % en een temperatuur van 1773 K, duurde reductie in 7,5 % H_2 502 s om een PRD (voor-reductie graad) van 24,2 % te bereiken. Toen het H_2-gehalte in de atmosfeer werd verhoogd naar 22,5 %, duurde de reactie slechts 375 s om een PRD van 25,0 % te bereiken. Door de PCR verder te verlagen tot 40 % en daarmee het H_2-gehalte te verhogen tot 37,5 %, had de reactie slechts 206 s nodig om een PRD van 27,1 % te bereiken. SEM-EDS-analyse gaf aan dat de reductie werd gecontroleerd door diffusie van het reducerende gas door een zich ontwikkelende productlaag. Bij dezelfde PCR daalde de activatie-energie van 77,60 kJ/mol naar 69,12 kJ/mol door het verhogen van het H_2-gehalte, maar nam toe tot 79,91 kJ/mol bij een lagere PCR. Niet-isotherme experimenten bevestigden dat mineralogie, met name het goethietgehalte, hematiet-naar-wüstietreductie versterkt, terwijl onder isotherme condities deze effecten beperkt waren na de initiële magnetietvorming. De water-gas shift-reactie werd waargenomen bij hogere temperaturen, wat de beschikbaarheid van H_2 tijdens reductie in vlucht beïnvloedt. In HTDF-experimenten met 7,5 %

H_2 vertoonde OreA hogere voorreduktie aan het oppervlak van de deeltjes, terwijl OreB meer bulkreductie vertoonde, wat wijst op oppervlakte-gestuurde interfaciale reactie voor OreA en waarschijnlijk meer gemengde controle van nucleatie en oppervlaktecontrole voor OreB. Testen van hogere H_2-niveaus onder flashcondities werd beperkt door snelle waterdampvorming via de water-gas shift-reactie, wat overmatige condensatie in de quench-zone veroorzaakte. Deze condensatie verhinderde betrouwbare staalafname na de experimenten.

Al met al biedt dit proefschrift een uitgebreid begrip van hoe ertsmijnalogie en H_2-verrijking de reactiemechanismen onder in-flight suspensiesmelten beïnvloeden. De bevindingen benadrukken dat onder in-flight flash-voorreduktie, goethiethoudende ertsen beter presteren dan ertsen die alleen hematiet bevatten vanwege gunstige fysische en morfologische eigenschappen. H_2-verrijking biedt een veelbelovende aanpak om reductie te versnellen, waardoor mogelijk de hoeveelheid koleninjectie die nodig is in de HIsarna-smeltfase kan worden verminderd. De toepassing moet echter rekening houden met problemen als gevolg van de water-gas shift-reactie, die H_2 consumeert en grote hoeveelheden waterdamp genereert. Dit werk levert cruciale mechanistische inzichten voor het optimaliseren van het HIsarna-ijzerproductieproces en toont aan dat controle van ertsselectie en gascompositie de efficiëntie van voorreduktie kan verbeteren en de ontwikkeling van duurzamere ijzerproductieprocessen kan ondersteunen.

1

INTRODUCTION

1

1.1. BACKGROUND

The steelmaking industry accounts for approximately 7-9 % of global anthropogenic CO_2-emissions [1]. These high emissions arise mainly from the large amounts of carbon used in the form of coal or coke during the ironmaking process [2]. Since the European Union aims to become carbon neutral by 2050 and to reduce emissions by 55 % by 2030 [3], it forces the steel industry, as one of the largest CO_2-emitters, to move towards more sustainable production routes. Conventional steelmaking routes (Figure 1.1) are based either on the blast furnace (BF) or the direct reduction of iron (DRI) ore as the ironmaking step [4]. In BF ironmaking, iron ore is reduced to molten metallic iron, which can either be cast directly to pig iron or refined to crude steel together with recycled steel in a basic oxygen furnace (BOF). In contrast, DRI processes produce solid iron, which is then treated with or without recycled steel in an electric arc furnace (EAF) to obtain molten steel [4, 5]. Alternatively, the ironmaking step can be skipped completely, feeding 100 % scrap in the EAF [5].

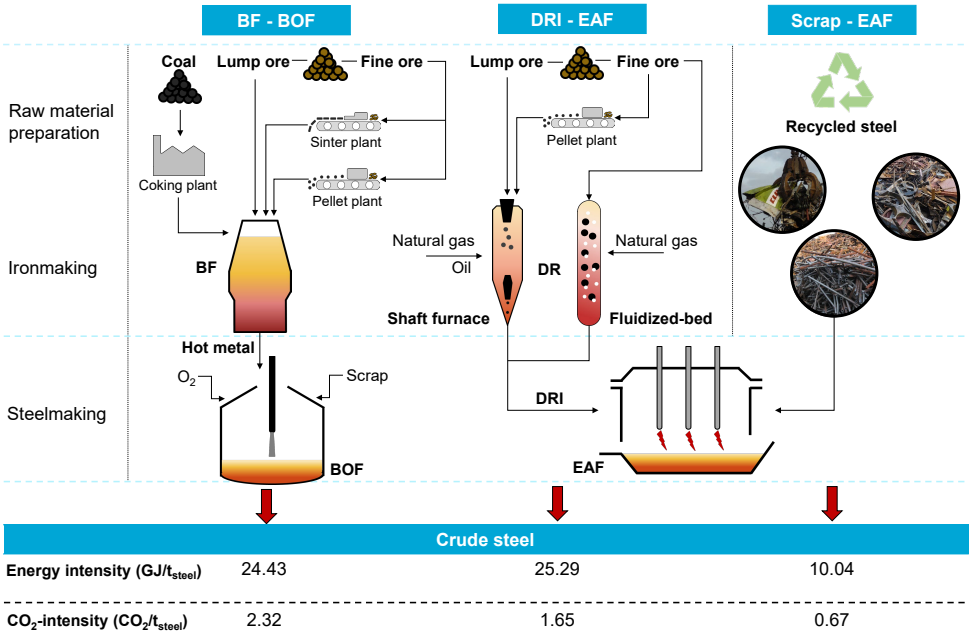


Figure 1.1: Conventional iron- and steelmaking routes based on BOF and EAF and their respective energy and CO_2-intensity [5], with permission from Elsevier.

In 2024, global pig iron production via blast furnaces reached 1293.5 Mt, while direct reduced iron amounted to only 144.1 Mt, underlining the dominant industrial role of the blast furnace [6]. Another commercial ironmaking possibility is smelting reduction, with COREX and FINEX as process examples [5]. However, its market share is significantly

lower compared to BF and DR ironmaking [5, 7]. The BF-BOF route shows high energy consumption (24.43 GJ/t_{steel}) and accounts for the highest CO_2-emissions (2.32 CO_2/t_{steel}) within the steelmaking routes. While DRI-based steelmaking is slightly more energy intensive (25.29 GJ/t_{steel}), its CO_2-emissions are lower (1.65 CO_2/t_{steel}). The recycling route, using scrap in the EAF shows the best environmental performance, with significant reduction in both energy use (10.04 GJ/t_{steel}) and emissions (0.67 CO_2/t_{steel}) [5, 8].

However, most crude steel is still produced via the BOF route (70.4 %), which is heavily relying on the blast furnace and utilizing iron ores as input material [6]. Various technologies have been developed to reduce emissions from fossil fuel based ironmaking, including carbon capture and storage or utilization (CCS/U), H_2-based reduction, replacement of coal with biomass, hydrogen plasma and electrolytic reduction approaches [9]. H_2 reduction is currently seen as the most feasible near-term solution [9–11]. At temperatures below 843 K the H_2 reduction of iron oxide proceeds via Eq. (1.1) and Eq. (1.2) and above 843 K via Eq. (1.3) and Eq. (1.4) [5].

$$3Fe_2O_3 + H_2 \rightarrow 2Fe_3O_4 + H_2O \tag{1.1}$$

$$Fe_2O_3 + 4H_2 \rightarrow 3Fe + 4H_2O \tag{1.2}$$

$$Fe_3O_4 + H_2 \rightarrow 3FeO + H_2O \tag{1.3}$$

$$FeO + H_2 \rightarrow Fe + H_2O \tag{1.4}$$

Substituting carbon with H_2 eliminates CO_2-emissions by replacing them with H_2O while also offering kinetic advantages [2]. But despite its various benefits, technical challenges for its large scale implementation remain. The reduction of iron oxides with H_2 is endothermic, requiring additional heat input, and carbon is still needed for the consequent transition from iron to steel [12]. Thus, alternative carbon sources such as pulverized coal, bio-methane, or other biogenic inputs are required [13]. Importantly, only green H_2 can deliver the full environmental benefit [2].

Alternative European approaches to decrease CO_2-emission in ironmaking were developed during the ULCOS project. The initiative started in 2004 as a consortium between 48 European companies and organizations with the goal to reduce 50 % of the CO_2-emissions per ton of steel in production based on iron ores as input material. Following multiple selection rounds, four technologies were chosen for further investigation and up-scaling, evaluated based on criteria like CO_2 reduction and further environmental aspects, economical efficiency, and social acceptance of the processes. The HIsarna® process was chosen as one of the four promising approaches for further investigation. Other approaches include the top gas recycling blast furnace, advanced direct reduction and electrolysis of iron ores [14].

HIsarna® is being developed by Tata Steel in IJmuiden as an alternative ironmaking technology which can be classified as a smelting reduction process [5]. HIsarna is a registered trademark of Tata Steel. However, the top part, a pre-reduction stage, utilizes a mechanism called suspension smelting. Suspension smelting in ironmaking usually

describes processes utilizing flash reactions or cyclone processes [15], where iron is produced in a liquid state [16]. A comparable suspension smelting process is the flash ironmaking process, developed by the University of Utah [16–18]. Unlike conventional DRI processes, suspension smelting technology operates at much higher temperatures and very short residence times (few seconds), where thermal decomposition plays a major role alongside reduction by H_2 and CO [19].

The thermal decomposition of hematite (Fe_2O_3) to magnetite (Fe_3O_4) usually initiates at temperatures above 1312-1473 K [20–22], depending on the nature of the ore, and proceeds via the following reaction [23]:

$$6Fe_2O_3(s) \rightarrow 4Fe_3O_4(s) + O_2(g) \tag{1.5}$$

While hematite and magnetite are considered the main iron ores for ironmaking, goethite (FeOOH), a vast naturally occurring iron hydroxide, is another iron ore of interest for ironmaking processes [24]. Further iron-bearing mineralogies worth mentioning are limonite ($FeO(OH) + nH_2O$), siderite ($FeCO_3$), ilmenite ($FeO * TiO_2$) and pyrite (FeS_2) [5]. While hematite and magnetite can be directly reduced to a lower oxidation state [5] goethite first needs to be dehydrated and transformed to hematite, before being able to be reduced, as shown in Eq. (1.6) [25, 26]. This reaction can initiate approximately at temperatures of 465 K [25], eliminating the need for external pre-treatment due to the much higher temperatures involved in the ironmaking processes.

$$\alpha - 2FeOOH \rightarrow \alpha - Fe_2O_3 + H_2O \tag{1.6}$$

While HIsarna already provides several process advantages compared to the traditional blast furnace (removal of coking and ore agglomeration) [27], further greening of the process is crucial to support its implementation. This can, for example, be done by optimizing input material conditions, or by the enrichment of H_2 to partially replace pulverized coal in the process.

Overall, an important factor to consider for ironmaking is the ore grade, which varies strongly between naturally occurring ores. High-grade ore (> 65 % Fe) is usually obtained by physical treatment and is the required grade for DRI plants. Medium-grade ores (62-65 % Fe) can be used next to high-grade ores in blast furnace ironmaking. However, considering future demands and economical benefits, it is important to also consider lower-grade ores (<62 % Fe) as potential input material [5]. Goethite, for example, has a significantly lower total iron content compared to the common iron oxides, hematite and magnetite. HIsarna provides the possibility of utilizing low-grade iron ores, leading to even more flexibility in input material [28].

The sustainability of HIsarna can further be improved by decreasing the amount of coal injected and substituting it with more greener reducing agents. The use of carbonized biomass was already tested in the framework of the LoCO2Fe-project [29], where a replacement of 40 % fossil coal with sustainable charcoal was achieved. The application of H_2-injection into the smelting bath of HIsarna was investigated in a study by Htet et al. [30]. Even though certain amounts of carbon are needed to carburize the hot metal in HIsarna [31], further H_2 in the cyclone converter pre-reduction stage can decrease the amounts of coal even further by increasing pre-reduction degrees of the ores.

While research on suspension smelting ironmaking appears already limited compared to DRI research, most existing studies focus on the reduction of medium- to high-grade hematite or magnetite fines [21, 32–43]. When lower-grade ores are considered, particularly those with high goethite contents as the iron-bearing phase, the already complex reduction environment of suspension smelting becomes even more challenging. During rapid flash reduction, the thermal decomposition of hematite and goethite occurs simultaneously with the gas reduction of iron oxides. Although literature provides insights into these reaction mechanisms, it typically addresses either the reduction of a single iron-bearing phase or individual isolated reaction mechanisms of thermal decomposition or gas reduction with CO and H_2 [20, 23, 44–47]. A comprehensive understanding of the interactions between these mechanisms is therefore essential when investigated lower-grade, goethite-containing iron ore fines for suspension smelting ironmaking.

1.2. RESEARCH OBJECTIVES

The objective of this PhD is to study and understand the impact of hydrogen enrichment, as well as ore mineralogy and properties, on the reduction behaviour and kinetics in suspension smelting ironmaking, with a specific focus on the HIsarna process developed by Tata Steel in IJmuiden.

The experimental study was carried out using two main research equipments: a thermogravimetric analyser (TGA) and a high-temperature drop tube furnace (HTDF). The TGA is a standard tool for investigating isothermal and non-isothermal reaction kinetics, whereas the HTDF, developed at TU Delft [48], enables to study the reduction behaviour (in particular reduction degree and reduction kinetics) of iron ore fines under controlled particle residence times.

Within this framework, three iron ore fines (OreA, OreB and OreC), suitable for HIsarna ironmaking, were selected as input materials for this study. The objective was to analyze their mineralogical, chemical and physical characteristics and to identify how differences in ore properties influence reduction behaviour. The study further aimed to assess how thermal decomposition and H_2-enriched gas reduction influence reduction mechanisms and kinetics, with emphasis on the role of mineralogy.

1.3. THESIS OUTLINE

This PhD thesis contains a total of 7 chapters. Following this introduction (Chapter 1), the main body of the thesis is presented in Chapter 2 to Chapter 6, with the conclusions and recommendations for future research in Chapter 7. Chapter 2 presents a critical review of the state of the art in suspension smelting ironmaking. The core experimental work (Chapter 3-Chapter 6) is divided into two main blocks. The first block (Chapter 3 and Chapter 4) focuses on ore characterization and thermal decomposition under both long (TGA) and short (HTDF) residence times. The second block (Chapter 5 and Chapter 6) investigates the effects of hydrogen enrichment and ore mineralogy on the reduction behaviour. Chapter 2 to Chapter 5 are based on published scientific papers. A schematic representation of the outline of the thesis is shown in Figure 1.2 and the main body chapters are structured as follows:

- **Chapter 2** provides a critical review of hydrogen in ironmaking, with emphasis on

differences between conventional and suspension smelting routes. Thermodynamics and kinetics of H_2 and CO reduction are introduced, along with the role of the water-gas shift reaction (WGSR).

- **Chapter 3** presents a detailed material analysis of the three selected ores in this study, followed by an investigation of their thermal decomposition behaviour in the TGA. By a combination of kinetic and microscopical analysis, reaction mechanisms and kinetic parameters are obtained.
- **Chapter 4** examines in-flight thermal decomposition in the HTDF at temperatures of 1658-1760 K, including experiments under low reducing gas conditions. The main points of discussion are the influence of the reduction on the material properties, particle size and density of the reaction products, and the overall pre-reduction degree. The pre-reduction results are compared with TGA data to assess differences between short and long particle residence times.
- **Chapter 5** focuses on isothermal and non-isothermal reduction conditions under H_2-enriched atmospheres at temperatures up to 1773 K. Reaction mechanisms and kinetic parameters are derived for OreB as an example, and the influence of mineralogy and the WGSR is analyzed.
- **Chapter 6** investigates in-flight gas reduction behavior of the three iron ores, combining morphological, mineralogical, and kinetic analysis to understand how particle size, reduction atmosphere, and reduction time influence pre-reduction kinetics and its mechanisms, and compares these findings with isothermal TGA experiments.

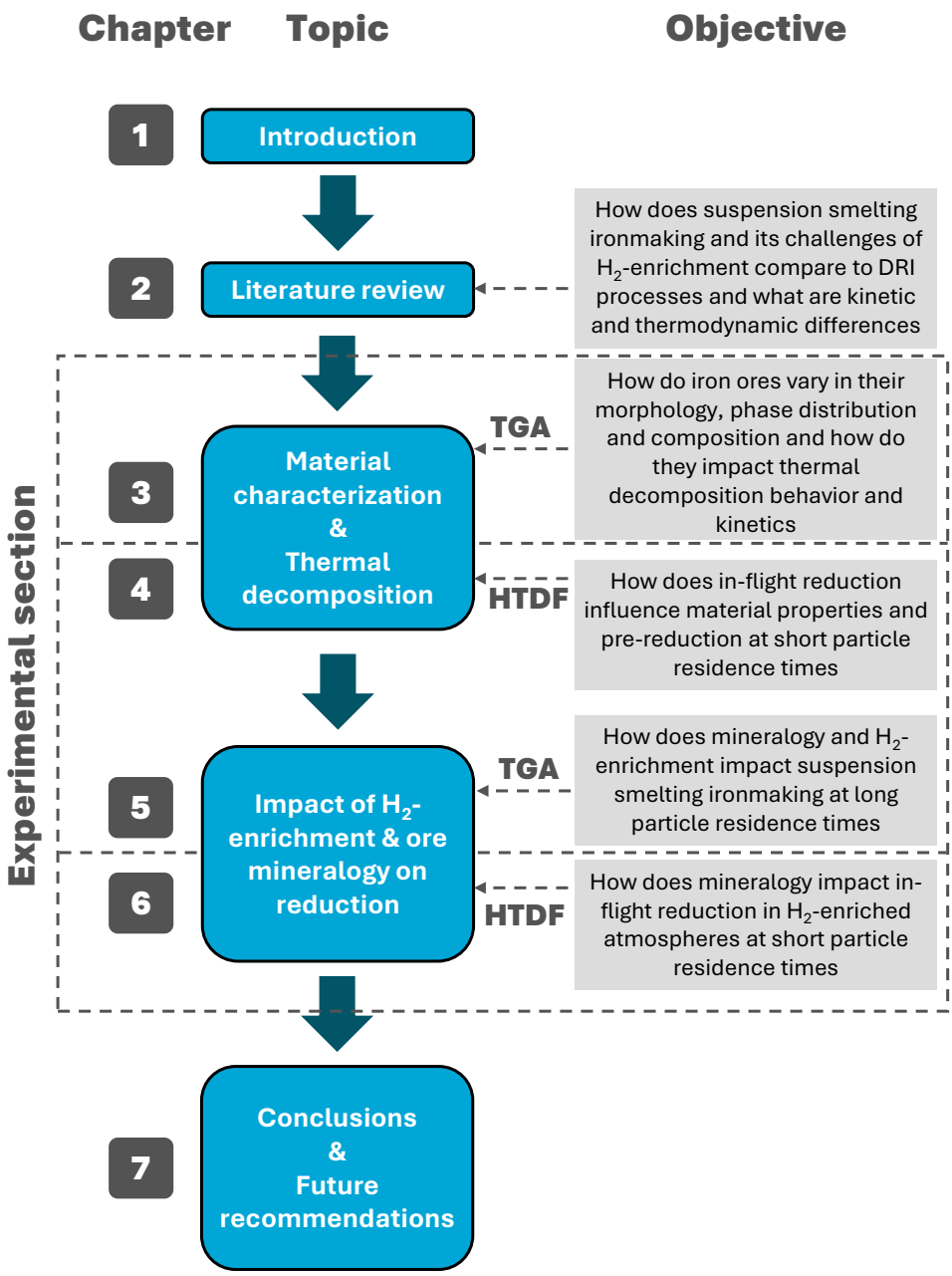


Figure 1.2: Outline of the thesis

1

REFERENCES

[1] Worldsteel Association. Climate change and the production of iron and steel. 2021.

[2] F. Patisson and O. Mirgaux. Hydrogen Ironmaking: How It Works. **Metals** 10, 922 (2020). DOI: 10.3390/met10070922.

[3] Hydrogen Europe. Hydrogen - Enabling a Zero-Emission Society. 2021.

[4] J. R. Vehec. Technology Roadmap Research Program for the Steel Industry. Dec. 2010. DOI: 10.2172/1011081.

[5] Y. Yang, L. Holappa, H. Saxen, and J. van der Stel. Treatise on Process Metallurgy Volume 3: Industrial Processes. Elsevier, 2024. Chap. Ironmaking. DOI: 10.1016/B978-0-323-85373-6.00001-6.

[6] Worldsteel Association. 2025 World Steel in Figures. 2025. URL: https://worldsteel.org/data/world-steel-in-figures/world-steel-in-figures-2025/.

[7] W. Liu, H. Zuo, J. Wang, Q. Xue, B. Ren, and F. Yang. The production and application of hydrogen in steel industry. **International Journal of Hydrogen Energy** 46 (2021), pp. 10548–10569. DOI: 10.1016/j.ijhydene.2020.12.123.

[8] Worldsteel Association. Sustainability performance of the steel industry 2003-2021. 2022.

[9] Roland Berger GMBH. The Future of Steelmaking - How the European Steel Industry Can Achieve Carbon Neutrality. 2020.

[10] M. Pei, M. Petäjäniemi, A. Regnell, and O. Wijk. Toward a fossil free future with hybrit: Development of iron and steelmaking technology in Sweden and Finland. **Metals** 10, 972 (2020). DOI: 10.3390/met10070972.

[11] Hydrogen Europe. Clean Hydrogen Monitor 2020. 2020.

[12] Y. Yang, K. Raipala, and L. Holappa. Treatise on Process Metallurgy. Vol. 3. Elsevier Ltd., 2014. Chap. Ironmaking, pp. 2–88. ISBN: 9780080969886. DOI: 10.1016/B978-0-08-096988-6.00017-1.

[13] V. Vogl, M. Åhman, and L. J. Nilsson. Assessment of hydrogen direct reduction for fossil-free steelmaking. **Journal of Cleaner Production** 203 (2018), pp. 736–745. DOI: 10.1016/j.jclepro.2018.08.279.

[14] K. Meijer, M. Denys, J. Lasar, J.-P. Birat, G. Still, and B. Overmaat. ULCOS: ultra-low CO_2 steelmaking. **Ironmaking & Steelmaking** 36 (2009), pp. 249–251. DOI: 10.1179/174328109X439298.

[15] P. C. Cavaliere. Hydrogen Assisted Direct Reduction of Iron Oxides. Springer International Publishing, 2022. ISBN: 9783030980566. DOI: 10.1007/978-3-030-98056-6.

[16] H. Y. Sohn. Energy consumption and CO_2 emissions in ironmaking and development of a novel flash technology. **Metals** 10, 54 (2020). DOI: 10.3390/met10010054.

[17] H. Y. Sohn. From Sulfide Flash Smelting to a Novel Flash Ironmaking Technology. Celebrating the Megascale. Cham: Springer International Publishing, 2014, pp. 69–76.

[18] H. Y. Sohn. Suspension Hydrogen Reduction of Iron Ore Concentrate in AISI/DOE Technology Roadmap Program for the Steel Industry. Tech. rep. Utah: American Iron and Steel Institute, 2008.

[19] Z. Chen, C. Zeilstra, J. van der Stel, J. Sietsma, and Y. Yang. Review and data evaluation for high-temperature reduction of iron oxide particles in suspension. **Ironmaking & Steelmaking** 47 (2020), pp. 741–747. DOI: 10.1080/03019233.2019.1589755.

[20] Z. Chen, C. Zeilstra, J. van der Stel, J. Sietsma, and Y. Yang. Thermal Decomposition Reaction Kinetics of Hematite Ore. **ISIJ International** 60 (2020), pp. 65–72. DOI: 10.2355/isijinternational.ISIJINT-2019-129.

[21] Y. Qu, Y. Yang, Z. Zou, C. Zeilstra, K. Meijer, and R. Boom. Thermal decomposition behaviour of fine iron ore particles. **ISIJ International** 54 (2014), pp. 2196–2205. DOI: 10.2355/isijinternational.54.2196.

[22] P. Leerhoff, J. C. Brouwer, A. M. Armaki, C. Zeilstra, K. Meijer, J. van der Stel, S. T. Abrahami, N. Dogan, and Y. Yang. Characterisation of Varying Iron Ores and Their Thermal Decomposition Kinetics Under HIsarna Ironmaking Conditions. **Metals** 14, 1271 (2024). DOI: 10.3390/met14111271.

[23] L. Xing, Y. Qu, C. Wang, L. Shao, Z. Zou, and W. Song. Kinetic Study on Thermal Decomposition Behavior of Hematite Ore Fines at High Temperature. **Metallurgical and Materials Transactions B** 51 (2020), pp. 395–406. DOI: 10.1007/s11663-019-01747-1.

[24] T. Battle, U. Srivastava, J. Kopfle, R. Hunter, and J. McClelland. Treatise on Process Metallurgy Volume 3: Industrial Processes. Elsevier, 2024. Chap. The Direct Redcution of Iron. DOI: 10.1016/B978-0-323-85373-6.00011-9.

[25] D. Walter, G. Buxbaum, and W. Laqua. The Mechanism of the Thermal Transformation From Goethite To Hematite. **Journal of Thermal Analysis and Calorimetry** 63 (2001), pp. 733–748.

[26] L. Diamandescu, D. Mihàilà-Tàràbàşanu, and M. Feder. On the solid phase transformation goethite → hematite. **Materials Letters** 17 (1993), pp. 309–311. DOI: 10.1016/0167-577X(93)90019-T.

[27] K. Meijer, C. Zeilstra, C. Teerhuis, M. Ouwehand, and J. van der Stel. Developments in Alternative Ironmaking. **Transactions of the Indian Institute of Metals** 66 (2013), pp. 475–481. DOI: 10.1007/s12666-013-0309-z.

[28] K. Meijer, C. Guenther, and R. J. Dry. HIsarna Pilot Plant Project. METEC InSteelCon 2011, 2011.

[29] J. van Boggelen. Development of a Low CO_2 Iron and Steelmaking Integrated Process Route for a Sustainable European Steel Industry, LoCO2Fe.

[30] T. T. Htet, Z. Yan, B. S. Kumar, J. Hage, K. Meijer, and Z. Li. Study on hydrogen smelting reduction behaviour in synthetic molten HIsarna slag. **Ironmaking & Steelmaking** 50 (2023), pp. 1590–1600. DOI: 10.1080/03019233.2023.2204267.

[31] J. Hage, C. Zeilstra, J. van Boggelen, K. Meijer, J. van der Stel, and T. Peeters. HIsarna: Benefits of an Innovative Smelting-Reduction Ironmaking Technology. AISTech 2021, 2021, pp. 1388–1399. DOI: 10.33313/382/143.

[32] D.-Q. Fan, M. Elzohiery, Y. Mohassab, and H. Y. Sohn. The kinetics of carbon monoxide reduction of magnetite concentrate particles through CFD modelling. **Ironmaking & Steelmaking** 48 (2021), pp. 769–778. DOI: 10.1080/03019233.2020.1861857.

[33] M. Elzohiery, H. Y. Sohn, and Y. Mohassab. Kinetics of Hydrogen Reduction of Magnetite Concentrate Particles in Solid State Relevant to Flash Ironmaking. **steel research international** 88 (2017). DOI: 10.1002/srin.201600133.

[34] D.-Q. Fan, M. Elzohiery, Y. Mohassab, and H. Y. Sohn. Rate-enhancement effect of CO in magnetite concentrate particle reduction by H_2+CO mixtures. **Ironmaking & Steelmaking** 48 (2021), pp. 1064–1075. DOI: 10.1080/03019233.2021.1915645.

[35] D.-Q. Fan, Y. Mohassab, M. Elzohiery, and H. Y. Sohn. Analysis of the Hydrogen Reduction Rate of Magnetite Concentrate Particles in a Drop Tube Reactor Through CFD Modeling. **Metallurgical and Materials Transactions B** 47 (2016), pp. 1669–1680. DOI: 10.1007/s11663-016-0603-3.

[36] D.-Q. Fan, H. Y. Sohn, Y. Mohassab, and M. Elzohiery. Computational Fluid Dynamics Simulation of the Hydrogen Reduction of Magnetite Concentrate in a Laboratory Flash Reactor. **Metallurgical and Materials Transactions B** 47 (2016), pp. 3489–3500. DOI: 10.1007/s11663-016-0797-4.

[37] Y. Qu, Y. Yang, Z. Zou, C. Zeilstra, K. Meijer, and R. Boom. Kinetic study on gas molten particle reduction of iron ore fines at high temperature. **Ironmaking and Steelmaking** 42 (2015), pp. 763–773. DOI: 10.1179/1743281215Y.0000000021.

[38] Y. Qu, Y. Yang, Z. Zou, C. Zeilstra, K. Meijer, and R. Boom. Reduction kinetics of fine hematite ore particles with a high temperature drop tube furnace. **ISIJ International** 55 (2015), pp. 952–960. DOI: 10.2355/isijinternational.55.952.

[39] Y. Qu, Y. Yang, Z. Zou, C. Zeilstra, K. Meijer, and R. Boom. Melting and reduction behaviour of individual fine hematite ore particles. **ISIJ International** 55 (2015), pp. 149–157. DOI: 10.2355/isijinternational.55.149.

[40] F. Chen, Y. Mohassab, T. Jiang, and H. Y. Sohn. Hydrogen Reduction Kinetics of Hematite Concentrate Particles Relevant to a Novel Flash Ironmaking Process. **Metallurgical and Materials Transactions B** 46 (2015), pp. 1133–1145. DOI: 10.1007/s11663-015-0332-z.

[41] F. Chen, Y. Mohassab, S. Zhang, and H. Y. Sohn. Kinetics of the Reduction of Hematite Concentrate Particles by Carbon Monoxide Relevant to a Novel Flash Ironmaking Process. **Metallurgical and Materials Transactions B** 46 (2015), pp. 1716–1728. DOI: 10.1007/s11663-015-0345-7.

[42] Z. Chen, C. Zeilstra, J. van der Stel, J. Sietsma, and Y. Yang. Reduction Mechanism of Fine Hematite Ore Particles in Suspension. **Metallurgical and Materials Transactions B** 52 (2021), pp. 2239–2252. DOI: 10.1007/s11663-021-02173-y.

[43] Z. Chen, C. Zeilstra, J. van der Stel, J. Sietsma, and Y. Yang. Reduction Kinetics of Fine Hematite Ore Particles in Suspension. **Metallurgical and Materials Transactions B** 52 (2021), pp. 3393–3402. DOI: 10.1007/s11663-021-02269-5.

[44] P. C. Beuria, S. K. Biswal, B. K. Mishra, and G. G. Roy. Study on kinetics of thermal decomposition of low LOI goethetic hematite iron ore. **International Journal of Mining Science and Technology** 27 (2017), pp. 1031–1036. DOI: 10.1016/j.ijmst.2017.06.018.

[45] B. Lyu, G. Wang, F. Yang, H. Zuo, Q. Xue, and J. Wang. Kinetic Analysis of Isothermal and Non-Isothermal Reduction of Iron Ore Fines in Hydrogen Atmosphere. **Metals** 12, 1754 (2022). DOI: 10.3390/met12101754.

[46] A. Hammam, Y. Li, H. Nie, L. Zan, W. Ding, Y. Ge, M. Li, M. Omran, and Y. Yu. Isothermal and Non-Isothermal Reduction Behaviors of Iron Ore Compacts in Pure Hydrogen Atmosphere and Kinetic Analysis. **Mining, Metallurgy & Exploration** 38 (2021), pp. 81–93. DOI: 10.1007/s42461-020-00317-3.

[47] N. Dilmaç. Isothermal and non-isothermal reduction kinetics of iron ore oxygen carrier by CO: Modelistic and model-free approaches. **Fuel** 296 (2021), p. 120707. DOI: 10.1016/j.fuel.2021.120707.

[48] Y. Qu. Experimental Study of the Melting and Reduction Behaviour of Ore Used in the HIsarna Process. PhD thesis. Technische Universiteit Delft, 2013.

2

H_2 ADAPTATION IN IRONMAKING: A REVIEW WITH FOCUS ON SUSPENSION SMELTING AND ITS REACTION MECHANISMS

Suspension smelting technology is emerging as a promising alternative in ironmaking to conventional hydrogen-based direct reduction (H-DRI) for low-carbon ironmaking. Unlike the slower solid-state reactions in DRI processes, suspension smelting uses rapid in-flight reduction of fine iron ore particles. Within seconds the ore fines undergo several phenomena like heating up, phase transformation, reduction and partially melting, due to the high temperatures. This review explores hydrogen adaptation in suspension smelting technologies such as the Flash Ironmaking Technology (FIT) and the HIsarna® process. The key reaction mechanisms, thermal decomposition and gas reduction with H_2*/CO, are examined through thermodynamic and kinetic analysis. A comparison of reduction kinetics between classical DRI processes and suspension smelting is provided, highlighting the significantly faster reaction rates of suspension smelting. Finally, the influence of the water-gas shift reaction and its potential negative impact on the reduction behaviour is analysed.*

This chapter has been published in P Leerhoff et al. "H_2 adaptation in ironmaking: a review with focus on suspension smelting and its reaction mechanisms." In: Mineral Processing and Extractive Metallurgy: Transactions of the Institutions of Mining and Metallurgy **2026** [1].

2.1. INTRODUCTION

The steelmaking industry accounts for 7 to 9 % of the global anthropogenic emitted CO_2-emissions [2], with an annual contribution estimated around 2.6 Gt (2019) [3]. The conventional iron- and steelmaking route is commonly based on either the blast furnace (BF) or the direct reduction of iron ores as initial ironmaking step [4]. In 2019, the amount of pig iron produced by the blast furnace was 1280.7 Mt, while the amount produced by direct reduced iron (DRI) was 107.6 Mt, indicating the much stronger industrial presence of the blast furnace [5]. In BF ironmaking, iron ore is transferred to molten metallic iron which can be directly casted to pig iron or mixed and treated with recycled steel in a Basic Oxygen Furnace (BOF), whereas solid iron is produced by direct reduction which is treated together with recycled steel in the electric arc furnace (EAF) to create molten steel [4]. Around 75 % of iron used in the BOF steelmaking route is based on the BF hot metal and around 25 % is scrap. In contrast, the EAF can run on up to 100 % scrap, but also utilize large shares of DRI [6, 7]. The World Steel Association summarizes H_2-emissions and energy consumption for the main steelmaking routes [8]. Data from 2021 [8] shows that most of the global steel production (71 %) is based on the BF-BOF route. However, this route is responsible for high energy consumption and the most CO_2-emissions. Even though DRI based steelmaking shows (slightly) higher energy intensity compared to the BF-BOF route, its CO_2-emissions are lower. Lastly, recycling route using scrap as an input in the EAF shows the best environmental performance, both in terms of energy consumption and CO_2-emissions. While recycling is clearly the most sustainable option, recycling alone cannot fulfil the ever-growing demand for steel. Hence, primary production will remain significant in the future [9].

Table 2.1: CO_2-emissions and energy consumption of steelmaking routes in 2021 [8].

	CO_2-emission intensity [$\frac{t_{CO_2}}{t_{\text{crude steel}}}$]	Energy intensity [GJ/$t_{\text{crude steel}}$]	Share in global production [%]
Global average	1.91	21.31	100
BF–BOF	2.32	24.43	71
Scrap–EAF	0.67	10.04	22
DRI–EAF	1.65	25.29	7

The conventional steelmaking route heavily depends on the use of carbon in the form of coal or coke as a reducing agent [10]. The EU aims to become carbon neutral by 2050 and to cut 55 % of its emissions by 2030 [11], which forces the steel industry, as a large emitter, to move towards more sustainable production. Multiple strategies have been investigated to help reduce carbon emissions. Examples include the use of carbon capture and storage/use (CCS/U), the use of biomass in the reduction process, plasma-based iron ore reduction or electrolytic approaches [12]. Yet, the most popular approach to actively decrease the emitted CO_2 from the production process is using green hydrogen to substitute carbon as reducing agent for iron ore [12]. The adaptation of H_2 in ironmaking processes could lead to various advantages compared to carbon-based reduction. First, pure H_2-based reduction will only emit H_2O. Secondly, H_2 shows faster kinetics compared to carbon-based reduction [10], resulting in a higher productivity. However, problems can also arise from utilizing H_2. In contrast to CO reduction, the reduction of iron oxides with hydrogen is endothermic [7], requiring additional (external) energy supply to keep

the high temperatures needed during the process. In addition, carbon is an essential component for the transition of iron to steel, which cannot be completely omitted [13].

To decrease the CO_2-emissions arising from this intense use of carbon, hydrogen is increasingly investigated as a substitute. Ironmaking processes utilizing hydrogen as a reducing gas can be classified based on the type and shape of input material, the reducing gas composition or furnace technology, where for example shaft furnace processes like MIDREX operates with pellets and fluidized bed applications like CIRCORED with fine ore as an input material [14]. Most H_2 adaptation nowadays focuses on the direct-reduced iron (DRI) processes, where the shaft furnace is currently at the furthest state considering the technology readiness [12]. However, processes like HIsarna, developed by Tata Steel, and the Flash Ironmaking process, developed by the university of Utah are two new alternative ironmaking approaches based on the principle of suspension smelting [15, 16]. A significant difference of the suspension smelting process compared to the DRI processes are the much higher temperatures, which lead to a faster reduction, within seconds [16, 17]. Since such high temperatures are not achieved during DRI processes, the resulting reaction mechanisms differ and include thermal decomposition next to gas-reduction [16]. Moreover, these processes are more flexible in their input material, leading to a more sustainable ironmaking by eliminating the material pre-treatment steps [12]. This review explores the differences between the two methods, covering H_2 adaptation in both DRI and suspension smelting processes [15]. Next, the two reaction mechanisms in suspension smelting, thermal decomposition and gas reduction, are discussed in terms of thermodynamics and kinetics and compared to the more established DRI technology.

2.2. HYDROGEN IN DRI PROCESSES

2.2.1. DRI IN SHAFT FURNACE

Direct reduction refers to the one-step conversion of iron ore to solid metallic iron using gas-based or coal-based reduction technologies [7]. In direct reduction ironmaking, gas-based reduction is responsible for over 90 % of the annual DRI output [18, 19]. DRI is primarily used as feedstock for the EAFs or as clean alternative to scrap iron in the BOF [20]. The most established DRI technology is the MIDREX process, operating in the shaft furnace. Around 60 % of global DRI production can be assigned to it. It uses pellets or lump ore as input material and reformed natural gas (primarily hydrogen and carbon monoxide) as reducing agents. The raw material is charged into the furnace from the top, while the reducing gas is blown in at the middle. The exhaust gas leaves the shaft furnace at the top and is cleaned, cooled and reintroduced into the process. To create the reducing gases, the exhaust gas (containing H_2O and CO_2) is pressurized, mixed with natural gas, heated and passed through a reformer to produce CO and H_2. After reduction, the DRI is discharged at the bottom of the shaft furnace [20]. The reducing gas composition of the MIDREX process varies between 24-36 % CO, 40-60 % H_2, with N_2 as the remaining part [18]. To decrease emissions even further, natural gas can be mixed with pre-heated hydrogen before the reducing gas mixture is injected into the shaft furnace. This can decrease the use of natural gas in a MIDREX plant by up to one-third [21]. To achieve a complete transition from natural gas to hydrogen, ArcelorMittal is investigating a direct reduction demonstration plant based on the MIDREX process in Hamburg Germany in

the framework of the H_2-project [22]. The plant in Hamburg currently operates with natural gas. The objective is to utilize 100 % hydrogen as reductant with a production of 100,000 tDRI/a by the end of 2025 [22, 23]. Another commercial shaft furnace based DRI process is HYL, operating with natural gas or coal based (Energiron HYL) [24]. An advantage of HYL is the possibility to recycle its reducing gases and recharge some H_2 and CO back into the DR plant [25]. However, the production share of HYL is currently lower compared to MIDREX and accounts for approximately 15 % of DRI output [26].

Figure 2.1 shows a general illustration of a possible decarbonized steelmaking route by hydrogen-based direct reduction (H-DRI) compared to natural gas in a classic MIDREX furnace, with the resulted DRI converted to steel together with scrap in an EAF. In this illustration, emissions are further reduced with the hydrogen supply to DRI generated based on electrolysis with renewable electricity. The hydrogen and iron ore are fed to the DRI process, resulting in either direct reduced iron (DRI) or made into hot briquetted iron (HBI) as output. The resulting product can then be fed into the EAF (with the option of adding more steel scrap), resulting in crude steel as a final product.

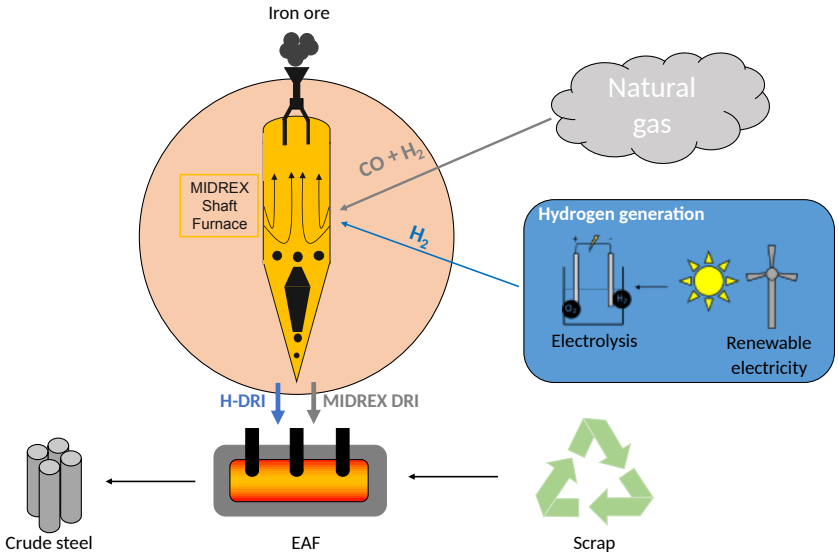


Figure 2.1: Decarbonization of steelmaking based on H-DRI and EAF route, adapted from [20] with permission from Kobelco and from [27].

2.2.2. DRI IN FLUIDIZED BED REACTOR

In the framework of gas-solid reduction processes based on hydrogen as the reducing gas, fluidized bed (FB) technology is an alternative to shaft furnaces. The reaction takes place in fluidized bed reactor chambers, where fine iron ores and reducing gases are continuously injected and brought in contact with each other [12]. The use of fine ores as input material leads to further reduction in the environmental footprint since no prior agglomeration of the material is necessary, eliminating the CO_2-emissions arising in

these pre-processing step [28]. In general, fluidized bed technology can achieve higher metallization (95 %) compared to the shaft furnace (90 %) due to less sticking problems of the fine ores compared to the pellets in the shaft furnace [12]. However, the application of fluidized bed technologies also brings disadvantages, leading to less market dominance than the shaft furnace-based processes. First, fine ores have a wide distribution of particle sizes, meaning that not all particles can be fluidized equally during the process. A second drawback is the trade-off between low and high temperatures during the process. While a high temperature leads to kinetic advantages and counter acts the endothermic reaction behaviour of hydrogen-based reduction, a lower temperature would prevent sticking of the fine ores during the process [6]. Industrial processes using fluidized bed technology are FINMET and the Metso Outotec CIRCORED. In contrast to the FINMET process, the CIRCORED process uses pure hydrogen as a reducing gas [28]. The CIRCORED process is based on a two-stage reduction process. First, the ores are treated in a circulating fluidized-bed (CFB) reactor. The CFB reactor can be defined as a pre-reduction stage, where 70 % metallization is reached. Since the reactions taking place in the CFB reactor are endothermic, energy is supplied by pre-heating the fine ores and through the combustion of natural gas and air. Processing of fine ores at high temperatures can lead to sticking of the material. To prevent this, the CFB reactor only operates at 630 °C. Next, the material from the CFB is supplied to the second stage, the fluidized bed reactor. Here, final reduction takes place to achieve metallization rates of 92-93 % at temperatures of 850-900 °C. The off-gas from the second stage fluidized-bed reactor is reintroduced into the CFB reactor as a secondary process gas. Briquetting requires a material temperature of approximately 700 °C. Therefore, the reduced iron is supplied to a flash heater before briquetting [14, 15, 29]. If pure hydrogen is used, the final product of the CIRCORED process shows no carbon contents [14].

2.3. SMELTING REDUCTION IRONMAKING

Even though the dominant trend in Europe is moving in the direction of establishing H-DRI processes for ironmaking [3, 30], smelting reduction is another alternative that can reduce the carbon footprint of iron production. Smelting reduction currently accounts for 7.5-7.8 Mt iron per year [18], a much low number compared to the 1354 Mt (2021) produced by the blast furnace and 114 Mt (2021) produced by DRI technology [15]. The COREX and FINEX processes (illustrated in Figure 2.2) are the only commercially available smelting reduction installations. In general, smelting reduction combines an iron ore pre-reduction step, followed by smelting in a reactor without coke usage. The product is liquid pig iron, which is comparable to the hot metal exiting the blast furnace [7]. The initial pre-reduction stage follows the DRI principle and can be performed in a shaft furnace (Figure 2.2 (a)) or fluidized bed (Figure 2.2 (b)), at comparable low temperatures (800 – 900 °C). However, it is now followed by a melting stage (Figure 2.2 (c)) operating at a much higher temperatures of 1000 – 1800 °C, depending on zones of the melting reactor [31]. Another difference from the DRI processes is the ratio of CO and H_2 in the reducing gasses. In smelting reduction, the hydrogen content is usually much lower [18]. The hydrogen content in COREX is 20-25 % [15] and therefore relatively lower than the 40-60 % in MIDREX [18].

The COREX process is commercially the most common form of smelting reduction [7].

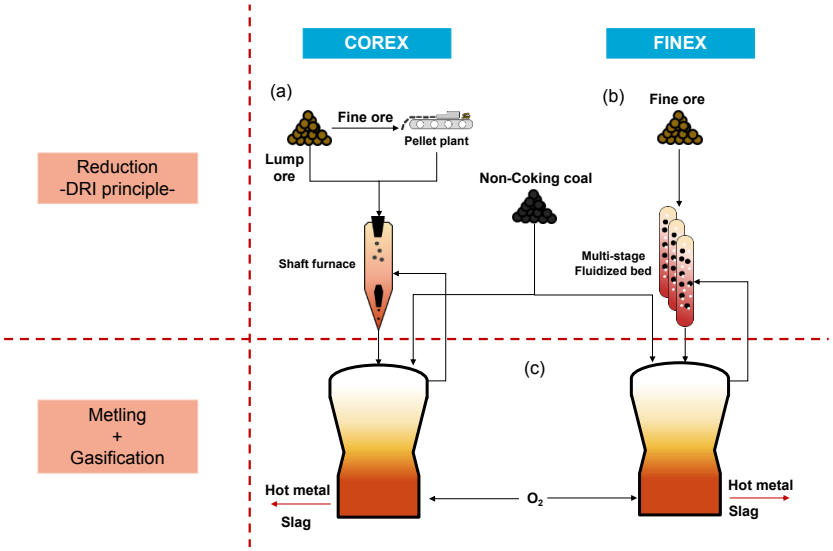


Figure 2.2: Simplified presentation of a COREX and FINEX process, adapted from [15] with permission from Elsevier.

A commercial example of COREX implementation is JSW Steel in India, implementing the world's biggest COREX based DRI plant (2014) [32]. COREX works in 2 stages. In the first step, the reduction from iron ore to sponge iron takes place. This pre-reduction works according to the shaft furnace principle with CO and H_2 as reducing gasses. The reducing gasses are obtained by the gasification of coal with a resulting composition containing between 65-70 % CO, 20-25 % H_2 and 2-4 % CO_2. The reduced iron ore is then melted during the second step in a melter-gasifier. The resulting heat, from the coal combustion, is used to melt the reduced ore which drops from the shaft furnace to the melter-gasifier. The hot gas then leaves the melter-gasifier and is mixed with a cooling gas to reach a temperature of 850 °C. After purification of the gas, it is fed back to the shaft furnace as a reducing gas [7].

The FINEX process can be considered as a variant of the COREX process, with the first commercial plant of POSCO in Pohang started operating in 2007. The main difference is that the FINEX process uses fine ore, while COREX uses lump ore and pellets. Furthermore, the reduction process is based on the fluidized bed principle instead of the shaft furnace [7]. Generally, FINEX operates as four-unit process with a multi-stage fluidized bed reactor as pre-reduction steps, hot-compacting, coal-briquetting and a melter-gasifier needed for the final reduction [33]. Compared to the shaft furnace approach of the COREX process, the fluidized bed approach leads to a better contact between the reducing gasses and the material. The more uniform gas flow and ore distribution leads to more even reduction degrees of the material compared to the pellets in the shaft furnace [33]. FINEX allows to operate with low-cost fine ores with a higher content of iron oxide, thereby reducing costs and emissions for the input material and generating gases which can be reused in power generation and metallurgical applications [34]. To further reduce CO_2-emissions, POSCO

plans to continue the transition from coal to H_2 as reducing agent in its ironmaking processes by 2050 [34]. The newly planned HyREX approach, based on FINEX technology, will help POSCO achieve carbon neutrality. In this new approach, DRI will be produced in fluidized bed reactors with 100 % H_2 (compared to the current 25 % H_2) before being processed in an EAF to molten iron [35, 36].

Another commercially available smelting reduction technology is HIsmelt, developed by Rio Tinto. HIsmelt is a single-reactor smelting reduction process, currently operating in China (Molong plant) [15, 37]. Before being injected into the smelting bath, fine ores can be pre-heated and partially reduced for example by means of a two-stage circulating fluidized bed reactor [38, 39]. In the HIsmelt reactor reduction and melting of pre-reduced fine iron ores occur simultaneously [40, 41]. The fine ores, fluxes, and coal are injected directly into a molten metal bath ($\approx$ 1673 K), which is covered by a layer of molten slag. The injection is performed via water-cooled lances, while a hot oxygen-enriched air blast post-combusts the off-gases generated during iron oxide reduction [37]. The submerged injection of the solid reagents further induces stirring, causing slag droplets to erupt into the upper regions of the reactor, promoting heat transfer from the post-combustion zone into the liquid slag/metal zone [37, 40].

At the Molong plant (in operation since 2016), rotary kilns are used for the pre-treatment of the ores. The first kiln dries the hematite ores, while the second heats them up to around 1073 K using pulverized coal combustion [37]. An advantage of HIsmelt over the blast furnace is its ability to process ores with high phosphorus content without significantly increasing the phosphorus content in the liquid iron, due to the more oxidizing conditions in the reactor [40].

From a sustainability perspective, HIsmelt theoretically allows partial substitution of coal with H_2 [38, 42]. However, no industrial implementation exists to date [38]. Other potential improvements include the use of sustainable biomass (converted to biochar) to replace coal, enrichment of H_2 during the ore pre-reduction, or CO_2-capture from off-gases [42].

2.4. SUSPENSION SMELTING IRONMAKING

Two new approaches currently under development utilize a method known as suspension smelting ironmaking. The reduction part of the process takes place in suspension, using flash or cyclone processes, leading to the reduction of iron ore fines at high temperatures and short particle residence times (seconds) [43]. One such process under development is the Flash Ironmaking Technology (FIT), which is investigated at the University of Utah [44–49]. In the FIT, iron ore concentrates are reduced in a flash reactor using reducing gases such as hydrogen, natural gas, bio/coal gas or their mixtures. In the case of natural gas and pure hydrogen, the injected mixtures are H_2+CO+H_2O+CO_2 and H_2+H_2O, respectively. This technology could be scaled up to industrial applications with the prerequisite that the concentrate is smaller than 100 μm [17]. In terms of energy efficiency and emission savings, the advantages of this technology arise from the input material, since no agglomeration or coking steps are necessary as pre-treatment. Another advantage is the very short residence times (only seconds) needed for reduction at the operating temperatures of 1473 to 1873 K [17]. Total energy savings using FIT are expected to be around 38 % compared to the traditional blast furnace route [49]. Additional

advantage is the combination of the two-steps previously discussed in smelting reduction [45]. The process could be established in an overall continuous direct steelmaking route, leading to products in either molten- or solid state for EAF steelmaking [17].

The development of FIT started in 2005, primarily at the University of Utah with support from the U.S. Department of Energy [49]. The article by Sohn, Elzohiery and Fan [50] provides a comprehensive overview of the research progress achieved within FIT related projects. Early studies focused on understanding reaction kinetics under FIT conditions and on formulating reduction rate equations in temperature range of 1423 – 1873 K [51–55]. These investigations demonstrated that high metallization degrees of magnetite fine ores could be achieved within seconds. Building on the kinetic analysis, studies were subsequently conducted utilizing a laboratory flash reactor operating at temperature between 1423 and 1473 K [56–58]. Applying $H_2 - H_2O$ mixtures, reduction degrees exceeding 90 % were obtained. In contrast, experiments employing post-combustion of methane with pure oxygen generated reducing gas mixtures of $H_2 + CO + H_2O + CO_2$, but resulted in lower overall reduction degrees (approx. 80 %).

In a subsequent step, upscaling of the process to pilot scale was investigated. The pilot flash reactor, with a reactor volume of 1.01 m^3, was operated at temperatures between 1473 and 1823 K and material feeding rates ranging from 1 to 7 kg/h. The pilot-scale experiments demonstrated good reproducibility, and complete reduction was achieved at temperatures between 1573 and 1673 K using H_2 with an excessive driving force of 1.51, a fine ore feeding rate of 5 kg/h, and a nominal particle residence time of 14.6 s. Overall, these results indicted the technical feasibility of up-scaling FIT towards industrial iron production [50, 59]. To further support the scale-up efforts, a CFD model of the laboratory flash reactor was extended and refined based on the experimental findings obtained from the pilot-scale reactor [60]. Despite FIT being regarded as a promising technology for next-generation, low-emission ironmaking, challenges remain with respect to large-scale implementation. To the author's knowledge, no additional upscaling efforts beyond the pilot-scale investigations reported in the literature have been made public.

Another process utilizing the principle of suspension smelting is the HIsarna® process. HIsarna was developed in the framework of the ULCOS (Ultra-low-CO_2-steelmaiking) initiative [61]. The initiative (2004) aimed to reduce 50 % of CO_2-emissions per ton of steel in a production based on iron ores as input material [61]. As part of the initiative, a pilot plant was built at Tata Steel in IJmuiden (Netherlands), with construction completed in 2010. The hot metal capacity of the pilot plant is approx. 65 ktpa (≈ 8 t/h) [62]. HIsarna combines the two process steps of a cyclone converter furnace (CCF) and a smelting reduction vessel (SRV) into a single furnace (Figure 2.3), operating in a counter-current principle, where the injected iron ores are in contact with the hot processing gases [63]. Overall, HIsarna can be categorized as smelting reduction technology, due to final melting in the SRV, which is based on HIsmelt technology [15]. However, the mechanism occurring in the CCF (top part) of the furnace can be compared to suspension smelting. HIsarna operates by injecting the iron ores at the top of the CCF section of the furnace, together with oxygen and potentially also fluxes [64]. The upcoming off-gases from the SRV containing pre-heated H_2 and CO gases, result in the pre-reduction and even melting of the injected ores, since temperatures in the CCF can reach up to 1773 K [64]. Due to the high temperatures, two reaction mechanisms can influence the reduction of the injected

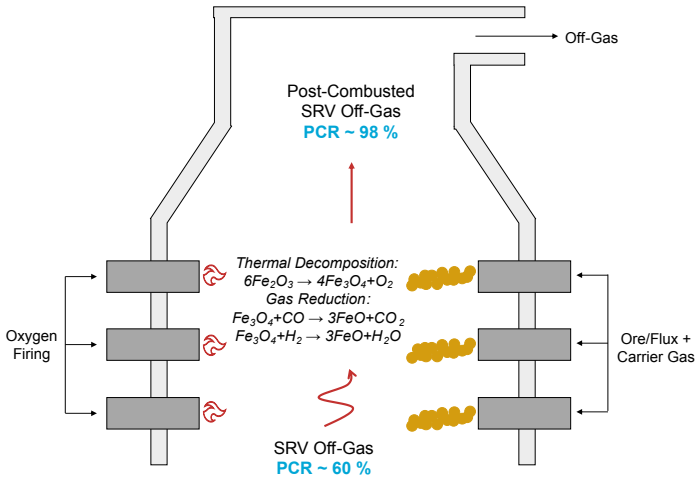
ores: thermal decomposition and gas reduction [16]. The gas reduction ability of the SRV off-gas is described by the post-combustion ratio (PCR) that gives the percentage of the total CO and H_2 that was converted to CO_2 and H_2O, as in Eq. (2.1) [63]:

$$PCR = \frac{\%CO_2 + \%H_2O}{\%CO + \%CO_2 + \%H_2 + \%H_2O} \times 100 \tag{2.1}$$

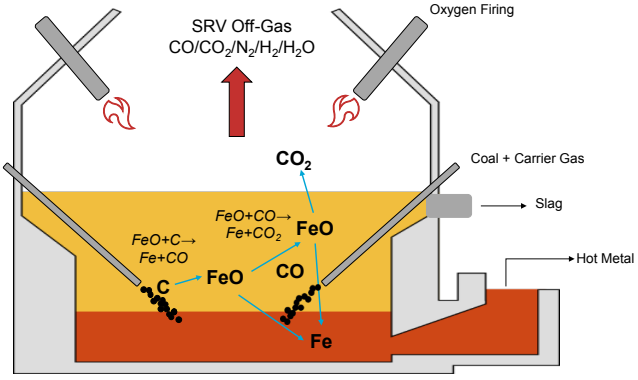
When the off-gases from the SRV enter the CCF, the gas composition is characterized by a PCR of around 60 % and contains usually more CO (32 %) than H_2 (3.4 %) [64]. While reacting with the injected ores, the off-gas is further oxidized, reaching PCRs values of around 98 % at the end of the CCF, consisting of mainly CO_2 and H_2O and only marginal amounts of reducing gases [64]. In the CCF section, reduced ore exhibits pre-reduction degrees of 20-25 % which indicates FeO as the main product. Following the pre-reduction, the molten droplets directly fall into the SRV section, where the final reduction to liquid iron is achieved by the injection of coal into the molten bath [65].

Hot commissioning and the first pilot campaign (campaign A) were carried out in 2011. Between 2011 and 2014, a total of four pilot campaigns (A-D) were conducted, each consisting of multiple production runs over several months. The main objective was the verification of technical feasibility and stable operation of HIsarna. These campaigns further revealed high flexibility in raw materials quality (including steel scrap, dust and sludge utilization) and supplied the first hot metal to a BOF plant [62]. Campaigns B and C specifically aimed to improve the production rate compared to campaign A, to increase the run length, and optimize key parameters such as the PCR, oxygen distribution in the reactor and coal injection. The increase of PCRs from approx. 80 % to 90-95 % was achieved and led to higher production rates (up to 6 $t_{hot\ metal}$/h) and reduced specific coal consumption. During these campaigns the influence of ore particle size and dust losses were quantified and stable hot metal chemistries with very low Si (<0.02%), Mn (<0.02%), and P (0.015-0.03%), contents demonstrated [66]. After conclusion of campaign D, the main objective was to demonstrate industrial feasibility of the process, and therefore demonstrate strong CO_2 reduction potential at long runs with stable operation. To achieve this, the pilot plant underwent major upgrades between 2014 and 2017. These changes were for example, the off-gas handling system, addition of raw materials handling and preparation area, and a scrap handling system [62].

In terms of environmental footprint, HIsarna provides the same advantages as FIT due to the direct production of liquid hot metal from iron ores without pre-treatment of the coke (coking) or ore agglomeration [40]. In combination with carbon capture and storage (CCS) technology, HIsarna can save up to 80 % of CO_2-emissions compared to the traditional blast furnace ironmaking [15]. In order to further improve HIsarna from an environmental perspective, it is possible to partly substitute the injected coal with biomass, natural gas or hydrogen [67]. Earlier studies indicated the potential to replace around 40% of fossil coal with the more sustainable charcoal. Even though complete removal of the solid carbon source is not possible for HIsarna to guarantee carburisation of the hot metal, injection of gaseous reducing agents (CH_4, H_2) could further improve the process [67]. Another advantage of HIsarna is the flexibility in the input material, since it is also possible to use low-grade ores and secondary materials from the steel production [63, 67]. The first pilot plant trials utilizing scrap and biomass-derived charcoal were



(a)



(b)

Figure 2.3: Schematic of HIsarna process with (a) the CCF top and (b) the SRV bottom section shown separately, adapted from [64], CC BY 4.0 license.

conducted in 2017-2018, as part of the H2020 LoCO2Fe project, demonstrating low CO_2-potential (55 % lower than HIsarna base case). Stable operation with up to 37 % hot metal produced from scrap and up to 42 % renewable carbon input was achieved [62].

More recently (2022), accumulated pilot data have been used to develop fundamental process models for HIsarna, describing the chemical, physical and thermodynamic phenomena of the process. This model is used to support further up-scaling of the process by combining theory with plant data. The model devides HIsarna into two parts, consisting of the "main process" and the "secondary process". The two parts consist of 7 zones. The main process includes the hot metal (zone 1), slag (zone 2) and evolved gas (zone 3), while the secondary process includes metal splash, char and volatiles above the slag layer (zone 4), metal droplets in the slag layer (zone 5), the surplus carbon in the metal (zone 6), as well as the process gases from both the smelting and pre-reduction section (zone 7) [68]. In 2025, following the successful pilot-scale operations and trials in IJmuiden, Tata Steel has approved the initiation of engineering and regulatory activities for a 1 million t/a HIsarna demonstration plant in Jamshedpur (India), signalling its strategic intent to advance the low-carbon technology towards industrial development [69].

Another process worth mentioning in the framework of flash ironmaking technologies, utilizing H_2, is ZESTY (Zero Emissions Steel Technology) (Figure 2.4), which is currently under development and tested in pilot plant scale by Calix in Australia [70, 71]. Due to its lower reaction temperatures of 950 to 1100 °C compared to HIsarna and the FIT, the ZESTY process creates a DRI powder product, even though it follows more the principle of the flash ironmaking technology [71, 72]. Therefore, ZESTY doesn't operate in suspension, but in the temperature range of classic DRI processes. Pilot testing has been done with a large range of particle size distributions (< 500 μm) of several Australian iron ore samples, where most were mixtures of hematite and goethite, but also ores with magnetite as iron bearing phase [70–72]. The iron ores are fed from the top using a screw feeder and are following reduced over the length of the furnace (18 m) by H_2, flowing in counter-current contact with the ores. The product is water-cooled to stop following reactions [71]. With approximate residence times of 60 s the reduction is longer compared to the FIT and pre-reduction in HIsarna, but significantly shorter that the reduction in a MIDREX shaft furnace, which can take several hours [71]. In pilot testing, ZESTY was able to achieve high metallization degrees of 98 %. The tested magnetite ores achieved lower metallization compared to the hematite/goethite mixtures, explained by lower surface area and porosity [70].

Comparing HIsarna and the FIT to other smelting reduction processes like COREX and FINEX, the main difference is the pre-reduction of the ores. While in COREX and FINEX pre-reduction is based on the DRI principle, HIsarna and FIT rely on suspension smelting technology, in which the ores are pre-reduced at significantly higher temperatures and shorter residence time, making use of the accelerated kinetics of gas reduction and thermal decomposition at high temperatures [16]. The following sections discuss in detail the two reaction mechanisms, namely; thermal decomposition and gas reduction responsible for reduction in suspension smelting and compare them to the reduction mechanisms in DRI processes.

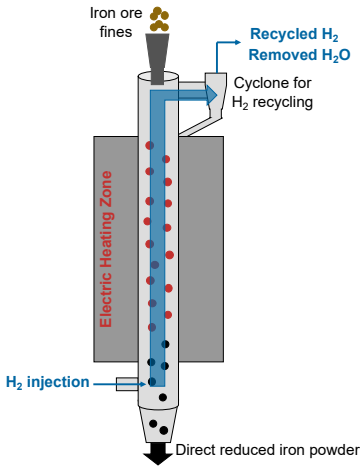


Figure 2.4: Schematic of the ZESTY process, adapted from [71, 72], CC BY 4.0 license and public report.

2.5. REACTION MECHANISMS IN SUSPENSION SMELTING

Due to the much higher temperatures in suspension smelting ironmaking, thermal decomposition of the iron ore plays a crucial role in addition to gas reduction. In considering the thermal decomposition, it is important to account for the presence of multiple iron-bearing phases in the ore. Some interesting ores to consider from an industrial perspective are magnetite (Fe_3O_4), hematite (Fe_2O_3) and goethite (FeOOH), while many others are mined as well [15]. The main reactions of interest are the dehydration of the goethite phase, as well as oxygen removal from the hematite phase, which are discussed separately.

2.5.1. THERMAL DECOMPOSITION OF GOETHITE

At relatively low temperatures, goethite transforms into hematite under the release of water-vapour, following Eq. (2.2): [73]

$$\alpha - 2\mathrm{FeOOH} \rightarrow \alpha - \mathrm{Fe_2O_3} + \mathrm{H_2O} \tag{2.2}$$

The temperature range of goethite thermal decomposition has been studied by Walter et al. [74] for several goethite ores with varying particle sizes and specific surface areas. They determined that the initiation temperature for dehydration varies between 465 and 523 K and found a single or two stage process decomposition process, depending on ore properties (specific surface are and particle geometry). The peak temperature varied between 545 and 551 K for the first stage and between 578 and 595 K for the second stage. Ammasi [75] investigated the decomposition for several heating rates and observed similar initiation temperatures, with complete conversion occurring between 593 and 623 K (higher temperature corresponding to higher heating rates).

Several experimental studies [76–79] have been conducted under non-isothermal conditions to determine the kinetic parameters and mechanisms of the goethite dehydration, with the results of selected studies presented in Table 2.2. Przepiera and Przepiera [78] described goethite decomposition based on Eq. (2.3), in which the removal of water first

creates an amorphous hematite phase before forming crystalline hematite at increasing temperature.

$$\alpha - \mathrm{FeOOH} \rightarrow \mathrm{Fe_2O_3}\,(\text{amorphous phase}) \rightarrow \alpha - \mathrm{Fe_2O_3}\,(\text{hematite}) \tag{2.3}$$

They determined that the overall decomposition reaction is controlled by nucleation. Grygar et al. [79] and Leerhoff et al. [77] also reported a two-stage decomposition of goethite but proposed separate mechanisms. Both identified chemical reaction control in the first stage and diffusion in the second. Other studies, such as Beuria et al. [80], suggest that the overall reaction is governed by nucleation in isothermal conditions. While the studies which report nucleation as dominant mechanism [78, 80], indicate lower activation energies, the values of Beuria et al. are comparable to Leerhoff et al. for ores with lower goethite content during the reaction controlled stage. In contrast, Grygar et al. reported significantly higher activation energies across both stages. Leerhoff et al. further found, that an increasing goethite content in the ore raises the activation energy for the chemical reaction controlled, but reduces it for the diffusion controlled stage. These results indicate that the amount of goethite in the ore does not have an influence on the decomposition mechanism, but on the activation energy needed to initiate the stage dependent reaction.

Table 2.2: Kinetic findings of goethite thermal decomposition.

Reference	Temperature [K]	Atmosphere	Heating Rate [K/min]	Method	Mechanisms	Activation Energy [kJ/mol]
López et al. [76]	RT–1723	Ar	5–30	Iso-conversional	unclear	105.44–124.97
Leerhoff et al. [77]	RT–1773	Ar	1,2,5	Coats–Redfern	1. Chemical reaction 2. Diffusion	1. 46.55–134.47 2. 7.79–44.76
Przepiera et al. [78]	RT–800	Air	3	Coats–Redfern	Nucleation (Avrami–Erofeev)	Dehydroxylation: 22.17 Hematite transformation: 27.32
Grygar et al. [79]	453–533	Air	80	GRO kinetic law	1. Chemical reaction 2. Diffusion	123–132
Beuria et al. [80]	673–1473	Air	–	Model fitting	Random nucleation	58.74–65.74

Strezov et al. [81] studied the influence of goethite transformation to hematite on the structural changes within the ore particle. Their proposed mechanism, based on initial findings from [82] is presented in Figure 2.5. They observed diameter increase upon heating, with a volume expansion of 110 % at 673 K and 1173 K at 112.5 % (measured with custom designed spring loaded linear velocity displacement transducer). This was followed by cracking of the particle, which they assigned to the formation of water-vapour.

They found that most strain occurs at the particle surface, reaching up to 20 % of its depth. They further found the influence of dehydration on the particle size of the goethite particle to be dependent on the initial particle size. For a particle size between 1.5 and 10 μm, the particle size decreased and for a particle size of 40 to 100 μm the particle size increased. This indicates that the expansion and not the fragmentation to finer fractions was the dominant effect. A change in material properties after heating was also observed by Li et al. [83], who studied the behaviour of fluxes and goethite ore during sintering. During the heating stage, crack formation on the goethite ore was observed once more, which led to a more porous structure. This change in the particle structure enhanced the diffusion of the fluxes during the process. Murakami et al. [84] found a link between the water content in the ore and the affected surface area during heating. A higher amount

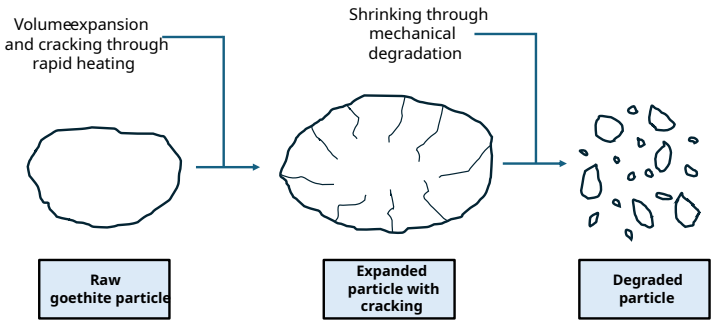


Figure 2.5: Mechanism of goethite decomposition through heating proposed by and adapted from Strezov et al. [81] with permission from Elsevier and Ariyama et al. [82] with permission from the author.

of water led to a higher specific surface area at a heating temperature of 673 K. Upon further heating the goethite to 1073 K, the specific surface area still increased compared to the raw material but decreased compared to the values measured after heating to 673 K, which they explained by the formation of larger pores at higher temperatures as also proposed in the study of Hirokawa et al. [85].

2.5.2. THERMAL DECOMPOSITION OF HEMATITE

Iron can be present in different oxide states, namely hematite (Fe_2O_3), magnetite (Fe_3O_4) and wüstite (FeO), depending on the applied temperature and oxygen potential. Besides their composition, these iron oxides differ in their thermal stability. Magnetite exhibits the highest melting point (1870 K), followed by hematite (1838 K) and wüstite (1644 K) [86]. From a thermodynamic view point, the thermal decomposition and gas reduction of the hematite phase describe the same fundamental principle: the removal of oxygen from the iron oxide. The main reactions of hematite thermal decomposition are shown in Eq. (2.4) and Eq. (2.5) [87]:

$$6Fe_2O_3(s) = 4Fe_3O_4(s) + O_2(g) \tag{2.4}$$

$$2Fe_3O_4(s) = 6FeO(l) + O_2(g) \tag{2.5}$$

Figure 2.6 shows calculations for the thermal decomposition of 100 g of pure hematite in argon atmosphere, calculated with the equilib module of FactSage 7.0 [88].

Based on these thermodynamic calculations in Figure 2.6, first significant thermal decomposition of hematite to magnetite starts at 1200 K, even though marginal amounts can be detected before. At 1367 K all hematite is converted to magnetite. At temperatures present during suspension smelting only minor amounts of wüstite can be created based on thermal decomposition. The thermodynamic calculations indicate that for example at

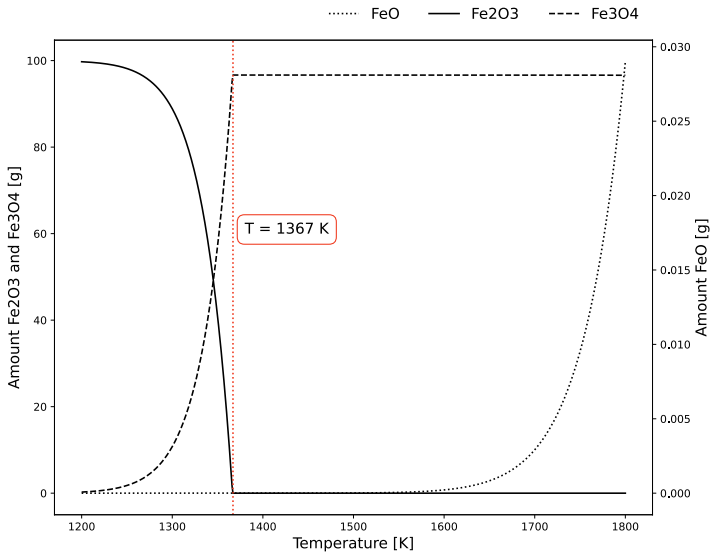


Figure 2.6: Thermodynamic equilibrium of thermal decomposition of Fe_2O_3 in Ar atmosphere, calculated with the equilib module of FactSage 7.0 [88] (Database FactPS [89]).

1800 K, 0.03 g of wüstite is released into the gas phase, indicating that Eq. (2.4) is the main reaction of thermal decomposition.

To determine the decomposition temperature of hematite in the ores in practice, TGA measurements have been widely used in the literature. Chen et al. [90] reported that the hematite within a low-grade ore decomposes via a two stage process; the first stage occurs between 1423 and 1593 K, while the second stage takes place at temperatures above 1593 K. Similarly, Qu et al. [86] determined the thermal decomposition temperature of hematite in higher grade ores (94.94 wt.% Fe_2O_3) to be between 1473-1573 K. Leerhoff et al. [77] studied the decomposition behaviour of varying low-grade iron ores and also identified a two stage process. Depending on the mineralogy and heating rate, the first stage occurred between 1312 and 1419 K, and the second stage at temperatures above 1676 K. However, the influence of mineralogy on the decomposition temperature was only marginal and mainly influenced by the applied heating rate. Xing et al. [87] examined the effect of particle size on the decomposition temperature of hematite ores and observed no significant influence. The decomposition range they reported was between 1480 and 1532 K, depending on the heating rate and particle size. Generally, it's clear that the initiation temperatures of the thermal decomposition determined with the TGA are significantly higher compared to the theoretical thermodynamic calculations shown in Figure 5, indicating kinetic barriers to thermal decomposition.

Several studies [77, 87, 90, 91] were carried out to determine the reaction mechanisms of hematite thermal decomposition. The main findings from selected studies are presented in Table 2.3. These kinetic mechanisms are usually determined under non-

isothermal conditions using several heating rates, with kinetic parameters commonly determined via model-free iso-conversional methods, like the Ozawa Flynn and Wall method [92] or the model-fitting Coats-Redfern method [93]. Overall, there seems to be a consensus that the hematite thermal decomposition is controlled by chemical reaction. Only Chen et al. [90] defined different reaction mechanisms, consisting of inner diffusion of iron at the first stage, followed by slag diffusion. The reported activation energies vary significantly across studies. Salmani et al. [91] reported comparably lower values for the main decomposition stage, while Chen et al. [90] observed higher values, particularly in the first stage. Leerhoff et al. [77] found a wide range of activation energies, influenced by ore mineralogy, and Xing et al. [87] reported higher values than those observed in other studies. These trends highlight a strong dependence of the activation energy on the applied method, but also on material properties.

Table 2.3: Kinetic findings of hematite thermal decomposition.

Reference	Temperature [K]	Atmosphere	Heating Rate [K/min]	Method	Mechanisms	Activation Energy [kJ/mol]
Chen et al. [90]	RT–1773	N_2	2, 3, 5, 10	Iso-conversional	1423–1593 K: Inner diffusion of iron in solid phase >1593 K: Diffusion of iron in slag phase	1423–1593 K: 636±75 >1593 K: 327±41
Leerhoff et al. [77]	RT–1773	Ar	1, 2, 5	Coats–Redfern	Chemical reaction	424–832
Xing et al. [87]	RT–1773	N_2	10, 15, 20	Coats–Redfern	Chemical reaction	1256
Salmani et al. [91]	RT–1723	Air, N_2	5, 7.5, 10	Iso-conversional	Chemical reaction	Air: 382 N_2: 324

2.5.3. GAS REDUCTION OF IRON OXIDES

During the pre-reduction stage of smelting reduction and DRI processes, iron ores are reduced via gas-solid reactions with H_2 and/or CO. Below 843 K, only hematite and magnetite are stable, and reduction proceeds in two steps via the disproportionation reactions Eqs. (2.6), (2.7), (2.10) and (2.11), producing magnetite and metallic iron. Above 843 K, wüstite becomes more thermodynamically stable, and the reduction shifts to a three-step process involving wüstite. This temperature marks the threshold for a change in the dominant reduction pathway [86, 94]. The chemical reactions of iron oxides with H_2 and CO are presented in Eq. (2.6) - Eq. (2.13) with their reaction enthalpy given at room temperature (25 °C) [95, 96]:

$$3Fe_2O_3 + H_2 \rightarrow 2Fe_3O_4 + H_2O; \quad \Delta H = -11.72\ \text{kJ/mol} \tag{2.6}$$

$$Fe_2O_3 + 4H_2 \rightarrow 3Fe + 4H_2O; \quad \Delta H = 148.96\ \text{kJ/mol} \tag{2.7}$$

$$Fe_3O_4 + H_2 \rightarrow 3FeO + H_2O; \quad \Delta H = 77.41\ \text{kJ/mol} \tag{2.8}$$

$$FeO + H_2 \rightarrow Fe + H_2O; \quad \Delta H = 23.85\ \text{kJ/mol} \tag{2.9}$$

$$3Fe_2O_3 + CO \rightarrow 2Fe_3O_4 + CO_2; \quad \Delta H = -52.87\ \text{kJ/mol} \tag{2.10}$$

$$Fe_3O_4 + 4CO \rightarrow 3Fe + 4CO_2; \quad \Delta H = -15.66\ \text{kJ/mol} \tag{2.11}$$

$$Fe_2O_3 + CO \rightarrow 3FeO + CO_2; \quad \Delta H = 36.25\ \text{kJ/mol} \tag{2.12}$$

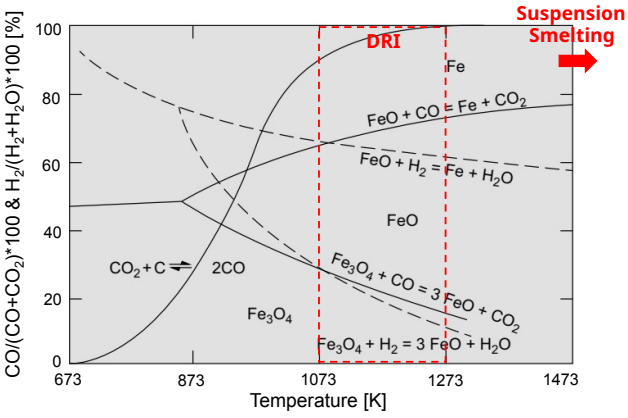
$$FeO + CO \rightarrow Fe + CO_2; \quad \Delta H = -17.31\ \text{kJ/mol} \tag{2.13}$$

Examining H_2-based reductions Eq. (2.6) - Eq. (2.9), only the reduction from hematite to magnetite is exothermic. The following steps of the reduction are endothermic. This indicates that additional energy has to be supplied to the system after the pre-reduction of hematite to magnetite. For CO-based reduction, the reduction of magnetite to wüstite is endothermic. All other reduction steps of the iron oxides are exothermic and, therefore, release energy to the system. Hence, CO reduction has a better influence on the overall energy balance of the system.

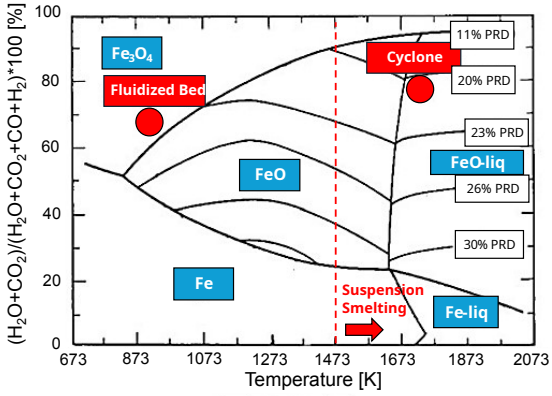
Figure 2.7 (a) represents the classic Bauer-Glaessner diagram, where the influence of the reducing gas partial pressure is displayed for the ratio of CO to the total gas volume of $CO+CO_2$ and similar for the case of H_2 and H_2O. The main takeaway from the diagram is that CO is a better reducing agent at lower temperature, while H_2 is preferred at higher temperatures, from a thermodynamic perspective. This indicates that under the DRI conditions, H_2 is better suited as the reducing agent. Figure 2.7 (b) shows a broader temperature range, which is more relevant for the suspension smelting processes. The gas composition displays the post-combustion ratio, present in the cyclone converter of the HIsarna furnace (Eq. (2.1)) and, therefore, considers the presence of both reducing gases H_2 and CO and the resulting gases H_2O and CO_2. A pre-reduction degree of 33.33 % would indicate the reduction from hematite to wüstite [86]. Therefore, the figure highlights that wüstite is the thermodynamic limit of pre-reduction in the HIsarna furnace, where a decrease in the PCR would increase the pre-reduction degree (PRD). During the Flash Ironmaking, which operates at higher amounts of reducing gases, the reduction to metallic iron in solid and liquid form is theoretically possible.

REACTION KINETICS OF HEMATITE REDUCTION WITH H2 AND/OR CO

Spreitzer et al. [97] and Heidari et al. [98] summarized multiple parameters that influence the reduction kinetics of iron oxides and therefore their reduction rate. These parameters can be categorized into process parameters (such as temperature, pressure and gas composition) and material properties (such as particle size, morphology and porosity). Comparing differences between suspension smelting and DRI ironmaking processes, most interesting parameters to consider are the influence of the processing temperatures, material properties like particle size and mineralogy and of course the reducing gas composition. From a kinetic point of view, another important processing parameter is the reduction time. Thermodynamics indicate that reduction of iron ores is already possible at lower temperatures, but the significantly higher temperatures in suspension smelting processes have the potential of decreasing the reduction time. A general approach to describe the kinetics of the gas-solid reduction of pellets or particles is the (un-)reacted shrinking core model [99, 100]. In the shrinking core model, the first reactions take place at the outer surface of the particle. The reaction zone then progresses inward toward the core, while the reducing agents CO and H_2 diffuse through the developing product layer and towards the unreacted core. The product layer is the already converted material phase surrounding the unreacted solid iron ore core. The developing reduction



(a)



(b)

Figure 2.7: Bauer-Glaessner Diagram for (a) the general reduction of hematite with CO and H_2, adapted from [15] with permission from Elsevier and (b) the Bauer-Glaessner diagram with special focus on the conditions during the cyclone pre-reduction in HIsarna ironmaking, adapted from [40] with permission of Springer Nature.

products (CO_2 and H_2O) diffuse back through the product layer and into the gas film [100]. The shrinking core model considers interfacial chemical reactions, internal diffusion or a mixed mechanisms of both as possible reaction mechanisms [100–103]. Generally, chemical reaction-controlled mechanisms are much more temperature dependent than diffusion-controlled mechanisms. Therefore, chemical reaction is often the rate-limiting step at lower temperatures, whereas diffusion becomes more likely to be rate-controlling at higher temperatures [97]. One disadvantage of the shrinking core model is that it assumes a reduction from the outside to the inside of the particle, disregarding the possibility of (internal) nucleation and growth being the underlying mechanism. Based on the selected model, the reaction rate constant can be determined using the Arrhenius equation Eq. (2.14) [104].

$$k = A \cdot e^{-\frac{Ea}{RT}} \tag{2.14}$$

Where A is the collision factor (1/s), Ea is the activation energy (J/mol), R is the ideal gas constant (J/(mol*K) and T is the temperature (K). The influence of temperature on the reduction kinetics is generally described by its exponential dependency on the rate constant indicating an increase of the reaction rate with increasing temperature [98], which is highly beneficial for the suspension smelting processes. A lot of research has been done on the reduction kinetics of iron ore pellets and fines with H_2 and CO, and a selection of studies focusing on the reduction under isothermal conditions are summarized in Table 2.4. In terms of kinetic aspects of the gas reduction, it is important to evaluate the influence of H_2 and CO on the reaction rate, the underlying reaction mechanism and the arising activation energy.

Literature reports that the presence of hydrogen gas in the reducing atmosphere offers an advantage over carbon monoxide, due to increased reduction rates [105–107]. This is generally attributed to the faster diffusion of hydrogen due to its smaller molecular size and lower viscosity [105]. Regarding the reaction mechanism of H_2 or CO reduction, literature indicates a change in the reaction mechanism throughout the reduction process from hematite to metallic iron. Sohn et al. [108] investigated hematite pellet reduction in pure H_2 at 973-1173 K and found a transition from a topochemical reaction in the early stages to pore diffusion in later stages. Similar observations were reported by other studies [105, 107, 109], explained by the formation of an initial iron or wüstite layer on the surface, limiting the gas diffusion through the product layer. However, some authors propose slightly different mechanisms. Kuila et al. [110] studied the reduction of magnetite fines with H_2 at temperatures between 973 and 1273 K and found that both the reduction from Fe_3O_4 to FeO and the subsequent reduction from FeO to Fe is controlled by pore diffusion. Lyu et al. [111] used a mixture of 30 % H_2 and 70 % N_2 for the reduction of hematite fines and proposed that the first stage of the reduction is already a mixed mechanism of gaseous diffusion and chemical reaction at the interface, before it shifts to the mixed mechanism of interfacial chemical reaction and solid diffusion.

The influence of H_2 and CO on the activation energy was investigated by Piotrowski et al. [109]. The reduction of hematite to wüstite was investigated for temperatures between 973 and 1173 K in reducing gas mixtures of H_2, CO and N_2. The calculated activation energies varied between 25 to 125 kJ/mol, depending on the gas composition. For the reduction with pure hydrogen significantly lower activation energies (Ea=28.08

kJ/mol) are determined in comparison to CO-based gas mixtures (Ea=122.52 kJ/mol). For the mixture of the two gases, an activation energy of Ea=93.72 kJ/mol was determined. Conversely, Moon et al. [107] observed an increasing activation energy with an increasing amount of H_2 in the atmosphere.

The influence of particle size on the reduction rate of hematite fines in H_2 atmosphere has been investigated by Hou et al. [112] (pure Fe_2O_3), Wagner et al. [113] (pure Fe_2O_3) and Pang et al. [114] (62.7 wt.-% T.Fe, Fe_2O_3+Fe_3O_4). All observed a general increase in reaction rate with decreasing particle size. Hou et al. [112] found 0.045 mm as lower limit of the influence because the internal diffusion resistance doesn't have an influence on the overall reduction rates at these dimensions. Pang et al. [114] further states a co-dependency of the temperature and particle size. The influence of temperature on the reduction is stronger with decreasing particle sizes.

Even though significant reduction with H_2 is already achieved at lower DRI processing temperatures, the advantage of higher temperatures is the acceleration of the reaction and, therefore, decrease in the needed reduction time for the pre-reduction under industrial process conditions relevant to HIsarna and Flash Ironmaking Technology. In contrast to DRI ironmaking, thermal decomposition of the hematite ore becomes a crucial part of the process. Considering the reduction of iron ore fines at elevated temperatures, significant research was conducted at Delft University of Technology [96, 103, 115–119] in the framework of investigating fine ore reduction in the pre-reduction section of HIsarna and at the University of Utah [17, 44, 45, 53] for flash ironmaking. Both approaches focus on a fast reduction at high temperatures. A common experimental apparatus used in these studies is the drop tube furnace, where the ore concentrates are transported through a defined reaction zone filled with the reducing gases present in laminar flow. The rough principle of a laminar flow reactor as it is used in the studies at Delft University of Technology and the University of Utah is portrayed in Figure 2.8. The particles are generally introduced into the hot reaction zone via a pneumatic powder feeder, with the powders being carried with an injected gas stream into the furnace, where they are gradually reduced via the laminar reducing gas flow. Next, the reduced particles are quenched to prevent reoxidation and collected at the bottom using a sample collector [53, 96, 120].

Qu et al. [103, 115, 116] studied the impact of gas reduction mechanisms on the overall reduction of fine hematite ores at short particle residence times (210 – 2020 ms). They investigated the reaction kinetics for a gas mixture containing 42.2 % CO and 57.8 % CO_2, and found that the reduction was chemical reaction-controlled in the temperature range of 1550 to 1650 K, with an activation energy of 270 kJ/mol. With an increase in temperature (1700-1750 K), the reaction mechanisms shifted to diffusion and the activation energy decreased to 156 kJ/mol. They also found a significant influence of the temperature, with only 3.3 % of reduction degree at 1550 K and a particle residence time of 210 ms and an increase to 26.3 % at 1750 K and a residence time of 970 ms. Based on their observations, they were able to explain the influence of thermal decomposition and gas reduction on the pre-reduction degree in the drop tube furnace [116]. The results are summarised in Figure 2.9. Until 1700 K, thermal decomposition is the dominant reduction mechanism, with particularly low contribution of gas reduction at lower temperatures. Gas reduction becomes the significant reduction mechanism at 1750 K. However, the

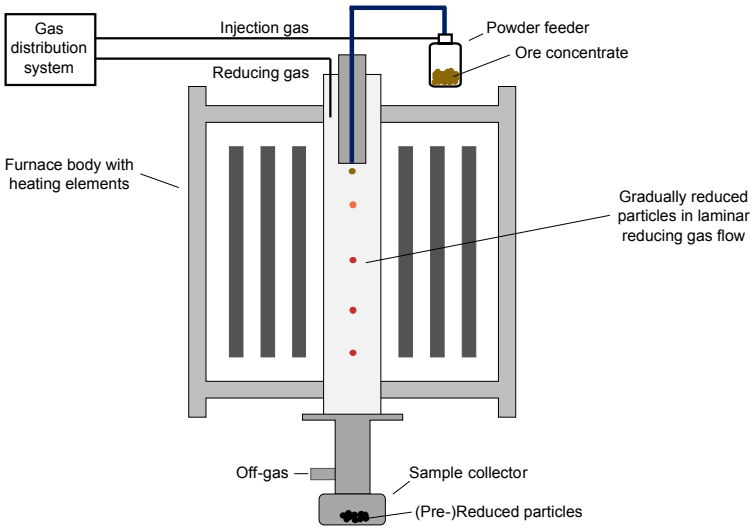


Figure 2.8: Setup for a laminar flow drop tube furnace experiments, adapted from [119] (CC.BY.4.0) and adapted from [53] with permission from John Wiley and Sons.

influence of thermal decomposition is only significant in the first 210 ms of the reaction. Since thermal decomposition is mostly completed in this fast timeframe, gas reduction becomes more influential at increasing particle residence times.

Additionally, Qu et al. [115] studied the impact of hydrogen enrichment on the reduction degree in the drop tube furnace by testing 5 different atmospheres at 1650 K and a relatively long particle residence time of 2020 ms. They showed that by changing the atmosphere from 25 % CO and 75 % N_2 to 25 % H_2 and 75% N_2, the reduction degree increased from 26.4 % to 77.1 %. Moreover, increasing the hydrogen content in the atmosphere to 75%, the reduction degree increased further to 97 %, even at the short particle residence times.

The influence of the reducing gas atmosphere in suspension smelting processes was further studied by Chen et al. [120, 121] in the framework of developing the flash ironmaking technology. They studied the reduction of hematite concentrates (d = 21 μm) in a temperature range of 1423 to 1623 K in H_2 and CO separately. Both H_2 and CO reduction followed nucleation and growth as reduction mechanisms and achieved reduction degrees above 90 %. However, they observed faster reduction with H_2, achieving a similar amount of reduction in 3 s, as it took 5 s for the CO reduction. Building up on the reduction of hematite concentrates, Elzohiery et al. [53] tested the H_2 reduction of magnetite concentrates (d=20-25, 32-38, 45-53 μm). Again, they found that the reaction completed within seconds, whereas the duration of the reduction was influenced by the temperature and particle size. All three studies determined nucleation and growth as the governing reaction mechanism, and reported the lowest activation energy for the reduction of the magnetite concentrates (193 kJ/mol), followed by the reduction of hematite concentrates with H_2 (214 kJ/mol) and CO (231 kJ/mol), respectively.

Table 2.4: Overview of isothermal kinetic studies on H_2-CO reduction in ironmaking.

Reference	Input Material	Reduction step	Temperature [K]	Atmosphere	Mechanism	Activation Energy [kJ/mol]	Reduction degree [%]	Set-up
DRI conditions								
Zhang et al. [122]	Pellets	$Fe_2O_3 \rightarrow Fe$	1043–1443	H_2	1043 K: interfacial reaction + diffusion >1143 K: interfacial reaction	31.3 ± 1.3	~97	TGA
Sohn et al. [108]	Pellets	$Fe_2O_3 \rightarrow Fe$	973–1173	H_2	Initial: Topochemical reaction Later: Pore diffusion	15–29	~100	TGA
Piotrowski et al. [109]	Fines	$Fe_2O_3 \rightarrow FeO$	973–1173	90%N_2+10%CO 90%N_2+10%H_2 90%N_2+5.7%CO+4.3%H_2	Initial: Topochemical reaction at surface Later: Diffusion after oxide layer	122.52 28.08 93.72	–	TGA
Zuo et al. [105]	Pellets	$Fe_2O_3 \rightarrow Fe$	1073–1273	H_2–CO	Initial: chemical reaction Final: internal gas diffusion	–	50.01–98	Reducing furnace
Moon et al. [107]	Compacted Fines	$Fe_2O_3 \rightarrow Fe$	1073–1223	H_2–CO	Initial: chemical reaction at interface Later: diffusion through product layer	19.8–42.1	~90	Cahn balance
Lyu et al. [111]	Fines	$Fe_2O_3 \rightarrow Fe$	1073–1373	30%H_2+70%N_2	Initial: gaseous diffusion + interface reaction Later: interface + solid diffusion	27–93	~90–100	TGA
Hammam et al. [123]	Compacted Fines	$Fe_2O_3 \rightarrow Fe$	1073–1373	H_2	Initial: gaseous diffusion + interface reaction Later: interface reaction	R=5–10%: 28.34 R=85–95%: 41.15	100	TGA
Kuila et al. [110]	Fines	$Fe_3O_4 \rightarrow Fe$	973–1273	H_2	Pore diffusion	$Fe_3O_4 \rightarrow Fe$: 42 $FeO \rightarrow Fe$: 55	70–100	TGA
Suspension smelting conditions								
Qu et al. [116]	Fines	$Fe_2O_3 \rightarrow FeO$	1550–1750	42.2%CO+57.8%CO_2	–	–	3.3–26.3	Drop tube
Qu et al. [103]	Fines	$Fe_2O_3 \rightarrow FeO$	1550–1650	42.2%CO+57.8%CO_2	Chemical reaction	270	3.3–26.3	Drop tube
Qu et al. [115]	Fines	$Fe_2O_3 \rightarrow FeO$	1700–1750	42.2%CO+57.8%CO_2	Diffusion	156	3.3–26.3	Drop tube
Qu et al. [115]	Fines	$Fe_2O_3 \rightarrow Fe$	1650	CO–CO_2–H_2–N_2	–	–	23.1–97	Drop tube
Chen et al. [120]	Fines	$Fe_2O_3 \rightarrow Fe$	1423–1623	H_2	Nucleation + growth	214	>90	Drop tube
Chen et al. [121]	Fines	$Fe_2O_3 \rightarrow Fe$	1423–1623	CO	Nucleation + growth	231	>90	Drop tube
ElZohiery et al. [53]	Fines	$Fe_3O_4 \rightarrow Fe$	1423–1623	H_2	Nucleation + growth	193	>90	Drop tube

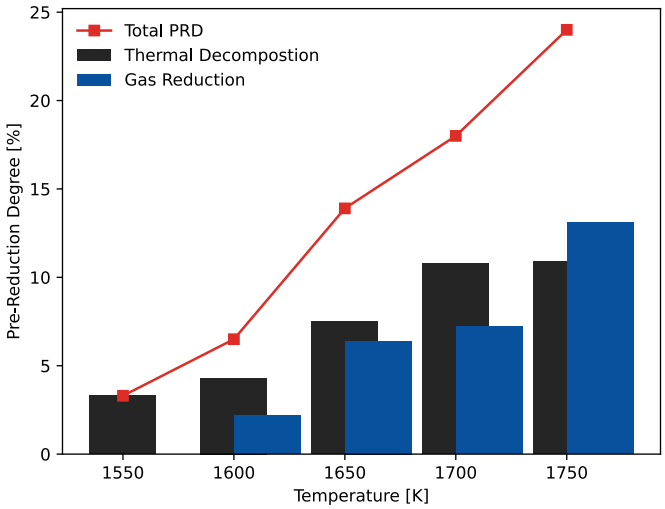


Figure 2.9: Influence of gas reduction (42.2 % CO + 57.8 % CO_2) and thermal decomposition (100 % CO_2) on the pre-reduction degree at a particle residence time of 210 ms and a particle size of 45-53 μm, adapted from [116] with permission from ISIJ.

Qu et al. [124] investigated the impact of temperature and reduction degree on particle morphology during flash reduction (Figure 2.10). In the temperature range of 1450 to 1600 K, with corresponding reduction degrees of approximately 9.6 - 47.5 %, the particles maintained their irregular shape. Under these temperatures the reaction occurs as gas-solid reduction. However, at temperatures exceeding 1600 K and a reduction degree of 52.2 %, the reduction mechanism transitioned to a gas-liquid reduction, leading to the formation of spherical particles, with melting mostly driven by the developing wüstite phase. Initially, iron products disperse across the wüstite particle before changing into a spherical form as the temperature increases.

The particle size plays a crucial role in the reduction process in suspension smelting. Here again, Qu et al. [116] investigated the influence of particle size on the reduction behaviour of iron ores at high temperatures (1650 K). they studied four particle size fractions (38-45, 45-53, 53-75 and 75-90 μm) in gas atmospheres consisting of CO-CO_2 and CO-CO_2-H_2-N_2 and varying contents of reducing gases. For all the tested gas compositions, the reduction degree increases approximately linear with decreasing particle size. Chen et al. [117, 118] found an influence of the particle size on the reaction rate constant for the reduction of hematite, described by a nucleation and growth mechanism of magnetite grains, within the hematite particle. The reaction rate constant increased for an increase in particle size from 67 to 85 μm. However, after a threshold of 85 μm the reaction rate constant decreased with a further increase in particle size. An increase in particle size, however, can yield a negative influence on the heating of the particle which has a significant influence on the thermal decomposition at the short particle residence

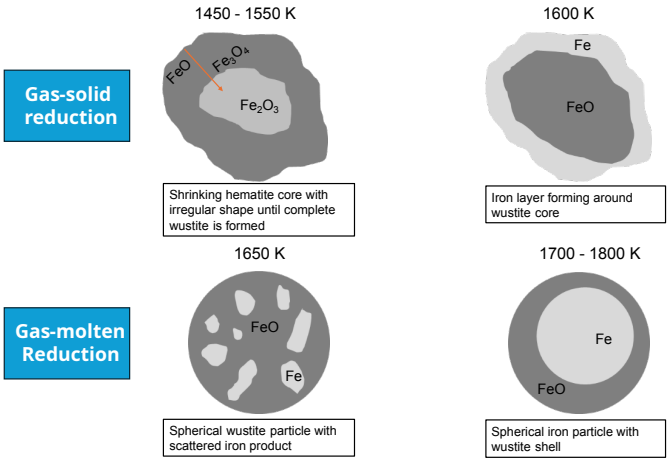


Figure 2.10: Influence of temperature on hematite particle during gas reduction in a drop tube furnace, adapted from [124] with permission from Elsevier.

times during suspension smelting and therefore lead to a negative effect on the reduction degree [117].

When comparing the reaction kinetics of suspension smelting studies to those of DRI-based ironmaking, a key difference is the substantially higher activation energy observed in suspension smelting. This increased energy requirement is attributed to the high degrees of reduction achieved within very short reduction times. The higher activation energy is therefore higher in suspension smelting processes. However, its significant advantage is the rapid reduction, which enables the formation of metallic iron under the appropriate atmospheric and temperature conditions.

2.5.4. WATER-GAS SHIFT REACTION

The reduction of iron ores with H_2 and CO produces H_2O and CO_2 as combustion products, both of which can participate in the water-gas shift reaction (WGSR), (Eq. (2.15)), wherein steam (water vapour) reacts with carbon monoxide to form carbon dioxide and hydrogen gas [125]. This reaction plays an important role in influencing the local gas composition during reduction, potentially enhancing the availability of H_2 and thereby affecting the overall reduction kinetics.

$$H_2O(g) + CO(g) \rightleftharpoons CO_2(g) + H_2(g), \quad \Delta H = -40.6\,\text{kJ/mol} \tag{2.15}$$

The reaction (Eq. (2.15)) is exothermic and reversible [125]. An important factor for the evaluation of the WGSR is its equilibrium constant, K_P, which is defined by Eq. (2.16):

$$K_P = \frac{P_{CO_2} \cdot P_{H_2}}{P_{CO} \cdot P_{H_2O}} \tag{2.16}$$

With P_i being the partial pressure of the different gaseous species. While pressure does

not affect the equilibrium due to constant mol numbers [125], it can increase the reaction rate and CO conversion before the equilibrium is reached. If large amounts of steam are present ($H_2O/CO > 1$), the equilibrium shifts towards product formation, increasing CO conversion [126]. Temperature strongly affects the WGSR via the equilibrium constant K_P, given in Eq. (2.17) (best applicable: 588 to 753 K) [125, 126].

$$K_P = e^{\left(\frac{4577.8}{T} - 4.33\right)} \tag{2.17}$$

Figure 2.11 compares K_P values calculated via the Reactions Module in FactSage 7.0 [127] and Eq. (2.17) across 298-1800 K. Both show decreasing K_P with rising temperature, indicating that the forward reaction is favoured at lower temperatures. A brief plateau appears in the FactSage calculations at low temperatures but is negligible for high-temperature ironmaking. At approx. 1058 K (Eq. (2.17)) and 1101 K (FactSage), K_P becomes negative, favouring CO and H_2O formation. This shift is crucial in suspension smelting as it may lead to more endothermic conditions, requiring external energy supply [7, 128].

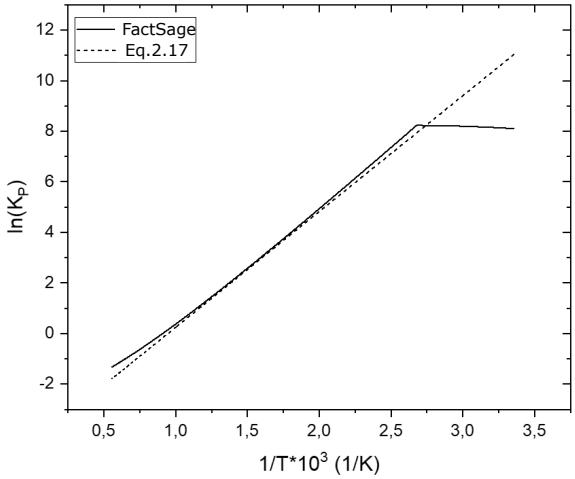


Figure 2.11: Temperature dependence of WGSR after FactSage7.0 [127] calculations and Eq. (2.17).

Another issue with the WGSR at high temperatures is the development of water-vapour. Water vapour decreases the thermodynamic driving force for the reduction of the iron oxides. In addition, the water vapour can be absorbed at the reaction interfaces and thus block the reactive surfaces and inhibit reduction [97]. Abdelrahim et al. [129] studied iron ore reduction using $CO\text{-}CO_2\text{-}H_2\text{-}H_2O\text{-}N_2$ gas mixtures. They found that when the H_2O content exceeds 2 % at 1073-1173 K, the reduction efficiency decreases. This was explained by H_2O blocking the actives sites on the wüstite. Lorente et al. [130] observed that up to 5 % steam has little effect on Fe_2O_3 to Fe_3O_4 reduction but significantly limits the Fe_3O_4 to Fe step. Similarly, Kim et al. [131] studied magnetite reduction in $H_2\text{-}H_2O$ mixtures (P_{H2O}=0.1 atm) and observed that H_2O negatively affects the reduction rate, particularly at temperatures between 773 to 973 K. However, the influence diminished at

higher temperatures.

The influence of the WGSR reaction becomes increasingly interesting due to the intense use of H_2-CO-mixtures and high temperatures in flash ironmaking processes. If H_2O and CO_2 are present in the system, the occurrence of the WGSR is possible. From Figure 2.11, the equilibrium constant is smaller than one around 1100 K, meaning that at this temperature the H_2/CO ratio decreases as CO formation is favoured. Gas-based DRI processes operate at these high temperatures. The MIDREX process, for example, operates with a gas feeding temperature around 1173 – 1223 K [6]. Particularly in the temperature range relevant to suspension smelting ironmaking processes, where the equilibrium strongly favours the formation of H_2O and CO, it is essential to verify the actual composition of reducing gases and asses if the WGSR could reduce the available H_2 content. This can become an issue for processes like the cyclone converter of the HIsarna furnace, where large amounts of CO_2 are present in the atmosphere, together with H_2. Figure 2.12 shows the influence of the WGSR on a potential gas atmosphere for PCR ~ 60 % for two cases: one based on plant data from literature [64] and another from a theoretical calculation assuming a potential increase in H_2 content in the CCF, both calculated with the Equilib module of FactSage 7.0 [88] and the FactPS database [89].

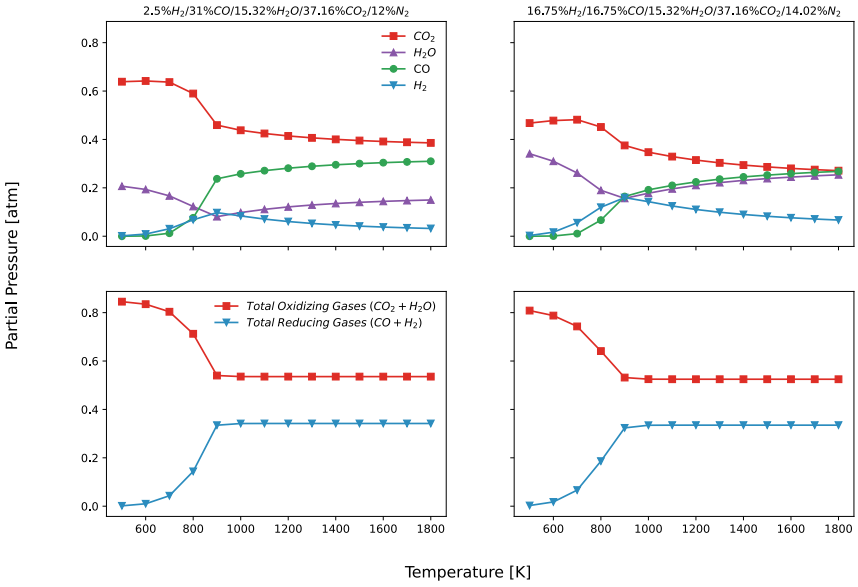


Figure 2.12: Influence of WGSR reaction of PCR ~ 60 % atmospheres in HIsarna CCF based on plant data from literature [64] and a potential H_2-enriched scenario.

In both cases the equilibrium shifts towards CO and H_2O with increasing temperatures, leading to lower amounts of H_2 in the reducing gas atmosphere. At high temperatures, the total concentration of reducing and oxidizing gases saturates, indicating that although the overall amount of reducing gasses remains constant, the proportion of H_2 decreases.

This shift could lead to a significant decline in the reduction potential of the gas mixture, which is especially crucial in smelting reduction process where the reactions occur in a very short time.

2.6. CONCLUSIONS

The transition of the steel industry towards a more sustainable production is becoming an urgent necessity to reduce emissions and comply with the EU goals. Currently, the blast furnace is still the dominant technology for ironmaking, but this will change soon. New approaches with either less limitations in terms of input material or more sustainable reducing agents are being developed. In this framework, the adaptation of hydrogen in DRI processes, especially shaft furnace based, seems most promising. In the current state of the art, hydrogen is already utilized in DRI ironmaking, where the transition to high hydrogen concentrations and consequently, a significant reduction in CO_2-emissions appears most feasible. Compared to the more established DRI ironmaking processes, this article focuses on suspension smelting technologies as potential alternative, which are currently still under development, including the Flash Ironmaking Technology (FIT) and the pre-reduction stage of the HIsarna process. The FIT and HIsarna both bring an advantage by eliminating material pre-treatment steps, since fine ores can be directly used without agglomeration. The objective of this review is to understand the reaction mechanisms involved in suspension smelting ironmaking processes, examine how they differ from the more conventional DRI routes and evaluate the role of hydrogen within these processes.

According to the literature, the two primary reaction mechanisms in suspension smelting are thermal decomposition and gas-solid reduction, with a transition to gas-molten reduction at elevated temperatures. Regarding thermal decomposition, an important parameter is the nature of the iron ore. In the case of goethite being present in the ore, its conversion to hematite can influence the material properties due to volume expansion and cracking. This can potentially increase the gas-reduction, for example due to the change in particle size and potential reactive surfaces. The thermal decomposition of the hematite phase is mostly described by the reduction to magnetite and has a stronger influence on the reduction during the first 210 ms of suspension smelting. Most literature agrees that the thermal decomposition of hematite to magnetite is chemical reaction-controlled. The kinetic on-set of thermal decomposition was determined to lay between 1312 and 1480 K, making it an insignificant mechanisms in DRI ironmaking.

From a thermodynamic perspective, reduction with H_2 has the disadvantage of being largely endothermic, in contrast to the typically exothermic reduction with CO. This results in a less favourable energy balance and the need to apply additional energy input to sustain the process. In terms of thermodynamic preference, the reduction with CO is favoured at lower, while H_2 becomes advantageous at higher temperatures. However, more critical than thermodynamics is the impact of H_2 on the reduction kinetics. Overall, H_2 enables higher reduction rates compared to CO, which is explained by its better diffusivity. While various parameters influence the reaction mechanism, many studies report a mixed-controlled mechanism. The process is first controlled by chemical reaction at the pellet or particle interface and subsequently transitioned to diffusion control as a product layer of wüstite or iron is formed.

The most commonly used equipment to study the kinetics of suspension smelting processes is a laminar flow drop tube furnace, which allows for studying the in-flight flash reduction of the particles under isothermal conditions. In suspension smelting, the particles are reduced within seconds. In this rapid process, the kinetic advantage of H_2 becomes particularly relevant for achieving high reduction degrees in a very short residence time. A significant difference from DRI is the higher activation energy observed for suspension smelting, attributed to the fast reduction kinetics. In processes such as HIsarna, achieving high reduction degrees in the pre-reduction cyclone could further improve the environmental performance by reducing the amount of carbon needed for the final reduction in the smelting section. One important consideration during reduction with CO or H_2 is the influence of the water-gas shift reaction (WGSR) in the presence of CO_2 or H_2O in the gas phase. At elevated temperatures, the equilibrium of the WGSR shifts towards greater production of CO and H_2O, which can lower the effective H_2 content in the atmosphere and diminish its kinetic advantage. Furthermore, the presence of excessive water-vapour in the system may further negatively affect the reduction behaviour.

In conclusion, suspension smelting remains a rather relatively new technology compared to the more established DRI processes. Further research is essential to understand how material properties and gas atmosphere influence the reduction kinetics. Nevertheless, hydrogen-enriched atmospheres must be applied with caution, particularly due to the possible limitations imposed by the water-gas shift reaction at high temperatures.

REFERENCES

[1] P. Leerhoff, C. Zeilstra, K. Meijer, J. van der Stel, S. T. Abrahami, N. Dogan, and Y. Yang. H_2 adaptation in ironmaking: a review with focus on suspension smelting and its reaction mechanisms. **Mineral Processing and Extractive Metallurgy: Transactions of the Institutions of Mining and Metallurgy** (2026). DOI: 10.1177/25726641261463593.

[2] Worldsteel Association. Climate change and the production of iron and steel. 2021.

[3] IEA. Iron and Steel Technology Roadmap. 2020. URL: https://www.iea.org/reports/iron-and-steel-technology-roadmap.

[4] J. R. Vehec. Technology Roadmap Research Program for the Steel Industry. Dec. 2010. DOI: 10.2172/1011081.

[5] Worldsteel Association. 2020 World Steel in Figures. 2020.

[6] T. Battle, U. Srivastava, J. Kopfle, R. Hunter, and J. McClelland. The Direct Reduction of Iron. Vol. 3. Elsevier Ltd., 2014, pp. 89–176. ISBN: 9780080969886. DOI: 10.1016/B978-0-08-096988-6.00016-X.

[7] Y. Yang, K. Raipala, and L. Holappa. Treatise on Process Metallurgy. Vol. 3. Elsevier Ltd., 2014. Chap. Ironmaking, pp. 2–88. ISBN: 9780080969886. DOI: 10.1016/B978-0-08-096988-6.00017-1.

[8] Worldsteel Association. Sustainability performance of the steel industry 2003-2021. 2022.

[9] Worldsteel Association. World Steel in Figurers. 2024.

[10] F. Patisson and O. Mirgaux. Hydrogen Ironmaking: How It Works. **Metals** 10, 922 (2020). DOI: 10.3390/met10070922.

[11] Hydrogen Europe. Hydrogen - Enabling a Zero-Emission Society. 2021.

[12] Roland Berger GMBH. The Future of Steelmaking - How the European Steel Industry Can Achieve Carbon Neutrality. 2020.

[13] V. Vogl, M. Åhman, and L. J. Nilsson. Assessment of hydrogen direct reduction for fossil-free steelmaking. **Journal of Cleaner Production** 203 (2018), pp. 736–745. DOI: 10.1016/j.jclepro.2018.08.279.

[14] A. Markotic, N. Dolic, and V. Trujic. State of the direct reduction and reduction smelting processes. **Journal of Mining and Metallurgy, Section B: Metallurgy** 38 (2002), pp. 123–141. DOI: 10.2298/jmmb0204123m.

[15] S. Seetharaman, R. Guthrie, A. McLean, S. Seetharaman, and H. Y. Sohn. Treatise on Process Metallurgy Volume 3: Industrial Processes. 2024. DOI: 10.1016/C2020-0-01069-8.

[16] Z. Chen, C. Zeilstra, J. van der Stel, J. Sietsma, and Y. Yang. Review and data evaluation for high-temperature reduction of iron oxide particles in suspension. **Ironmaking & Steelmaking** 47 (2020), pp. 741–747. DOI: 10.1080/03019233.2019.1589755.

[17] H. Y. Sohn. Energy consumption and CO_2 emissions in ironmaking and development of a novel flash technology. **Metals** 10, 54 (2020). DOI: 10.3390/met10010054.

[18] W. Liu, H. Zuo, J. Wang, Q. Xue, B. Ren, and F. Yang. The production and application of hydrogen in steel industry. **International Journal of Hydrogen Energy** 46 (2021), pp. 10548–10569. DOI: 10.1016/j.ijhydene.2020.12.123.

[19] C. Ramakgala and G. Danha. A review of ironmaking by direct reduction processes: Quality requirements and sustainability. **Procedia Manufacturing** 35 (2019), pp. 242–245. DOI: 10.1016/J.PROMFG.2019.05.034.

[20] M. Atsushi, H. Uemura, and T. Sakaguchi. MIDREX® Processes. **Kobelco Technology Review** 29 (2010), pp. 50–57.

[21] J. Ripke and J. Kopfle. MIDREX H_2: Ultimate Low CO_2 Ironmaking and its place in the new Hydrogen Economy. 2017. URL: https://www.midrex.com/tech-article/midrex-h2-ultimate-low-co2-ironmaking-and-its-place-in-the-new-hydrogen-economy/.

[22] ArcelorMittal. Hamburg H2. URL: https://corporate.arcelormittal.com/climate-action/decarbonisation-technologies/hamburg-h2-working-towards-the-production-of-zero-carbon-emissions-steel-with-hydrogen#.

[23] ArcelorMittal. Hydrogen-based steelmaking to begin in Hamburg. URL: https://corporate.arcelormittal.com/media/case-studies/hydrogen-based-steelmaking-to-begin-in-hamburg.

[24] P. Cavaliere. Clean Ironmaking and Steelmaking Processes. Springer International Publishing, 2019. DOI: 10.1007/978-3-030-21209-4.

[25] P. E. Duarte, A. M. Tavano, D. Sales, and E. Zendejas. Achieving Carbon Free Emissions via the ENERGIRON DR Process. June 2010. URL: https://www.energiron.com/media/papers-publications?page=1.

[26] Z. Miškovičová, J. Legemza, P. Demeter, B. Buľko, S. Hubatka, M. Hrubovčáková, P. Futáš, and R. Findorák. An Overview Analysis of Current Research Status in Iron Oxides Reduction by Hydrogen. **Metals** 14, 589 (2024). DOI: 10.3390/met14050589.

[27] Fuel Cells and Hydrogen 2 Joint Undertaking. Hydrogen Roadmap Europe. 2019.

[28] D. Spreitzer and J. Schenk. Iron Ore Reduction by Hydrogen Using a Laboratory Scale Fluidized Bed Reactor: Kinetic Investigation—Experimental Setup and Method for Determination. **Metallurgical and Materials Transactions B** 50 (2019), pp. 2471–2484. DOI: 10.1007/s11663-019-01650-9.

[29] D. Nuber, H. Eichenberger, and B. Rollinger. Circored fine ore direct reduction. **MILLENIUM Steel** (2006), pp. 37–40.

[30] IEA. The Future of Hydrogen - Seizing today's opportunities. 2019.

[31] B. Anameric and S. K. Kawatra. Direct Iron Smelting Redcution Processes. **Mineral Processing and Extractive Metallurgy Review** 30 (2008), pp. 1–51. DOI: 10.1080/08827500802043490.

[32] L. R. Singh. JSW Steel—Journey with Speed and Innovation. 2024, pp. 99–103. DOI: 10.1007/978-981-99-5060-7_9.

[33] S.-H. Yi, M.-E. Choi, D.-H. Kim, C.-K. Ko, W.-I. Park, and S.-Y. Kim. FINEX® as an environmentally sustainable ironmaking process. **Ironmaking & Steelmaking** 46 (2019), pp. 625–631. DOI: 10.1080/03019233.2019.1641682.

[34] X. Zhang, K. Jiao, J. Zhang, and Z. Guo. A review on low carbon emissions projects of steel industry in the World. **Journal of Cleaner Production** 306, 127259 (2021). DOI: 10.1016/j.jclepro.2021.127259.

[35] Posco newsroom. POSCO starts to design the HyREX demonstration plant. Aug. 2022. URL: https://newsroom.posco.com/en/posco-starts-to-design-the-hyrex-demonstration-plant/.

[36] S. Park, Y.-J. Lee, J.-H. Kim, E.-S. Lee, and K. D. Song. Simulation of the hydrogen reduction process for the production of direct reduced iron. Ed. by J. Kim, K. D. Song, I. Oh, and M. Porfiri. SPIE, Apr. 2022, p. 40. ISBN: 9781510649651. DOI: 10.1117/12.2626947.

[37] N. Goodman. Operation of the First HIsmelt Plant in China. AIST, 2019, pp. 593–600. DOI: 10.33313/377/063.

[38] M. Shahabuddin, G. Brooks, and M. A. Rhamdhani. Decarbonisation and hydrogen integration of steel industries: Recent development, challenges and techno-economic analysis. **Journal of Cleaner Production** 395, 136391 (2023). DOI: 10.1016/j.jclepro.2023.136391.

[39] A. Orth, N. Anastasijevic, and H. Eichberger. Low CO_2 emission technologies for iron and steelmaking as well as titania slag production. **Minerals Engineering** 20 (2007), pp. 854–861. DOI: 10.1016/j.mineng.2007.02.007.

[40] K. Meijer, C. Zeilstra, C. Teerhuis, M. Ouwehand, and J. van der Stel. Developments in Alternative Ironmaking. **Transactions of the Indian Institute of Metals** 66 (2013), pp. 475–481. DOI: 10.1007/s12666-013-0309-z.

[41] C.-z. Cao, Y.-j. Meng, F.-x. Yan, D.-w. Zhang, X. Li, and F.-m. Zhang. Analysis on Energy Efficiency and Optimization of HIsmelt Process. Ed. by T. Wang, X. Chen, D. P. Guillen, L. Zhang, Z. Sun, C. Wang, N. Haque, J. A. Howarter, N. R. Neelameggham, S. Ikhmayies, Y. R. Smith, L. Tafaghodi, and A. Pandey. Springer International Publishing, 2019. DOI: 10.1007/978-3-030-06209-5.

[42] N. Goodman. The production of green steel via HIsmelt. 2021.

[43] P. C. Cavaliere. Hydrogen Assisted Direct Reduction of Iron Oxides. Springer International Publishing, 2022. ISBN: 9783030980566. DOI: 10.1007/978-3-030-98056-6.

[44] H. Y. Sohn. From Sulfide Flash Smelting to a Novel Flash Ironmaking Technology. Celebrating the Megascale. Cham: Springer International Publishing, 2014, pp. 69–76.

[45] H. Y. Sohn and Y. Mohassab. Development of a Novel Flash Ironmaking Technology with Greatly Reduced Energy Consumption and CO_2 Emissions. **Journal of Sustainable Metallurgy** 2 (2016), pp. 216–227. DOI: 10.1007/s40831-016-0054-8.

[46] H. K. Pinegar, M. S. Moats, and H. Y. Sohn. Process Simulation and Economic Feasibility Analysis for a Hydrogen-Based Novel Suspension Ironmaking Technology. **steel research international** 82 (2011), pp. 951–963. DOI: 10.1002/srin.201000288.

[47] H. K. Pinegar, M. S. Moats, and H. Y. Sohn. Flowsheet development, process simulation and economic feasibility analysis for novel suspension ironmaking technology based on natural gas: Part 1 – Flowsheet and simulation for ironmaking with reformerless natural gas. **Ironmaking & Steelmaking** 39 (2012), pp. 398–408. DOI: 10.1179/1743281211Y.0000000053.

[48] H. K. Pinegar, M. S. Moats, and H. Y. Sohn. Flowsheet development, process simulation and economic feasibility analysis for novel suspension ironmaking technology based on natural gas: Part 2 – Flowsheet and simulation for ironmaking combined with steam methane reforming. **Ironmaking & Steelmaking** 40 (2013), pp. 32–43. DOI: 10.1179/030192312X13345671456851.

[49] H. Y. Sohn. Suspension Hydrogen Reduction of Iron Ore Concentrate in AISI/DOE Technology Roadmap Program for the Steel Industry. Tech. rep. Utah: American Iron and Steel Institute, 2008.

[50] H. Y. Sohn, M. Elzohiery, and D.-Q. Fan. Development of the Flash Ironmaking Technology (FIT) for Green Ironmaking with Low Energy Consumption. **Journal of Energy and Power Technology** 3, 3 (2021). DOI: 10.21926/jept.2103042.

[51] D.-Q. Fan, M. Elzohiery, Y. Mohassab, and H. Y. Sohn. The kinetics of carbon monoxide reduction of magnetite concentrate particles through CFD modelling. **Ironmaking & Steelmaking** 48 (2021), pp. 769–778. DOI: 10.1080/03019233.2020.1861857.

[52] M. Elzohiery, D.-Q. Fan, Y. Mohassab, and H. Y. Sohn. Kinetics of hydrogen reduction of magnetite concentrate particles at 1623–1873 K relevant to flash ironmaking. **Ironmaking & Steelmaking** 48 (2021), pp. 485–492. DOI: 10.1080/03019233.2020.1819942.

[53] M. Elzohiery, H. Y. Sohn, and Y. Mohassab. Kinetics of Hydrogen Reduction of Magnetite Concentrate Particles in Solid State Relevant to Flash Ironmaking. **steel research international** 88 (2017). DOI: 10.1002/srin.201600133.

[54] D.-Q. Fan, M. Elzohiery, Y. Mohassab, and H. Y. Sohn. Rate-enhancement effect of CO in magnetite concentrate particle reduction by H_2+CO mixtures. **Ironmaking & Steelmaking** 48 (2021), pp. 1064–1075. DOI: 10.1080/03019233.2021.1915645.

[55] D.-Q. Fan, Y. Mohassab, M. Elzohiery, and H. Y. Sohn. Analysis of the Hydrogen Reduction Rate of Magnetite Concentrate Particles in a Drop Tube Reactor Through CFD Modeling. **Metallurgical and Materials Transactions B** 47 (2016), pp. 1669–1680. DOI: 10.1007/s11663-016-0603-3.

[56] M. Elzohiery, D.-Q. Fan, Y. Mohassab, and H. Y. Sohn. Experimental Investigation and Computational Fluid Dynamics Simulation of the Magnetite Concentrate Reduction Using Methane-Oxygen Flame in a Laboratory Flash Reactor. **Metallurgical and Materials Transactions B** 51 (2020), pp. 1003–1015. DOI: 10.1007/s11663-020-01809-9.

[57] D.-Q. Fan, H. Y. Sohn, Y. Mohassab, and M. Elzohiery. Computational Fluid Dynamics Simulation of the Hydrogen Reduction of Magnetite Concentrate in a Laboratory Flash Reactor. **Metallurgical and Materials Transactions B** 47 (2016), pp. 3489–3500. DOI: 10.1007/s11663-016-0797-4.

[58] Y. Mohassab, M. Elzohiery, and H. Y. Sohn. Flash Reduction of Magnetite Concentrate Based on Partial Oxidation of Natural Gas Relevant to a Novel Ironmaking Process. AISTech 2016, 2016.

[59] M. H. Elzohiery. Flash Reduction of Magnetite Concentrate Related to a Novel Flash Ironmaking Process. PhD thesis. The University of Utah, 2018.

[60] A. Abdelghany, D.-Q. Fan, M. Elzohiery, and H. Y. Sohn. Experimental Investigation and Computational Fluid Dynamics Simulation of a Novel Flash Ironmaking Process Based on Partial Combustion of Natural Gas in a Reactor. **steel research international** 90 (2019). DOI: 10.1002/srin.201900126.

[61] K. Meijer, M. Denys, J. Lasar, J.-P. Birat, G. Still, and B. Overmaat. ULCOS: ultra-low CO_2 steelmaking. **Ironmaking & Steelmaking** 36 (2009), pp. 249–251. DOI: 10.1179/174328109X439298.

[62] J. van Boggelen, K. Meijer, C. Zeilstra, H. Hage, and P. Broersen. HIsarna-Demonstrating low CO_2 ironmaking at pilot scale. Sept. 2018.

[63] K. Meijer, C. Guenther, and R. J. Dry. HIsarna Pilot Plant Project. METEC InSteelCon 2011, 2011.

[64] Z. Yan, T. T. Htet, J. Hage, K. Meijer, and Z. Li. HIsarna Process Simulation Model: Using FactSage with Macro Facility. **Metallurgical and Materials Transactions B** 54 (2023), pp. 868–879. DOI: 10.1007/s11663-023-02732-5.

[65] T. Peeters, K. Meijer, and J. van der Stel. Development of HIsarna Ironmaking Technology for Low CO_2 Steelmaking. VDEh-CSM Seminar, 2014.

[66] European Commission: Directorate-General for Research and Innovation. Hisarna experimental campaigns B and C (HISARNA B and C) : final report. 2015. URL: https://data.europa.eu/doi/10.2777/107258.

[67] J. Hage, C. Zeilstra, J. van Boggelen, K. Meijer, J. van der Stel, and T. Peeters. HIsarna: Benefits of an Innovative Smelting-Reduction Ironmaking Technology. AISTech 2021, 2021, pp. 1388–1399. DOI: 10.33313/382/143.

[68] D. J. Gavel, C. Barnes, C. Zeilstra, K. Meijer, A. Hamoen, and J. van Boggelen. Descriptive modelling of the HIsarna process. STIS 2022, 2022.

[69] Tata Steel. Tata Steel Board affirms the long-term strategy for growth in India. Dec. 2025. URL: https://www.tatasteel.com/newsroom/press-releases/india/2025/tata-steel-board-affirms-the-long-term-strategy-for-growth-in-india/.

[70] C. Ormston, Y. Xia, T. Dufty, S. Sabah, S. Al-Assafi, A. Okely, J. Fu, S. V. Dorp, A. Rhamdhani, G. Brooks, M. Sceats, and M. Boot-Handford. Breakthrough Pilot Testing Results for the Hydrogen Direct Flash Reduced Iron Process. Association for Iron & Steel Technology, 2025, pp. 2251–2265. DOI: 10.33313/389/240.

[71] T. Dufty. Calix Zesty Tech – Zero Emissions Iron and Steel – KS5 Pilot Plant Study Report. 2023. URL: https://arena.gov.au/knowledge-bank/calix-zesty-tech-zero-emissions-iron-and-steel-ks5-pilot-plant-study-report/.

[72] B. Mokhtarani, M. Jafarian, S. Sabah, T. Dufty, G. Brooks, W. Saw, A. Chinnici, and G. J. Nathan. New Insights Into Hydrogen Reduction of Hematite in an Indirectly Heated Flash Reactor from Measurements and First-Order Modeling. **Metallurgical and Materials Transactions B** 56 (2025), pp. 1928–1941. DOI: 10.1007/s11663-025-03465-3.

[73] L. Diamandescu, D. Mihàilà-Tàràbàşanu, and M. Feder. On the solid phase transformation goethite → hematite. **Materials Letters** 17 (1993), pp. 309–311. DOI: 10.1016/0167-577X(93)90019-T.

[74] D. Walter, G. Buxbaum, and W. Laqua. The Mechanism of the Thermal Transformation From Goethite To Hematite. **Journal of Thermal Analysis and Calorimetry** 63 (2001), pp. 733–748.

[75] A. Ammasi. Effect of Heating Rate on Decomposition Temperature of Goethite Ore. **Transactions of the Indian Institute of Metals** 73 (2020), pp. 93–98. DOI: 10.1007/s12666-019-01806-w.

[76] F. A. López, M. C. Ramirez, J. A. Pons, A. López-Delgado, and F. J. Alguacil. Kinetic study of the thermal decomposition of low-grade nickeliferous laterite ores. **Journal of Thermal Analysis and Calorimetry** 94 (2008), pp. 517–522. DOI: 10.1007/s10973-007-8679-2.

[77] P. Leerhoff, J. C. Brouwer, A. M. Armaki, C. Zeilstra, K. Meijer, J. van der Stel, S. T. Abrahami, N. Dogan, and Y. Yang. Characterisation of Varying Iron Ores and Their Thermal Decomposition Kinetics Under HIsarna Ironmaking Conditions. **Metals** 14, 1271 (2024). DOI: 10.3390/met14111271.

[78] K. Przepiera and A. Przepiera. Kinetics of Thermal Transformations of Precipitated Magnetite and Goethite. **Journal of Thermal Analysis and Calorimetry** 65 (2001), pp. 497–503. DOI: 10.1023/A:1012441421955.

[79] T. Grygar, I. H. D. Ruan, and R. J. Gilkes. Re-examination of the Kinetics of the Thermal Dehydroxylation of Goethite. **Journal of Thermal Analysis and Calorimetry** 55 (1999), pp. 301–309. DOI: 10.1023/A:1010181416785.

[80] P. C. Beuria, S. K. Biswal, B. K. Mishra, and G. G. Roy. Study on kinetics of thermal decomposition of low LOI goethetic hematite iron ore. **International Journal of Mining Science and Technology** 27 (2017), pp. 1031–1036. DOI: 10.1016/j.ijmst.2017.06.018.

[81] V. Strezov, T. J. Evans, V. Zymla, and L. Strezov. Structural deterioration of iron ore particles during thermal processing. **International Journal of Mineral Processing** 100 (2011), pp. 27–32. DOI: 10.1016/j.minpro.2011.04.005.

[82] T. Ariyama, S. Isozaki, S. Matsubara, H. Kawata, and I. Kobayashi. Fluidization and Degradation Characteristics of Iron Ore Fines in Prereduction Fluidized Bed. **ISIJ International** 33 (1993), pp. 1220–1227. DOI: 10.2355/isijinternational.33.1220.

[83] H. Li, D. J. Pinson, P. Zulli, L. Lu, R. J. Longbottom, S. J. Chew, B. J. Monaghan, and G. Zhang. Interaction Between Mineral Phases in a Goethitic Iron Ore and Fluxing Materials During Sintering. **Metallurgical and Materials Transactions B** 52 (2021), pp. 996–1011. DOI: 10.1007/s11663-021-02072-2.

[84] T. Murakami, T. Nishimura, and E. Kasai. Lowering Reduction Temperature of Iron Ore and Carbon Composite by Using Ores with High Combined Water Content. **ISIJ International** 49 (2009), pp. 1686–1693. DOI: 10.2355/isijinternational.49.1686.

[85] S. Hirokawa, T. Naito, and T. Yamaguchi. Effect of atmosphere on the goethite decomposition and pore structure of product particles. **Journal of Colloid and Interface Science** 112 (1986), pp. 268–273. DOI: 10.1016/0021-9797(86)90091-3.

[86] Y. Qu, Y. Yang, Z. Zou, C. Zeilstra, K. Meijer, and R. Boom. Thermal decomposition behaviour of fine iron ore particles. **ISIJ International** 54 (2014), pp. 2196–2205. DOI: 10.2355/isijinternational.54.2196.

[87] L. Xing, Y. Qu, C. Wang, L. Shao, Z. Zou, and W. Song. Kinetic Study on Thermal Decomposition Behavior of Hematite Ore Fines at High Temperature. **Metallurgical and Materials Transactions B** 51 (2020), pp. 395–406. DOI: 10.1007/s11663-019-01747-1.

[88] CRCT - ThermFact Inc. and GTT-Technologies. FactSage, Equilib Module. 2015. URL: https://factsage.com/.

[89] CRCT -ThermFact Inc. and GTT-Technologies. FactPS Database. 2015. URL: https://factsage.com/.

[90] Z. Chen, C. Zeilstra, J. van der Stel, J. Sietsma, and Y. Yang. Thermal Decomposition Reaction Kinetics of Hematite Ore. **ISIJ International** 60 (2020), pp. 65–72. DOI: 10.2355/isijinternational.ISIJINT-2019-129.

[91] M. Salmani, E. K. Alamdari, and S. Firoozi. Isoconversional analysis of thermal dissociation kinetics of hematite in air and inert atmospheres. **Journal of Thermal Analysis and Calorimetry** 128 (2017), pp. 1385–1390. DOI: 10.1007/s10973-016-5981-x.

[92] T. Ozawa. Kinetics of non-isothermal crystallization. **Polymer** 12 (1971), pp. 150–158. DOI: 10.1016/0032-3861(71)90041-3.

[93] A. W. Coats and J. P. Redfern. Kinetic Parameters from Thermogravimetric Data. **Nature** 201 (1964), pp. 68–69. DOI: 10.1038/201068a0.

[94] W. K. Jozwiak, E. Kaczmarek, T. P. Maniecki, W. Ignaczak, and W. Maniukiewicz. Reduction behavior of iron oxides in hydrogen and carbon monoxide atmospheres. **Applied Catalysis A: General** 326 (2007), pp. 17–27. DOI: 10.1016/J.APCATA.2007.03.021.

[95] S. S. Sun. A study of kinetics and mechanisms of iron ore reduction in ore/coal composites. PhD thesis. McMaster University, 1997.

[96] Y. Qu. Experimental Study of the Melting and Reduction Behaviour of Ore Used in the HIsarna Process. PhD thesis. Technische Universiteit Delft, 2013.

[97] D. Spreitzer and J. Schenk. Reduction of Iron Oxides with Hydrogen—A Review. **steel research international** 90, 1900108 (2019). DOI: 10.1002/srin.201900108.

[98] A. Heidari, N. Niknahad, M. Iljana, and T. Fabritius. A Review on the Kinetics of Iron Ore Reduction by Hydrogen. **Materials** 14, 7540 (2021). DOI: 10.3390/ma14247540.

[99] A. Meshram, J. Govro, R. J. OMalley, S. Sridhar, and Y. Korobeinikov. Modeling Isothermal Reduction of Iron Ore Pellet Using Finite Element Analysis Method: Experiments & Validation. **Metals** 12, 2026 (2022). DOI: 10.3390/met12122026.

[100] O. Levenspiel. Fluid-Particle Reactions: Kinetics. 3rd ed. John Wiley & Sons, 1999.

[101] Y. H. Han, J. S. Wang, R. Z. Lan, L. T. Wang, X. J. Zuo, and Q. G. Xue. Kinetic analysis of iron oxide reduction in top gas recycling oxygen blast furnace. **Ironmaking & Steelmaking** 39 (2012), pp. 313–317. DOI: 10.1179/1743281211Y.0000000058.

[102] L. Y. Xing, Z. S. Zou, Y. X. Qu, L. Shao, and J. Q. Zou. Gas–Solid Reduction Behavior of In-flight Fine Hematite Ore Particles by Hydrogen. **Steel Research International** 90, 1800311 (2019). DOI: 10.1002/srin.201800311.

[103] Y. Qu, Y. Yang, Z. Zou, C. Zeilstra, K. Meijer, and R. Boom. Reduction kinetics of fine hematite ore particles with a high temperature drop tube furnace. **ISIJ International** 55 (2015), pp. 952–960. DOI: 10.2355/isijinternational.55.952.

[104] P. Šimon. Isoconversional methods. **Journal of Thermal Analysis and Calorimetry** 76 (2004), pp. 123–132. DOI: 10.1023/B:JTAN.0000027811.80036.6c.

[105] H.-b. Zuo, C. Wang, J.-j. Dong, K.-x. Jiao, and R.-s. Xu. Reduction kinetics of iron oxide pellets with H_2 and CO mixtures. **International Journal of Minerals, Metallurgy, and Materials** 22 (2015), pp. 688–696. DOI: 10.1007/s12613-015-1123-x.

[106] L.-y. Yi, Z.-c. Huang, H. Peng, and T. Jiang. Action rules of $H2_2$ and CO in gas-based direct reduction of iron ore pellets. **Journal of Central South University** 19 (2012), pp. 2291–2296. DOI: 10.1007/s11771-012-1274-0.

[107] I.-J. Moon, C.-H. Rhee, and D.-J. Min. Reduction of hematite compacts by H2-CO gas mixtures. **steel research** 69 (1998), pp. 302–306. DOI: 10.1002/srin.199805555.

[108] I. Sohn and S. M. Jung. Effect of Metal Additions to the Reduction of Iron Oxide Composite Pellets with Hydrogen at Moderate Temperatures. **steel research international** 82 (2011), pp. 1345–1354. DOI: 10.1002/srin.201100144.

[109] K. Piotrowski, K. Mondal, H. Lorethova, L. Stonawski, T. Szymański, and T. Wiltowski. Effect of gas composition on the kinetics of iron oxide reduction in a hydrogen production process. **International Journal of Hydrogen Energy** 30 (2005), pp. 1543–1554. DOI: 10.1016/J.IJHYDENE.2004.10.013.

[110] S. K. Kuila, R. Chatterjee, and D. Ghosh. Kinetics of hydrogen reduction of magnetite ore fines. **International Journal of Hydrogen Energy** 41 (2016), pp. 9256–9266. DOI: 10.1016/j.ijhydene.2016.04.075.

[111] B. Lyu, G. Wang, F. Yang, H. Zuo, Q. Xue, and J. Wang. Kinetic Analysis of Isothermal and Non-Isothermal Reduction of Iron Ore Fines in Hydrogen Atmosphere. **Metals** 12, 1754 (2022). DOI: 10.3390/met12101754.

[112] B. Hou, H. Zhang, H. Li, and Q. Zhu. Study on kinetics of iron oxide reduction by hydrogen. **Chinese Journal of Chemical Engineering** 20 (2012), pp. 10–17. DOI: 10.1016/S1004-9541(12)60357-7.

[113] D. Wagner, O. Devisme, F. Patisson, D. Ablitzer, and D. A. Ablitzer. A laboratory study of the reduction of iron oxides by hydrogen. Aug. 2006, pp. 111–120. URL: https://hal.archives-ouvertes.fr/hal-00265636.

[114] J.-m. Pang, P.-m. Guo, P. Zhao, C.-z. Cao, and D.-w. Zhang. Influence of size of hematite powder on its reduction kinetics by H_2 at low temperature. **Journal of Iron and Steel Research International** 16 (2009), pp. 7–11. DOI: 10.1016/S1006-706X(10)60002-7.

[115] Y. Qu, Y. Yang, Z. Zou, C. Zeilstra, K. Meijer, and R. Boom. Kinetic study on gas molten particle reduction of iron ore fines at high temperature. **Ironmaking and Steelmaking** 42 (2015), pp. 763–773. DOI: 10.1179/1743281215Y.0000000021.

[116] Y. Qu, Y. Yang, Z. Zou, C. Zeilstra, K. Meijer, and R. Boom. Melting and reduction behaviour of individual fine hematite ore particles. **ISIJ International** 55 (2015), pp. 149–157. DOI: 10.2355/isijinternational.55.149.

[117] Z. Chen, C. Zeilstra, J. van der Stel, J. Sietsma, and Y. Yang. Reduction Kinetics of Fine Hematite Ore Particles in Suspension. **Metallurgical and Materials Transactions B** 52 (2021), pp. 3393–3402. DOI: 10.1007/s11663-021-02269-5.

[118] Z. Chen, C. Zeilstra, J. van der Stel, J. Sietsma, and Y. Yang. Reduction Mechanism of Fine Hematite Ore Particles in Suspension. **Metallurgical and Materials Transactions B** 52 (2021), pp. 2239–2252. DOI: 10.1007/s11663-021-02173-y.

[119] Z.-y. Chen, Y.-x. Qu, C. Zeilstra, J. van der Stel, J. Sietsma, and Y.-x. Yang. Prediction of density and volume variation of hematite ore particles during in-flight melting and reduction. **Journal of Iron and Steel Research International** 26 (2019), pp. 1285–1294. DOI: 10.1007/s42243-019-00265-3.

[120] F. Chen, Y. Mohassab, T. Jiang, and H. Y. Sohn. Hydrogen Reduction Kinetics of Hematite Concentrate Particles Relevant to a Novel Flash Ironmaking Process. **Metallurgical and Materials Transactions B** 46 (2015), pp. 1133–1145. DOI: 10.1007/s11663-015-0332-z.

[121] F. Chen, Y. Mohassab, S. Zhang, and H. Y. Sohn. Kinetics of the Reduction of Hematite Concentrate Particles by Carbon Monoxide Relevant to a Novel Flash Ironmaking Process. **Metallurgical and Materials Transactions B** 46 (2015), pp. 1716–1728. DOI: 10.1007/s11663-015-0345-7.

[122] A. O. Zhang, B. J. Monaghan, R. J. Longbottom, M. Nusheh, and C. W. Bumby. Reduction Kinetics of Oxidized New Zealand Ironsand Pellets in H2 at Temperatures up to 1443 K. **Metallurgical and Materials Transactions B** 51 (2020). DOI: 10.1007/s11663-020-01790-3.

[123] A. Hammam, Y. Li, H. Nie, L. Zan, W. Ding, Y. Ge, M. Li, M. Omran, and Y. Yu. Isothermal and Non-Isothermal Reduction Behaviors of Iron Ore Compacts in Pure Hydrogen Atmosphere and Kinetic Analysis. **Mining, Metallurgy & Exploration** 38 (2021), pp. 81–93. DOI: 10.1007/s42461-020-00317-3.

[124] Y. Qu, L. Xing, C. Wang, L. Shao, and Z. Zou. Kinetic characterization of flash reduction process of hematite ore fines under hydrogen atmosphere. **International Journal of Hydrogen Energy** 45 (2020), pp. 31481–31493. DOI: 10.1016/j.ijhydene.2020.08.196.

[125] D. S. Newsome. The Water-Gas Shift Reaction. **Catalysis Reviews** 21 (1980), pp. 275–318. DOI: 10.1080/03602458008067535.

[126] G. K. Reddy and P. G. Smirniotis. Introduction About WGS Reaction. Elsevier, 2015, pp. 1–20. DOI: 10.1016/B978-0-12-420154-5.00001-2.

[127] CRCT - ThermFact Inc. and GTT - Technologies. FactSage, Reactions Module. 2015. URL: https://factsage.com.

[128] H. Idriss, M. Scott, and V. Subramani. Introduction to hydrogen and its properties. Elsevier, 2015, pp. 3–19. DOI: 10.1016/b978-1-78242-361-4.00001-7.

[129] A. Abdelrahim, M. Iljana, M. Omran, T. Vuolio, H. Bartusch, and T. Fabritius. Influence of H_2–H_2O Content on the Reduction of Acid Iron Ore Pellets in a CO–CO_2–N_2 Reducing Atmosphere. **ISIJ International** 60 (2020), pp. 2206–2217. DOI: 10.2355/isijinternational.ISIJINT-2019-734.

[130] E. Lorente, J. Herguido, and J. A. Peña. Steam-iron process: Influence of steam on the kinetics of iron oxide reduction. **International Journal of Hydrogen Energy** 36 (2011), pp. 13425–13434. DOI: 10.1016/j.ijhydene.2011.07.111.

[131] W.-H. Kim, S. Lee, S.-M. Kim, and D.-J. Min. The retardation kinetics of magnetite reduction using H_2 and H_2–H_2O mixtures. **International Journal of Hydrogen Energy** 38 (2013), pp. 4194–4200. DOI: 10.1016/j.ijhydene.2013.01.147.

3

CHARACTERISATION OF VARYING IRON ORES AND THEIR THERMAL DECOMPOSITION KINETICS UNDER HISARNA IRONMAKING CONDITIONS

In the pre-reduction cyclone of the HIsarna® process, both thermal decomposition and gas reduction of the injected iron ores occur simultaneously at gas temperatures of 1723–1773 K. In this study, the kinetics of the thermal decomposition of three iron ores (namely OreA, OreB and OreC) for HIsarna ironmaking were analysed as an isolated process with a symmetrical thermogravimetric analyser (TGA) under an inert atmosphere. Using various methods, the chemical and mineralogical composition, particle size distribution, morphology and phase distribution of the ores were analysed. The ores differ in their mineralogy and morphology, where OreA only contains hematite as iron-bearing phase and OreB and OreC include goethite and hematite. To obtain the kinetic parameters in non-isothermal conditions, the Coats–Redfern Integral Method was applied for heating rates of 1, 2 and 5 K/min and a maximum temperature of 1773 K. The TGA results indicate that goethite and hematite decomposition occur as a two-stage process in an inert atmosphere of Ar. The proposed reaction mechanism for the first stage of goethite decomposition is a chemical re-action with an activation energy ranging from 46.55 to 60.38 kJ/mol for OreB and from 69.90 to 134.47 kJ/mol for OreC. The proposed reaction mechanism for the second stage of goethite de-composition is diffusion, showing an activation energy ranging between 24.43 and 44.76 kJ/mol for OreB and between 3.32 and 23.29 kJ/mol for OreC. In terms of hematite decomposition, only the first stage was analysed. The proposed reaction mechanism is chemical reaction control. OreA shows an activation energy of 545.47 to 670.50 kJ/mol, OreB one of 587.68 to 831.54 kJ/mol and OreC one of 424.31 to 592.32 kJ/mol.

This chapter has been published in P Leerhoff et al. "Characterisation of Varying Iron Ores and Their Thermal Decomposition Kinetics Under HIsarna Ironmaking Conditions." In: Metals **2024**, 14, 1271 [1].

3.1. INTRODUCTION

The iron- and steelmaking industry alone is responsible for around 7–9 % of anthropogenic-generated CO_2 emissions [2]. The main reason for this is the blast furnace (BF), which is the dominant operating technology for ironmaking, contributing up to 71 % of the global CO_2 emissions for steel production [3]. Comparing the currently commercially available established steelmaking routes, BF-BOF, Scrap-EAF, and DRI-EAF, the blast furnace route exhibits the highest amounts of CO_2 emissions per tonne of crude steel [3]. Our society is strongly dependent on steel production and considering the increasing production trend over last few decades, steel production is expected to grow further [4], and it is of utmost importance to reduce the CO_2 emissions arising from the steel industry.

Iron ores can generally be categorized into high-grade (>65 % Fe), medium-grade (62–65 % Fe) and low-grade (<62 % Fe) ores. The most commercially used iron ores are hematite (69.94 % Fe) and magnetite (72.36 % Fe), exhibiting the highest amounts of iron content in available ores. Next to hematite and magnetite, multiple other iron ores are present [5]. One of them is goethite, which is abundantly available in India [6]. Goethite $FeO * (OH) * nH_2O$, a medium-grade ore, contains chemically bound water [5]. Alongside the environmental problems arising from the blast furnace route, demand issues in the primary production of steel can become critical. Large amounts of goethite are important to tackle future demand problems in ironmaking industry, but its use leads to technical challenges due to its lower iron content.

In the framework of the ULCOS project, HIsarna (Figure 3.1) was developed by Tata Steel as an alternative ironmaking process with the objective to substitute the blast furnace [7]. HIsarna operates using a counter-current principle, where the injected iron ore is in contact with the hot process gas in a temperature range of 1723–1773 K, thereby combining the two process steps of cyclone converter and smelting reduction in a single operating furnace [8]. In the upper section, the solid particles are heated up, melted and pre-reduced with reducing gas mixtures of $CO - CO_2 - H_2 - H_2O$, arising from the reactions in the lower section of the furnace [8, 9]. In the lower section of the furnace, the final reduction of the pre-reduced molten ores with coal to metallic iron takes place. Due to this reaction, the reducing gas mixture needed in the top section is produced [8]. The degree of pre-reduction that occurs in the top section is around 10–20 %. The use of HIsarna, instead of the blast furnace, reduces the three blast furnace process steps, coking, agglomeration and ironmaking, to only one process step, the ironmaking itself. This leads to a lower energy consumption and less CO_2 emissions [8]. In combination with carbon capture and storage (CCS) technology, HIsarna is expected to reduce CO_2 emissions by up to 80 % compared to traditional blast furnace ironmaking [9]. HIsarna has the further advantage of using low-grade, untreated (industrial) ores, with a high amount of gangue material, which are lower in iron content and other residues arising from iron-bearing processes within and outside the steelmaking industry. Further, hydrogen enrichment and the use of renewable carbon sources to improve HIsarna ironmaking technologies are under investigation.

In the top section of a HIsarna furnace, two main reaction mechanisms prevail: thermal decomposition and gas–solid reduction by a gas mixture of CO and H_2. During the injection, the fine ores are rapidly heated up, thermally decomposed, pre-reduced by the gas atmosphere and partly melted. Most particles experience short residence in the top

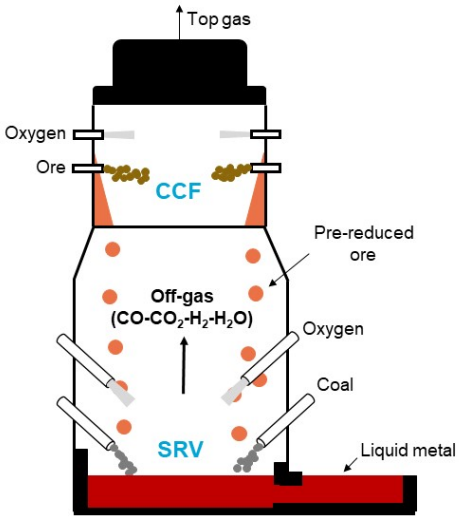


Figure 3.1: Schematic of HIsarna process (Adapted from [8]).

section of the HIsarna furnace, but some particles can hit the walls and become deposited as a molten film. Considering thermodynamics, the reduction of the ores by thermal decomposition and gas reduction has the same effect. Both reactions describe the removal of oxygen from the ore leading to a lower oxygen content. Regarding kinetics, however, both the residence time of the particle in the top section and the mechanisms that occur influence the reaction rates and rate-limiting steps. Qu et al. [10] investigated the thermal decomposition behaviour of hematite ores with low gangue materials and Chen et al. [11] focused on the thermal decomposition behaviour of hematite ores with higher gangue contents. The current study aims to extend this research to the investigation of hematite ores with high contents of gangue materials as well as goethite-based iron ores and to analyse the influence of ore mineralogy on the decomposition kinetics.

3.2. MATERIAL ANALYSIS

Varying types of commercial iron-bearing ores were provided by Tata Steel Netherlands, which we called OreA, OreB and OreC. The ores were classified into two different particle size fractions ($< 63\ \mu$m, (63–125) μm) by wet sieving. The particle size is defined as the particle diameter. The size ranges were verified via light scattering technology with the Microtrac Bluewave. Each sample was automatically measured in triplicate. The resulting mean diameter of the volume distribution (MV), number distribution (MN) and area distribution (MA) are presented in Table 3.1 and the overall particle size distribution in Figure 3.2. It is important to mention that the three values of MV, MN and MA are used to generate a broad overview on the averaged particle sizes from different perspectives. MV is strongly influenced by coarser particles and therefore usually shows larger average particle sizes. MA is a particle surface measurement and is less affected by coarse particles,

leading to smaller average particle sizes. MN is related to the population of the particles and is more sensitive towards small particles, therefore showing the smallest average particle size. Figure 3.2 portrays the passing percentage in relation to the particle size. A larger passing at low particle sizes, therefore indicates an overall smaller particle size distribution. The < 63 μm fractions of OreA, OreB and OreC show almost no particles larger than the defined fraction. The fraction of (63 – 125) μm OreC shows the largest passing in the defined ranges, followed by OreB and OreA.

Table 3.1: Particle size metrics for different ore fractions.

	OreA		OreB		OreC	
Fraction [μm]	<63	63–125	<63	63–125	<63	63–125
MV [μm]	50.74	103.6	44.22	100.2	22.79	115.9
MN [μm]	19.55	51.96	3.66	66.29	1.106	89.55
MA [μm]	39.41	84.86	25.52	87.58	6.80	105.5

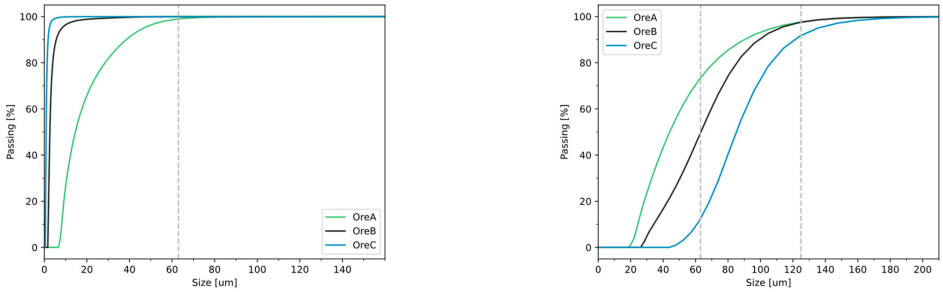


Figure 3.2: Particle size distribution of OreA, OreB and OreC for size fractions of (a) < 63 μm and (b) (63 – 125) μm.

3.2.1. COMPOSITION ANALYSIS

X-Ray diffraction (XRD) with a Bruker D8 Advance diffractometer Bragg-Brentano geometry and Lynxeye position sensitive detector (Bruker, Germany) was used to evaluate the mineralogy of the samples and to determine the main differences in composition of the different iron ores. In general, the XRD signal is complex, containing a lot of smaller peaks due to the high amount of gangue materials in the ores (Figure A.1, appendix A). For OreA, hematite (Fe_2O_3), quartz (SiO_2) and dolomite ($CaMg(CO_3)_2$) were detected as the main phases. Additionally, for the fraction < 63 μm a few small magnetite (Fe_3O_4) peaks occurred, which were not measured in the other samples. OreB and OreC contained a goethite phase as an iron-bearing mineral in addition to hematite. The mineralogical composition of OreB was goethite (FeOOH), hematite, quartz and kaolinite ($Al_2Si_2O_5(OH)_4$). For OreC only hematite, goethite and quartz were detected as mineral phases.

In order to obtain deeper insights in the elemental composition of the ores, the chemical compositions of the ore fractions were determined by X-Ray fluorescence (XRF)

Table 3.2: Chemical composition of varying iron ores based on XRF and LOI.

Compound [wt.%]	Fraction [µm]	OreA		OreB		OreC	
		<63	63–125	<63	63–125	<63	63–125
Fe_2O_3		85.93	91.50	88.07	85.07	81.21	82.92
total-Fe		60.10	64.00	61.60	59.50	56.80	58.00
SiO_2		5.18	2.96	4.96	5.83	6.84	5.30
Al_2O_3		2.24	1.44	3.81	4.78	3.52	3.00
MgO		0.71	0.41	0.04	0.04	0.14	0.11
CaO		1.99	1.23	0.05	0.05	0.11	0.07
TiO_2		1.04	0.92	0.33	0.35	0.18	0.16
MnO		1.20	0.60	0.03	0.03	1.07	1.24
total-C		0.41	0.23	0.06	0.07	0.18	0.14
H_2O (crystal)		–	–	2.19	3.26	6.05	6.39
Rest		0.37	0.21	0.25	0.31	0.26	0.26

(Panalytical AXIOS XRF, Netherlands) and loss of ignition (LOI) analysis (dissolution in nitric acid and TGA (LECO, Germany)). The results are listed in Table 3.2, after normalisation and conversion to the expected oxide phases. The total-C in the system was calculated based on the assumption that all measured carbon is present as CO_2 in the sample. The content of gangue and iron-bearing phases varies not only between the different ores, but also between the different size fractions. For all ores, the main gangue components were SiO_2 and Al_2O_3. OreB shows the highest amounts of Al_2O_3, underlined by the detected kaolinite phase in the XRD measurements. All ores show similar contents of SiO_2, varying in particle size fraction. In contrast to OreB and OreC, the measurements for OreA show higher amounts of CaO and MgO, from the detected dolomite phase. Further, OreB and OreC show lower amounts of carbon compared to OreA, due to the association of carbon to the dolomite phase in OreA. The crystal water in OreB and OreC indicates a goethite phase, with larger amounts present in OreC.

3.2.2. MORPHOLOGICAL ANALYSIS

To observe the morphology of the different ores, SEM images were taken by a Jeol JSM-IT100 (Jeol, The Netherlands). Representative images of the chosen fractions of the ores are displayed in Figure 3.3. Significant differences in morphology are visible between the goethite and hematite ores. The morphology of OreA appears to be angular in shape with almost no spherical particles. The structure is close-grained and does not seem to be porous. Bright particles assumed to be further gangue components, are visible either as individual particles or as inclusions on the hematite particles. OreB appears to be less angular and more spherical in structure. The presence of crystal water could be a reason for the apparent porosity of the particles. For OreC, the particles of the larger size fraction (Figure 3.3f) again appear to be more close-grained, despite the larger amounts of crystal water. Again, the particles shape appears to be more spherical compared to OreA. However, for the < 63 μm size fraction (Figure 3.3c), the particles seem to agglomerate and many fine ore particles are observable as clusters. This is also reflected in the low

average particle size values of MV, MN and MA of this fraction. For OreB and OreC no bright particles are visible either on the particle surface or as individual particles.

3.2.3. PHASE DISTRIBUTION

To further investigate the distribution of impurities (gangue) in the samples, the particles of the small fractions (< 63 μm) were mounted in a resin, followed by sanding and polishing to create a cross-section of the particles. The cross-sections were again analysed under the SEM, together with EDS mapping to gain insight into the elemental distribution of the particles (Figure 3.4). Displayed here are only the main elements of the ore, Fe, Al and Si. The mapping of OreA supports the findings from the morphological study, indicating that the distribution of impurities is seen as single, brighter particles, as well as inclusions on the hematite particles. The elemental distribution of OreC indicates a similar distribution compared to OreA. Aluminium and silicon are distributed as distinct particles across the sample, with high intensities of these elements. For OreB, a different elemental distribution is observable. For silicon, a few distinct small particles are visible. Apart from that, the aluminium and silicon compounds seem to be coexisting with the iron ore particles. However, the distribution of iron shows that several iron ore particles are present without the additional presence of aluminium or silicon.

It is not possible to distinguish between hematite and goethite using SEM-EDS due to the elemental characteristics of hydrogen. To gain more insights into the distribution of the goethite phase in OreB and OreC, surface-enhanced Raman spectroscopy (alpha300 R-Raman imaging microscope (WITec, Germany)) was carried out for both size fractions of OreB and OreC (Figure 3.5). Data from the literature for pure hematite and goethite [12] were used to identify pure hematite and goethite particles in the samples. Based on the Raman shift in these particles, the reference spectrum presented in Figure 3.5a was created to map the phase distribution. Next, different representative spots in the samples were measured and compared to the reference spectra. If the shift in the peaks is similar to the reference spectra, it is assumed to be the same phase. Apart from the pure goethite and hematite, a mixed phase was measured, shown in the example spectrum in Figure 3.5b.

Considering the distribution of goethite and hematite in the large size fraction (63-125) μm, four different particle structures were identified for both OreB and OreC (Figure 3.5d,f). OreC consists of almost pure hematite and goethite particles, hematite particles with smaller amounts of goethite and goethite particles with distinctive hematite inclusions and a mixed phase. OreB also contains almost pure hematite and goethite particles. However, goethite particles with hematite inclusions and the mixed phase appear to be present in larger quantities. For the smaller size fraction (< 63 μm), no individual particles were analysed, but a selected area was scanned for the mapping. It must be noted that the dark area in the scan relates to the resin the particles were embedded in. OreC in Figure Figure 3.5c shows a distinctive separation of the goethite and hematite phase and small spots of the mixed phase. OreB in Figure 5e also shows a segregation of the hematite and goethite phases. However, the mapping of OreB further indicates the co-existence of goethite and hematite in some areas.

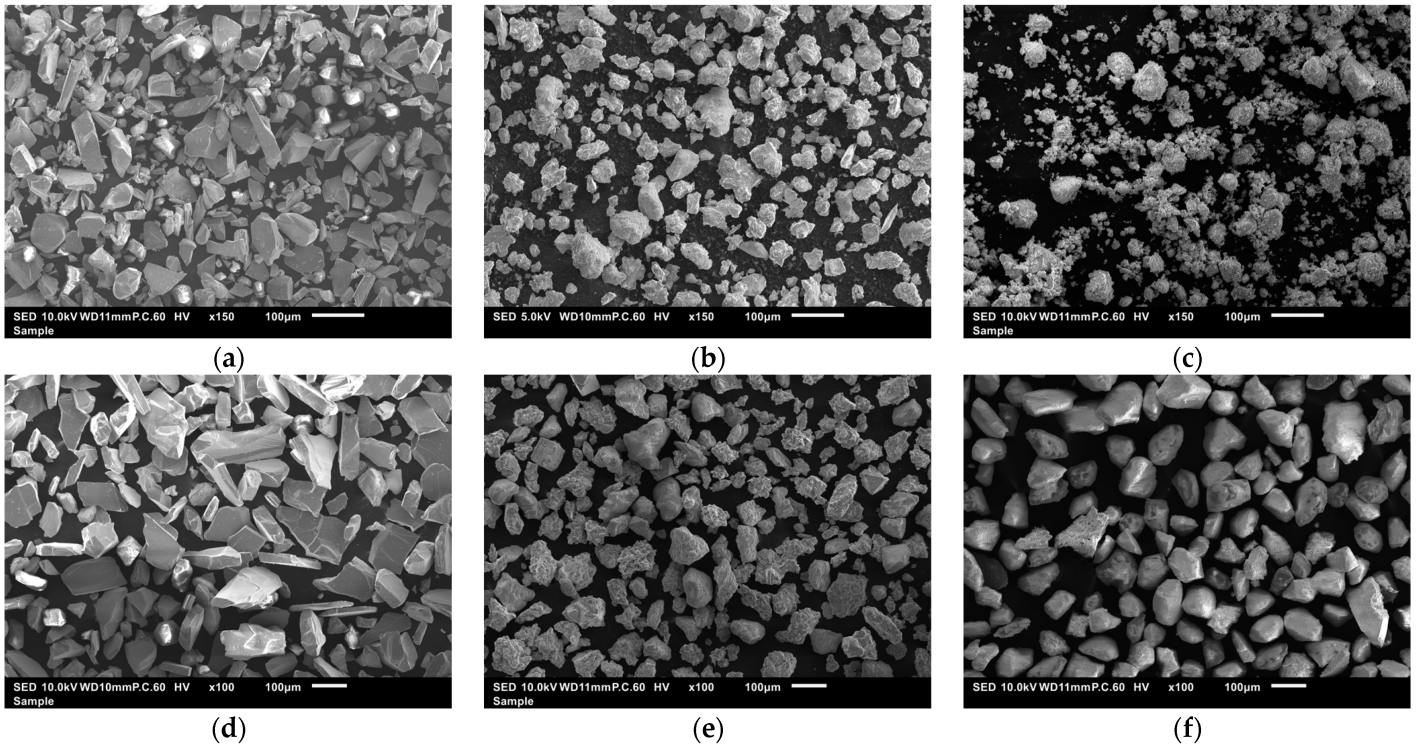


Figure 3.3: SEM images for (a) OreA fraction < 63 μm (150×); (b) OreB fraction < 63 μm (150×); and (c) OreC fraction < 63 μm (150×); (d) OreA fraction (63 – 125) μm (100×); (e) OreB fraction (63 – 125) μm (100×); and (f) OreC fraction (63 – 125) μm (100×).

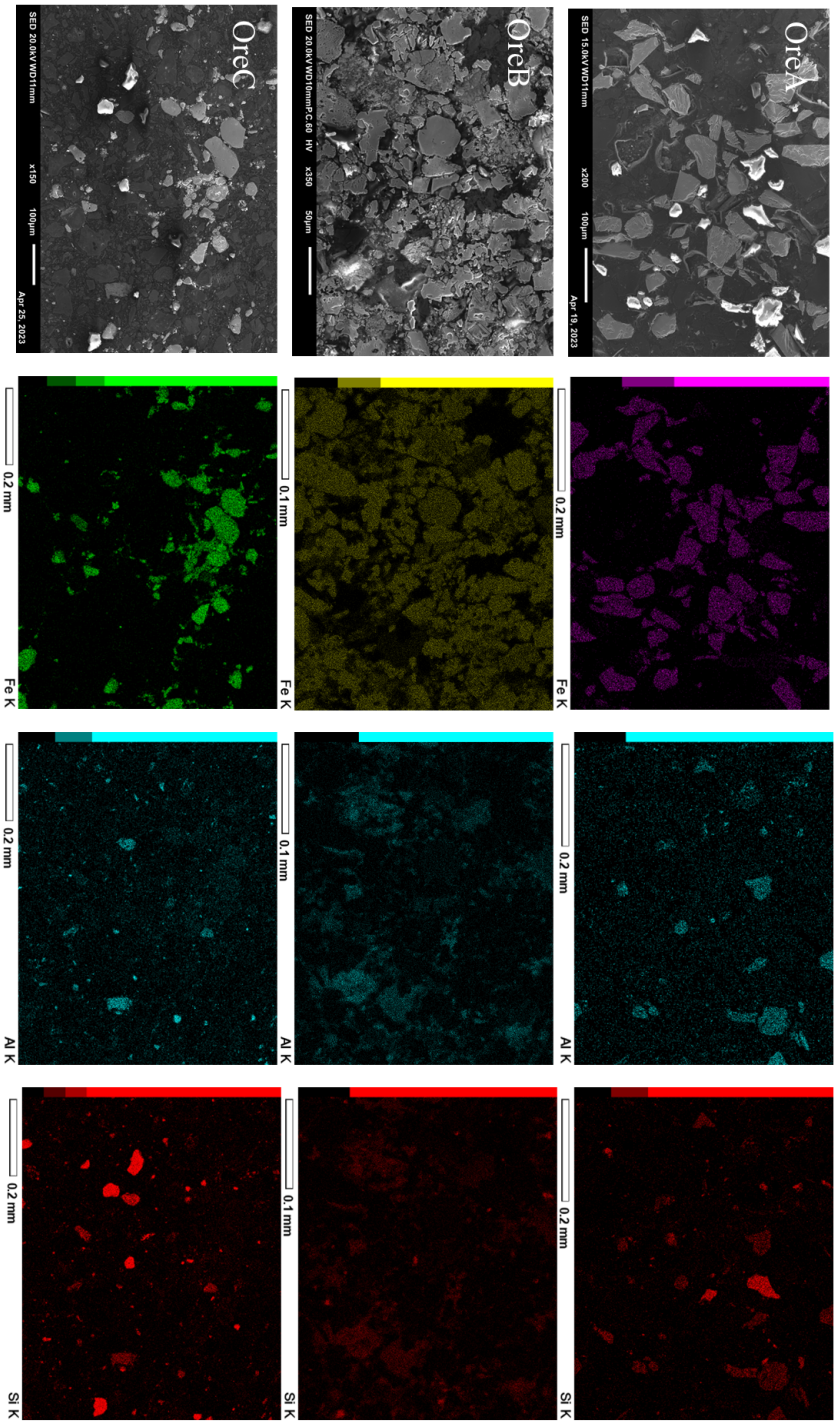


Figure 3.4: Elemental distribution of ore fractions < 63 μm in mounted resin (purple/yellow/green: Fe, blue: Al, red: Si).

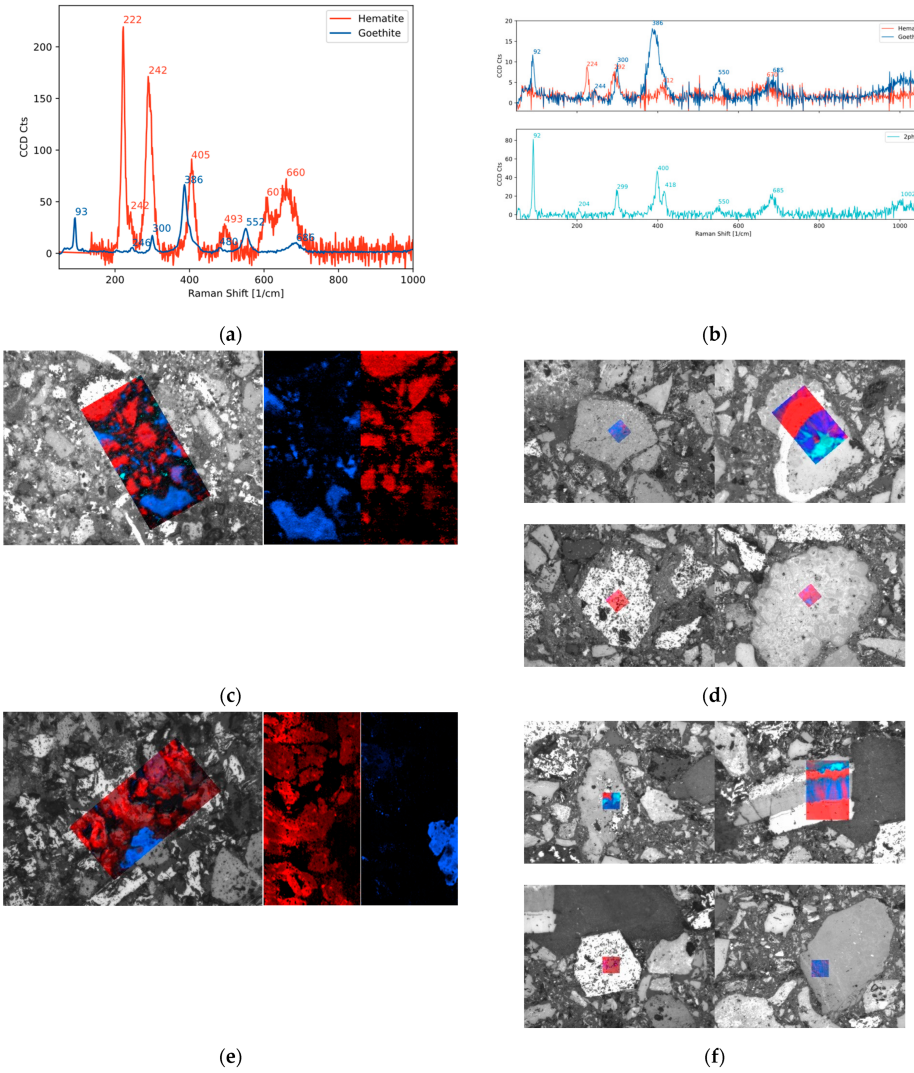


Figure 3.5: Raman spectroscopy for (a) the reference spectra; (b) the spectra of OreC < 63 μm; (c) mapping for OreC < 63 μm (left for complete mapping; right for separated mapping); (d) OreC (63 – 125) μm; (e) OreB < 63 μm (left for complete mapping; right for separated mapping); and (f) OreB (63 – 125) μm (red: hematite, dark blue: goethite, light blue: mixed phase).

3.3. METHODS

3.3.1. TGA EXPERIMENTS

To obtain insights into the non-isothermal decomposition behaviour and kinetics of the goethite and hematite ores, experiments were carried out in a symmetrical thermogravimetric analyser (TGA, Setaram TAG 16/18, Caluire, France). Around 300 mg of ore sample was placed into Alsint crucibles with an inner diameter of 10 mm and a wall thickness of 2 mm. The total height of the crucible is 20 mm. The operating parameters are presented in Table 3.3. In order to evaluate the thermal decomposition of the ores, the experiments were carried out in an argon atmosphere with a flow rate of 100 mL/min. The ore particles with a size fraction < 63 μm were gradually heated at three heating rates (1, 2 and 5 K/min) until a temperature of 1773 K was reached. Experiments for the particle size fraction of (63 – 125) μm were only carried out with a heating rate of 2 K/min to compare the results to the smaller particle size fraction at the same heating rate. After 1773 K was reached, a holding time of two hours was applied to achieve the limit of thermal decomposition. After that, the system was cooled to room temperature with a controlled cooling rate of 5 K/min. The mass loss over an increasing temperature at a constant heating rate was measured as the basic data for performing the decomposition and kinetic analysis.

Table 3.3: Experimental conditions in TGA, Setaram TAG 16/18.

Experimental Condition	Operating Parameter
Sample	Hematite fine ore, Goethite fine ore
Holding time (h)	2
Heating rate (K/min)	1, 2, 5
Particle size (μm)	<63, 63–125
Temperature (K)	298-1773
Atmosphere	Ar

3.3.2. ASSESSMENT OF REACTION KINETICS OF THERMAL DECOMPOSITION

The kinetic parameters, activation energy (Ea) and pre-exponential factor A of hematite and goethite decomposition under non-isothermal conditions with a constant heating rate were determined using the Coats–Redfern Integral Method [13]. Through model fitting, the most applicable model describing the thermal decomposition of hematite and goethite was estimated. Commonly used models for gas–solid reactions are listed in Table 3.4. The essential characteristic parameter for all the kinetic models is the conversion factor α (equation (Eq. (3.1))).

$$\alpha = \frac{m_0 - m_t}{m_0 - m_a} \tag{3.1}$$

where m_0 is the mass of the initial sample (mg), m_t is the mass of the sample at time t (mg) and ma is the mass of the sample after complete conversion or thermal decomposition (mg). In the following analysis, the final conversion state was considered to be the decomposition from either Fe_2O_3 to Fe_3O_4 or from FeOOH to Fe_2O_3. Hence, a conversion factor of 0 equals the initial state of hematite or goethite and a conversion

factor of 1 equals the complete decomposition to magnetite or hematite. The general expression of the reaction rate of the thermal decomposition process is presented in equation (Eq. (3.2)). Applying the Arrhenius equation, the expression for the reaction rate constant can be determined through equation (Eq. (3.3)). Considering a constant heating rate, the reaction rate equation can be written as equation (Eq. (3.4)).

$$\frac{d\alpha}{dt} = kf(\alpha) \tag{3.2}$$

$$k = A\exp\left(-\frac{E_a}{RT}\right) \tag{3.3}$$

$$\frac{d\alpha}{dT} = \frac{A}{\beta}\exp\left(-\frac{E_a}{RT}\right)f(\alpha) \tag{3.4}$$

where k is the reaction rate constant (s^1), f(α) is a function of the conversion factor α, A is the exponential factor (s^1), Ea is the activation energy (J/mol), β is the heating rate (K/s), T is the temperature (K) and R is the gas constant (8.314 J/(mol·K)). The kinetic parameters of hematite and goethite decomposition were determined by the Coats–Redfern Integral Method (equation (Eq. (3.5))).

$$\ln\left(\frac{g(\alpha)}{T^2}\right) = \ln\left(\frac{AR}{\beta E_a}\left(1-\frac{2RT}{E_a}\right)\right) - \frac{E_a}{RT} \tag{3.5}$$

where g(α) is the integrated form of the function f(α). The activation energy (Ea) and the pre-exponential factor (A) can be determined from the slope and intercept of the plot $\ln\left(\frac{g(\alpha)}{T^2}\right)$ vs. $\frac{1}{T}$. Assuming that the activation energy is significantly larger than $2RT$, the term $\left(1-\frac{2RT}{E_a}\right)$ in equation Eq. (3.5) is approximated as 1. Thus, the slope of the plot equals $\frac{-E_a}{R}$, and the intercept equals $\ln\left(\frac{AR}{\beta E_a}\right)$. For the calculation of the activation energy, the intercept, the reaction rate constant, and the resulting reaction rate of the model with the best linear fit (R^2 close to 1) were used.

3.4. RESULTS AND DISCUSSION

Even though most fine ores injected into the HIsarna furnace experience very short residence times (ms) in the pre-reduction cyclone of the system, particles can agglomerate in clusters or deposit on the walls of HIsarna furnace, leading to longer particle residence times. Gas reduction and thermal decomposition are expected to occur as co-existing phenomena. This paper studies the limits of thermal decomposition as an isolated mechanism of the presented ores. The Results section will first focus on the general thermal decomposition behaviour of the varying ores to identify the different decomposition stages and their temperature ranges. For this, the mass loss and QMS (quadrupole mass spectrometer) off-gas data will be presented. Based on the mass loss's dependency on temperature, a kinetic analysis is further carried out. First, the conversion factor will be determined as an underlying kinetic parameter for the defined temperature ranges and applied to the model fit. Based on the model fit, the activation energy for the varying iron ores will be compared.

Table 3.4: Reaction models for gas-solid reaction processes (Adapted from [11, 14]).

Reaction Model		f(α)	g(α)
Nucleation			
Power law	P1	$4\alpha^{3/4}$	$\alpha^{1/4}$
	P2	$3\alpha^{2/3}$	$\alpha^{1/3}$
	P3	$2\alpha^{1/2}$	$\alpha^{1/2}$
Avrami-Erofeev	A2	$2(1-\alpha)[-\ln(1-\alpha)]^{1/2}$	$[-\ln(1-\alpha)]^{1/2}$
	A3	$3(1-\alpha)[-\ln(1-\alpha)]^{2/3}$	$[-\ln(1-\alpha)]^{1/3}$
	A4	$4(1-\alpha)[-\ln(1-\alpha)]^{3/4}$	$[-\ln(1-\alpha)]^{1/4}$
Diffusion			
n-Dimensional Diffusion	D1	$1/(2\alpha)$	α^2
	D2	$[1-(1-\alpha)^{1/2}]^{-1}$	$(1-\alpha)\ln(1-\alpha)+\alpha$
	D3	$3/2[1-(1-\alpha)^{1/3}]^{-1}$	$[1-(1-\alpha)^{1/3}]^2$
	D4	$3(1-\alpha)^{2/3}[1-(1-\alpha)^{1/3}]^{-1}$	$1-(1-\alpha)^{1/3}$
Geometrical Contraction			
Contracting Area	R2	$2(1-\alpha)^{1/2}$	$1-(1-\alpha)^{1/2}$
Contracting Volume	R3	$3(1-\alpha)^{2/3}$	$1-(1-\alpha)^{1/3}$
Reaction order			
	F0	1	α
	F1	$1-\alpha$	$-\ln(1-\alpha)$
	F2	$(1-\alpha)^2$	$(1/(1-\alpha))-1$
	F3	$(1-\alpha)^3$	$[(1-\alpha)^{-2}-1]/2$

3.4.1. THERMAL DECOMPOSITION

Figure 3.6 shows different mass loss curves from the thermogravimetric measurement of the feed materials with particle size fractions of OreA, OreB and OreC with varying heating rates (Figure 3.6a) and a comparison to the larger particle size of (63 – 125) μm is shown in Figure 3.6b. Three mass loss stages are observed for OreA, while four stages are seen for OreB and OreC. The initiation of the individual mass loss curves shows slight dependencies on the heating rate for all ores. The mass loss and therefore the decomposition starts earlier with the lower heating rate. Larger dependencies are visible for the ores based on mineralogy. OreC shows the highest mass loss, while OreA shows the lowest mass loss under the same thermal conditions.

To obtain details regarding the decomposing gas phases, the off-gas was measured via QMS. Examples of the mass loss curves in combination with the QMS data are presented in Figure 3.7 for each ore at a heating rate of 2 K/min. Only the main measured gas phases are presented. It must be mentioned that the presented analysis only provides qualitative data, meaning the height of the peaks cannot be compared between experiments. All ores show a distinct O_2 peak at later stages in the reaction. This peak indicates the decomposition of the hematite phase under the removal of oxygen. Above temperatures of 570°C, the reduction of hematite (Fe_2O_3) occurs step-wise, initially forming porous magnetite (Fe_3O_4) and later wüstite ($Fe_{(1x)}O$) [15]. Additionally, OreA contains a distinct peak of CO_2 emission. Based on the initial composition of OreA, this peak reflects the

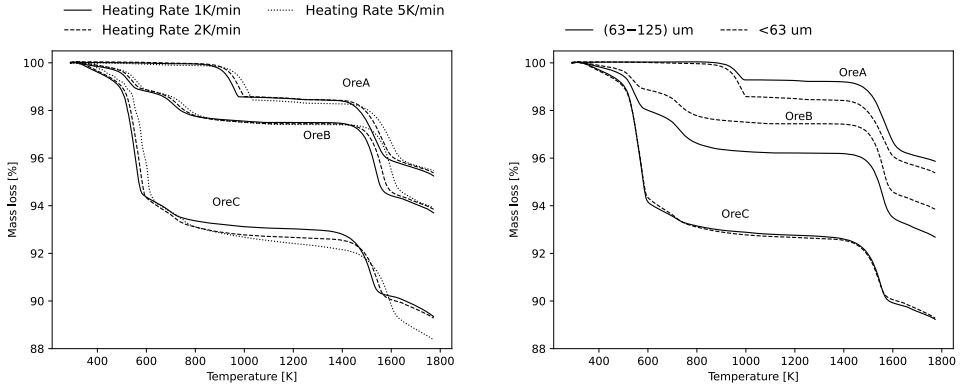


Figure 3.6: Mass loss curves of hematite and goethite ore particles: (a) fraction of < 63 μm for varying heating rates and (b) fraction of < 63 μm and (63 – 125) μm for a heating rate of 2 K/min.

decomposition of carbonates (dolomite). The decomposition of dolomite occurs at low CO_2 partial pressures as a single step reaction (equation (Eq. (3.6))) [16].

$$CaMg(CO_3)_2 \longrightarrow CaO + MgO + 2\,CO_2 \tag{3.6}$$

This behaviour of OreA was also observed in the publication of Chen et al. [11], in which the first mass loss stage was described as calcination (thermal decomposition) of carbonates and the two later mass loss stages were described as the two-stage decomposition of hematite. The QMS signals of OreB and OreC further indicate the emission of water vapour. Water vapour is emitted as the goethite phase converts into hematite based on equation (Eq. (3.7)) [17].

$$2\,\alpha FeOOH \longrightarrow \alpha Fe_2O_3 + H_2O \tag{3.7}$$

OreC shows a generally higher mass loss due to the larger amount of goethite in the raw material, leading to a larger (yet, sharp) emission of water vapour. A more continuous emission of water vapour is observed for OreB, indicating a stronger inclusion of the compound in the ore matrix. This behaviour is supported by the Raman spectroscopy presented in Figure 3.5. It is expected that the goethite present as individual particles is more accessible and therefore decomposes earlier. Consequently, the first stronger peak, which is present for both ores, is assigned to the decomposition of the almost pure goethite particles in the sample. The second peak, as seen in Figure 3.7b and to lesser extend in Figure 3.7c, is presumed to be the decomposition of the goethite from the mixed phase or the goethite which is intertwined with hematite in the particles.

The start and end temperatures for the individual decomposition stages are determined by the temperature boundaries of the first derivative of the mass loss curves, presented in Table 3.5 in combination with the measured mass loss in the respective stages. Walter et al. [18] investigated conversion temperatures of goethite to hematite for different particle sizes and observed conversion temperatures between 465 and 523 K.

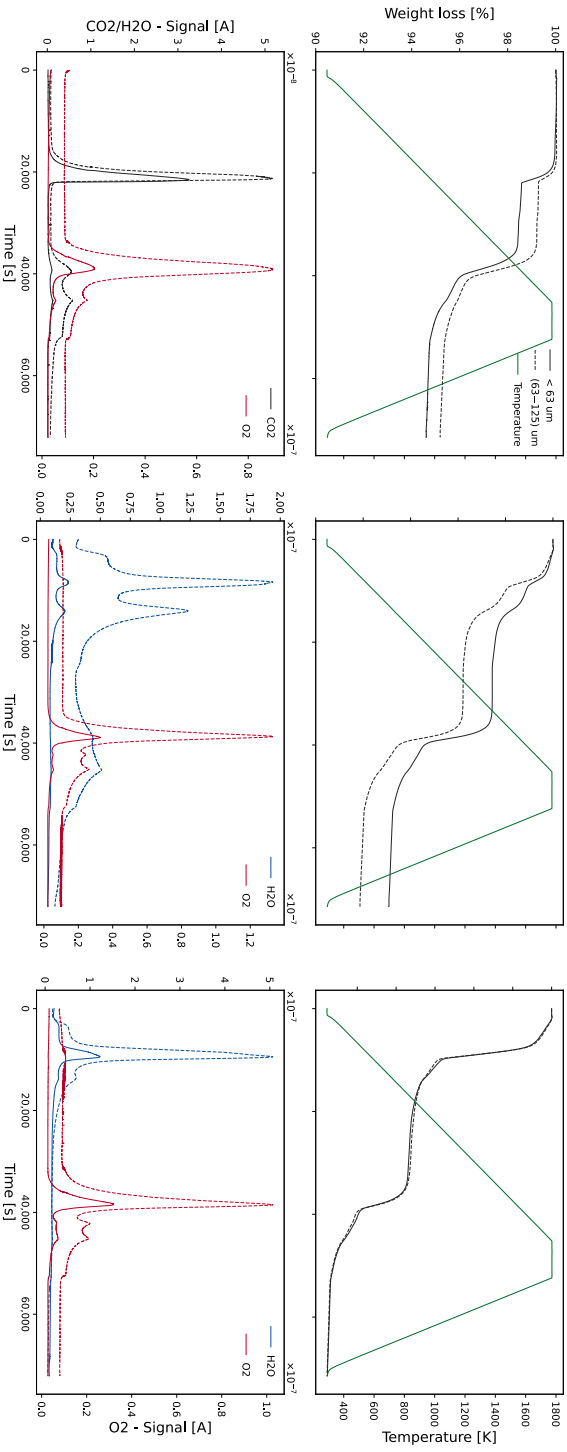


Figure 3.7: TGA data in combination with temperature profile and QMS data for (a) OreA, (b) OreB and (c) OreC for a heating rate of 2 K/min (solid line: < 63 μm size fraction, dotted line: (63 – 125) μm size fraction).

Depending on the particle volume and surface area, they further found either one or two peaks arising in the differential thermal analysis (DTA) measurements. The maximum of the first peak varied between 545 and 551 K and that of the second peak between 578 and 595 K. It is observed in here that, for OreB and OreC, the temperature of the two goethite decomposition stages varies between the two ores. For OreB the decomposition appears in two steps with a similar wide temperature range. Depending on the heating rate, the first stage initiates between 385 and 436 K and ends between 595 and 631 K, exhibiting a mass loss of 0.56 % to 0.67 %. In comparison, the first decomposition stage of OreC initiates between 395 and 502 K and ends between 616 and 680 K, with a respective mass loss of 3.81 % to 4.10 %. For OreC, a comparably low mass loss of 0.13 to 0.20 % is observed in the second stage. For OreB, the mass loss is similar compared to the first stage (0.55 to 0.65 %), with initiation temperatures of 600 to 634 K and ending temperatures of 834 to 917 K. The general higher mass loss of OreC is explained by the higher goethite content in the original ore. Further, the ores vary in average particle size and morphology, possibly influencing the initiation of the peaks.

Chen et al. [11] defined two temperature regions for hematite decomposition. The first stage ranges from 1423 to 1593 K and the second stage is defined as being above 1593 K. Qu et al. [10] observed a similar temperature range for hematite decomposition between 1473 and 1573 K. This study observed slightly lower initiation temperatures for hematite decomposition, between 1312 and 1419 K. Contrary to this study, Chen et al. and Qu et al. used lower amounts of input material and samples differing in particle size and mineralogy from this study, which could be reasons for the variation in the decomposition temperature. Further, Qu et al. only tested a heating rate of 10 K/min and Chen et al., heating rates between 2 and 10 K/min, whereas a higher heating rate usually moves the on-set of decomposition to higher temperatures. In the first stage of hematite decomposition, the corresponding mass loss is between 1.95 % and 2.66 %. The second stage, which begins at temperatures between 1676 and 1743 K, records a significantly lower mass loss, ranging between 0.06 % and 0.38 %, signifying that most thermal decomposition occurs in the first stage. Chen et al. [11] compared the significantly larger first stage to the pre-reduction of a particle in suspension, forming clusters with a molten slag phase. The second stage was described to be the reaction of the ores accumulating at the walls of HIsarna, which is in alignment with the differences in weight loss of the two hematite decomposition stages in this study.

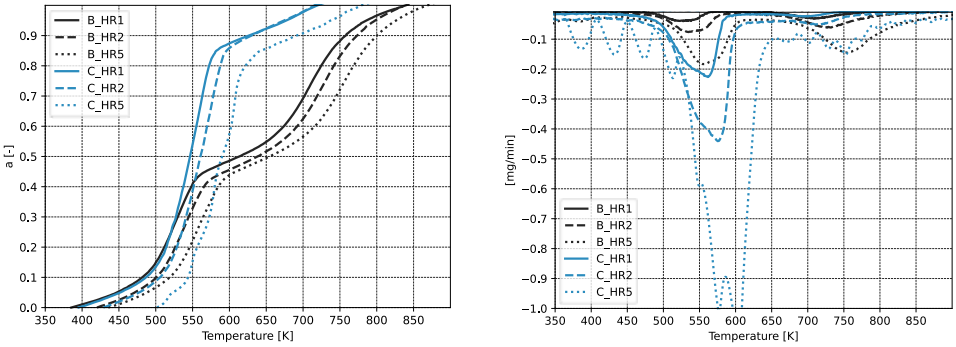
3.4.2. KINETICS OF GOETHITE DECOMPOSITION

INFLUENCE OF ORE MINERALOGY

To analyse the conversion of goethite to hematite through the decomposition of OreB and OreC, the conversion results for the particle size fraction of < 63 μm, are plotted in Figure 3.8a. Figure 3.8b shows the first derivative of the weight loss curves explaining the conversion stages. Two distinctive peaks are visible for both ores, indicating the two decomposition stages of the goethite phase. A conversion factor of 1 equals complete decomposition of the goethite phase to hematite under the release of water vapour, as presented in Eq. (3.7). The initial decomposition of the goethite phase is comparably slow but increases steeply at around 500 K. Due to the strong decomposition of OreC in the first stage, the conversion is steeper throughout the first stage and almost reaches

Table 3.5: Decomposition stages of OreA, OreB and OreC for the particle size fraction < 63 μm.

		OreA Heating Rate [K/min]					OreB Heating Rate [K/min]			OreC Heating Rate [K/min]		
		1	2	5			1	2	5	1	2	5
Stage I (Carbonate decomposition)	Start_T [K]	743	719	796	Stage I (Goethite decomposition)	Start_T [K]	385	420	436	395	429	502
	End_T [K]	1053	1047	1125		End_T [K]	595	616	631	616	647	680
	Mass loss [%]	1.38	1.38	1.43		Mass loss [%]	0.67	0.56	0.65	4.10	4.06	3.81
Stage II (Hematite decomposition)	Start_T [K]	1325	1397	1382	Stage II (Goethite decomposition)	Start_T [K]	600	623	634	621	670	687
	End_T [K]	1687	1625	1724		End_T [K]	834	871	918	793	784	830
	Mass loss [%]	2.28	1.95	2.24		Mass loss [%]	0.55	0.62	0.65	0.20	0.13	0.14
Stage III (Hematite decomposition)	Start_T [K]	1699	1708	1726	Stage III (Hematite decomposition)	Start_T [K]	1331	1353	1419	1312	1375	1376
	End_T [K]	–	–	–		End_T [K]	1625	1647	1671	1588	1623	1695
	Mass loss [%]	0.26	0.23	0.06		Mass loss [%]	2.66	2.55	2.23	2.37	2.26	2.09
Stage IV (Hematite decomposition)					Stage IV (Hematite decomposition)	Start_T [K]	1721	1720	1742	1676	1708	1705
						End_T [K]	–	–	–	–	–	–
						Mass loss [%]	0.18	0.13	0.05	0.38	0.14	0.06



(a) (b)

Figure 3.8: Dependency of temperature on (a) conversion factor of goethite decomposition for OreB and OreC at varying heating rates (HR) and (b) the first derivate of the representative weight loss curves.

full conversion in this stage. This increase occurs in a short temperature range, and a conversion factor above 0.8 is reached. The conversion in the second stage continues more slowly, until full conversion is reached. Compared to that, OreB conversion occurs over a larger temperature range with a significant amount of conversion occurring in the second stage of goethite thermal decomposition. The differences in conversion can again be explained by the results of the Raman spectroscopy in Figure 3.5. First, a steep increase in conversion can be expected due to the initial decomposition of almost pure and, therefore, more accessible goethite particles. Since the goethite content in OreC is significantly higher compared to OreB, more conversion happens at lower temperatures, while the conversion of the mixed phases occurs at a later stage.

It is important to understand how the decomposition behaviour influences the decomposition kinetics. The most essential kinetic parameter to determine is the reaction rate constant, containing the activation energy and the pre-exponential factor. The model fitting approach, explained in the previous section, has been applied to the different experimental results regarding goethite decomposition. Based on the best linear fit, the rate-determining models can be evaluated. The R^2 for the linear fit of the different decomposition experiments are presented in Table A.1 in the appendix A. The bold values of the fitting mark the reaction model, which has been used for further calculations. A number of models were not able to present the experimental data in the second stage of goethite decomposition, due to them violating the assumption that the activation energy needs to be larger than 0. The assumption-violating models for OreB are the nucleation models P1, P2 and P3 and for OreC they are the nucleation models P1, P2, P3 and P4 and the zero-order reaction model F0. For both ores, the first stage of goethite decomposition appears to be limited by the reaction order, followed by diffusion control for the second stage of goethite decomposition. Based on the chosen models, the activation energy (Ea) and pre-exponential factor (A) were calculated in order to describe the reaction rate constant (Table 3.6). The reaction rate constant shows differences depending on the heating rate and ore mineralogy. For OreB the activation energy increases in stage I with the increasing heating rate (46.55 kJ/mol, 56.44 kJ/mol, 60.38 kJ/mol) and decreases with the increasing

heating rate in stage II (44.76 kJ/mol, 33.38 kJ/mol, 32.36 kJ/mol). In the case of OreC, no clear trend is observed for the activation energy in stage I. The heating rate of 5 K/min still shows the highest activation energy (134.47 kJ/mol), but the activation energy for the heating rate of 2 K/min (77.86 kJ/mol) is lower compared to the heating rate of 1 K/min (102.62 kJ/mol). The reason for this might be the model selection in the experiment with a heating rate of 1 K/min. For the second decomposition stage, the activation energy again decreases with an increasing heating rate (23.29 kJ/mol, 8.60 kJ/mol, 7.79 kJ/mol). The influence of the heating rate on the activation energy is also observed in further studies [11, 19, 20]. A difference in the activation energy is visible between the two ores. OreC shows a much higher activation energy in the first decomposition stage and OreB in the second, implying that the two-stage decomposition of OreB is more significant.

Table 3.6: Reaction rate constant for two stage goethite decomposition of OreB and OreC with respect to heating rate.

Experiments		Stage I		Stage II	
Ore	Heating Rate [K/min]	Model	Rate constant	Model	Rate constant
OreB	1	F3	$k = 369.27\,\mathrm{min}^{-1} \cdot \exp\left(-\frac{46{,}550\,\frac{J}{mol}}{RT}\right)$	D3	$k = 3.06\,\mathrm{min}^{-1} \cdot \exp\left(-\frac{44{,}759\,\frac{J}{mol}}{RT}\right)$
OreB	2	F3	$k = 5002.42\,\mathrm{min}^{-1} \cdot \exp\left(-\frac{56{,}441\,\frac{J}{mol}}{RT}\right)$	D2	$k = 1.48\,\mathrm{min}^{-1} \cdot \exp\left(-\frac{33{,}378\,\frac{J}{mol}}{RT}\right)$
OreB	5	F3	$k = 1.97 \times 10^{3}\,\mathrm{min}^{-1} \cdot \exp\left(-\frac{60{,}382\,\frac{J}{mol}}{RT}\right)$	D2	$k = 2.40\,\mathrm{min}^{-1} \cdot \exp\left(-\frac{32{,}357\,\frac{J}{mol}}{RT}\right)$
OreC	1	D3	$k = 9.25 \times 10^{6}\,\mathrm{min}^{-1} \cdot \exp\left(-\frac{102{,}620\,\frac{J}{mol}}{RT}\right)$	D3	$k = 0.17\,\mathrm{min}^{-1} \cdot \exp\left(-\frac{23{,}289\,\frac{J}{mol}}{RT}\right)$
OreC	2	F2	$k = 1.24 \times 10^{6}\,\mathrm{min}^{-1} \cdot \exp\left(-\frac{77{,}860\,\frac{J}{mol}}{RT}\right)$	D2	$k = 0.016\,\mathrm{min}^{-1} \cdot \exp\left(-\frac{8459\,\frac{J}{mol}}{RT}\right)$
OreC	5	F3	$k = 2.96 \times 10^{11}\,\mathrm{min}^{-1} \cdot \exp\left(-\frac{134{,}465\,\frac{J}{mol}}{RT}\right)$	D2	$k = 0.025\,\mathrm{min}^{-1} \cdot \exp\left(-\frac{7787\,\frac{J}{mol}}{RT}\right)$

Studying the non-isothermal decomposition kinetics of commercial goethite ores, Walter et al. [18] observed activation energies varying between 107.4 and 137.8 kJ/mol for an overall dehydration of goethite, which they compared to the activation energy found by Pelino et al. [21] (119 kJ/mol) who investigated the decomposition of α-goethite. The activation energies found for the first decomposition stage of OreC are in a similar range, indicating that a difference in ore mineralogy does not have a significant influence on the activation energy. However, considering OreB, with lower goethite contents, the activation energy is lower for both individual stages compared to the overall activation energy values found in the literature. Beuria et al. [22] investigated the isothermal decomposition of iron ores with a goethite content of 47.41 wt.% and found an activation energy ranging between 58.74 and 65.75 kJ/mol, slightly higher compared to stage I of OreB.

INFLUENCE OF PARTICLE SIZE

In order to compare the influence of particle size on the decomposition kinetics of industrial goethite ores, TGA experiments of the particle size fractions $< 63\ \mu$m and $(63 - 125)\ \mu$m were carried out at a heating rate of 2 K/min. Figure 9 compares the conversion factors of OreB and OreC for the two particle size fractions at a heating rate of 2 K/min. The results show that the conversion rate depends more on the goethite content than on the particle size. As concluded from the XRD and XRF measurements in Section 3.2.1, the amount of crystal water in OreC is similar for both particle sizes (approx. 6 wt.%).

In accordance, the course of the conversion over temperature is similar. The results of the particle size comparison of OreB indicate that higher amounts of crystal water can lead to earlier conversion of the goethite phase. The amount of crystal water in the sample of the larger fraction is 3.26 wt.%, compared to 2.19 wt.% in the smaller size fraction. This results in an earlier conversion of the (63 – 125) μm size fraction. With the increase in particle size, the initiation temperature of the first stage of goethite decomposition of OreB decreases from 420 to 407 K and for the second stage from 623 to 616 K.

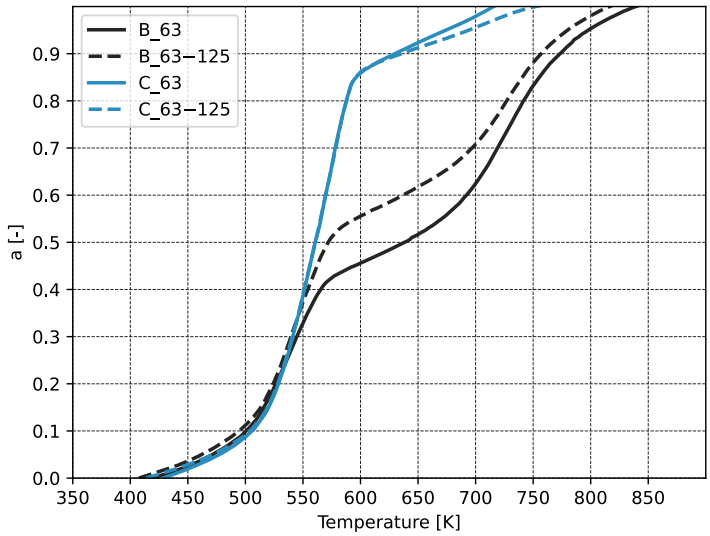


Figure 3.9: Dependency of particle size on the conversion factor at a heating rate of 2 K/min.

The model fitting approach leads to the same rate-determining mechanism for the different particle size fractions of the same ore (Stage I: chemical reaction; Stage II: diffusion). The kinetic data is displayed in Table 3.7. For OreC, there is a negligible effect of particle size on the conversion factor. As discussed in Section 3.2.3, the goethite phase is present as a mixed phase with hematite and as a pure phase. The identical reaction mechanisms between the two size fractions indicate that the reaction mechanism is independent of the particle size and more dependent on the nature of the ore. Comparing the reaction rate constants of the larger particle size fractions, a slight influence of the particle size on the activation energy of the goethite decomposition in OreC becomes visible. The activation energy for the larger size fraction (63 – 125) μm size fraction of OreC is lower for stage I (69.90 kJ/mol) and stage II (3.32 kJ/mol) compared to the activation energy of the smaller size fraction < 63 μm at a heating rate of 2 K/min. For OreB, the activation energy of the (63 – 125) μm size fraction in stage I (56.26 kJ/mol) is similar compared to the smaller fraction. However, the activation energy calculated for stage II of the larger size fraction of (63 – 125) μm, 24.43 kJ/mol, is significantly lower compared to the smaller size fraction. The lower activation energy indicates that the goethite present as a mixed phase with hematite is easily accessible for the larger particle size fraction. The similar activation energy in the first stage of goethite decomposition of OreB indicate

a similar behaviour of the initially decomposing pure goethite particles in the samples.

Table 3.7: Reaction rate constants for two-stage goethite decomposition of OreB and OreC with a size fraction of (63 – 125) μm.

Stage I				
Ore	Heating Rate [K/min]	R^2	Model	Rate Constant
OreB	2	0.9653	F3	$k = 6659.33\,\mathrm{min}^{-1} \cdot \exp\left(-\frac{56{,}254\,\frac{J}{mol}}{RT}\right)$
OreC	2	0.9657	F2	$k = 207273.76\,\mathrm{min}^{-1} \cdot \exp\left(-\frac{69{,}901\,\frac{J}{mol}}{RT}\right)$
Stage II				
Ore	Heating Rate [K/min]	R^2	Model	Rate Constant
OreB	2	0.9461	D2	$k = 0.32\,\mathrm{min}^{-1} \cdot \exp\left(-\frac{24{,}431\,\frac{J}{mol}}{RT}\right)$
OreC	2	0.9043	D2	$k = 0.0024\,\mathrm{min}^{-1} \cdot \exp\left(-\frac{3316\,\frac{J}{mol}}{RT}\right)$

3.4.3. KINETICS OF HEMATITE DECOMPOSITION

The start temperatures in Table 3.5 (stage II for OreA and stage III for OreB and OreC) define the beginning of the hematite thermal decomposition. The lowest measured initiation temperature is 1312 K. The non-isothermal decomposition zone is the temperature range of the start temperature in the respective stage until the set temperature of 1773 K is reached. The isothermal zone is the following fixed temperature of 1773 K at a holding time of 2 h. In order to first evaluate the differences in the decomposition behaviour between the ores, the total degree of reduction R[%] at the end of the non-isothermal zone and the total degree of reduction at the end of the isothermal period are presented in Figure 3.10. The degree of reduction describes how much of the hematite is converted to metallic iron or its intermediate products of magnetite and wüstite, due to the removal of oxygen. The figure shows the degree of reduction depending on time and compares the three ores at individual heating rates. A degree of reduction of 11.11 % would indicate a complete conversion from hematite to magnetite. A further increase in the degree of reduction to 33.33 % would consequently indicate a full conversion to wüstite. Depending on the heating rate, the degree of reduction of the < 63 μm fraction of OreA varies between 9.48 and 10.75 at the end of the non-isothermal zone and between 11.82 and 12.42 % at the end of the isothermal zone. These reduction degrees are similar to the reduction degrees achieved by Qu et al. [10] for hematite ores (11.8 %). The degrees of reduction at the beginning of the isothermal zone are higher for OreB (11.90–12.90 %) and OreC (11.91–13.81 %) and increase further until the end of the isotherm (OreB: 14.23–14.57 %, OreC: 14.18–16.49 %). Comparing the degrees of reduction of the < 63 μm size fraction to the (63 – 125) μm size fraction at a heating rate of 2 K/min, no significant increase in the total degree of reduction is observed for any of the ores (OreA: 12.33 → 12.82 %, OreB: 14.23 % → 14.34 %, OreC: 14.18 % → 14.35 %). For all ores, the reduction

by thermal decomposition is almost completed at the beginning of the isothermal period. The reduction degrees of all the ores indicate that a complete conversion to magnetite occurred and small amounts of wüstite should be present.

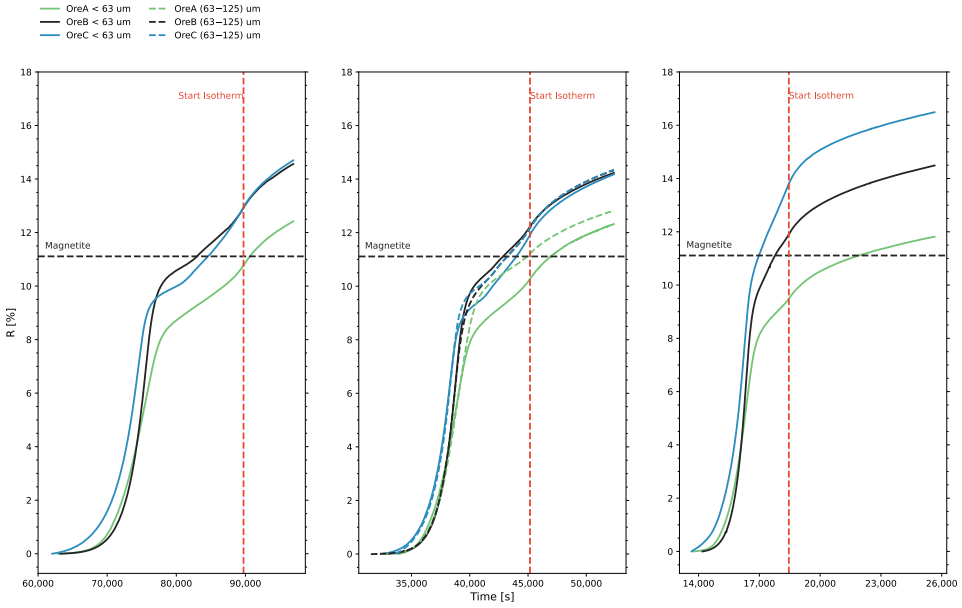
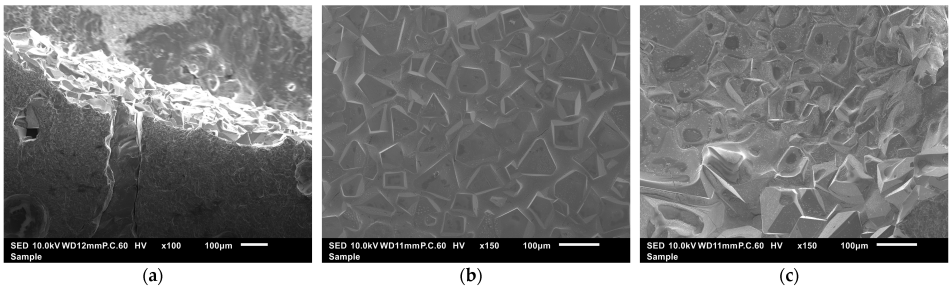


Figure 3.10: The degree of reduction at the end of the non-isothermal and isothermal heating zone for varying ores and particle sizes at a heating rate of (a) 1 K/min, (b) 2 K/min and (c) 5 K/min (see Table 5 for starting temperatures of hematite decomposition).

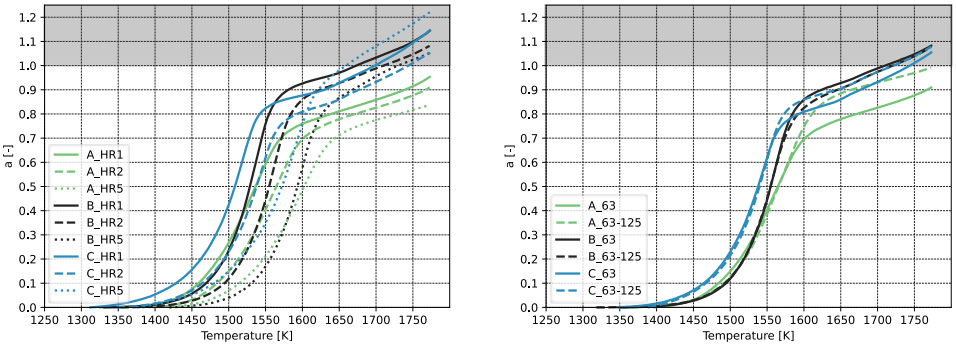
In order to validate the presence of the magnetite phase for the further kinetic calculations, example XRD measurements of decomposition products of the size fraction $< 63\ \mu$m were carried out. For this, a cross-section sample of the solidified material in the crucibles was prepared for analysis. The samples were cut with the Accutom-100 by Struers. Since it was not possible to remove the solidified samples from the crucible, the cross-section was made through the whole crucible. The Alsint crucibles are brittle in nature. Therefore, the cutting spot varies between the samples. The material was solidified by cooling the material in argon atmosphere with a cooling rate of 5 K/min back to room temperature. SEM images of the cross-sections are presented in Figure 3.11. The sample in the crucible presented in Figure 3.11a,c was cut vertically, whereas the sample in Figure 3.11b was cut horizontally.

For all observed ores, the cross-section appears similar, showing solidified pre-reduced particles. In contrast to the original ores (Figure 3.3), the particles now appear in a similar angular shape. The similar shape indicates that the hematite and goethite transitioned to the same iron oxide phase, regardless of the varied initial ore phases. The XRD pattern are displayed in Figure A.2 in the appendix A. For the samples in Figure 3.11a,b, the XRD measurements of these cross-sections confirm magnetite as the only iron oxide phase. For the sample in Figure 3.11c small amounts of fayalite (Fe_2SiO_4) were detected in the XRD



(a) (b) (c)

Figure 3.11: SEM images of cross-sections of (a) OreA, < 63 μm, heating rate of 2 K/min, (b) OreB, < 63 μm, heating rate of 2 K/min and (c) OreC, < 63 μm, heating rate of 5 K/min.



(a) (b)

Figure 3.12: Dependency of temperature on conversion factor of hematite decomposition for (a) varying heating rates (HR) for a particle size of < 63 μm and (b) for a heating rate of 2 K/min for particle size of (63 – 125) μm and < 63 μm.

pattern next to the magnetite phase. Following the XRD results, magnetite was chosen as the final product for the calculation of the conversion factor of hematite decomposition (Figure 3.12).

In the following section, only the non-isothermal decomposition kinetic parameters will be calculated. Therefore, for the calculations of the conversion factor the isothermal zone is disregarded. Due to this, the smaller size fraction of OreA does not reach full conversion to magnetite in the presented temperature range. The larger particle size, however, leads to a faster conversion and has reached full conversion to magnetite in the non-isothermal heating zone. Due to the higher reduction degrees in the non-isothermal zone, full conversion to magnetite is reached before the beginning of the isothermal zone for OreB and OreC. The grey area of the figure marks when the conversion factor exceeds unity and the conversion to magnetite is completed and the conversion to wüstite has started already. This area is excluded from the kinetic analysis. OreC shows a faster conversion compared to OreB at all heating rates. In general, a lower heating rate leads to an earlier conversion to magnetite. Model fitting was again applied in order to analyse

the present reaction mechanisms of hematite decomposition. As shown in Table 5, most of the decomposition occurs during the first stage (third peak of first derivative) and the influence of the second stage (fourth peak of first derivative) is comparably negligible. Due to this, only the first stage of hematite decomposition is analysed in terms of kinetics. Based on the best linear fit, the rate determining models are evaluated. The R^2 values for the linear fit for the different decomposition experiments for the particle size fraction $< 63\ \mu$m are presented in Table A.2in the appendix A. The bold values in the fitting mark the reaction model, which has been used for further calculations. Independent of ore mineralogy and heating rate, all model fittings indicate chemical reaction control as reaction mechanism. The hematite decomposition of OreA is a third-order reaction for all heating rates. For OreB and OreC the heating rate influences the order of reaction. For both ores, a heating rate of 1 or 2 K/min leads to a second-order reaction. For OreB, a heating rate of 5 K/min leads to a third-order and for OreC to a first-order reaction. These results contradict the findings of Chen et al. [11], who described the reaction mechanism of hematite decomposition in a temperature range of 1425–1593 K in non-isothermal conditions as the inner diffusion of iron in the solid phase. The results of our study are more in alignment with the findings of Xing et al. [19], who also found that a second-order reaction as most applicable to the experimental data. The reason for this may be the use of the applied method. As in this study, Xing et al. [19] applied the Coat–Redfern method to determine the kinetic parameters, whereas Chen et al. [11] chose iso-conversional methods to obtain kinetic parameters, before applying them to determine the reaction mechanism. Based on the best-fitting models, the reaction rate constants of the present study were determined and are presented in Table 3.8.

Comparing the heating rates of the various ores, no distinct effect of the heating rate is observable. A larger influence is seen for the ore mineralogy. The lowest activation energies are present for OreC, ranging between 424.31 kJ/mol and 505.47 kJ/mol. Higher activation energies were observed for OreA (545.47 kJ/mol–667.45 kJ/mol) and for OreB (654.98 kJ/mol–831.54 kJ/mol). Despite the different methods applied, the activation energy of the first stage of hematite decomposition is in alignment with the activation energy determined by Chen et al. [11] for the first stage of hematite decomposition (636 kJ/mol). The activation energy in the study of Xing et al. [19] was much higher with an average of 1256 kJ/mol. The reason for this may be that the model fit was applied to the overall reaction and not the individual stages of hematite decomposition.

Table 3.9 presents the reaction rate constants for the larger particle size fractions. The reaction mechanism did not change with the increase in particle size. Directly comparing the results to the smaller size fractions, OreA and OreC show a higher activation energy at an increased particle size. Interestingly, the activation energy of OreB decreases with an increase in particle size to 587.68 kJ/mol at a heating rate of 2 K/min.

Based on the results, Figure 3.13 summarises the process of the thermal decomposition of the iron ore used in this study. The illustration shows the decomposition of hematite as only iron-bearing phase (OreA) and the decomposition if both hematite and goethite are present (OreB and OreC) as separated flows. In the decomposition process of OreA, dolomite present in the sample first decomposes, leading to the emission of CO_2. For OreB and OreC, goethite decomposition occurs as a two-stage process and is the first identified decomposition process. The first stage of goethite decomposition is assumed

Table 3.8: Reaction rate constant of the first stage of hematite decomposition for particle size of < 63 μm.

Ore	Heating Rate [K/min]	Model	Rate Constant
A	1	F3	$k = 1.01 \times 10^{17}\,\mathrm{min}^{-1} \cdot \exp\left(-\frac{545{,}473\,\frac{J}{mol}}{RT}\right)$
A	2	F3	$k = 2.01 \times 10^{21}\,\mathrm{min}^{-1} \cdot \exp\left(-\frac{667{,}451\,\frac{J}{mol}}{RT}\right)$
A	5	F3	$k = 7.8 \times 10^{17}\,\mathrm{min}^{-1} \cdot \exp\left(-\frac{573{,}024\,\frac{J}{mol}}{RT}\right)$
B	1	F2	$k = 9.44 \times 10^{20}\,\mathrm{min}^{-1} \cdot \exp\left(-\frac{654{,}981\,\frac{J}{mol}}{RT}\right)$
B	2	F2	$k = 7.27 \times 10^{20}\,\mathrm{min}^{-1} \cdot \exp\left(-\frac{655{,}272\,\frac{J}{mol}}{RT}\right)$
B	5	F3	$k = 7.77 \times 10^{26}\,\mathrm{min}^{-1} \cdot \exp\left(-\frac{831{,}543\,\frac{J}{mol}}{RT}\right)$
C	1	F2	$k = 5.47 \times 10^{15}\,\mathrm{min}^{-1} \cdot \exp\left(-\frac{498{,}181\,\frac{J}{mol}}{RT}\right)$
C	2	F2	$k = 7.13 \times 10^{15}\,\mathrm{min}^{-1} \cdot \exp\left(-\frac{505{,}468\,\frac{J}{mol}}{RT}\right)$
C	5	F1	$k = 1.03 \times 10^{13}\,\mathrm{min}^{-1} \cdot \exp\left(-\frac{424{,}311\,\frac{J}{mol}}{RT}\right)$

Table 3.9: Reaction rate constant in the first stage of hematite decomposition for particle size of (63 – 125) μm.

Ore	Heating Rate [K/min]	R^2	Model	Rate Constant
A	2	0.9910	F3	$k = 3.03 \times 10^{21}\,\mathrm{min}^{-1} \cdot \exp\left(-\frac{670{,}499\,\frac{J}{mol}}{RT}\right)$
B	2	0.9899	F2	$k = 3.18 \times 10^{18}\,\mathrm{min}^{-1} \cdot \exp\left(-\frac{587{,}682\,\frac{J}{mol}}{RT}\right)$
C	2	0.9773	F2	$k = 6.11 \times 10^{23}\,\mathrm{min}^{-1} \cdot \exp\left(-\frac{592{,}322\,\frac{J}{mol}}{RT}\right)$

to be that of the almost pure goethite particles detected with the Raman spectroscopy. The conversion of goethite to hematite in this stage is found to be controlled by the chemical reaction. In the second stage it is expected that the less accessible goethite, which co-exists with hematite in the same particle, decomposes. The decomposition control shifts from a chemical reaction to diffusion in this stage. The decomposition of the goethite phase is identified by the emission of water vapour. For all ores, the last observed decomposition is the conversion from hematite to magnetite under the release of oxygen at elevated temperatures. Independent of the input ore, the hematite conversion initiates

at similar temperatures and is found to be controlled by a chemical reaction for all of the ores.

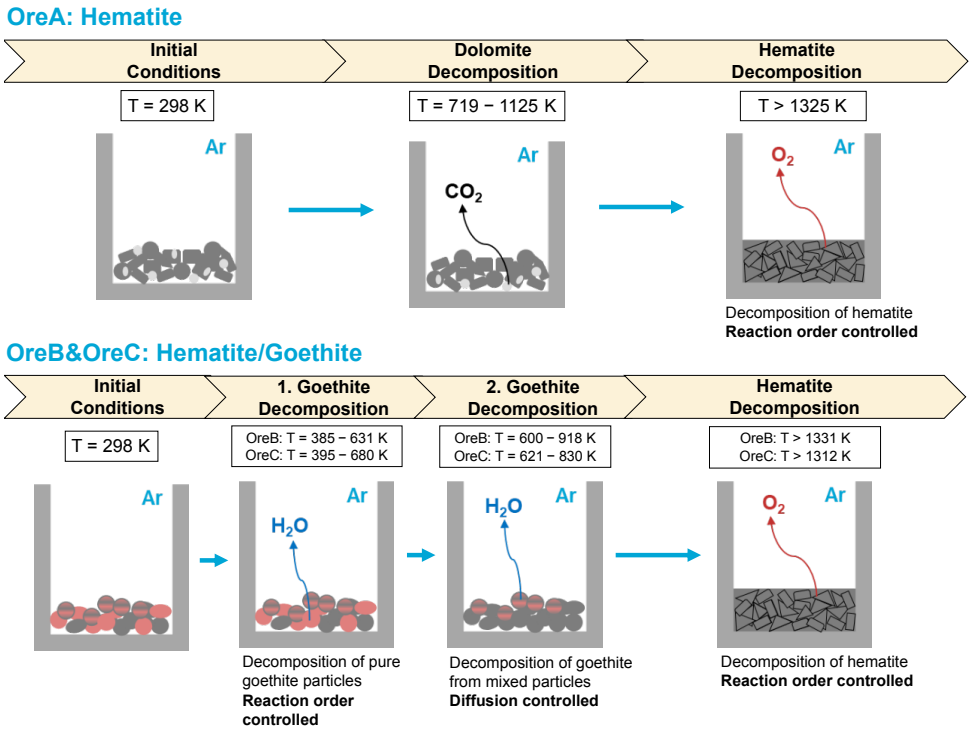


Figure 3.13: Schematic illustration of the thermal decomposition process of varying iron ore fines.

3.5. CONCLUSIONS

- The varying raw iron ores investigated in this study (elaborated in Section 3.2) differ from one another in morphology, mineralogy and chemical composition. However, after the pre-reduction in an argon atmosphere in the TGA experiments at 1773 K, the morphology of the pre-reduced magnetite phases appeared to be identical.

- The thermal decomposition of goethite ore occurs as a two-stage process. The mass loss in the individual goethite stages depends on the goethite content in the ore. For the particle size fraction of < 63 μm, OreB shows two similar mass loss stages, with an observed mass loss of 0.56–0.67 wt.% in the first and 0.55–0.65 wt.% in the second stage. OreC shows stronger differences with a mass loss of 3.81 wt.%–4.10 wt.% in the first and 0.13–0.20 wt.% in the second stage.

- The proposed reaction mechanisms for goethite decomposition are a chemical reaction in the first stage and diffusion in the second stage (temperature intervals stated in Table 3.5). The order of reaction and dimension of diffusion partially varied

and is difficult to prove due to the nature of the TGA. Therefore, the investigation of reaction order and diffusion dimension will be within the scope of future research. Due to the significant differences in weight loss in both decomposition stages between OreB and OreC, OreC shows higher activation energies in the first stage (77.86–134.47 kJ/mol) and OreB in the second stage (32.36–44.76 kJ/mol) for a particle size fraction < 63 μm.

- An increase in particle size has no influence on the reaction mechanisms of goethite thermal decomposition. However, the activation energy remains similar for OreB in the first stage (56.44 → 56.26 kJ/mol) but decreases in the second stage (33.38 → 24.43 kJ/mol). The reason for the change in activation energy is proposed to be the difference in mineralogy between the two particle size fractions. The larger fraction of OreB contains higher amounts of crystal water, possibly leading to an easier release in the second decomposition stage. For OreC, however, the activation energy decreases in both stages (77.86 → 69.90 kJ/mol and 8.46 → 3.32 kJ/mol) with increasing particle size, despite a similar level of crystalline water, arguing for the influence of particle size on the activation energy.

- Hematite thermal decomposition also occurs as a two-stage process, with the first stage initiating between 1311 and 1419 K and the second stage between 1676 and 1742 K, depending on ore composition and heating rate. A significant amount of decomposition takes place in the first stage. The order of highest average total reduction degree for the size fraction < 63 μm is OreC (14.18–16.49 %) > OreB (14.23–14.57 %) > OreA (11.82–12.42 %). At the same heating rate, an increase in particle size leads to no significant increase in the degree of reduction for all ores.

- The proposed first stage of hematite decomposition is chemical reaction controlled, while the order of the reaction rate depends on the heating rate and ore type. Again, due the nature of the TGA, the order of the reaction is difficult to prove and will be within the scope of future research. No influence of the particle size on the reaction mechanism was observed. The lowest activation energy for the < 63 μm size fraction was found for OreC (424.31–505.47) kJ/mol. A higher activation energy was determined for OreA (545.47–667.45) kJ/mol and OreB (654.98–831.54) kJ/mol. For OreA and OreC the activation energy increases and for OreB it decreases with an increase in particle size.

REFERENCES

[1] P. Leerhoff, J. C. Brouwer, A. M. Armaki, C. Zeilstra, K. Meijer, J. van der Stel, S. T. Abrahami, N. Dogan, and Y. Yang. Characterisation of Varying Iron Ores and Their Thermal Decomposition Kinetics Under HIsarna Ironmaking Conditions. **Metals** 14, 1271 (2024). DOI: 10.3390/met14111271.

[2] Worldsteel Association. Climate change and the production of iron and steel. 2021.

[3] Worldsteel Association. Sustainability performance of the steel industry 2003-2021. 2022.

[4] Worldsteel Association. 2022 World Steel in Figures. 2022.

[5] Y. Yang, K. Raipala, and L. Holappa. Treatise on Process Metallurgy. Vol. 3. Elsevier Ltd., 2014. Chap. Ironmaking, pp. 2–88. ISBN: 9780080969886. DOI: 10.1016/B978-0-08-096988-6.00017-1.

[6] A. K. Biwas. Principles of blast furnace ironmaking: theory and practice. Cootha Publishing House: Brisbane, 1981.

[7] M. Naito, K. Takeda, and Y. Matsui. Ironmaking Technology for the Last 100 Years: Deployment to Advanced Technologies from Introduction of Technological Know-how, and Evolution to Next-generation Process. **ISIJ International** 55 (2015), pp. 7–35. DOI: 10.2355/isijinternational.55.7.

[8] K. Meijer, C. Guenther, and R. J. Dry. HIsarna Pilot Plant Project. METEC InSteelCon 2011, 2011.

[9] K. Meijer, C. Zeilstra, C. Teerhuis, M. Ouwehand, and J. van der Stel. Developments in Alternative Ironmaking. **Transactions of the Indian Institute of Metals** 66 (2013), pp. 475–481. DOI: 10.1007/s12666-013-0309-z.

[10] Y. Qu, Y. Yang, Z. Zou, C. Zeilstra, K. Meijer, and R. Boom. Thermal decomposition behaviour of fine iron ore particles. **ISIJ International** 54 (2014), pp. 2196–2205. DOI: 10.2355/isijinternational.54.2196.

[11] Z. Chen, C. Zeilstra, J. van der Stel, J. Sietsma, and Y. Yang. Thermal Decomposition Reaction Kinetics of Hematite Ore. **ISIJ International** 60 (2020), pp. 65–72. DOI: 10.2355/isijinternational.ISIJINT-2019-129.

[12] M. Hanesch. Raman spectroscopy of iron oxides and (oxy)hydroxides at low laser power and possible applications in environmental magnetic studies. **Geophysical Journal International** 177 (2009), pp. 941–948. DOI: 10.1111/j.1365-246X.2009.04122.x.

[13] A. W. Coats and J. P. Redfern. Kinetic Parameters from Thermogravimetric Data. **Nature** 201 (1964), pp. 68–69. DOI: 10.1038/201068a0.

[14] P. Pourghahramani and E. Forssberg. Reduction kinetics of mechanically activated hematite concentrate with hydrogen gas using nonisothermal methods. **Thermochimica Acta** 454 (2007), pp. 69–77. DOI: 10.1016/j.tca.2006.12.023.

[15] S. S. Sun. A study of kinetics and mechanisms of iron ore reduction in ore/coal composites. PhD thesis. McMaster University, 1997.

[16] R. Otsuka. Recent studies on the decomposition of the dolomite group by thermal analysis. **Thermochimica Acta** 100 (1986), pp. 69–80. DOI: 10.1016/0040-6031(86)87051-4.

[17] L. Diamandescu, D. Mihàilà-Tàràbàşanu, and M. Feder. On the solid phase transformation goethite → hematite. **Materials Letters** 17 (1993), pp. 309–311. DOI: 10.1016/0167-577X(93)90019-T.

[18] D. Walter, G. Buxbaum, and W. Laqua. The Mechanism of the Thermal Transformation From Goethite To Hematite. **Journal of Thermal Analysis and Calorimetry** 63 (2001), pp. 733–748.

[19] L. Xing, Y. Qu, C. Wang, L. Shao, Z. Zou, and W. Song. Kinetic Study on Thermal Decomposition Behavior of Hematite Ore Fines at High Temperature. **Metallurgical and Materials Transactions B** 51 (2020), pp. 395–406. DOI: 10.1007/s11663-019-01747-1.

[20] Y. Sun, Y. Han, X. Wei, and P. Gao. Non-isothermal reduction kinetics of oolitic iron ore in ore/coal mixture. **Journal of Thermal Analysis and Calorimetry** 123 (2016), pp. 703–715. DOI: 10.1007/s10973-015-4863-y.

[21] M. Pelino, L. Toro, M. Petroni, A. Florindi, and C. Cantalini. Study of the kinetics of decomposition of goethitein vacuo and pore structure of product particles. **Journal of Materials Science** 24 (1989), pp. 409–412. DOI: 10.1007/BF01107419.

[22] P. C. Beuria, S. K. Biswal, B. K. Mishra, and G. G. Roy. Study on kinetics of thermal decomposition of low LOI goethetic hematite iron ore. **International Journal of Mining Science and Technology** 27 (2017), pp. 1031–1036. DOI: 10.1016/j.ijmst.2017.06.018.

4

THERMAL DECOMPOSITION AND PRE-REDUCTION OF GOETHITIC IRON ORE FINES AND THEIR EFFECTS ON PHASE TRANSFORMATION AND MATERIAL PROPERTIES

During high-temperature in-flight flash reduction of iron ores, goethitic particles undergo rapid structural changes. This study examines the influence of goethite on pre-reduction performance in a drop-tube furnace, focusing on the hematite to magnetite reduction step. Three iron ores (OreA, OreB, and OreC) with distinct mineralogical and physical characteristics were reduced in N_2 and atmospheres containing 95 % CO_2 with 5 % CO or H_2 at temperatures between 1658 and 1760 K. Compared to ores containing hematite as the sole iron-bearing phase, goethite-containing ores exhibit enhanced cracking and fragmentation during thermal decomposition, leading to changes in particle size and density. A comparison of OreB (lower goethite) and OreC (higher goethite) shows that the importance of particle residence time increases with goethite content. Higher pre-reduction was achieved at 80 ms for OreB and at 430 ms for OreC during thermal decomposition. Despite the use of reducing gases, reduction beyond magnetite was not observed due to large particle sizes (> 100 µm) and residence-time limitations of the drop-tube furnace. Further reduction ($Fe_3O_4 \rightarrow FeO$) was assessed using thermogravimetric analysis. Across both experimental set-ups, thermal decomposition has a higher impact on the total reduction than the gas reduction. EBSD analysis identified two reaction mechanisms, internal pore diffusion and surface product layer diffusion. Balanced mineralogical properties (as in OreB) were found to be critical for effective early stage in-flight flash reduction.

This chapter has been published in P Leerhoff et al. "Thermal decomposition and pre-reduction of goethitic iron ore fines and their effects on phase transformation and material properties." In: Sci Rep **2026** [1]

4.1. INTRODUCTION

To tackle the large emissions arising from the iron- and steelmaking industry, HIsarna® ironmaking technology was developed as an alternative to the blast furnace process within the framework of the ULCOS initiative [2]. HIsarna enables the direct use of pulverized coal and lower-grade iron ores, in contrast with the metallurgical coke and higher-quality ores typically required for conventional blast furnace operations [3, 4], thereby eliminating the material pre-treatment steps of coking and ore agglomeration. HIsarna is classified as a single-reactor smelting reduction process, consisting of a pre-reduction stage in the upper part of the reactor (where the fine iron ores are rapidly heated, partially melted and pre-reduced) and a smelting stage in the lower part of the reactor (where the final reduction occurs) [3].

The pre-reduction stage can be described as a suspension smelting process, in which fine ore particles are maintained in suspension and undergo flash reduction [5]. A comparable technology using suspension smelting is applied in the flash ironmaking process developed at the University of Utah [6, 7]. In the top pre-reduction section of HIsarna (called previously as Cyclone Converter Furnace - CCF), the injected ores are partially reduced by a gas mixture of $H_2 - CO - CO_2 - H_2O - N_2$ at high temperatures ($\approx$ 1773 K) [8]. The reducing gas mixture is generated from the off-gas of the final reduction in the smelting reduction vessel (bottom part of the furnace). This mixture of gases reacts with the ores throughout the whole length of the pre-reduction cyclone [8, 9]. Its reducing ability is defined by the post-combustion ratio (PCR) of the gas mixture, which describes the ratio of oxidizing gases to the total gas mixture, as given by Eq. (4.1) [9]:

$$\mathrm{PCR} = \frac{\%H_2O + \%CO_2}{\%H_2O + \%CO_2 + \%H_2 + \%CO} \times 100\% \tag{4.1}$$

The PCR therefore directly reflects the reducing potential of the gas atmosphere in the HIsarna pre-reduction stage. When the gas mixture enters the pre-reduction stage of the HIsarna process, it has an approximate PCR value of 60 %, which continuously increases with the (pre-)reduction of the injected ores, reaching a final PCR value of about 98 % at the exit [8]. Consequently, the gas atmosphere at the top of the furnace has a relatively low reducing ability (high PCR values), and the injected ores initially undergo reduction primarily through thermal decomposition. So far, most suspension smelting studies examined the reaction kinetics of hematite- or magnetite-based fine ores and concentrates [10–20]. For example, Qu et al. [15] studied the impact of thermal decomposition on the reduction of fine hematite ores (≈95 % Fe_2O_3, 45-53 μm). They observed a strong dependence of the pre-reduction degree (PRD) on temperature, increasing from 3.5 % at 1650 K to 7.9 % at 1800 K for a particle residence time of 970 ms in an N_2 atmosphere. Chen et al. [10] highlighted the negative influence of particles size on reduction of hematite iron ore fines ($\approx$ 72 % Fe_2O_3) in an atmosphere mimicking a PCR value of 95 %, consisting of CO:CO_2 =5:95. At 1735 K, the PRDs were approximately 12 % for particle sizes ranging from 67 and 110 μm. Increasing the particle size to 142 and 244 μm resulted in significantly lower PRDs of about 5.5 % and 2 %, respectively.

Another alternative is to use goethite rich iron ore fines, which are abundant in India [21]. Goethite (α-FeOOH) is a hydrated iron oxide that undergoes dehydration upon heating, transforming into hematite while releasing water [22]. When both goethite and

hematite are present in the ore, two thermal decomposition reactions occur. First, the conversion of goethite to hematite (Eq. (4.2), followed by the conversion from hematite to magnetite (Eq. (4.3) [18, 23].

$$2\alpha\text{FeO(OH)}(s) \rightarrow \alpha\text{Fe}_2\text{O}_3(s) + \text{H}_2\text{O}(g) \tag{4.2}$$

$$3\text{Fe}_2\text{O}_3(s) \rightarrow 2\text{Fe}_3\text{O}_4(s) + \frac{1}{2}\text{O}_2(g) \tag{4.3}$$

The on-set temperature of goethite thermal decomposition is significantly lower than that of hematite. While literature indicates that goethite begins to decompose at around 465 K [22], the thermal decomposition of hematite to magnetite only initiates at temperatures above 1312 K [24]. Strezov et al. [25] reported that the thermal decomposition of goethite to hematite first causes a volume expansion accompanied by particle cracking, followed by fragmentation. This cracking behaviour can strongly influence product properties during reduction and may accelerate gas-solid reduction due to more active reduction sites. The use of such low-grade ores is particularly relevant for HIsarna, as the process is able to directly utilize low-grade iron ore fines like goethite [9, 26]. Consequently, understanding the behaviour of goethite-rich iron ore fines is essential for evaluating their performance in suspension smelting processes.

Most studies on the thermal decomposition of goethite-based iron ores have employed thermogravimetric analysis to investigate reduction at increasing temperatures and consequently longer reduction times (heating rate: 1-50 K/min) [24, 27, 28]. The typical pre-reduction time in suspension smelting ironmaking, however, is < 5 s [19, 20], and requires studies in a drop-tube furnace [10–20]. Chen et al. [29] estimated the impact of the reduction on particle volume and density of hematite ores with high gangue content, using a modified Mills-Keene model. In this density prediction model, they assumed the reduced samples were in a semi-molten state due to the co-occurrence of magnetite and wüstite. Their results predicted a particle density decrease by 6.6-15.0 % and a volume increase (mostly by thermal expansion) by 6.6-9.4 %. They noted that such changes in particle density and volume could lead to underestimation of particle residence times in the HIsarna pre-reduction stage. Given this impact, it is important to experimentally determine the effect of pre-reduction on material properties in order to evaluate how strongly they influence particle behaviour in the HIsarna process. This is particularly relevant when considering the use of low-grade ore materials containing goethite.

Overall, findings in literature suggest that high-temperature reduction of iron ore fines can alter product properties, such as particle size and density compared to their initial state. Consequently, it is expected that the initial ore properties at the point of injection into HIsarna differ from those after interaction with the reducing gas mixture across the pre-reduction stage. In contrast to previous studies, which primarily investigate thermal decomposition and reduction behaviour under thermogravimetric conditions with relatively slow heating rates and long residence times, the present work focuses on goethite-containing industrial iron ore particles under flash reduction conditions in a high-temperature drop-tube furnace (HTDF). This enables the investigation of early-stage pre-reduction under short residence times, where particle heating, phase transformation,

and reduction occur simultaneously. In addition, a direct comparison with TGA experiments is provided to assess the influence of heating rate and residence time on reduction behaviour. This approach allows for a more process-relevant evaluation of goethite-containing ores in early stage HIsarna ironmaking. To investigate goethite-containing low-grade iron ore fines under realistic suspension smelting ironmaking conditions, this study examines the initial conversion of goethite to hematite and the subsequent pre-reduction to magnetite via thermal decomposition and low reducing atmospheres (high PCR). Emphasis is placed on how these processes influence particle properties, including morphology, density, and size, as well as on the evaluation of the corresponding phase evolution and how these impact kinetic parameters for the operations of HIsarna process.

4.2. METHODOLOGY

4.2.1. MATERIALS - ORE CHARACTERIZATION

This study focuses on the thermal decomposition and reduction behaviour of three different iron ores, hereafter referred to as OreA, OreB and OreC, provided by Tata Steel in IJmuiden. The ores were wet sieved into different size fractions. For OreB, the fractions of < 63, 63-125 and 125-250 μm sized particles were investigated, whereas for OreA and OreC only the particles with a 63-125 μm size fraction were studied. The chemical composition obtained by X-ray fluorescence (XRF) (Panalytical AXIOS XRF, Netherlands) and loss of ignition (LOI) analysis (dissolution in nitric acid and TGA, LECO, Germany) for the three ores are summarized in Table 4.1. The main difference between the ores is the amount of crystal water, which reflects the presence of goethite. The amount of crystal water is identified by closing the balance of LOI determination. No crystal water is detected in any size fraction of OreA. In OreB, the crystal water content increases with particle size, while OreC exhibits the highest overall content. The presence of goethite also reduces the overall ore grade, resulting in significantly lower total iron content in OreB and OreC compared to OreA.

Mineralogical differences between the ores were verified by X-ray diffraction (XRD) with a Bruker D8 Advance diffractometer Bragg-Brentano geometry and Lynxeye position sensitive detector (Bruker, Germany). An overview of the detected phases for each size fraction of the ores is provided in Table 4.2, with detailed XRD patterns available in Figure B.1 (appendix B). In addition to the varying goethite content, differences in secondary phases were observed. OreB contains kaolinite in all fractions, whereas OreA contains dolomite. Quartz is detected in all ores and size fractions.

The ores also differ in their physical properties, which are summarized in Table 4.3. The mean particle diameters were determined by light scattering technology (Microtrac Bluewave). The samples were suspended in distilled water and measured in triplets to form the average particle size. Among the 63-125 μm fractions, the average particle size followed the trend dOreC>dOreA>dOreB. The theoretical density of the ores was calculated based on Eq. (4.4):

$$\rho = \sum_i x_i \rho_i \tag{4.4}$$

With x_i being the mass fraction of component i and ρ_i the density of the pure component i. The true particle density, as measured with a helium pycnometer, deviates

Table 4.1: Chemical composition of as-received iron ore fractions based on XRF and LOI analysis (wt.%) (Rest includes Cr_2O_3, Na_2O, P_2O_5, S, V, Zn).

Ore	A	B	B	B	C
Fraction [µm]	63–125	< 63	63–125	125–250	63–125
Fe_2O_3	91.50	88.07	85.07	84.07	82.92
total-Fe	64.00	61.60	59.50	58.80	58.00
SiO_2	2.96	4.96	5.83	6.17	5.30
Al_2O_3	1.44	3.81	4.78	5.10	3.00
MgO	0.41	0.04	0.04	0.031	0.11
CaO	1.23	0.05	0.05	0.041	0.07
TiO_2	0.92	0.33	0.35	0.32	0.16
MnO	0.60	0.03	0.03	0.029	1.24
total-C	0.23	0.06	0.07	0.07	0.14
H_2O (crystal)	–	2.19	3.26	3.63	6.39
Rest	0.21	0.25	0.31	1.01	0.26

Table 4.2: Overview of mineralogical phases obtained via XRD analysis for as-received ores (X indicates that the mineralogical phase is present in the ore fraction).

Ore	Size fraction [µm]	Phase				
		Hematite	Goethite	Quartz	Kaolinite	Dolomite
OreA	63–125	X				X
OreB	< 63	X	X	X	X	
	63–125	X	X	X	X	
	125–250	X	X	X	X	
OreC	63–125	X	X	X		

increasingly from the theoretical density for ores with higher goethite content. This trend was further confirmed by BET (Brunauer–Emmett–Teller) surface analysis, which provides data on specific surface area and porosity. OreA shows good agreement between theoretical and true density, consistent with its low surface area and porosity. In contrast, OreB and OreC exhibit higher surface areas and porosities which increase with goethite content and result in larger discrepancies between theoretical and measured densities.

Table 4.3: Physical properties of as-received iron ores measured by helium pycnometer and BET and calculated by Eq. (4.4).

Ore	Particle size fraction [µm]	Mean particle diameter [µm]	Theoretical density [kg m^{-3}]	True particle density [kg m^{-3}]	Specific surface area [m^2 g^{-1}]	Total pore volume [cm^3 g^{-1}]	Mean pore diameter [nm]
OreA	63–125	103.6	5063	5036	0.061	0.0003	19.610
OreB	< 63	44.22	4922	4788	6.684	0.0298	17.852
OreB	63–125	100.2	4829	4592	7.883	0.0291	14.738
OreB	125–250	201.5	4796	4465	10.001	0.0310	12.385
OreC	63–125	115.9	4691	4224	10.842	0.0385	14.217

4.2.2. DROP TUBE FURNACE EXPERIMENTS

The main equipment used in this study is a high-temperature drop tube furnace (HTDF), which allows to investigate the in-flight behaviour of fine ore particles exposed to high temperatures and a laminar reducing gas flow under isothermal conditions at short particle residence times (Figure 4.1). Due to the reduction at short residence times and high temperatures, the experiments in the HTDF will be termed as 'flash reduction'.

In the HTDF, the as-received iron ore particles are charged into an electrically heated Alsint tube reactor via a horizontal syringe feeder, using N_2 as a carrier gas. The isothermal reaction zone has a predefined length of 39 cm. With the help of a water-cooled injection probe, the particles are directly charged into the isothermal zone, preventing earlier reaction. The reducing gas mixture is separately preheated to approx. 673 K before being injected into the reaction zone. The particle residence time in the isothermal zone is controlled by adjusting the N_2 carrier gas flow. After the allocated particle residence time, reacted particles are quenched with cooling water (indirect cooling) and N_2 (direct cooling) through the sampling tube to ensure that all reactions stop immediately after leaving the isothermal zone. This guarantees that the reaction products only form within the defined isothermal zone.

The experiments in the HTDF are divided into two approaches:

1. **Pre-reduction by thermal decomposition:** Experiments were conducted in an inert atmosphere consisting of solely N_2 (Table 4.4). All three ores were investigated in this approach to study the effect of initial ore mineralogy, with a particular focus on the impact of the goethite content in the ores.

2. **Pre-reduction by low reducing gas atmospheres:** Experiments were conducted in representative atmospheres of a PCR=95 % (Table 4.5). Two different atmospheres were tested. The first one contained 4.3 % CO and the other 4.3 % H_2 reducing gas component. For both gas compositions the remaining atmosphere consisted of 80.7 % CO_2 and 15 % N_2. Since water-vapour injection is not yet implemented into the experimental system, substituting CO_2 with H_2O as oxidizing gas was not possible. For this approach, only OreB was tested, to focus on the influence of gas reduction.

Table 4.4: Experimental parameters of thermal decomposition experiments.

Parameter	Experimental condition
Ore	A, B, C
Particle size fraction [µm]	63–125
Set temperature [K]	1658, 1681, 1710, 1760
Atmosphere	N_2
Reacting gas flow rate [L min^{-1}]	4
Feeding gas flow rate [L min^{-1}]	0.07–0.6
Particle residence time [ms]	80–460

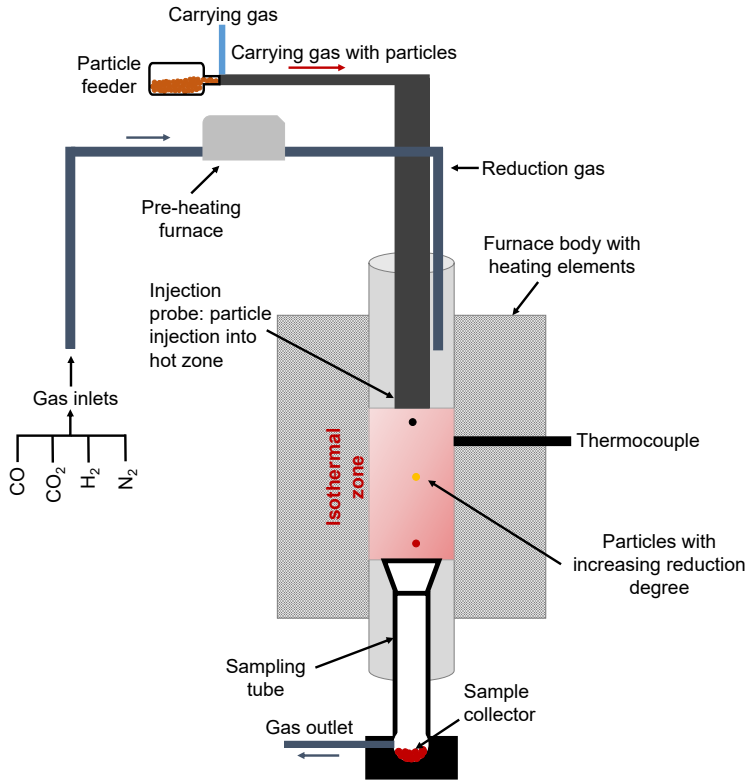


Figure 4.1: Schematic presentation of the High-Temperature Drop Tube furnace (HTDF)

The calculation of the particle residence time, as well as the influence of particle properties on particle velocity, is detailed in the appendix B (Eq. (B.1)-Eq. (B.6), Figure B.2. The most important influence on the particle residence time was determined to be the particle size. Larger particles significantly increased the particle velocity and, consequently, limited the residence times achievable within a given size fraction. Calculations of the particle residence time followed the procedure detailed in previous studies [10, 14] and in the thesis of Qu [30]. The particle residence time is estimated based on gas flow conditions, reactor geometry and particle properties. Therefore, it should be noted that the calculated residence time represents an estimated value, as variations in particle size, density, and trajectory may lead to deviations in the actual residence time of the

Table 4.5: Experimental parameters of reduction experiments in PCR=95% atmosphere.

Parameter	Experimental condition
Ore	B
Particle size fraction [μm]	63–125, 125–250
Set temperature [K]	1658, 1681, 1710
Atmosphere	$PCR95_{CO}$: 4.3% CO + 80.7% CO_2 + 15% N_2 $PCR95_{H2}$: 4.3% H_2 + 80.7% CO_2 + 15% N_2
Reacting gas flow rate [$L min^{-1}$]	4
Feeding gas flow rate [$L min^{-1}$]	0.05–0.6
Particle residence time [ms]	74–460

individual particles. However, these variations are considered to be within the same order of magnitude and do not affect the overall trends observed in the experiments.

Reaction time is a key factor during in-flight reduction in suspension and flash iron-making processes, where achieving a high pre-reduction degree within (milli)seconds is crucial. The reduction (or pre-reduction) degree, is calculated in reference to metallic iron as [10, 12]:

$$PRD = 1 - \frac{3(Fe^{3+})_i + 2(Fe^{2+})_i}{3(Fe^{3+})_o + 2(Fe^{2+})_o} = \frac{1}{3}\left(\frac{Fe^{2+}}{TFe}\right) \tag{4.5}$$

With i representing the reduced state to metallic iron and o being the initial state of hematite. The total iron (TFe) was determined with XRF, while the amount of iron in Fe^{3+} and Fe^{2+} state was measured by chemical titration with potassium dichromate.

4.2.3. TGA EXPERIMENTS

In addition, experiments in PCR=95 % atmosphere were also conducted using a thermogravimetric analyser (TGA). Results of the thermal decomposition behaviour in the TGA for OreA, OreB and OreC have been reported in an earlier study by the current authors [24]. The TGA results provide a basis for comparison with the HTDF experiments. The main differences between the TGA and HTDF setups are the particle residence times, the particle-gas contact state, and the heating behaviour. In the TGA, particles were gradually heated in Ar atmosphere at a heating rate of 5 K/min until reaching the set-temperature of 1723 K. After completion of thermal decomposition, the reducing gas mixture was introduced for 1 h to reduce the already thermally decomposed particles. The long exposure time allows the particles to approach complete reduction. By contrast, the reduction time in the HTDF is in the order of hundreds of milliseconds, with thermal decomposition and gas reduction occurring simultaneously. Consequently, the overall final reduction degrees in the TGA are expected to be significantly higher than those achieved in the HTDF. The detailed experimental conditions are summarized in Table 4.6.

The chemical titration method cannot be applied to the TGA output materials as a result of the sample amounts being too low. Therefore, the pre-reduction degree is calculated based on the measured mass loss of the ore over time as:

Table 4.6: Experimental Conditions in TGA, Setaram TAG 16/18.

Experimental condition	Operating parameter
Ore	B
Holding time under isothermal conditions [h]	2 + 1
Heating rate [K min^{-1}]	5
Particle size [µm]	< 63, 63–125, 125–250
Set temperature [K]	1723
Gas flow rate [mL min^{-1}]	200
Reducing atmosphere [vol%]	$PCR95_{CO}$: 4.3% CO + 80.7% CO_2 + 15% N_2 $PCR95_{H2}$: 4.3% H_2 + 80.7% CO_2 + 15% N_2

$$PRD = \frac{m_0 - m_t}{m_0 - m_{Fe_2O_3 \rightarrow Fe}} \tag{4.6}$$

Where m_0 is the initial mass of the ore sample, m_t is the mass measured at time t, and $m_{Fe_2O_3 \rightarrow Fe}$ is the theoretical mass after complete reduction to metallic iron (including gangue minerals).

4.3. RESULTS AND DISCUSSION

This section investigates the impact of ore mineralogy and gas atmosphere on the two pre-reduction mechanisms: thermal decomposition and gas reduction. In suspension smelting ironmaking, fine ores are injected directly into high-temperature zones, where they are rapidly heated up and undergo immediate changes in their material properties. To assess their role in the overall suspension smelting process, it is essential to track how rapid heating and decomposition affect particle morphology, size and density, and reduction performance. The results are presented in four parts: (i) the influence of thermal decomposition on particle morphology, (ii) the combined effects of thermal decomposition and pre-reduction on material properties (particle size and true density), (iii) the impact of these processes on mineralogy change, and (iv) the role of the reduction time on the pre-reduction degree. Special focus will be placed on how a goethite presence in the ore influence these results. For part (i) to (iii) the HTDF was used as the main equipment, and for part (iv) both the HTDF and TGA were applied.

4.3.1. PARTICLE MORPHOLOGY AFTER FLASH THERMAL DECOMPOSITION

SEM images of the as-received ore particles and of the particles after thermal decomposition are shown in Figure 4.2. The goethite-containing ores (OreB and OreC) exhibit a pronounced cracking visible at the particle surface. In contrast, only few OreA particles exhibit minor cracking. Literature suggests that during goethite decomposition, particles typically undergo a sequence of cracking followed by fragmentation, caused by the structural changes within the ore particle as goethite converts to hematite under the release of water-vapour (Eq. (4.2)) [25, 31]. This aligns with the extensive cracking behaviour observed in OreB and OreC. As observed in literature [25], the release of water vapour during rapid heating is likely a contributing factor, explaining the absent cracking in OreA.

To verify the role of rapid heating, additional experiments were conducted in a TGA

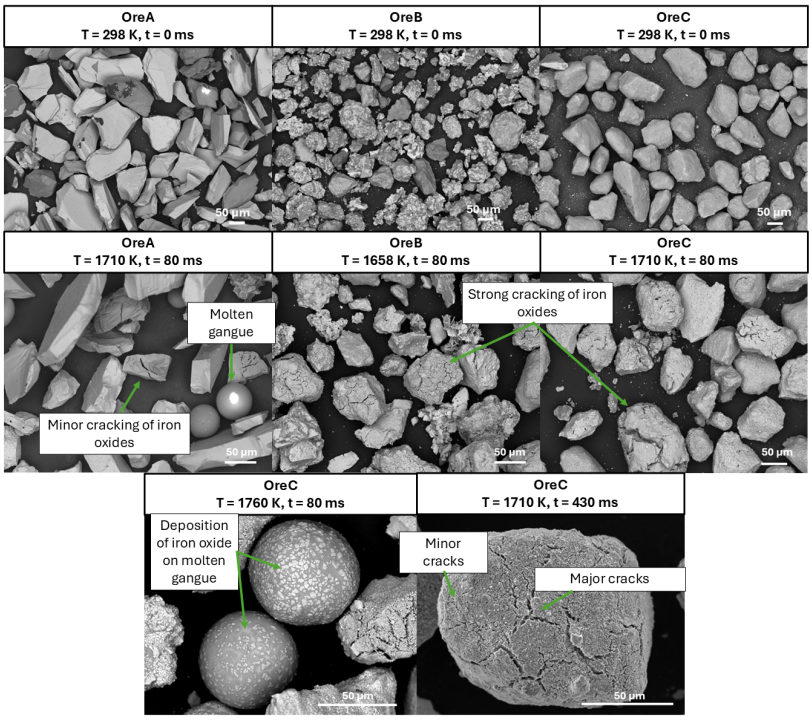


Figure 4.2: Impact of flash thermal decomposition on particle morphology for the medium particle size fraction (63-125 μm) of OreA, OreB and Orec.

(NETZSCH Thermal Analysis STA 409, Germany), where samples were heated up in Ar to 973 K (just beyond the completion of goethite decomposition) at a controlled heating/cooling rate of 10 K/min. The corresponding SEM images are shown in Figure B.3 (appendix B). Under these conditions, OreB showed no cracking, and OreC displayed only minor cracking in isolated particles. These findings support the hypothesis that cracking of goethite ores is promoted under suspension smelting conditions, due to the more rapid heating, and therefore, fast water-vapor evolution.

SEM analysis also reveals that gangue-rich particles tend to undergo melting earlier than Fe-rich oxide particles. As a result, iron oxide fragments are deposited on the molten gangue surfaces, originating either from the gangue particles themselves or from fragmented goethite particles.

4.3.2. EVOLUTION OF PARTICLE SIZE AND DENSITY DURING FLASH REDUCTION

Figure 4.3 shows the effect of flash thermal decomposition at short particle residence times on the particle size (Figure 4.3 (a)) and true particle density (Figure 4.3 (b)). Like the input material, the particle size of the reduced samples was determined by light scattering technology (Microtrac Bluewave) and the particle density was determined by the

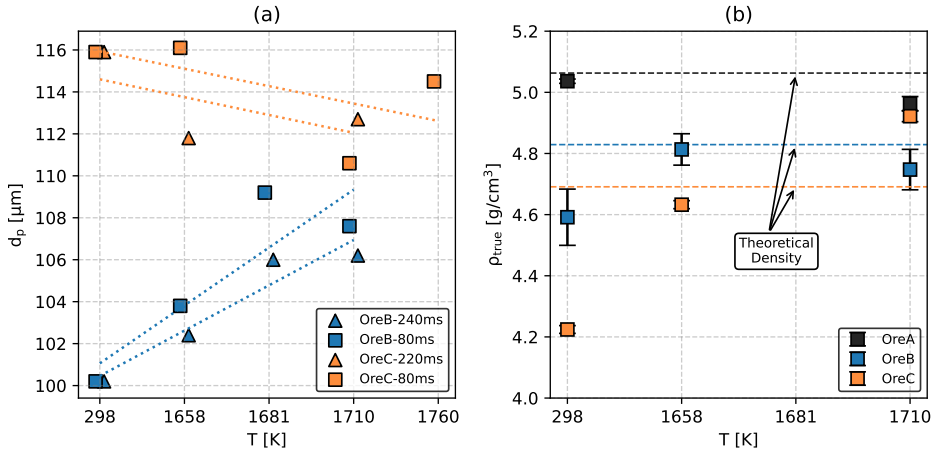


Figure 4.3: Impact of flash thermal decomposition on (a) particle size and (b) true particle density for selected particle residence times (OreA: 1710 K, t = 400 ms; OreB: 1658 K, t = 240 ms; 1710 K, t = 460 ms; OreC: 1658 K, t = 220 ms; 1710 K, t = 220 ms) for the medium particle size fraction (63-125 μm) in all three ores.

He-pycnometer. Clear differences are visible between OreB and OreC. For OreB, particle size increases continuously with temperature. The effect slightly decreases with increasing residence time. In contrast, OreC shows a decrease in particle size with increasing temperature, and the effect is slightly enhanced at longer residence times. These trends reflect the influence of the initial goethite content, which is higher in OreC compared to OreB. The present authors suggest that the limited cracking in OreB could lead to particle expansion, whereas the higher goethite content in OreC promotes an extensive cracking that leads to partial fragmentation, thereby reducing the particle size. A similar phenomenon for goethite ores was also observed by Strezov et al. [25] and Ariyama et al. [31].

In terms of true particle density (Figure 4.3 (b)), both OreB and OreC show an increase after thermal decomposition, compared to the initial state at room temperature. OreA only displays marginal changes. This trend is consistent with the higher initial porosity of OreB and OreC (0.029 and 0.039 g/cm^3, respectively) compared to OreA (0.0003 g/cm^3). It also reflects the phase transformation from goethite to hematite, as the density of hematite (5.26 g/cm^3[32]) is significantly higher than the density of goethite (4.27-4.29 g/cm^3[33]). Since OreA contains no goethite, its particle density remains largely unchanged.

Figure 4.4 introduces the effect of gas pre-reduction under PCR = 95 % conditions on OreB particles. Figure 4.4(a) shows the effect of atmosphere and residence time for the OreB particles with a medium size fraction (63-125 μm). The particle size increase with the residence time is similar in all atmospheres, indicating that this is primarily due to thermal decomposition. In PCR95$_{CO}$, the medium size fraction (63-125 μm) increases in size, while the large size fraction (125-250 μm) decreases (Figure 4.4(b)). The higher goethite content of the larger fraction supports the trends observed during thermal decomposition. It has to be mentioned that the shift in average particle size is still in the

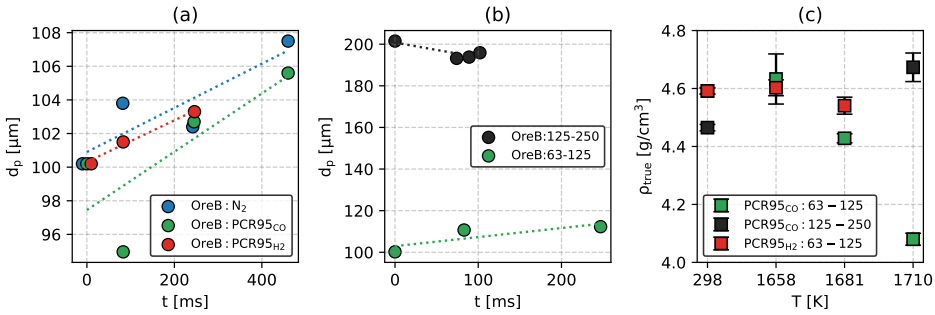


Figure 4.4: Impact of (a) atmosphere on particle size for the medium size fraction (63–125 μm), (b) initial particle size of the as-received material on particle size after pre-reduction in $PCR95_{CO}$, and (c) atmosphere in $PCR95_{CO}$ and in $PCR95_{H2}$ on true particle density for selected particle residence times (63–125 μm: $PCR95_{CO}$ 1658 K, t = 85 ms; 1681 K, t = 85 ms; 1710 K, t = 245 ms; $PCR95_{H2}$ 1658 K, t = 85 ms; 1681 K, t = 85 ms; 125–250 μm: $PCR95_{CO}$ 1710 K, t = 90 ms) in flash conditions.

pre-defined size fractions of the ores and therefore needs to be considered with caution. However, the slight trend between the experiments gives a good indication for the shift in particle size. The corresponding particle size distributions for all experimental conditions are provided in the appendix B (Figure B.4). Each subplot shows the volume frequency for the respective experimental conditions.

The true particle density of OreB (Figure 4.4(c)) decreases with temperature under reducing gas conditions, consistent with further phase transformations such as hematite to magnetite reduction under oxygen release. However, the decrease is much stronger for the $PCR95_{CO}$ and only marginal for the $PCR95_{H2}$ atmosphere. An exception occurs for the larger (125-250) μm fraction in $PCR95_{CO}$, where particle density still increases, suggesting that the goethite to hematite transformation remains dominant.

4.3.3. PHASE EVOLUTION DURING FLASH PRE-REDUCTION

To evaluate the influence of flash reduction on the phase evolution in the HTDF, selected samples were analyzed with XRD (Figure B.5, appendix B). The gangue components show limited reactivity, with the largest gangue component, SiO_2, remaining unaltered. In OreB, peaks of mullite ($Al_{4.8}Si_{1.2}O_{9.6}$) are detected across all samples, consistent with its higher Al_2O_3 content compared to the other ores. No goethite (FeOOH) is detected in OreB or OreC, confirming its complete decomposition in flash conditions at all tested temperatures even at low particle residence times. Hematite (Fe_2O_3) is still present in significant amounts, indicating incomplete reduction to magnetite (Fe_3O_4). For all ores except OreA, an intermediate phase between hematite and magnetite is identified. Among the thermal decomposition experiments, the relative amount of magnetite follows the trend of OreB > OreC > OreA, for the analyzed samples. For OreB, the difference in Fe_3O_4 content between thermal decomposition and gas reduction in $PCR95_{CO}$ atmosphere is marginal, which implies only a small impact of the low reducing gas enriched atmosphere on the pre-reduction compared to thermal decomposition.

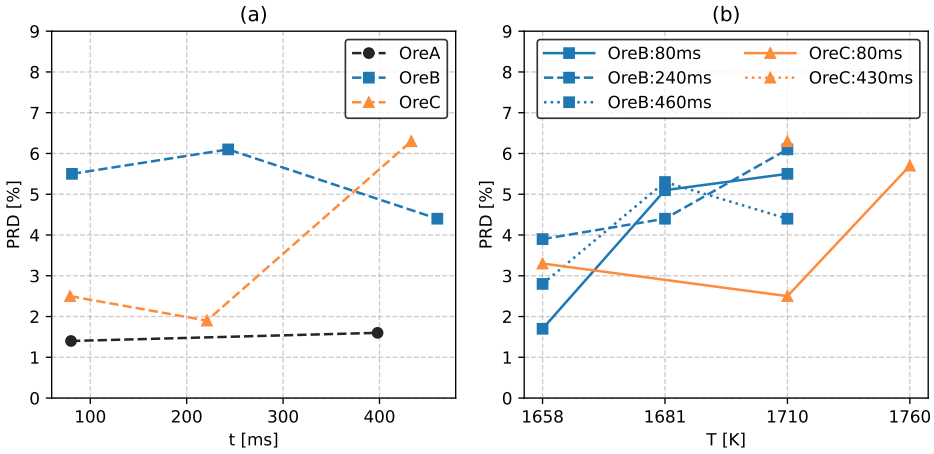


Figure 4.5: Influence of particle residence time and (a) ore mineralogy at 1710 K and (b) temperature on the pre-reduction degree of the medium size fraction (63-125 μm) of all three ores by flash thermal decomposition.

4.3.4. EFFECT OF RESIDENCE TIME ON THE PRE-REDUCTION DEGREE

Figure 4.5 shows the thermal decomposition experiments in the HTDF, with reaction time varying from 100 to 460 ms. At 1710 K, the goethite-containing ores (OreB and OreC) achieve higher PRDs compared to OreA, which only contains hematite as an iron-bearing phase. Increasing the temperature improves PRDs for all ores. OreB generally shows higher PRDs than OreC at shorter residence times (80 ms), but OreC approaches or even surpasses OreB at residence times of 430 ms. This trend likely reflects the higher goethite content in OreC, which takes longer to decompose, and therefore, initially delays the hematite reduction. After goethite decomposition, the reduction can be enhanced due to structural changes such as porosity increase due to fragmentation.

The effect of low reducing gas atmospheres is shown in Figure 4.6. PRDs in $PCR95_{CO}$ and $PCR95_{H2}$ atmospheres are generally slightly higher than those from thermal decomposition alone, but the overall contribution of thermal decomposition remains dominant. Particle size strongly affects the reduction degree (Figure 4.6 (b)). The particles with a larger size fraction of 125-250 μm experience significantly lower PRDs than those with the medium fraction (63-125 μm).

Table B.1 (appendix B) summarizes all HTDF experiments with exact residence times and PRDs. Overall, the achieved reduction degree generally remains low (< 9 %) and does not lead to complete conversion of hematite to magnetite under short residence times (< 400 ms) and high temperatures (1600-1710 K), whether by thermal decomposition or by reduction in $PCR95_{CO}$ atmospheres. Repeat experiments under identical conditions were not performed for the HTDF set-up. However, multiple particles were later microscopically investigated, allowing assessment of particle-to-particle variability. The consistency of observed trends across different conditions supports the reliability of the results.

Therefore, to explore the maximum achievable reduction, complementary TGA experiments were performed as detailed in Table 4.6.

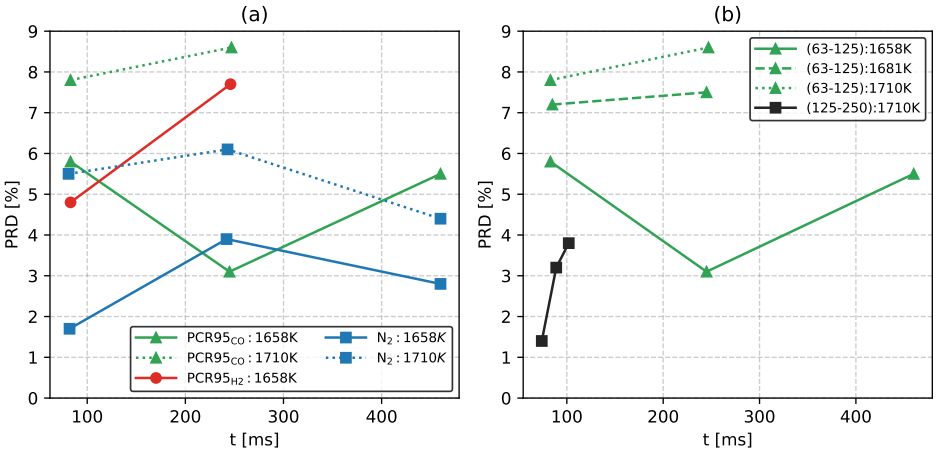


Figure 4.6: Influence of (a) reducing atmosphere on OreB of medium size fraction (63-125 μm) and (b) initial particle size of the ore on the pre-reduction degree of OreB in $PCR95_{CO}$ flash conditions.

Figure 4.7 shows the PRDs of OreB after isothermal reduction at 1723 K, highlighting the effect of particle size and reducing atmosphere. Figure 4.7(a) portraits the complete course of reduction including thermal decomposition, whereas Figure 4.7(b) is a zoomed-in view on the gas reduction. A PRD of 11 % corresponds to full conversion to magnetite, and 33 % to wüstite, based on stoichiometry. When the reducing gases are injected, during the isotherm, the PRDs indicate the presence of magnetite as iron-oxide phase and that hematite has already been fully reduced. After the reducing gas injection additional mass loss is recorded, indicating the reduction to wüstite. The gas reduction proceeds relatively slow. Generally, only minor amounts of wüstite are formed and the particle size has little influence under TGA conditions. All OreB fractions eventually reach similar ΔPRDs during the gas reduction (≈4.2 % in $PCR95_{CO}$), with only marginal differences in reaction speed. In contrast, the reducing atmosphere has a strong effect. While all size fractions show comparable PRDs in $PCR95_{CO}$, the $PCR95_{H2}$ atmosphere leads to lower overall gas reduction (≈2.8 %).

In the TGA experiments, thermal decomposition and gas reduction occur sequentially within a single experimental run, allowing their combined effects to be evaluated in a single dataset. In contrast, during the HTDF experiments both reactions occur simultaneously, requiring separate experiments to evaluate the impact of thermal decomposition and gas reduction. Figure 4.8 compares the pre-reduction results for OreB obtained from TGA and HTDF experiments under comparable conditions. The results highlight the importance of particle residence time. While the long residence times in the TGA enable substantially higher pre-reduction degrees, the short residence times in the HTDF under flash conditions limit the extent of the reduction. The error bars indicate the average of the particle residence times in the HTDF experiments at 1723 K as set-temperature at the otherwise same conditions. For the TGA experiments the final achieved PRDs are indicated. In the TGA all size fractions reach similar pre-reduction degrees of around 17

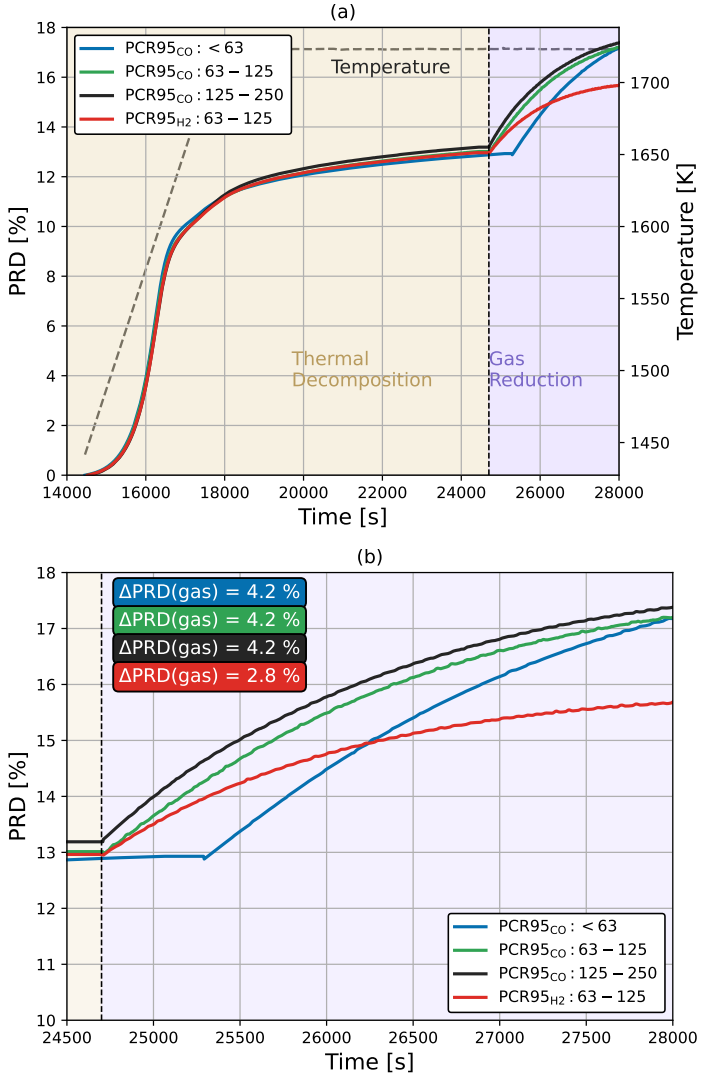


Figure 4.7: Influence of atmosphere and particle size on the PRDs in $PCR95_{CO}$ and $PCR95_{H2}$ conditions in a TGA (T=1723 K) for (a) the complete process including heating (thermal decomposition) and subsequent isothermal gas reduction and (b) a zoomed in view on the isothermal gas reduction.

% in $PCR95_{CO}$, indicating that particle size becomes less relevant when sufficient time is available to complete the reaction. In contrast, in the HTDF, the particles with a medium size fraction achieve notably higher pre-reduction degree compared to those with larger size fraction, underlining the stronger influence of particle size at short residence times. The distinction between thermal decomposition and gas reduction in this comparison is based on the use of reference conditions. In the TGA experiments, the PRD achieved under inert conditions (before gas injection) is attributed to thermal decomposition, while the additional increase in PRD after gas injection is attributed to the gas reduction. In the HTDF experiments, the impact of thermal decomposition is isolated through the experiments first conducted in N_2, whereas the difference to reducing atmosphere is interpreted as the contribution of gas reduction. The interpretation assumes that both contributions can be approximately separated based on differences in PRD between experimental conditions. Nevertheless, both conditions confirm that thermal decomposition is the main contributor to the reduction, with PCR = 95 % gas atmospheres providing only a modest additional effect.

While the HTDF simulates the in-flight reduction behaviour of the particles in the HIsarna pre-reduction stage, the results of the TGA experiments help to understand how longer reduction could benefit the (pre-)reduction degree. In case a molten particle film forms on the walls of the HIsarna furnace due to the high temperatures, this material is most likely converted to at least magnetite and is expected to be in molten or partially molten state. Such a liquid film remains in contact with the reducing gases for a significant longer period compared to the in-flight particles. While the HTDF represents the rapid in-flight regime and the TGA experiments operate under isothermal conditions with significantly lower heating rates, the TGA may still provide qualitative insight into reaction behavior under conditions where iron oxide is molten and extended gas–phase contact times are present. In the TGA experiments, the long residence times allow for substantially higher pre-reduction degrees compared to the HTDF, where short residence times under flash reaction conditions limit the extent of reduction.

4.3.5. EVALUATION OF SINGLE PARTICLE REDUCTION AND HEATING BEHAVIOR

During the in-flight reduction, limited time is available and many processes such as heating, partial melting and, pre-reduction happen simultaneously. Consequently, the energy required for both particle heating and reduction strongly affects the overall reduction behavior. For energy consuming reactions, both the thermal decomposition of goethite (Eq. (4.2) and hematite (Eq. (4.3) need to be considered. The enthalpy required for decomposing a single particle was calculated using theoretical reaction enthalpies for both reactions and material properties such as true density and particle size. Excluding the particle mass from the calculations would also eliminate the influence of particle density and size. As these physical properties strongly affect flash reduction in the HTDF, they must be accounted for in the enthalpy calculations. The particle mass was determined as:

$$m_{particle} = \frac{4}{3}\pi R_i^3 \cdot \rho_{true,i} \tag{4.7}$$

Where r is the average particle radius of the size fraction and $\rho_{\text{ture,i}}$ is the true particle

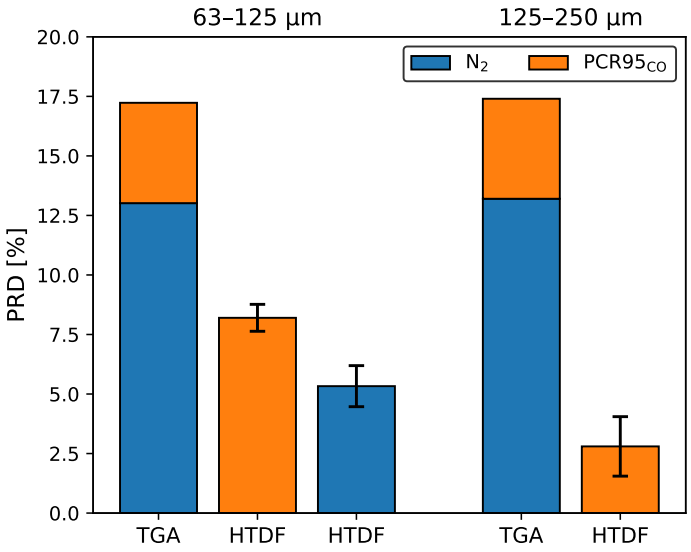


Figure 4.8: Comparison of pre-reduction in thermal decomposition and $PCR95_{CO}$ conditions between TGA (long reduction times, total experiment time t ≈ 28,000 s; thermal decomposition proceeds predominantly between ≈ 14,500–1800 s, followed by a gas reduction stage between ≈ 24,700–28,000 s; intermediate periods show only minor reaction progress) and HTDF (flash conditions, t = 74 – 460 ms) with a set-temperature of 1723 K for OreB. For the TGA, the bar portraits the complete reduction (blue=thermal decomposition, blue + orange=thermal decomposition + $PCR95_{CO}$ gas reduction).

density of ore (i=OreA,OreB,OreC). The values were taken from Table 4.3.

Reaction enthalpies for goethite and hematite were determined according to Eq. (4.8) and Eq. (4.9), respectively, with start and end temperatures taken from TGA results of our previous study [24]. Reaction enthalpy values were calculated using the Equilib module of FactSage 7.0 [34] with the FactPS database [35]:

$$\Delta H_{\mathrm{FeOOH}} = \frac{M_{\mathrm{Fe_2O_3}}}{2 \times M_{\mathrm{FeOOH}}} \times H_{\mathrm{Fe_2O_3}}(T_{\mathrm{end}}) + \frac{M_{\mathrm{H_2O}}}{2 \times M_{\mathrm{FeOOH}}} \times H_{\mathrm{H_2O}}(T_{\mathrm{end}}) - H_{\mathrm{FeOOH}}(T_{\mathrm{start}}) \quad (4.8)$$

$$\Delta H_{\mathrm{Fe_2O_3}} = \frac{2 \times M_{\mathrm{Fe_3O_4}}}{3 \times M_{\mathrm{Fe_2O_3}}} \times H_{\mathrm{Fe_3O_4}}(T_{\mathrm{end}}) + \frac{0.5 \times M_{\mathrm{O_2}}}{3 \times M_{\mathrm{Fe_2O_3}}} \times H_{\mathrm{O_2}}(T_{\mathrm{end}}) - H_{\mathrm{Fe_2O_3}}(T_{\mathrm{start}}) \quad (4.9)$$

Where $\Delta H_{\mathrm{FeOOH}}$ and $\Delta H_{\mathrm{Fe_2O_3}}$ are the decomposition enthalpies of goethite and hematite (J), respectively, M_i is the molecular weight of the compound i (g/mol) and $H_i(T)$ is the enthalpy of compound i (J) at temperature T (K). The total enthalpy for complete decomposition of a single particle was then calculated as:

$$\Delta H_{\mathrm{particle}} = m_{\mathrm{particle}} \times (\Delta H_{\mathrm{FeOOH}} + \Delta H_{\mathrm{Fe_2O_3}}) \quad (4.10)$$

Since the reduction in the HTDF occurs at very short residence times, particle heating behavior in the hot zone was also calculated. The ore specific true particle density and average particle size were included as input material properties, while other parameters were kept constant. Heating calculations were performed for an initial particle temperature of 330 K, an isothermal zone temperature of 1723 K, an isothermal zone length of 0.39 m, and an initial particle velocity of 0 (at the start of the isothermal zone) in N_2 atmosphere. In the applied code a single, spherical particle is assumed to be in a stationary, isothermal cylindrical furnace (representing the HTDF), exchanging heat with the walls and gas via convection and radiation, while moving under gravity and drag force. The gas and wall properties are constant, and complex effects like chemical reactions, gas absorption and emission, or multiple particles are ignored. The calculations assume laminar flow is present in the experimental set-up.

The results of the enthalpy calculations and heating profiles are shown in Figure 4.9. Both indicate a strong influence of particle properties. For the decomposition enthalpy, hematite contributes more strongly than goethite. However, the high goethite content and larger particle size of OreC result in the highest overall energy requirement. By contrast, OreB shows the most favorable reaction conditions, requiring even less energy than OreA despite containing goethite. Reason for this is the lower energy required for hematite reduction. This lower required energy can be explained by the lower mass of the OreB particle and the narrower temperature range for the hematite decomposition (based on [24]) of OreB compared to OreA and OreC.

The heating profiles also differ slightly due to differences in particle density and size between the ores. OreB reaches the maximum temperature faster than both OreA and OreC. OreB reaches for example 1600 K already at 0.128 m in the isothermal zone, whereas OreA (0.164 m) and OreC (0.158 m) reach the temperature later. The slower heating of OreC is consistent with its lower PRDs at short residence times but higher PRDs at longer times. These trends match the experimental results in section 4.3.4. The higher energy demand and slower heating of OreC explains its poor reduction at very short particle residence times, while its high porosity and fragmentation after decomposition promotes reactivity during extended residence times. By contrast, OreB combines moderate energy requirements with a faster heating profile, through beneficial material properties of lower particle size and density (input conditions). This facilitates a higher degree of pre-reduction and leads to superior performance under HTDF conditions. OreA, however, deviates from what would be expected solely based on its heating profile and energy demand. Although its overall energy demand is lower than OreC and its heating is similar to OreC, OreA consistently shows almost no reduction by thermal decomposition based on the PRDs. This can be explained by its distinguished characteristics. First, the absence of goethite limits cracking and fragmentation effects that promote reactivity, and second its initially low specific surface area and porosity (Table 4.3), which further limits the decomposition degree. As a result, OreA thermally decomposes slower than the goethite-containing ores.

In the context of suspension smelting, given the very short available time, this means that ores with high goethite content (like OreC) require either longer residence times or more intense process conditions to reach comparable pre-reduction levels, whereas ores with balanced properties (like OreB) appear more suitable for rapid in-flight reduction.

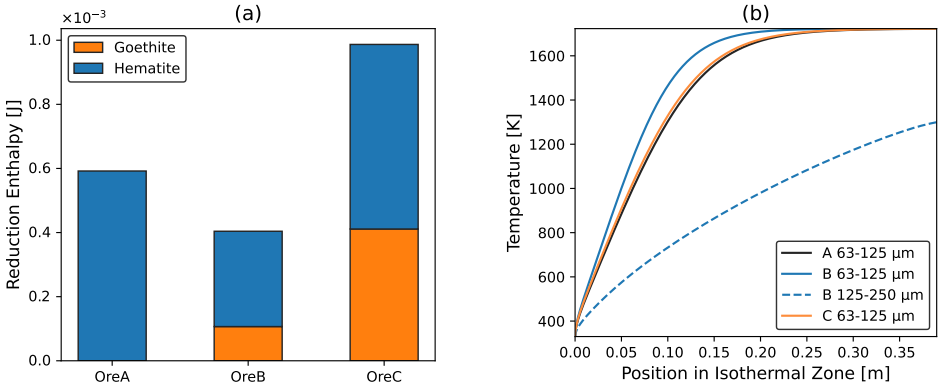


Figure 4.9: (a) Reaction enthalpy for the thermal decomposition of a single particle (63-125 μm) for OreA, OreB and OreC and (b) heating profile of a single particle in the isothermal zone of the HTDF (considering ore specific true particle density and average particle size (Table 4.3)).

Ores, not containing goethite (OreA), appear even more limited on their reduction and are expected to need even more time to sufficiently decompose thermally.

4.3.6. MICROSCOPICAL AND KINETIC ANALYSIS OF FLASH REDUCED PARTICLES

To gain further insights into the single particle reduction in flash conditions (HTDF), cross-sections of quenched samples were analyzed from the partially reduced particles under different experimental conditions. Figure B.6 (appendix B) summarizes all the SEM/EDS results. The analysis showed that while some particles exhibit a relatively uniform gangue distribution, others show that the gangue is concentrated around iron oxide grains or near particle surfaces. In contrast, the distribution of Fe appears homogeneous. At the early reduction stages from hematite to magnetite, however, EDS cannot reliably distinguish between the two iron phases due to their similar oxygen contents. To overcome this limitation, EBSD was used to identify phases based on crystal structure, rather than their elemental composition [36]. Samples of OreB (N_2 and $PCR95_{CO}$), OreC (N_2), and OreA (N_2) were selected for EBSD analysis to obtain insights on the impact of atmosphere and ore mineralogy on the phase distribution after reduction. The EBSD maps are shown in Figure 4.10.

In all cases, partial transformation of hematite to magnetite is observed, but the phase distribution differs strongly even within the same experimental batch. The images include the pre-reduction degree for the specific measured phases in each image, indicating the heterogenous reduction over a sample batch. For OreB in both N_2 and $PCR95_{CO}$ atmosphere and in OreC, some particles show reduction initiating at the external particle surface, forming a Fe_3O_4 layer which progresses inwards. In contrast, other particles exhibit Fe_3O_4 formation within the particle at internal pores, indicating that reduction can also proceed locally from inside the ore particles. Therefore, two overall reduction modes can be concluded. First, the reduction at the particle surface, consistent with a

shrinking core mechanism and second, the internal diffusion at the pore sites. Based on the calculated (pre-)reduction degrees in the images, it is clear that the surface reduction contributes more to the overall reduction compared to the reduction at the internal pores. Consistent with the similar PRDs achieved by thermal decomposition and gas reduction in $PCR95_{CO}$ for OreB, no clear distinction between these two reaction mechanisms is possible. For OreA only very limited reduction is observable, which makes it difficult to conclude a reaction mechanism. The almost absent reduction in OreA also indicates that the reduction by thermal decomposition is enhanced by the presence of goethite in the ore, either due to already higher initial porosity, or increasing internal porosity due to water-vapor release and cracking during goethite thermal decomposition. EBSD did not reliably detect SiO_2, so potential limitations from silica cannot by fully assessed.

The kinetic analysis is based on a single particle approach which is considered appropriate for the present HTDF conditions due to the laminar flow regime and short particle residence times, where particle-particle interactions are assumed to be limited. Each particle is assumed to react independently under the surrounding gas atmosphere. Despite the low overall PRDs, measured by chemical titration (chapter 4.3.4), the data can be used to approximate apparent diffusion coefficients. The calculated apparent diffusion coefficients should be regarded as model-derived parameters reflecting the simplified assumptions of the applied diffusion models rather than direct physical diffusion coefficients. Since this study focuses on industrial ores, individual particles vary in size, morphology, goethite and gangue content, leading to significant variations in actual heating rate and reduction behavior from particle to particle. While these factors limit the reliability of a kinetic model fit, we can still estimate the apparent diffusion coefficients from the particle residence time and reduction degree. However, a complication arises from the coexistence of the two mechanisms. While reduction at the particle surface is better described by the Jander equation (Eq. (4.11)) [37–39], internal pore diffusion is more consistent with the Ginstling-Brounshtein equation (Eq. (4.12)) [37–39]:

$$D_0 * t = \left(1 - (1 - PRD)^{\frac{1}{3}}\right)^2 \tag{4.11}$$

$$D_0 * t = \left(1 - \left(\frac{2PRD}{3}\right)\right) - (1 - PRD)^{\frac{2}{3}} \tag{4.12}$$

Where D_0 is the apparent diffusion coefficient (1/ms), t is the particle residence time (ms) and PRD is the reduction degree. Both models describe diffusion-controlled reactions in spherical particles. However, the Jander equation is typically applied to systems where a solid unreacted core is surrounded by a product layer, and reaction rates are limited by diffusion through this layer, embodying a shrinking-core behavior. It should be noted that both the Jander and Ginstling-Brounsthein models are based on simplifying assumptions, including a single rate-controlling diffusion step, which implicitly assumes that parallel competing reactions do not significantly influence the overall rate, and a well-defined spherical particle geometry [40–42]. These assumptions are not strictly fulfilled under the present HTDF flash conditions, where thermal decomposition and gas-phase reduction occur simultaneously and multiple reaction pathways coexist. Therefore, the models are not applied as rigorous mechanistic descriptions, but rather as effective

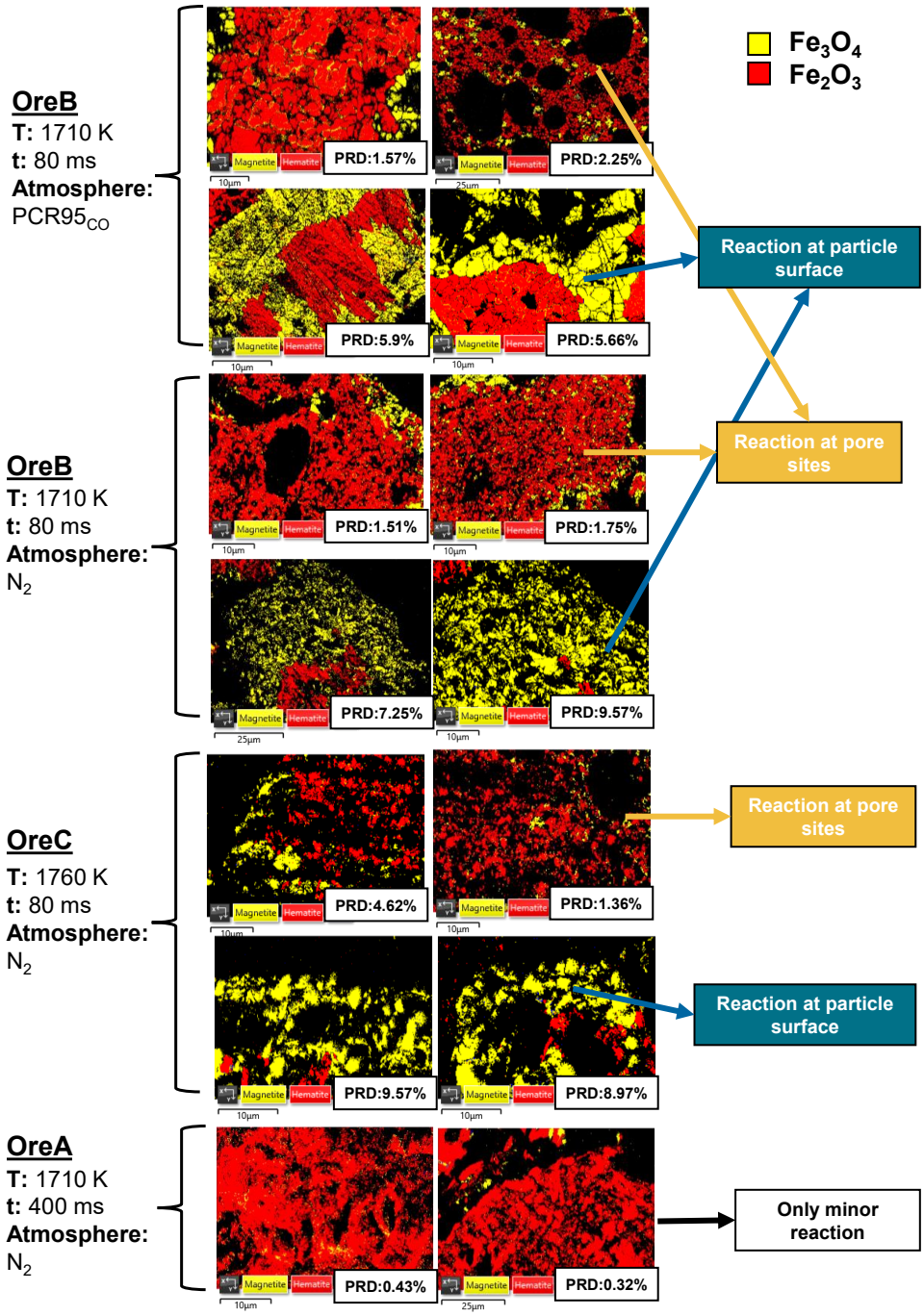


Figure 4.10: EBSD analysis of 2-4 selected particles of the medium size fraction (63-125 μm) of each OreA, OreB and OreC for selected flash in-flight experimental conditions (magnetite: yellow; hematite: red)

approaches to approximate diffusion-controlled behavior and enable a comparative evaluation of the experimental data. It should be noted that all kinetic interpretations refer to a low-conversion degree regime (PRD < 9 %), and therefore represent early stage reduction behaviour rather than fully developed reaction kinetics. The Ginstling-Brounshtein equation provides a more rigorous treatment of diffusion through a porous product layer [38, 41]. In porous materials, the diffusion pathway is often dominated by internal pore diffusion [43]. Since both mechanisms are observed microscopically, apparent diffusion coefficients were calculated with both models and compared (Table B.2, appendix B). This dual-model approach directly reflects the EBSD observations, where both surface-initiated and internal pore-initiated reduction are present within the same particles, indicating that diffusion cannot be described by a single idealized pathway. In this work, the reaction mechanisms of thermal decomposition and reduction in low reducing gas-enriched atmospheres are difficult to distinguish, as thermal decomposition appears to be the dominant driver of reduction. From a mass transfer perspective, thermal decomposition involves the diffusion of oxygen released from the particle, whereas gas reduction involves the diffusion of reducing gases into the particle through the surface or internal pores. However, under the present conditions, it is challenging to separate the contributions of the two mechanisms. Therefore, the model approach is applied to both the thermal decomposition and gas reduction experiments. Since the resulting values are very similar and both models could be applied based on the EBSD analysis, for further calculations, the average of both models is used. The natural logarithm of the apparent diffusion coefficients for varying experimental conditions are presented in Figure 4.11.

The apparent diffusion coefficients obtained for the thermal decomposition experiments (Figure 4.11(a)) lie in the range of 7.22×10^{-8} and 4.69×10^{-6} [1/ms]. Apparent diffusion coefficients are higher for OreB and OreC compared to OreA, and a positive temperature dependence is evident. Ore specific and time dependent differences are also visible. OreB exhibits the highest D_0 values at short residence times, reflecting a relatively open pore structure, but D_0 decreases with time, consistent with densification of a magnetite product layer. OreA shows consistently low diffusivities, indicative of a compact or highly close-grained structure. This aligns with the very low porosities measured for OreA in section 4.2.1. In contrast, OreC demonstrates a pronounced increase in D_0 at higher temperatures, suggesting thermally induced cracking and pore opening, as also observed in the morphological analysis (section 4.3.1). Overall, the absolute values and trends of the apparent diffusion coefficients highlight the role of ore specific microstructural evolution. Figure 4.11(b) displays the apparent diffusion coefficients of OreB (63-125 μm) medium size fraction in PCR95 atmosphere. The values range between 4.45×10^{-7} and 8.59×10^{-6} and are therefore slightly higher than those from thermal decomposition. The PCR95 reduction shows a strong dependence on both time and temperature, consistent with rapid microstructural evolution in the early stages of flash reduction. As already indicated by the higher (pre-)reduction degrees, reduction in CO yields higher apparent diffusion coefficients than in H_2, where research usually highlights the better diffusion ability of H_2 compared to CO [44]. This can be partly explained by the water-gas shift reaction (WGSR) (Eq. (4.13)) [45]:

$$H_2O(g) + CO(g) \rightleftharpoons CO_2(g) + H_2(g) \tag{4.13}$$

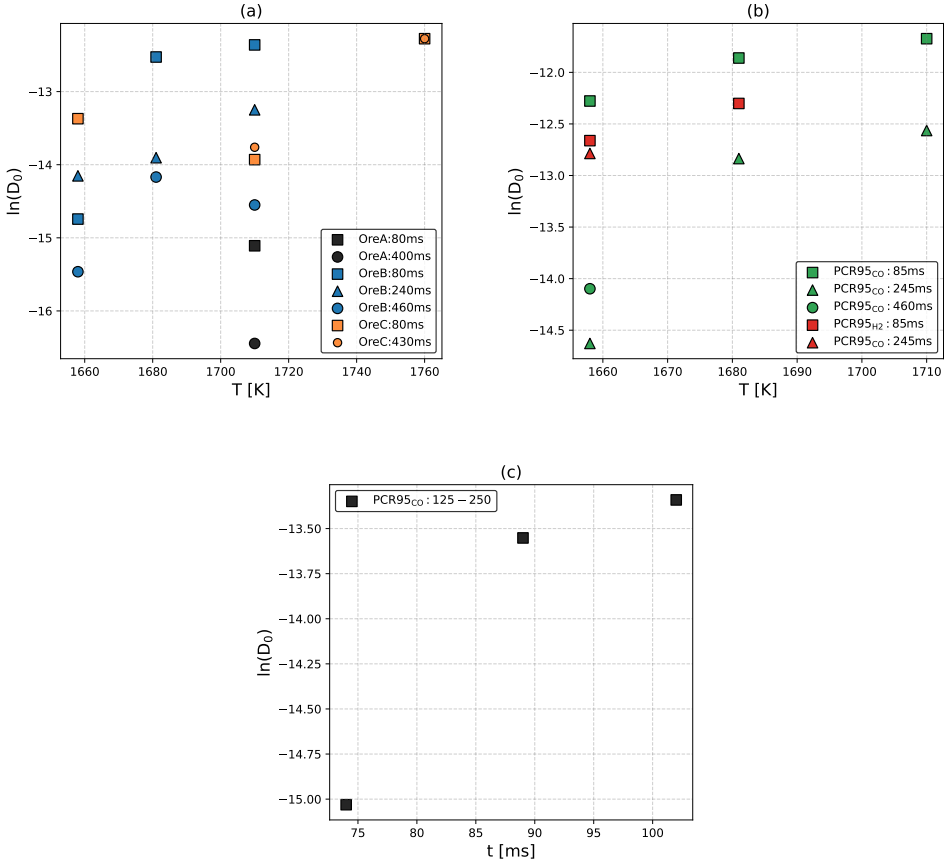


Figure 4.11: Apparent diffusion coefficients for (a) thermal decomposition experiments, (b) experiments in $PCR95_{CO}$ and $PCR95_{H2}$ atmosphere for a particle size of (63-125) μm of OreB and (c) experiments in $PCR95_{CO}$ atmosphere for a size fraction of (125-250) μm of OreB in flash conditions.

The WGSR has a high reaction rate at temperatures above 1073 K, and thermodynamically higher temperatures favor CO formation over H_2. In the presence of high concentrations of H_2 and CO_2, this increases the production of CO and H_2O and weakens the reduction ability of the atmosphere [45–47]. To estimate the impact of the WGSR on the $PCR95_{H2}$ atmosphere, the off-gas was measured with a HIDEN mass spectrometer at room temperature and at the experimental temperatures of 1658 K, 1681 K and 1710 K (Figure B.7, appendix B). The mass spectrometer analysis shows that at the applied experimental temperatures, almost no H_2 is present in the atmosphere, as it converted to H_2O and CO. This demonstrates that the actual gas composition deviates significantly from the experimental inlet $PCR95_{H2}$ composition due to the WGSR under high-temperature conditions. Abdelrahim et al. [48] found that H_2O content exceeding 2 % can have a negative impact on iron ore reduction in CO-CO_2-H_2-H_2O-N_2 atmospheres at temperature up to 1373 K, due to the blocking of active reaction sites by the H_2O. The deviation from

the intended gas composition explains the reduced contribution of H_2 and the lower (pre-)reduction degrees and diffusion coefficients observed under $PCR95_{H2}$ conditions. However, it is questionable if the same effect would occur at the higher temperatures present in flash conditions. The lower reducing power of the $PCR95_{H2}$ atmosphere can further explain the lower reduction achieved in Figure 4.7 compared to the $PCR95_{CO}$ atmosphere.

Figure 4.11(c) shows the reduction of larger OreB particles in $PCR95_{CO}$, where apparent diffusion coefficients increase rapidly from 2.97×10^{-7} to 1.61×10^{-6} with increasing reduction time. This trend indicates rapid pore opening in the early stages.

Although precise activation energies cannot be determined due to the limited dataset and low conversion levels, approximate values can be estimated for comparative purposes. Figure 4.12 shows Arrhenius fits for the thermal decomposition and PCR95 reduction experiments where sufficient data were available. It should be emphasized that the statistical quality of some fits (R^2 values) are relatively poor, especially for the thermal decomposition of OreC (80 ms) (R^2<0.39) and OreB (460 ms) (R^2<0.41). However, while approximate, the values show consistent trends that should be interpreted qualitatively rather than as intrinsic kinetic constants. For the thermal decomposition of Fe_2O_3, OreB shows a very high activation energy of 1047 kJ/mol at 80 ms, which decreases to 388 kJ/mol at 460 ms. The unusually high value at short times can reflect temporary effects during the initial reduction stages, such as pore opening and product layer formation, rather than a kinetic barrier. OreC shows a significantly lower activation energy of 252 kJ/mol at 80 ms, likely due to improved reactivity from particle cracking.

For reduction in PCR95, activation energies are lower than for thermal decomposition. At 85 ms, the activation energy is 270 kJ/mol in $PCR95_{CO}$ and 364 kJ/mol in $PCR95_{H2}$. The slightly higher value for $PCR95_{H2}$ can be attributed to the WGSR, where H_2O formation may increase kinetic barriers and limit the reduction potential.

Overall, the kinetic analysis is consistent with pre-reduction (including thermal decomposition) in flash conditions being governed by a mixed control of surface and pore diffusion, with ore-specific microstructural evolution strongly influencing diffusivity and apparent activation energies. These findings suggest that goethite rich ores exhibit high reactivity through cracking and pore formation, whereas dense, low-porosity hematite ores are diffusion-limited. For suspension smelting technologies such as HIsarna, this implies that ore mineralogy and structure must be carefully considered when selecting low-grade feedstocks, as they directly influence reduction efficiency under short residence times.

4.4. CONCLUSIONS

- Ore mineralogy strongly controls the thermal decomposition and pre-reduction behaviour under short residence times (flash conditions). Goethite-rich ores (OreB, OreC) undergo cracking and fragmentation during thermal decomposition, with increasing goethite content accelerating the fragmentation and reducing the particle size. Goethite decomposition increases true particle density for both OreB and OreC via outer pore closing and goethite to hematite phase transformation. This leads to a significant overall impact on the PRD, since both particle size and density strongly influence particle residence time during in-flight reduction.

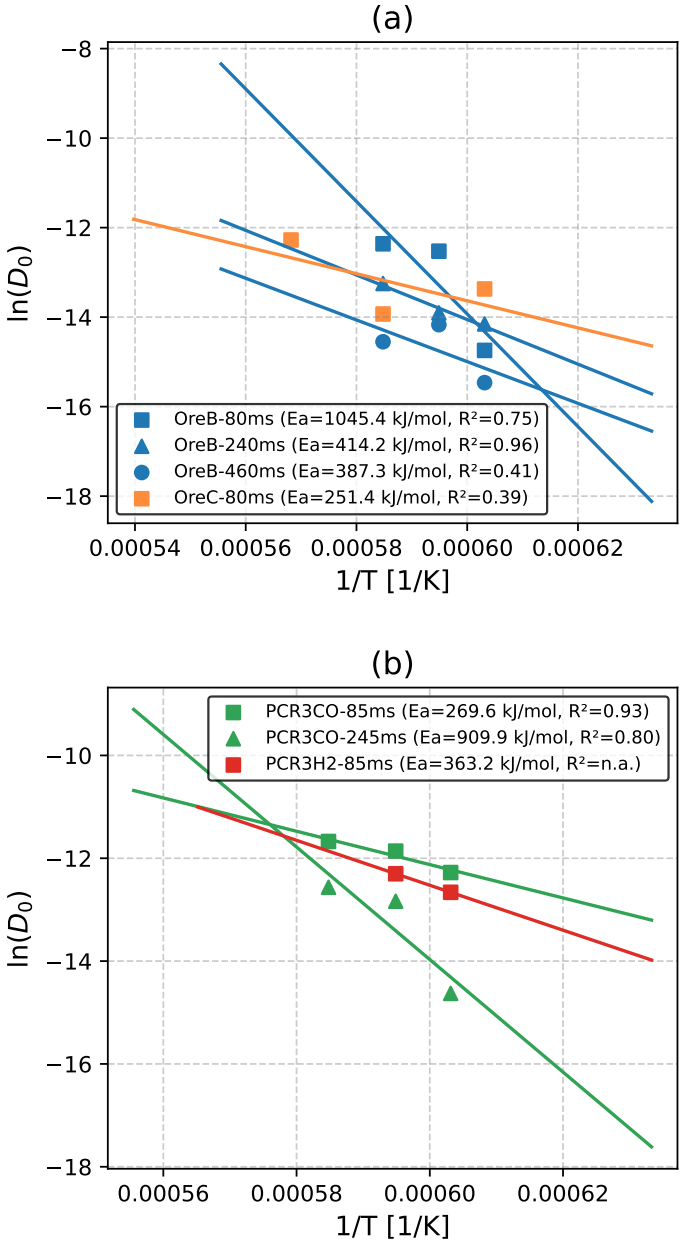


Figure 4.12: Arrhenius fitting of (a) reduction by thermal decomposition and (b) reduction by gas reduction in PCR95 atmosphere in flash conditions.

- Even though wüstite formation is possible in PCR95 conditions, it can only be achieved at long residence times of approx. 2000 s (in the TGA), but not during the in-flight process in the HTDF. Nevertheless, thermal decomposition is the dominant driver of pre-reduction, both in the TGA and the HTDF. Although gas reduction in PCR95 atmospheres yields slightly higher PRDs than decomposition alone (HTDF: ΔPRD $\approx$ 2.5 %, TGA: ΔPRD $\approx$ 4.2 %), thermal decomposition contributes more to the overall reduction. During in-flight thermal decomposition the goethite-rich ores (OreB, OreC) reduce more than the hematite ore (OreA), with OreA achieving PRDs up to 1.6 %, OreB up to 6.1 % and OreC up to 6.3 %. Due to its higher amounts of goethite and therefore longer goethite decomposition times, OreC shows stronger dependence on residence time than OreB, with PRDs increasing at longer times. While the particle size has no influence on the total reduction in the TGA (long residence times), larger particle sizes lead to slower heating and shorter particle residence times in the HTDF, thereby negatively influencing the PRD.

- EBSD analysis and diffusion modelling show that both surface product-layer diffusion and internal pore diffusion occur simultaneously, with relative contributions depending on ore type, temperature and atmosphere. The apparent diffusion coefficients are highest for goethite-rich ores (OreB and OreC), and remain consistently low if no goethite is present in the ore (OreA). This is caused by the cracking and fragmentation behaviour and the initial porosity and specific surface area of the ores. High activation energies (1047 kJ/mol for OreB) likely reflect early-stage pore opening and product-layer formation, while lower values in OreC (252 kJ/mol) highlight enhanced reactivity from cracking. In $PCR95_{H2}$ atmospheres, the WGSR reduces the impact by H_2 on the reduction by generating H_2O and limited availability of a reducing gas.

- In-flight reduction in the HTDF reveals that ores with balanced mineralogical properties (OreB, characterised by intermediate goethite-content and thus intermediate porosity and density) show the most favourable behaviour for early stage reduction during the rapid in-flight reaction when ores are injected at the top of the HIsarna furnace. Goethite-richer ores (OreC) may require longer residence times or adjusted process conditions. Dense hematite ores (OreA) are least reactive under short residence times and low reductive atmospheres. The observed enhancement in early-stage reduction for goethite-containing ores ($\approx$ 4.5 %) corresponds to the initial reaction stage and does not necessarily translate into higher reduction regimes as the residence time increases under the investigated conditions in the HTDF, and therefore should not be interpreted as absolute basis for an overall ranking of ore suitability for industrial application.

REFERENCES

[1] P. Leerhoff, C. Zeilstra, B. P. Wilson, K. Meijer, J. van der Stel, S. T. Abrahami, N. Dogan, and Y. Yang. Thermal decomposition and pre-reduction of goethitic iron ore fines and their effects on phase transformation and material properties. **Scientific Reports** (2026). DOI: 10.1038/s41598-026-62756-0.

[2] K. Meijer, M. Denys, J. Lasar, J.-P. Birat, G. Still, and B. Overmaat. ULCOS: ultra-low CO_2 steelmaking. **Ironmaking & Steelmaking** 36 (2009), pp. 249–251. DOI: 10.1179/174328109X439298.

[3] K. Meijer, C. Zeilstra, C. Teerhuis, M. Ouwehand, and J. van der Stel. Developments in Alternative Ironmaking. **Transactions of the Indian Institute of Metals** 66 (2013), pp. 475–481. DOI: 10.1007/s12666-013-0309-z.

[4] M. Geerdes, R. Chaigneau, I. Kurunov, O. Lingiardi, and J. Ricketts. Modern Blast Furnace Ironmaking an introduction. 3rd. IOS Press, 2015.

[5] P. C. Cavaliere. Hydrogen Assisted Direct Reduction of Iron Oxides. Springer International Publishing, 2022. ISBN: 9783030980566. DOI: 10.1007/978-3-030-98056-6.

[6] H. Y. Sohn. Suspension Hydrogen Reduction of Iron Ore Concentrate in AISI/DOE Technology Roadmap Program for the Steel Industry. Tech. rep. Utah: American Iron and Steel Institute, 2008.

[7] H. Y. Sohn. Energy consumption and CO_2 emissions in ironmaking and development of a novel flash technology. **Metals** 10, 54 (2020). DOI: 10.3390/met10010054.

[8] Z. Yan, T. T. Htet, J. Hage, K. Meijer, and Z. Li. HIsarna Process Simulation Model: Using FactSage with Macro Facility. **Metallurgical and Materials Transactions B** 54 (2023), pp. 868–879. DOI: 10.1007/s11663-023-02732-5.

[9] K. Meijer, C. Guenther, and R. J. Dry. HIsarna Pilot Plant Project. METEC InSteelCon 2011, 2011.

[10] Z. Chen, C. Zeilstra, J. van der Stel, J. Sietsma, and Y. Yang. Reduction Mechanism of Fine Hematite Ore Particles in Suspension. **Metallurgical and Materials Transactions B** 52 (2021), pp. 2239–2252. DOI: 10.1007/s11663-021-02173-y.

[11] Y. Qu, Y. Yang, Z. Zou, C. Zeilstra, K. Meijer, and R. Boom. Kinetic study on gas molten particle reduction of iron ore fines at high temperature. **Ironmaking and Steelmaking** 42 (2015), pp. 763–773. DOI: 10.1179/1743281215Y.0000000021.

[12] Z. Chen, C. Zeilstra, J. van der Stel, J. Sietsma, and Y. Yang. Reduction Kinetics of Fine Hematite Ore Particles in Suspension. **Metallurgical and Materials Transactions B** 52 (2021), pp. 3393–3402. DOI: 10.1007/s11663-021-02269-5.

[13] Y. Qu, Y. Yang, Z. Zou, C. Zeilstra, K. Meijer, and R. Boom. Melting and reduction behaviour of individual fine hematite ore particles. **ISIJ International** 55 (2015), pp. 149–157. DOI: 10.2355/isijinternational.55.149.

[14] Y. Qu, Y. Yang, Z. Zou, C. Zeilstra, K. Meijer, and R. Boom. Reduction kinetics of fine hematite ore particles with a high temperature drop tube furnace. **ISIJ International** 55 (2015), pp. 952–960. DOI: 10.2355/isijinternational.55.952.

[15] Y. Qu, Y. Yang, Z. Zou, C. Zeilstra, K. Meijer, and R. Boom. Thermal decomposition behaviour of fine iron ore particles. **ISIJ International** 54 (2014), pp. 2196–2205. DOI: 10.2355/isijinternational.54.2196.

[16] M. Elzohiery, H. Y. Sohn, and Y. Mohassab. Kinetics of Hydrogen Reduction of Magnetite Concentrate Particles in Solid State Relevant to Flash Ironmaking. **steel research international** 88 (2017). DOI: 10.1002/srin.201600133.

[17] L. Y. Xing, Z. S. Zou, Y. X. Qu, L. Shao, and J. Q. Zou. Gas–Solid Reduction Behavior of In-flight Fine Hematite Ore Particles by Hydrogen. **Steel Research International** 90, 1800311 (2019). DOI: 10.1002/srin.201800311.

[18] L. Xing, Y. Qu, C. Wang, L. Shao, Z. Zou, and W. Song. Kinetic Study on Thermal Decomposition Behavior of Hematite Ore Fines at High Temperature. **Metallurgical and Materials Transactions B** 51 (2020), pp. 395–406. DOI: 10.1007/s11663-019-01747-1.

[19] F. Chen, Y. Mohassab, T. Jiang, and H. Y. Sohn. Hydrogen Reduction Kinetics of Hematite Concentrate Particles Relevant to a Novel Flash Ironmaking Process. **Metallurgical and Materials Transactions B** 46 (2015), pp. 1133–1145. DOI: 10.1007/s11663-015-0332-z.

[20] F. Chen, Y. Mohassab, S. Zhang, and H. Y. Sohn. Kinetics of the Reduction of Hematite Concentrate Particles by Carbon Monoxide Relevant to a Novel Flash Ironmaking Process. **Metallurgical and Materials Transactions B** 46 (2015), pp. 1716–1728. DOI: 10.1007/s11663-015-0345-7.

[21] A. K. Biwas. Principles of blast furnace ironmaking: theory and practice. Cootha Publishing House: Brisbane, 1981.

[22] D. Walter, G. Buxbaum, and W. Laqua. The Mechanism of the Thermal Transformation From Goethite To Hematite. **Journal of Thermal Analysis and Calorimetry** 63 (2001), pp. 733–748.

[23] L. Diamandescu, D. Mihàilà-Tàràbàşanu, and M. Feder. On the solid phase transformation goethite → hematite. **Materials Letters** 17 (1993), pp. 309–311. DOI: 10.1016/0167-577X(93)90019-T.

[24] P. Leerhoff, J. C. Brouwer, A. M. Armaki, C. Zeilstra, K. Meijer, J. van der Stel, S. T. Abrahami, N. Dogan, and Y. Yang. Characterisation of Varying Iron Ores and Their Thermal Decomposition Kinetics Under HIsarna Ironmaking Conditions. **Metals** 14, 1271 (2024). DOI: 10.3390/met14111271.

[25] V. Strezov, T. J. Evans, V. Zymla, and L. Strezov. Structural deterioration of iron ore particles during thermal processing. **International Journal of Mineral Processing** 100 (2011), pp. 27–32. DOI: 10.1016/j.minpro.2011.04.005.

[26] J. Hage, C. Zeilstra, J. van Boggelen, K. Meijer, J. van der Stel, and T. Peeters. HIsarna: Benefits of an Innovative Smelting-Reduction Ironmaking Technology. AISTech 2021, 2021, pp. 1388–1399. DOI: 10.33313/382/143.

[27] P. C. Beuria, S. K. Biswal, B. K. Mishra, and G. G. Roy. Study on kinetics of thermal decomposition of low LOI goethetic hematite iron ore. **International Journal of Mining Science and Technology** 27 (2017), pp. 1031–1036. DOI: 10.1016/j.ijmst.2017.06.018.

[28] A. Ammasi. Effect of Heating Rate on Decomposition Temperature of Goethite Ore. **Transactions of the Indian Institute of Metals** 73 (2020), pp. 93–98. DOI: 10.1007/s12666-019-01806-w.

[29] Z.-y. Chen, Y.-x. Qu, C. Zeilstra, J. van der Stel, J. Sietsma, and Y.-x. Yang. Prediction of density and volume variation of hematite ore particles during in-flight melting and reduction. **Journal of Iron and Steel Research International** 26 (2019), pp. 1285–1294. DOI: 10.1007/s42243-019-00265-3.

[30] Y. Qu. Experimental Study of the Melting and Reduction Behaviour of Ore Used in the HIsarna Process. PhD thesis. Technische Universiteit Delft, 2013.

[31] T. Ariyama, S. Isozaki, S. Matsubara, H. Kawata, and I. Kobayashi. Fluidization and Degradation Characteristics of Iron Ore Fines in Prereduction Fluidized Bed. **ISIJ International** 33 (1993), pp. 1220–1227. DOI: 10.2355/isijinternational.33.1220.

[32] Mindat.org and H. I. of Mineralogy. Hematite: Mineral information, data and localities. URL: https://www.mindat.org/min-1856.html.

[33] Mindat.org and H. I. of Mineralogy. Goethite : Mineral information, data and localities. URL: https://www.mindat.org/min-1719.html.

[34] CRCT - ThermFact Inc. and GTT-Technologies. FactSage, Equilib Module. 2015. URL: https://factsage.com/.

[35] CRCT -ThermFact Inc. and GTT-Technologies. FactPS Database. 2015. URL: https://factsage.com/.

[36] A. J. Schwartz, M. Kumar, B. L. Adams, and D. P. Field, eds. Electron Backscatter Diffraction in Materials Science. Springer US, 2009. ISBN: 978-0-387-88135-5. DOI: 10.1007/978-0-387-88136-2.

[37] C. F. Dickinson and G. R. Heal. Solid–liquid diffusion controlled rate equations. **Thermochimica Acta** 340-341 (1999), pp. 89–103. DOI: 10.1016/S0040-6031(99)00256-7.

[38] J. R. Frade and M. Cable. Reexamination of the Basic Theoretical Model for the Kinetics of Solid–State Reactions. **Journal of the American Ceramic Society** 75 (1992), pp. 1949–1957. DOI: 10.1111/j.1151-2916.1992.tb07222.x.

[39] E. A. Giess. Equations and Tables for Analyzing Solid-state Reaction Kinetics. **Journal of the American Ceramic Society** 46 (1963), pp. 374–376. DOI: 10.1111/j.1151-2916.1963.tb11754.x.

[40] A.-M. O. Mohamed, M. E. Gamal, S. M. Hameedi, and E. K. Paleologos. Carbonation reaction kinetics. Elsevier, 2023, pp. 149–162. DOI: 10.1016/b978-0-12-823418-1.00017-2.

[41] A. Lahiri, E. J. Kumari, and A. Jha. Kinetic Studies on the Soda-Ash Roasting of Titaniferous Ores for the Extraction of TiO2. The Minerals, Metals & Materials Society (TMS), 2006, pp. 115–123.

[42] J. L. Provis. On the use of the Jander equation in cement hydration modelling. **RILEM Technical Letters** 1 (2016), pp. 62–66. DOI: 10.21809/rilemtechlett.2016.13.

[43] L. Fedunik-Hofman, A. Bayon, and S. W. Donne. Kinetics of Solid-Gas Reactions and Their Application to Carbonate Looping Systems. **Energies** 12, 2981 (2019). DOI: 10.3390/en12152981.

[44] H.-b. Zuo, C. Wang, J.-j. Dong, K.-x. Jiao, and R.-s. Xu. Reduction kinetics of iron oxide pellets with H_2 and CO mixtures. **International Journal of Minerals, Metallurgy, and Materials** 22 (2015), pp. 688–696. DOI: 10.1007/s12613-015-1123-x.

[45] D. S. Newsome. The Water-Gas Shift Reaction. **Catalysis Reviews** 21 (1980), pp. 275–318. DOI: 10.1080/03602458008067535.

[46] J. Li, P. Wang, L. Zhou, and M. Cheng. The Reduction of Wustite with High Oxygen Enrichment and High Injection of Hydrogenous Fuel. **ISIJ International** 47 (2007), pp. 1097–1101. DOI: 10.2355/isijinternational.47.1097.

[47] M. Bahgat, K. S. A. Halim, H. A. El-Kelesh, and M. I. Nasr. Fundamental Study of Water-Gas Shift Reaction in Ironmaking Process. 2012.

[48] A. Abdelrahim, M. Iljana, M. Omran, T. Vuolio, H. Bartusch, and T. Fabritius. Influence of H_2–H_2O Content on the Reduction of Acid Iron Ore Pellets in a CO–CO_2–N_2 Reducing Atmosphere. **ISIJ International** 60 (2020), pp. 2206–2217. DOI: 10.2355/isijinternational.ISIJINT-2019-734.

5

IMPACT OF H_2-ENRICHMENT AND ORE MINERALOGY ON THE REDUCTION OF VARYING IRON ORES IN SUSPENSION SMELTING IRONMAKING

Due to the high temperatures present in the HIsarna® process ($\approx 1773K$), the two reaction mechanisms thermal decomposition and gas reduction occur simultaneously during the pre-reduction of the injected iron ore fines. The objective of this study is to investigate the impact of H_2-enrichment in HIsarna reducing gas atmospheres on the pre-reduction of iron ores. Therefore, several iron ores, named OreA, OreB and OreC, with increasing amounts of goethite, were reduced by gas mixtures of $H_2 - CO - CO_2 - Ar$ in a thermogravimetric analyser (TGA). A first approach studied the gas reduction as isolated process in isothermal conditions, whereas the second, non-isothermal approach, investigated thermal decomposition and gas reduction occurring simultaneously. In isothermal conditions the increase of H_2 in the atmosphere leads to an increase in conversion to wüstite, and also to an increase in reaction speed. At 7.5 % H_2 in the atmosphere, the reaction saturates after 502–794 s, at 22.5 % H_2 after 375–583 s and at 37.5 % H_2 after 206–297 s, depending on the temperature. The reaction is controlled by the diffusion of the reducing gas through the developing product layer and the calculated activation energy is 77.60, 69.12 and 79.91 kJ/mol for H_2-contents of 7.5 %, 22.5 % and 37.5 %, respectively. In non-isothermal conditions, the influence of ore mineralogy is more significant compared to the H_2 increase in the atmosphere. An increase in total conversion is observed with an increase in goethite content in the ores.

This chapter has been published in P Leerhoff et al. "Impact of H_2-enrichment and ore mineralogy on the reduction of varying iron ores in suspension smelting ironmaking". In: Powder Technology (**2026**), 468 [1].

5.1. INTRODUCTION

The iron- and steelmaking industry is responsible for 7–9 % of the global anthropogenic produced CO_2-emissions [2]. A radical change in production methods is necessary to reduce emissions and lead the steel industry into a more sustainable future. The biggest potential impact will be the substitution of the blast furnace, which is contributing to 71 % of the CO_2-emissions, globally arising from iron and steel production [3].HIsarna® was developed by Tata Steel in IJmuiden as an alternative ironmaking process to the blast furnace [4]. HIsarna can be categorized as a smelting reduction process. Smelting reduction describes the combination of iron ore reduction and subsequent melting to liquid (pig) iron in a single reactor, without coke usage [5].The most commercially established forms of smelting reduction are the COREX and FINEX processes, with COREX operating with a shaft furnace and FINEX with a multi-stage fluidized bed as the pre-reduction stage, before the material is melted for complete reduction [5]. However, further alternatives are under investigation.

A significant advantage of HIsarna compared to the blast furnace is that HIsarna accepts various raw materials as input material. In contrast to the blast furnace, HIsarna operates with un-coked coal and un-agglomerated iron ore fines, thereby combining the three process steps of ore agglomeration, coking, and ironmaking into a single process step [6]. The pilot scale of HIsarna already indicates that CO_2-emissions can be reduced by up to 20 % compared to the classic blast furnace process, and by at least 80 % in combination with carbon capture and storage (CCS) technology [5, 7]. In HIsarna, the pre-reduction occurs in an upper cyclone converter before final reduction takes place in a lower molten bath, similar to the HIsmelt technology [8]. Initial reactions and pre-reduction occur very fast in the upper section of HIsarna. The ores are injected horizontally from the top-section of the furnace, where they immediately come into contact with the hot process gas arising from the lower section, which is a mixture of CO, CO_2, H_2, H_2O and N_2 [6]. The oxidation state and, therefore, the reduction capability of the off-gas arising from the smelting vessel is described by the post-combustion ratio (PCR) (Eq. (5.1)) [6].

$$\mathrm{PCR} = \frac{\%H_2O + \%CO_2}{\%H_2O + \%CO_2 + \%H_2 + \%CO} \times 100\% \tag{5.1}$$

The PCR is the lowest when the reducing gas reaches the pre-reduction section of the furnace. Following it reacts with the injected ores over the height of the furnace, until it is almost completely post-combusted at the top. The PCR value of the reducing gas entering the pre-reduction section of HIsarna is approximately 50-60 % while this value reaches 98 % when the gases are leaving the process [8, 9]. This change is due to the decrease in concentration of H_2 and CO as iron ore particles are reduced and the partial combustion with oxygen. The behaviour of the PCR in the pre-reduction section of HIsarna is presented in Figure 5.1. In this section of HIsarna, two main reaction mechanisms occur simultaneously. The first mechanism is the thermal decomposition of the injected ore particles, and a second is the gas-solid reduction with the reducing gases. From a thermodynamic perspective, the reduction of iron ore through thermal decomposition and gas reduction follows the same fundamental process that achieves the removal of oxygen from the ore.

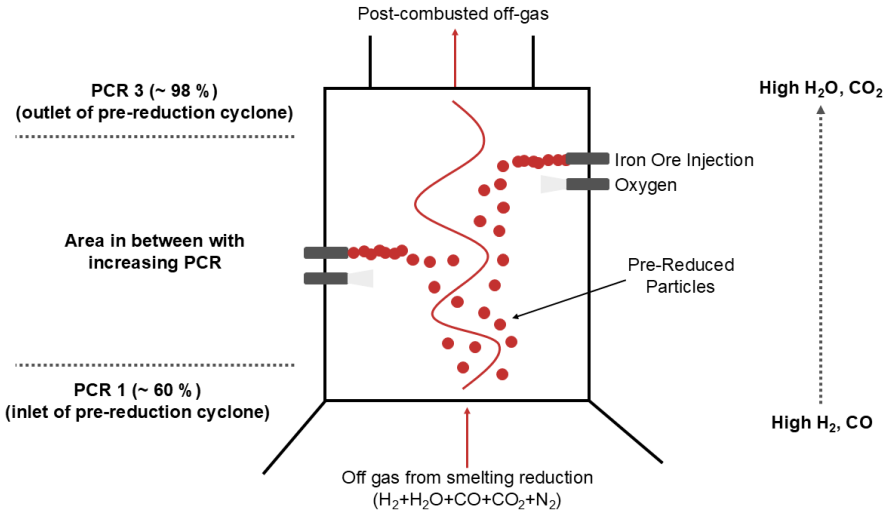


Figure 5.1: Schematic of HIsarna pre-reduction section, adapted from [9].

HIsarna has the further advantage that it can accept untreated, lower-grade ores as input ores and is not limited to hematite and magnetite, which are categorized as high-grade ores (>65 % Fe [10].Ores of interest for use in HIsarna are goethite ores, which are abundantly available in India [11]. Due to the lower iron content in the goethite phase (FeOOH) compared to the hematite phase (Fe_2O_3), an increase in goethite content in the ore would further decrease the grade of the ore. The influence of thermal decomposition on the reduction of various ores in HIsarna ironmaking has been studied in a previous publication [12], with a special focus on the impact of goethite content in the ores, and was based on preceding studies from Qu et al. [13] and Chen et al. [14]. The previous work related to goethite ores includes the kinetic analysis of goethite thermal decomposition as well as hematite thermal decomposition and investigates the influence of goethite content and further ore mineralogy on the overall reduction.

To complete this preceding research, the current study focuses on the mechanism of gas reduction and its influence on the reduction kinetics in smelting reduction processes, especially under HIsarna ironmaking conditions. Currently, HIsarna exhibits pre-reduction degrees of 20–25 % in its upper section [8]. Due to its nature, HIsarna is limited to the use of $CO - CO_2 - H_2 - H_2O$ gas mixtures as reducing gases. However, it is generally known that hydrogen enhances the reaction kinetics of iron ore reduction [15]. Therefore, this study aims to investigate the influence of increasing hydrogen levels in HIsarna reducing gas mixtures on the reduction degree and kinetics.

The reduction of iron oxides in isothermal conditions has been intensely studied in literature [16–23]. Zuo et al. [18] studied the reduction of hematite pellets in several H2-CO mixtures at 1073, 1173 and 1273 K and found a positive effect of hydrogen enrichment in the atmosphere on the speed of the reduction, explained by the enhanced diffusivity of the reducing gas through the sample. Therefore, it is critical to better understand the

impact of hydrogen on the mechanisms of gas reduction. Sohn et al. [17] studied the reduction of hematite pellets to metallic iron with hydrogen in a temperature range of 973 to 1173 K and found the reaction to be initially controlled by a topo-chemical reaction, forming in initial iron layer, before the rate-limiting mechanism shifts to pore diffusion in the later stages.

Next to the reaction mechanism, determining the activation energy is crucial to evaluate the influence of hydrogen enrichment on the reduction. Even though many studies have been carried out, insights vary considering the influence of H_2 and CO levels in the reducing gas on the activation energy. Zhang et al. [16] studied the conversion of New Zealand ironsand pellets and Sohn et al. [17] of metal doped hematite pellets to metallic iron with pure hydrogen. Zhang et al. calculated an activation energy of 31.3 kJ/mol, whereas Sohn et al. calculated activation energies between 15 and 29 kJ/mol depending on the reduction step. Also, Moon et al. [19] studied the reaction kinetics of varying H_2-CO reducing gas mixtures and determined activation energies between 19.8 and 42.1 kJ/mol, where the values decreased with an increase in CO content. Piotrowski et al. [24] tried to find differences between the influence of CO and H_2 as reducing gases by testing mixtures of 90 % N_2 with either 10 % H_2, CO or H_2 + CO for the conversion of hematite powder into wüstite. Even though the three mixtures have the same ratio of reducing gases, the arising activation energy differs strongly. The mixture containing only CO as reducing gas showed the highest activation energy (122.52 kJ/mol), followed by the mixture containing CO and H_2 (93.72 kJ/mol) and the mixture containing only H_2 showed by far the lowest activation energy (28.08 kJ/mol).

Considering the kinetic data, multiple parameters can influence the reduction mechanism and resulting activation energy: material properties, reducing gas atmosphere, the considered reduction step and many more [25], underlining the need for continuous research. Most studies, however, are focusing on the adaptation of hydrogen in temperature ranges which are more in relation to the direct-reduced iron (DRI) production conditions, which typically operate below 1273 K [5] and are therefore focusing on significantly lower temperatures then the gas-solid reduction in the HIsarna pre-reduction section ($T \approx$ 1773K [9]). The thermal decomposition of goethite and hematite as well as the reduction of hematite with reducing gases, containing H_2 and CO in non-isothermal conditions have also been significantly studied in literature [12, 14, 26–33]. However, these studies either focused on a single iron-bearing phase being reduced, or, when examining samples containing hematite and goethite, inert atmospheres were applied to only observe the thermal decomposition. This leaves the question open on how a mixed system of goethite and hematite would reduce in non-isothermal conditions with the two mechanisms thermal decomposition and gas reduction happening simultaneously. The influence of goethite content and further mineralogy on the reduction behaviour in hydrogen enriched HIsarna atmospheres requires further study, since it is important to understand the influence of a complex ore mineralogy on the overall reduction behaviour, particularly at temperatures greater than 1273 K.

To summarize, the objective of this experimental study is to gain a complete overview of the reduction behaviour and kinetics of the ores in the utilized gas atmospheres under HIsarna process operating conditions. Since the thermal decomposition behaviour of the ores has been discussed previously in [12], this study is meant to provide insight into

gas reduction as an isolated (isothermal approach) and co-occurring (non-isothermal approach) process with thermal decomposition. Focus is placed on the influence of ore mineralogy, hydrogen enrichment in the reducing gas atmosphere, and a potential decrease in PCR on the reducibility and reduction mechanisms of the varying iron ores.

5.2. METHOD

5.2.1. MATERIALS

The three iron-bearing ores, named OreA, OreB and OreC, with a particle size <63 μm were provided by Tata Steel. To gain insight into the differences in chemical composition and mineralogy between the ores, X-ray diffraction (XRD), X-ray fluorescence (XRF) and loss of ignition (LOI) analyses were conducted. XRD analysis was carried out with a Bruker D8 Advance diffractometer Bragg-Brentano geometry and Lynxeye position sensitive detector (Bruker Germany). The main mineralogical phases, according to XRD, for OreA are hematite (Fe_2O_3), quartz (SiO_2) and dolomite ($CaMg(CO_3)_2$, with small amounts of magnetite (Fe_3O_4). The main difference of OreB and OreC compared to OreA is the presence of the goethite phase. For OreB, the main phases, in addition to hematite and goethite, are quartz and kaolinite ($Al_2Si_2O_5(OH)_4$). The XRD of OreC measured only quartz as non-iron-bearing phase, next to hematite and goethite. Due to the complex chemical composition of the ores, the XRD signals show many smaller peaks, indicating additional gangue materials that cannot be accurately identified. The detailed XRD results are displayed in Figure C.1 in the appendix C.

The elemental composition of the ores was obtained by XRF (Panalytical AXIOS XRF, Netherlands) and LOI analysis (dissolution in nitric acid and TGA (LECO, Germany) and is summarized in Table 5.1. All three ores used in this study can be categorized as low-grade ores (< 62 % Fe [10]), with OreB showing the highest amounts of total iron (61.60 wt.-%) and OreC the lowest (56.80 wt.-%). In alignment with the XRD analysis, SiO_2 and Al_2O_3, are found to be the main gangue components in all three ores. OreB contains the highest amounts of Al_2O_3, while OreC contains the highest SiO_2 content. In contrast to OreB and OreC, OreA contains larger amounts of CaO and MgO due to the presence of a dolomite phase. The crystal water present in OreB and OreC indicate the goethite phase, which is absent in OreA. Considering the difference in crystal water between OreB (2.19 wt.-%) and OreC (6.05 wt.-%), the amount of goethite in OreC is expected to be substantially higher.

A deeper analysis of the input materials can be found in the preceding study [12], where differences in morphology, phase and impurity distribution and general mineralogy of the materials are explained in detail.

5.2.2. EXPERIMENTAL APPROACH

To obtain insights into the topo-chemical reduction behaviour of the varying iron ores and the reaction kinetics under non-isothermal and isothermal conditions, high temperature experiments were carried out under three different reduction conditions. The operating parameters are detailed in Table 5.2.In order to mimic the gas composition of HIsarna, a main PCR of 60 % was chosen. A total flow rate of 200 ml/min was applied. Of that 200 ml/min, 50 ml/min was always argon, necessary as a shielding gas for the thermocouples. The remaining 150 ml/min reflects the reducing gas composition. A decrease

Table 5.1: Chemical composition of OreA, OreB, and OreC, determined by XRF and LOI after normalization.

		OreA	OreB	OreC
	Fraction [μm]	<63	<63	<63
Compound	Fe_2O_3	85.93	88.07	81.21
[wt.-%]	total-Fe	60.10	61.60	56.80
	SiO_2	5.18	4.96	6.84
	Al_2O_3	2.24	3.81	3.52
	MgO	0.71	0.04	0.14
	CaO	1.99	0.05	0.11
	TiO_2	1.04	0.33	0.18
	MnO	1.20	0.03	1.07
	CO_2 (carbonate)	1.52	0.21	0.65
	H_2O (crystal)	–	2.19	6.05
	Rest	0.37	0.25	0.26

in PCR value would provide the option of higher hydrogen contents in the reducing gas. Two different atmospheres (A7.5H_2 A22.5H_2) were selected to evaluate the influence of hydrogen enrichment in an atmosphere with a PCR of 60 % on the reduction of the varying ores. To evaluate the influence of a lower PCR, a third atmosphere based on a PCR = 40 % (A37.5H_2) with the same total flow rate was tested. The experiments were conducted in a symmetrical thermogravimetric analyser (TGA, Setaram TAG 16/18, Caluire, France). Alsint crucibles with an inner diameter of 10 mm, a height of 20 mm, and a wall thickness of 2 mm were used as sample holders. A material amount of 300 mg was used as input.

In the non-isothermal approach, the ore particles were gradually heated in the reducing gas atmosphere at a heating rate of 5 K/min until a temperature of 1773 K was reached. After 1773 K was reached, a holding time of 2 h was applied to observe the behaviour of the reducing gas at elevated temperatures and to achieve the reduction limit. In the isothermal approach, the ores were gradually heated in an argon atmosphere at a heating rate of 5 K/min until a set temperature of 1673 K, 1723 K or 1773 K was reached. After the set temperature was reached, the material was held isothermally at that temperature for 2 h under an argon atmosphere to reach the limits of thermal decomposition. After 2 h, reducing gases were introduced for 1 h to observe the reduction kinetics under isothermal conditions. This approach enables the observation of gas reduction as an isolated phenomenon, considering that the thermal decomposition process had been completed earlier. The experiments under isothermal conditions were only carried out on OreB. In both tests, the material was cooled to room temperature in the system under an argon atmosphere at a controlled cooling rate of 5 K/min. The mass loss was measured as the primary output, either over increasing temperature at a constant heating rate (non-isothermal conditions) or over increasing time at a constant temperature (isothermal conditions), to analyse the reduction kinetics of the process.

Table 5.2: Experimental conditions in TGA, Setaram TAG 16/18.

Experimental Condition	Operating Parameter
Ore isothermal conditions	B
Ore non-isothermal conditions	A, B, C
Holding time non-isothermal conditions (h)	2
Holding time isothermal conditions (h)	2 + 1
Heating rate (K/min)	5
Particle size (µm)	< 63
Temperature (K)	298–1773
Flow rate	200 ml/min
Reducing atmosphere (vol-%)	A7.5H_2 (PCR = 60%): 7.5%H_2/22.5%CO/45%CO_2/25%Ar A22.5H_2 (PCR = 60%): 22.5%H_2/7.5%CO/45%CO_2/25%Ar A37.5H_2 (PCR = 40%): 37.5%H_2/7.5%CO/30%CO_2/25%Ar

5.3. RESULTS AND DISCUSSION

5.3.1. ISOTHERMAL REDUCTION

Figure 5.2 depicts the general mass loss of the isothermal experiments for OreB. The red line in the figure marks the start of the reducing gas injection while the green line shows the temperature profile over time. In general, six distinct stages can be observed. The first four stages are all part of the thermal decomposition of the ore, occurring before the reducing gas is injected. These stages were identified in our previous publication [12]. The first two stages were assigned to goethite decomposition, while stages three and four were assigned to the thermal decomposition of hematite. In this study, stages five and six are of interest, since these depict the reduction of the decomposed material with the defined reducing gas mixture. A sharp mass loss is observed directly after the injection of the reducing gas (V). The mass losses achieved in this stage are 3.8 %, 4.1 % and 4.5 % at 1673 K, 3.6 %, 3.8 % and 4.5 % at 1723 K and 3.2 %, 3.5 % and 4.1 % at 1773 K, for A7.5H_2, A22.5H_2 and A37.5H_2, respectively. At all temperatures, the mass loss increases with increasing hydrogen content in the atmosphere. The mass loss in stage five decreases with increasing temperature due to the higher mass loss already achieved through thermal decomposition at higher temperatures. Following this initial decrease, the mass loss remains constant for a period. At later stages of the isotherm, an increase in mass is observed. This phenomenon is related to pressure changes in the system caused by the water-gas shift reaction taking place. The reactions occurring and their influence on the system will be discussed in more detail in the section 5.3.4..

5.3.2. ISOTHERMAL REDUCTION KINETICS

The essential characteristic parameter for the kinetic models used in this study is the conversion factor α (Eq. (5.2)).

$$\alpha = \frac{m_0 - m_t}{m_0 - m_a} \tag{5.2}$$

Where m_0 is the mass of the initial sample (mg), m_t is the mass of the sample at time t (mg) and m_a is the mass of the sample after complete conversion (mg). Due to thermodynamic and kinetic limitations, the formation of metallic iron is not expected under the studied conditions. Therefore, wüstite (FeO) is considered the final reduction

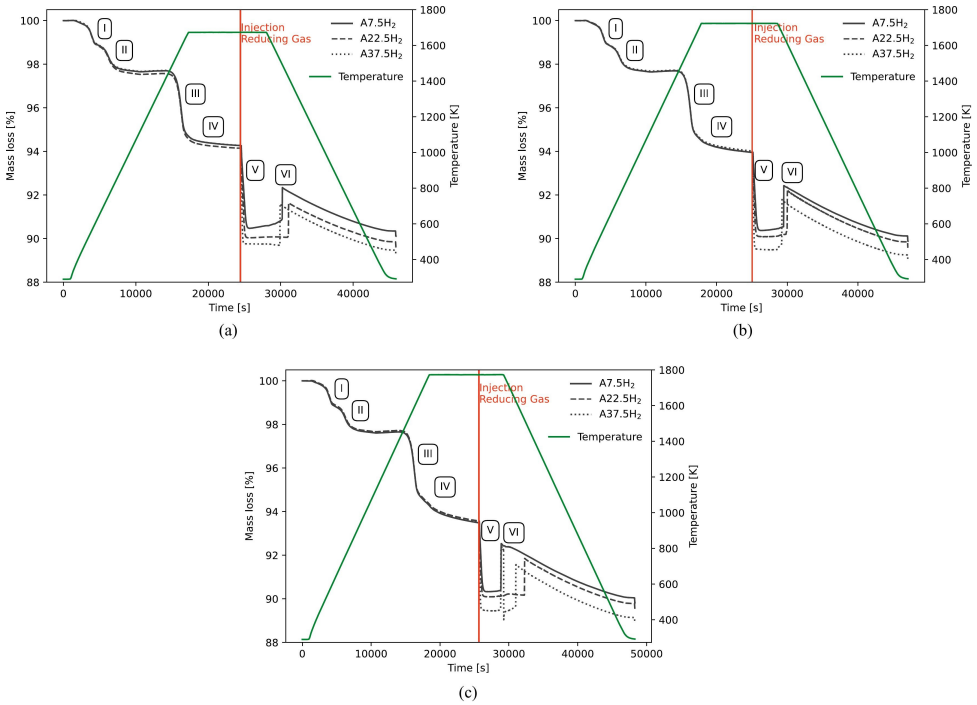


Figure 5.2: Mass loss over time with respect to reduction atmosphere for isothermal TGA experiments of OreB at (a) T=1673 K, (b) T=1723 K and (c) T=1773 K.

product, meaning that a conversion factor of 1 corresponds to the complete conversion of hematite to wüstite. The conversion degree Eq. (5.2) is calculated based on the conversion of hematite (Fe_2O_3) to wüstite (FeO) over the whole reaction range. After thermal decomposition (stages I-IV), it is expected that mostly magnetite is present as the iron bearing phase. However, to avoid assuming that only magnetite is present before the gas reduction, the conversion factor is defined over the entire reaction range, including thermal decomposition, as presented in Figure 5.3. The images show the calculated conversion factors for OreB at three temperatures and the respective atmospheres. The conversion of hematite to magnetite by thermal decomposition initiates around 1419 K, which also depicts the start of the figure. All reactions occurring before that temperature do not contribute to the calculated conversion degree.

At all temperatures, similar trends are seen for all three atmospheres after the reducing gases are introduced to the system (as indicated by the red line in Figure 5.3). Considering ($A7.5H_2$ and ($A22.5H_2$, an increase in H_2 content at the same PCR leads to a higher total conversion. At 1673 K the conversion degree increases from approximately 73.5 to 77 %, at 1723 K from 74.7 to 78 % and at 1773 K from 74.8 to 78 %. This further shows that there is no strong influence of the holding temperature on the total conversion. A decrease in PCR, and therefore an increase in reducing gas content, leads to an even higher total conversion during the gas reduction phase. The total conversion reached in ($A37.5H_2$ at 1673 K is

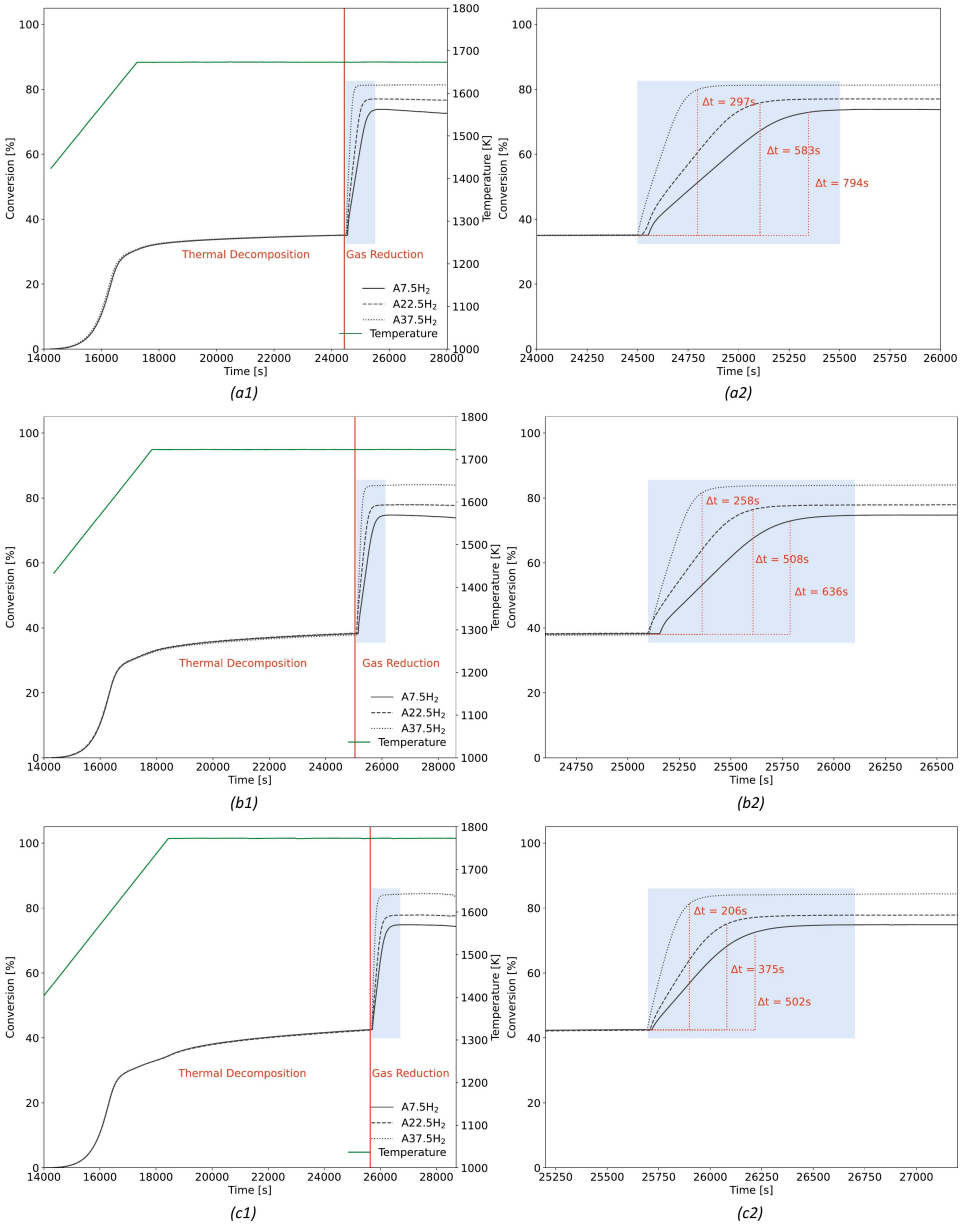


Figure 5.3: Conversion factor for thermal decomposition and gas reduction of OreB at (a1) T = 1673 K, (a2) 1673 K zoomed-in, (b1) T = 1723 K, (b2) 1723 K zoomed-in and (c1) T = 1773 K, (c2) 1773 K zoomed-in.

around 81.3 %, at 1723 K 84 % and at 1773 K 84 %. As comparison, the conversion factors at equilibrium for each atmosphere and temperature were calculated using FactSage 7.0 [34] (FactPS database) [35] and were determined to vary between 96 % and 103 %, depending on atmosphere and temperature. It can be noted that for all experimental conditions, complete conversion is never reached, indicating kinetic limitations for the gas reduction.

Figure 5.3 also highlights the strong influence of the atmosphere on the steepness of conversion during the gas reduction. To better visualize this influence, Figure 5.3 includes a zoomed-in view of the main area of gas reduction until the experimental equilibrium is reached ((a2), (b2), (c2)). Overall, the influence of hydrogen content is much stronger compared to the temperature influence. Even though higher temperatures always lead to faster reduction in the respective atmosphere, it cannot always compensate for the influence of increasing hydrogen levels. The increase in hydrogen level from (A7.5H_2 to (A22.5H_2 leads to a decrease in reduction time from 502–794 s to 375–583 s, depending on the temperature. A further change to lower PCR and even higher hydrogen levels in (A37.5H_2 decreases the reduction times further to 206–297 s.

In order to get a more detailed overview of the reduction achieved in the separate thermal decomposition and gas reduction stages, the calculated conversion degrees (Fe_2O_3 → FeO) for each stage are presented in Table 5.3. A small variation in the conversion after thermal decomposition (α_{TD}) is seen based on the set temperature. With an increase in temperature, slightly higher conversion, with a minimum of 35.2 % at 1673 K and a maximum of 42.6 % at 1773 K, is achieved during thermal decomposition. Further, it is observable that the influence of the atmosphere on the final conversion ((α_{Total}) is stronger than the influence of the temperature. For all temperatures, a final conversion of around 73 % is reached for A7.5H_2, around 75–76 % for A22.5H_2 and around 80–82 % forA37.5H_2, after 1 h reduction. Considering only the conversion achieved during gas reduction, ((α_{GR}) increases from 37.3 % to 44.6 % at 1673 K, from 34.7 % to 43.8 % at 1723 K, and from 29.9 % to 38.7 % at 1773 K with increasing H_2 content in the reducing gas. The decrease in α_{GR} with increasing temperature is explained by the higher degree of reduction already achieved during thermal decomposition at higher temperatures.

Table 5.3: Conversion degrees after thermal decomposition (TD) and after gas reduction (GR) of OreB.

	1673 K			**1723 K**			**1773 K**		
	A7.5H_2	A22.5H_2	A37.5H_2	A7.5H_2	A22.5H_2	A37.5H_2	A7.5H_2	A22.5H_2	A37.5H_2
α_{TD} **[%]**	35.6	35.4	35.2	38.2	39.0	37.8	42.6	42.4	42.6
α_{Total} **[%]**	72.9	75.8	79.8	72.9	76.4	81.6	72.5	75.1	81.3
α_{GR} **[%]**	37.3	40.4	44.6	34.7	37.4	43.8	29.9	32.7	38.7

In the next step, the reaction mechanism as well as the kinetic parameters of the isothermal experiments were determined. A common model used to explain reaction kinetics in ironmaking is the (un-)reacted shrinking core model (USCM) [36]. Based on the shrinking core model, the reaction first takes place at the outer skin of a particle, creating a stable product layer. The reaction front then moves inwards, shrinking the unreacted core of the particle [36].Normally, the shrinking core model assumes spherical particles. However, Luo and Wu [37] found that the shrinking core model is still applicable for an aspect ratio of $0 < h/2r < 1$, where h is the height and r the radius of the sample.

In this study, the whole sample in the crucible was considered and the aspect ratio of the studied samples is approximately 0.12. The authors assumed that the shrinking core model is applicable in this study. The reacting and shrinking of the core occur step-wise [36]. The reaction steps used to determine the mechanisms of the reductions in this study are the internal pore diffusion, chemical reaction, and the mixed mechanism of the two. The reaction rate constants can be derived based on the proposed reaction mechanisms using the following mathematical formulations [38–40]:

Internal Diffusion Control:

$$1-\tfrac{2}{3}\alpha-(1-\alpha)^{\frac{2}{3}}=kt=\frac{6D_e(C_0-C_e)}{\rho_0 r_0^2}\,t \tag{5.3}$$

Interface Chemical Reaction Control:

$$1-(1-\alpha)^{\frac{1}{3}}=kt=\frac{k(1+K_e)(C_0-C_e)}{K_e r_0 \rho_0}\,t \tag{5.4}$$

Mixed Control:

$$\frac{t}{1-(1-\alpha)^{1/3}}=\frac{\rho_0 r_0^2}{6D_e(C_0-C_e)}\left[1+(1-\alpha)^{1/3}-2(1-\alpha)^{2/3}\right]+\frac{\rho_0 r_0 K_e}{k(1+K_e)(C_0-C_e)} \tag{5.5}$$

Where α is the conversion factor of hematite to wüstite (), k is the reaction rate constant (s^1), t is the time (s), D_e is the diffusion coefficient of the reducing gas into the product layer (m^2/s), C_0 is the reducing gas concentration at the surface (mol/m^3) and C_e in equilibrium (mol/m^3), ρ_0 is the initial oxygen density (mol/m^3), r_0 is the initial radius (m) and K_e is the equilibrium constant ().

By plotting $1-(1-\alpha)^{\frac{1}{3}}$ vs. t (Chemical Reaction), $1-\frac{2}{3}\alpha-(1-\alpha)^{\frac{2}{3}}$ vs. t (Diffusion) and $\frac{t}{1-(1-\alpha)^{1/3}}$ vs. $1+(1-\alpha)^{1/3}-2(1-\alpha)^{2/3}$ (Mixed), the reaction mechanism can be determined based on the best fitting of the model. The reaction rate constant k can be obtained from the slope of the plot. The fitting results of the three mathematical models are presented in Table 5.4.

Table 5.4: Results of model fitting with shrinking core model.

Atmosphere	Temperature [K]	$\mathbf{R^2}$ (Mixed)	$\mathbf{R^2}$ (Chemical Reaction)	$\mathbf{R^2}$ (Diffusion)
$A7.5H_2$	1673	0.9246	0.9936	0.9940
	1723	0.9360	0.9957	0.9959
	1773	0.9416	0.9932	0.9965
$A22.5H_2$	1673	0.8939	0.9928	0.9957
	1723	0.9187	0.9925	0.9951
	1773	0.9315	0.9938	0.9975
$A37.5H_2$	1673	0.8892	0.9913	0.9931
	1723	0.9071	0.9952	0.9944
	1773	0.9146	0.9932	0.9963

It can be seen that the fitting of the mixed controlled model is the poorest, whereas the R^2 of the interface chemical reaction control and internal diffusion are all >0.99 and can therefore represent the experimental data very well. Even though the fitting is slightly better for the internal diffusion control, it is difficult to determine the best model relying only on the model fit, due to their close proximity. To further identify the reduction mechanism, SEM imaging combined with electron backscattering and EDS measurements was carried out. The imaging visualizes the distribution of phases and elements through the material. Therefore, a cross-section of the sample, solidified in the crucible from experiments with the three atmospheres A7.5H_2, A22.5H_2 and A37.5H_2, reduced at a temperature of 1773 K, was sanded and polished. The imaging of each sample cross-section in combination with the mapping of the EDS analysis is presented in Figure 5.4.

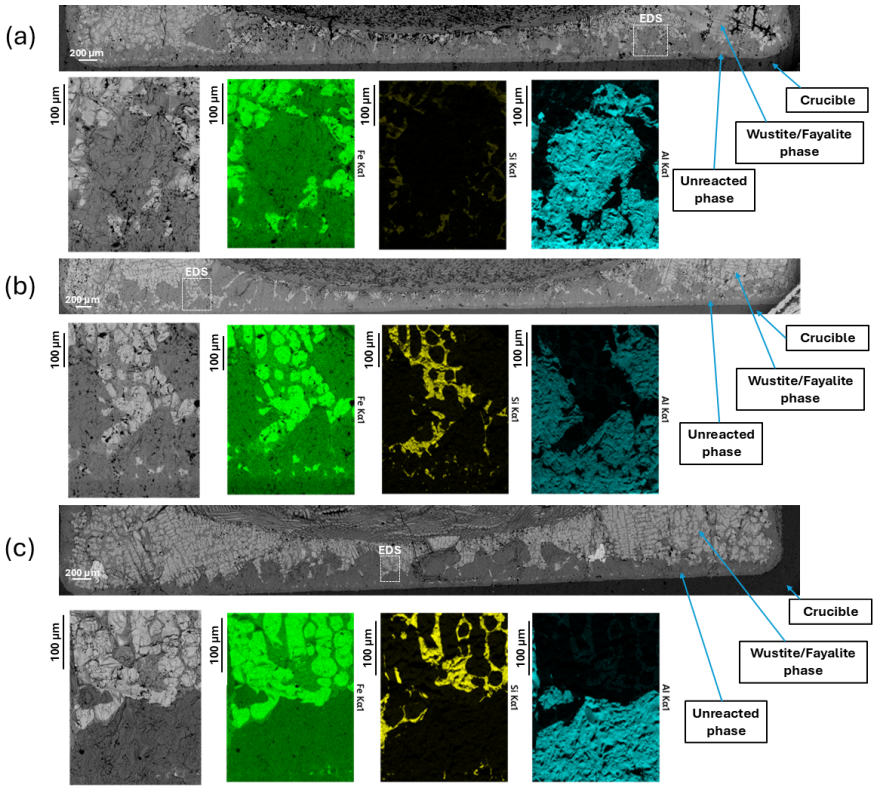


Figure 5.4: Results of SEM-EDS of a cross section of OreB sample under (a) A7.5H_2, (b) A22.5H_2 and (c) A37.5H_2 reducing atmospheres at 1773 K (Fe: green; Si: yellow; Al: blue).

The results of the backscattering measurement clearly illustrate the presence of different phases in the solidified sample. The area with brighter contrast is expected to be richer in wüstite, and the darker area in magnetite, due to the higher amount of iron in wüstite. The EDS measurements further confirm this statement. Comparing the brighter

color of the backscattering with the EDS results, higher iron content is measured in these areas. Furthermore, the distribution of silicon indicates that silicate mostly settles around areas of higher iron content. This indicates the formation of fayalite slag around areas of wüstite. Fayalite ($2FeO * SiO_2$) is a common slag-phase arising in the converter process of copper production based on the reaction of wüstite with silica (equation (Eq. (5.6))) [5].

$$2\,FeO(l) + SiO_2(s) = 2\,FeO \cdot SiO_2(l) \tag{5.6}$$

FactSage 7.0 [34, 35] calculations were carried out to evaluate the possible presence of the fayalite slag. Therefore, the final products of the thermal decomposition at the set-temperatures 1673, 1723 and 1773 K were calculated based on the chemical composition of OreB (Table 5.1). At the end of thermal decomposition, magnetite was the final iron-bearing phase and no fayalite slag was determined in the calculations. Next, the phases calculated at the end of thermal decomposition were used as input for the thermodynamic evaluation of the products arising during the isothermal gas reduction at the respective temperatures for $A7.5.5H_2$, $A22.5H_2$ and $A37.5H_2$. In these calculations three main phases were detected, which account for over 98 % of the total composition. For all three atmospheres and temperatures, approximately 73 % of the phase composition was wüstite, 18–19 % fayalite and around 7 % hercynite ($FeAl_2O_4$). The theoretical evaluation of fayalite presence supports the EDS findings of fayalite formation around the wüstite phase. The EDS images further indicate lower amounts of aluminum around the wüstite phase, which could potentially be the hercynite phase which is present in lower amounts based on the thermodynamic calculations. Other aluminum oxides are expected to stay unreacted during the reduction, probably even solid. The distribution of alumina shows that it settles at the bottom of the crucible, in the area of lower iron content. The imaging shows a strong reduction on the surface of the sample, forming a reduced product layer. The reduction further proceeds (un-uniformly) throughout the sample. This behaviour indicates that the reduction of the sample is not limited by the chemical reaction at the interface, but by the internal diffusion of the reducing gases. Based on these microscopical findings and the model fit, internal diffusion is assumed to be the rate-limiting mechanism. Sohn et.al [17] determined the reaction mechanism of hematite with hydrogen to be of mixed control, with the reaction rate to be initially governed by a topochemical reaction forming an initial iron layer (5–80 s), and following shifting to pore diffusion (119–671 s) after the product layer was formed. This second mechanism, which is responsible for most of the reduction time, is similar to the diffusion control found in this study. Considering the higher reaction temperatures in this study (1673 K – 1773 K) compared to Sohn et al. (973 K – 1173 K), it is possible that the initial formation of the product layer is occurring faster, making it difficult to distinguish between the two mechanisms, resulting in internal diffusion emerging as the overall rate defining mechanism. This is also underlined by the bad results of the model fitting for the mixed control in Table 5.4.

Based on this model choice, the reaction rate constant was calculated and is presented in Figure 5.5a. Considering the reaction rate constant, k, a coherent increase with hydrogen content and temperature is observable, indicating a more efficient diffusion process at higher H_2 levels. Overall, the chemical reaction is more sensitive to the temperature compared to physical mechanisms like diffusion [36]. Therefore, the impact of

the increasing H_2-levels in the atmosphere on the rate constant is much stronger than the influence of temperature, further supporting internal pore diffusion as the dominant mechanism compared to chemical reaction. The rate constants determined by Sohn et al. [17] are slightly higher compared to our study (lnk 6.2 to 5.2), which can be explained by the use of pure hydrogen increasing the reaction rate. A significant increase in reaction rate constant occurs, comparing A37.5H_2 to A7.5H_2 and A22.5H_2, which can be explained by the decrease in PCR and therefore a greater presence of reducing gases, facilitating the reduction process.

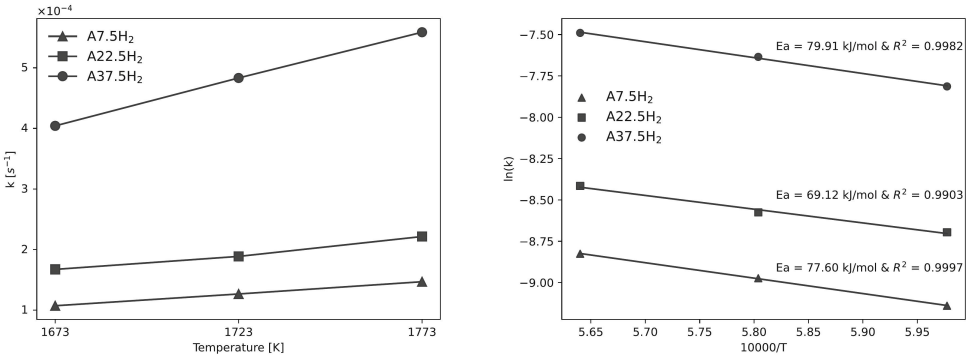


Figure 5.5: (a) Reaction rate constant based on diffusion as the rate-limiting step and (b) resulting Arrhenius fitting.

The general expression for the reaction rate of the thermal decomposition process is presented in equation (Eq. (5.7)). Applying the Arrhenius equation, the expression for the reaction rate constant is obtained through equation (Eq. (5.8)).

$$\frac{d\alpha}{dt} = kf(\alpha) \tag{5.7}$$

$$k(T) = A\exp\left(-\frac{E_a}{RT}\right) \tag{5.8}$$

To obtain the activation energies for the varying atmospheres, Arrhenius fitting (equation (Eq. (5.8))) was carried out and the results are presented in Figure 5.5b. In this study, the important influence on the activation energy under isothermal conditions is the increase in hydrogen content in the reducing gas. Considering A7.5H_2 and A22.5H_2, an increase in hydrogen content in the reducing gas leads to a decrease in activation energy from 77.60 to 69.12 kJ/mol. This is in alignment with the assumed diffusion model, considering the better diffusion ability of hydrogen compared to carbon monoxide, lowering the activation energy of A22.5H_2 compared to A7.5H_2 due to the shift from CO to H_2 as a dominant reducing gas. Bahgat et al. [41] observed the reduction of magnetite single crystals with hydrogen in a TGA at 1173–1373 K. Considering the reduction step of Fe_3O_4 to Fe, they concluded a solid state diffusion as the reduction mechanism, explained by wüstite phases entrapped in dense metallic iron, and calculated an activation energy of

99.2 kJ/mol This value is significantly higher compared to our study. The lower activation energies in our study can be explained by the higher temperatures applied and the lower achieved conversion degree. Based on the decrease in activation energy between A7.5H_2 and A22.5H_2, a logical conclusion would be a further decrease in activation energy for A37.5H_2, due to the higher amounts of hydrogen in the atmosphere. However, in this case, the activation energy increases to 79.91 kJ/mol, indicating kinetic limitations in this reaction. An explanation for this could be the higher achieved conversion in A37.5H_2. Despite the presence of more hydrogen in the atmosphere leading to a faster reaction, increasing the reaction rate constant, the push to a higher conversion degree could require more energy and therefore increases the overall activation energy for the reaction. Even though Hammam et al. [29] determined a decrease in activation energy with increasing conversion during hematite reduction by hydrogen, Chen et al. [42] found the activation energy to increase with increasing conversion in a gas mixture of CO – N_2, where the highest activation energy was found to be 47.14 kJ/mol for a conversion range of 20 to 90 %.

Considering the influence of H2 and CO levels in the reducing gas on the activation energy, insights vary between studies. Zhang et al. [16] determined an activation energy of 31.3 kJ/mol and Sohn et.al [17] of 17.52–20.01 kJ/mol at a conversion degree of 20 % and 14.81–20.50 kJ/mol at a conversion degree of 40 % for the reduction of hematite pellets to metallic iron with hydrogen. Moon et al. [19] calculated the activation energy to vary between 19.8 and 42.1 kJ/mol for different mixtures of H_2 and CO, with the highest activation energy determined for pure H_2 and the lowest for pure CO. These activation energies are lower compared to our study. The main difference is that our study applies gas mixtures containing oxidizing gases (CO_2), which limit the reduction and therefore increase the activation energy. The influence of H_2 and CO in the reducing gas on the conversion of hematite to wüstite was also studied by Piotrowski et al. [24]. For a gas mixture of 90 % N_2 and 10 % CO, they found an activation energy of 122.52 kJ/mol. When the 10 % CO was exchanged with 5.7 % CO and 4.3 % H_2, the activation energy decreased to 93.72 kJ/mol. A further shift to a gas mixture of 90 % N_2 and 10 % H_2 significantly decreased the activation energy to 28.08 kJ/mol. Even though they described the initial reaction as topochemical surface control, the reaction mechanism changed to diffusion control after an initial layer of Fe_3O_4/FeO formed, which is again in alignment with the mechanism determined in this study. Dilmac [31] used fine hematite ore as input material and CO-N_2 atmospheres (50 % CO) as reducing gas. Even though they investigated multiple reduction steps, the important step to compare to this study is the reduction from magnetite to wüstite. The model fitting of Dilmac led to a reaction mechanism of two-dimension contraction and an activation energy of 54.93 kJ/mol for the reduction of magnetite to wüstite.

In summary, research on the reduction of iron ores by varying reducing gas composition may be vast but differs strongly due to the various parameters influencing the reduction kinetics. It should be noted that the reduction temperatures in this study are significantly higher than in the studies mentioned above. However, the activation energies calculated in this study based on the internal diffusion model (69.12–79.91 kJ/mol) fit the trends in literature. While studies using pure H_2 generally show lower activation energies, the activation energies in our study are higher due to the presence of Ar and CO_2. Studies

with larger amounts of nitrogen or lower reducing gas contents come closer to or exceed the kinetic parameters in this study.

5.3.3. NON-ISOTHERMAL REDUCTION

During the reduction under non-isothermal conditions, gas-solid reduction occurs together with thermal decomposition as co-existing processes. In our previous study [12], the thermal decomposition behaviour of three ores (OreA, OreB, OreC) was studied and significant differences in mass loss were explained by the mineralogical differences of the ores. Two different decomposition processes were identified for each ore. OreA first shows the decomposition of the dolomite phase, before hematite decomposes as a two-stage process. OreB and OreC first show the decomposition of goethite as two-stage process and later exhibits the same two-stage hematite decomposition as OreA. In order to compare the differences between thermal decomposition and the mixed mechanism, Figure 5.6 relates the mass loss due to only thermal decomposition from our previous study [12], with the mixed mechanism reduction in this study for the three different atmospheres: A7.5H_2, A22.5H_2 and A37.5H_2. Considering the mass loss in reducing gas atmosphere, two distinctive stages are observed. Comparing the behaviour of the mixed reduction to the thermal decomposition, reactions can be assigned to the respective stages of the mixed reduction. The first stage for OreA is the initial reduction of hematite and the second stage the simultaneous decomposition of the dolomite phase and further iron oxide reduction. Considering OreB and OreC, the first mass loss stage is the simultaneous decomposition of the goethite phase and the reduction of hematite. The second stage is the further reduction of the iron oxides. In A7.5H_2 and A22.5H_2, all three ores reach a maximum of mass loss at a similar time, even before the set-temperature of 1773 K was reached. In A7.5H_2, the reaction saturates between 1125 and 1180 K, depending on the ore. In A22.5H_2, the reaction saturates at slightly lower temperatures, between 1095 and 1125 K. In A37.5H_2, however, the reaction seems to continue much longer and only reaches its mass loss peak between 1415 and 1440 K, depending on the ore, before the mass increases again. The mass gain phenomenon will be explained by the water-gas shift reaction (WGSR) in the following section (5.3.4. The influence of water-gas shift reaction).

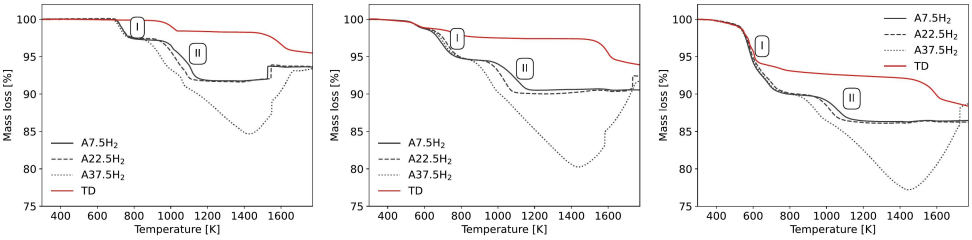


Figure 5.6: Comparison of thermal decomposition (TD) [12] and mixed reduction in non-isothermal conditions for (a) OreA, (b) OreB and (c) OreC.

5.3.4. THE INFLUENCE OF WATER-GAS SHIFT REACTION

The presence of hydrogen, carbon monoxide and carbon dioxide at increasing temperatures, as investigated in this study, leads to the occurrence of the water-gas shift reaction described in (equation (Eq. (5.9))) [43]. The water-gas shift reaction is reversible and exothermic [44].

$$H_2O(g) + CO(g) \leftrightarrow CO_2(g) + H_2(g) \tag{5.9}$$

Due to this reaction, the actual gas compositions present during reduction may differ from the injected gas streams and vary as a function of temperature. An important criteria to evaluate the equilibrium state of the reaction is the reaction rate constant (equation (Eq. (5.10))).

$$K = \frac{(P_{CO_2} * P_{H_2})}{(P_{CO} * P_{H_2O})} \tag{5.10}$$

FactSage 7.0 [34, 35] was used to investigate the temperature influence on the WGSR (Figure 5.7). Up to 1100 K, the equilibrium constant is larger than 1, indicating an exothermic reaction, hence favouring the products CO_2 and H_2. Exceeding this temperature, the equilibrium shifts, and the reaction turns endothermic, favouring the development of the reactants CO and H_2O.

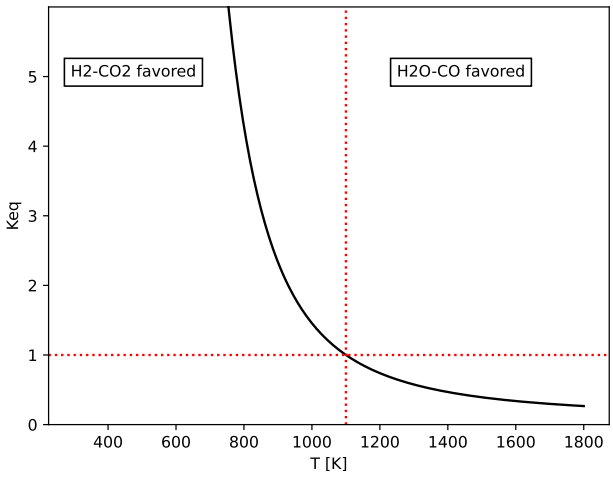


Figure 5.7: Influence of temperature on water-gas shift reaction in a temperature range of 300 to 1800 K (FactSage 7.0) [34, 35].

To further analyse the theoretical gas atmospheres in equilibrium, the Equilib module of FactSage 7.0 [34, 35] was used (Figure 5.8). The gas atmosphere was calculated for the volume of the reaction zone in the TGA (51 cm^3). The input streams were calculated so that the reaction chamber was completely filled with the reaction gas. The values were calculated for every 10 K.

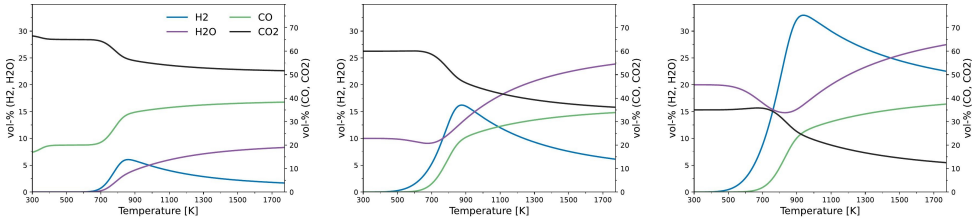


Figure 5.8: Influence of water-gas shift reaction on equilibrium composition of the gas phase for (a) A7.5H_2, (b) A22.5H_2 and (c) A37.5H_2 (Fact7.0, Equilib Module [34, 35]).

Since this study focuses on the influence of hydrogen on the conversion degree of the ores, it is important to evaluate the actual presence of hydrogen in the system. Based on Figure 5.7, the production of H_2 and CO_2 should be theoretically favoured up to around 1100 K. For all atmospheres in Figure 5.8, it is shown that the hydrogen content is low at lower temperatures (< 700 K), but it steadily increases until it reaches a maximum between 863 and 943 K. The maximum concentrations are somewhat lower than the actual input streams (6.1 %, 16.2 %, and 33.0 % for A7.5H_2, A22.5H_2, and A37.5H_2, respectively). After reaching its peak, the hydrogen concentration decreases until the end temperature of calculation (1773 K). The concentrations at 1773 K are 1.7 %, 6.1 % and 22.5 % for A7.5H_2, A22.5H_2 and A37.5H_2, respectively. Based on the thermodynamics of the WGSR, the water-vapour content should show an opposite trend to hydrogen. In Figure 5.8 the course of water-vapour depends on the amount of hydrogen in the input gas. Even though water-vapour is not present in the input gas stream, it increases to high levels, varying between 15 and 30 vol-% in A37.5H_2. As expected from the WGSR, CO_2 behaves opposite to the course of water-vapour and starts to decrease when the amount of water-vapour in the system increases. Even though the amount of CO_2 is still high in A7.5H_2 at 1773 K (51.5 %), it decreases to 12.8 % in A37.5H_2 at 1773 K. In A22.5H_2 and A37.5H_2, CO appears in equilibrium only from about 600 K, which is the temperature at which CO_2 begins to decrease. At 1773 K the CO content is the highest for A7.5H_2 (38.2 %). The CO content is higher in A37.5H_2 (37.5 %), compared to A22.5H_2 (33.9 %) even though the input amount is the same. This can be explained by the general lower amounts of CO_2 in the system.

To investigate the behaviour of the gas composition during the actual experiments, the off-gas signal was measured via a Quadruple Mass Spectrometer (QMS) in all experiments. Since the input material has no significant influence on the gas composition, the results are shown only for OreB. These include the complete mass loss over the experimental time, together with the logarithmic QMS signals (in ampere) for H_2, H_2O, CO and CO_2 as presented in Figure 5.9. The data is presented until the end of the isothermal holding time, since the system is cooled in argon atmosphere afterwards. The signal measured in the QMS analysis only provides semi-quantitative data. Therefore, the measured data cannot be directly translated into vol.-%, as presented for the thermodynamic calculations in Figure 5.8. Nevertheless, the signal measured via QMS still provides significant data on the behaviour of the different gases and how they interact with each other, and their course can be compared to the results of the thermodynamic analysis. The corresponding data for the other ores are provided in Figure C.2 and Figure C.3 of the appendix C.

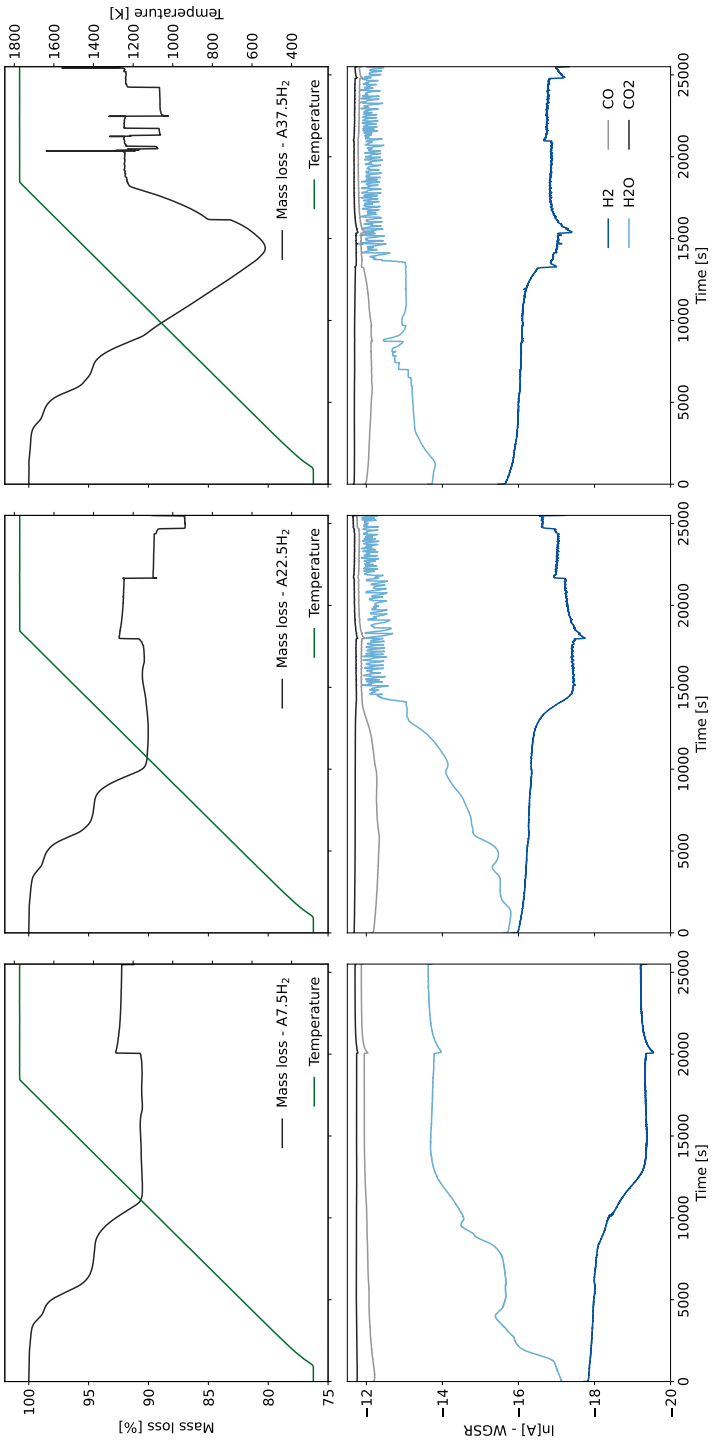


Figure 5.9: QMS off-gas measurements together with mass loss for A7.5H_2, A22.5H_2 and A37.5H_2 of OreB at 1773 K.

The course of CO_2 is measured to be relatively constant during the non-isothermal and following isothermal zone and does not indicate the same constant decrease as in the FactSage calculations. In A7.5H_2, CO behaves similarly to CO_2. However, A22.5H_2 and A37.5H_2, where the CO content is comparatively lower, CO initially decreases slightly before it increases back to its initial value. A more chaotic trend is observed for H_2 and H_2O. In all atmospheres, as expected based on the thermodynamic calculations, a strong increase in the H_2O signal during the heating stage is measured. It is important to note that the initially measuredH_2O can also be emitted from the decomposing goethite phase, which was found to decompose between 436 and 918 K at a heating rate of 5 K/min [12]. During the heating phase, the hydrogen signal behaves inversely to the water-vapour. While H_2O is partly produced by the reduction of the ore (consuming H_2), most hydrogen is produced by the water-gas shift reaction. In the QMS measurement, the initial increase in H_2 as in the thermodynamic modeling is not observed. Instead a slow continuous decrease is observed with increasing temperature. The impact of the reduction by H_2 is therefore more significant at lower temperatures and decreases with the increase in temperature.

If we consider the whole mass loss in Figure 5.9, also including the isothermal zone, a strange phenomenon is occurring in later stages of the experiment. During the isotherm, after the mass loss obtained in the heating zone, an increase in mass followed by a "noise" effect of fluctuating masses arises. The effect appears to be stronger for A22.5H_2 compared to A7.5H_2, apparently affected by the hydrogen increase in the atmosphere. Considering A37.5H_2, a further increase of hydrogen seems to intensify the phenomenon even more. Even though the gases are constantly fed into the system, only CO and CO_2 stay constant during the course of the experiment. For hydrogen and water-vapour, the stronger observed fluctuations are related to pressure changes in the system. These fluctuations initiate at approximate temperatures of 1410 K for A22.5H_2 and of 1370 K for A37.5H_2, indicating the on-set temperatures of strong reactions of the WGSR in the respective atmospheres. Figure 5.10 shows the total pressure profile measured in the system during the experiments of OreB for A7.5H_2, A22.5H_2 and A37.5H_2. During the heating zone, the total pressure profile follows the course of hydrogen gas, indicating that hydrogen consumption by reduction and the water-gas shift reaction causes a decrease in total system pressure. During the isotherm, the total pressure shows similar fluctuating behaviour compared to the H_2O signal and is similar in course to the hydrogen and mass loss. Based on this, the fluctuating mass loss during the isothermal zone is most likely explained by the total pressure changes in the system. This also explains the observed mass gain phenomenon mentioned in Figure 5.2 and Figure 5.6. To prove the fact that this doesn't affect the mass loss signal during the reaction in the non-isothermal zone, experiments without the addition of input material under A7.5H_2 and A37.5H_2 atmosphere were conducted. The results of these mass losses can be found in the appendix C, in Figure C.4. Also in these runs, the same "noise" effect occurs during the isothermal zone, but does not influence the mass loss observed for the experiments during the heating zone.

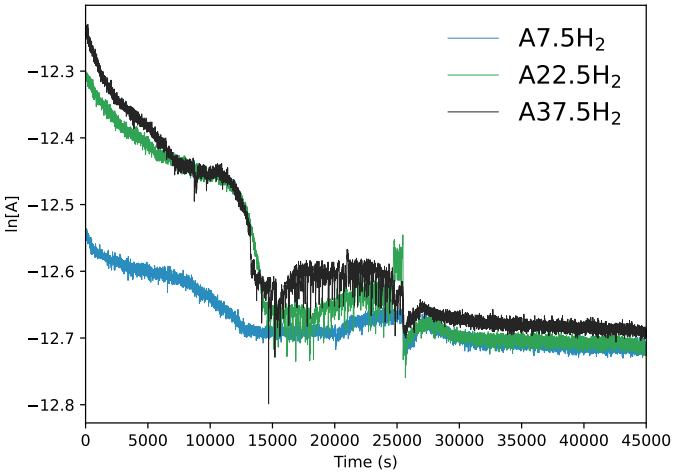


Figure 5.10: Total pressure during the experiments of OreB under the reducing atmosphere of A7.5H_2, A22.5H_2 and A37.5H_2.

5.3.5. NON-ISOTHERMAL IRON ORE CONVERSION

The non-isothermal reduction approach presents the challenge that, in addition to the reduction of Fe_2O_3, other components such as FeOOH and $CaMg(CO_3)_2$ also undergo thermal decomposition. A lot of literature is available on the thermal decomposition of goethite and hematite, as well as of the gas-solid reduction [12, 14, 26–33]. However, as mentioned before, these studies do not observe the gas-solid reduction and thermal decomposition as simultaneous mechanisms. Due to the co-occurrence of the gas reduction of the hematite phase and the thermal decomposition of the goethite and dolomite phases in this study, the individual mass loss stages cannot be assigned to a specific reaction. As a result, the calculation of the conversion factor must be adjusted, as shown in equation Eq. (5.11).

$$\alpha = \frac{m_0 - m_t}{m_0 - \left(m_0 - m_0^* \left(\frac{x_{H_2O}}{100} + \frac{x_{CO_2}}{100} + \frac{x_{O_{Fe_2O_3 \rightarrow FeO}}}{100}\right)\right)} \tag{5.11}$$

Where m_0 is the initial mass of the sample (mg), m_t is the mass at time t (mg), x_{H_2O} is the amount of crystal water measured in the sample (wt%), x_{CO_2} is the amount of CO_2 measured in the sample (wt%) and $x_{O_{Fe_2O_3 \rightarrow FeO}}$ is the theoretical amount of oxygen lost, considering a reduction from Fe_2O_3 to FeO.

This revised representation of the conversion factor accounts for the complete conversion of all phases that would be reduced during ore decomposition, contributing to the overall mass loss of the sample. Meaning, a conversion factor of 1 would describe the complete decomposition of dolomite (OreA) or goethite (OreB & OreC) combined with the reduction of hematite to wüstite. Therefore, the newly defined conversion degree does not reflect the reduction of the iron phase anymore and is solely used as a parameter,

describing the complete process. The conversion factors for the non-isothermal gas reduction of the three ores in A7.5H_2 and A22.5H_2, calculated based on equation Eq. (5.11), are presented in Figure 5.11. The high mass loss observed for A37.5H_2 in Figure 5.6 would lead to a conversion significantly larger than 1, which is unlikely to occur, as these numbers would imply the presence of iron. Since the reduction under isothermal conditions in the A37.5H_2 atmosphere also did not lead to a conversion degree larger than 1, it is unlikely to achieve it under non-isothermal conditions. The authors suggest that the conversion reaches a similar level compared to A7.5H_2 and A22.5H_2 and the following increase can be explained by the pressure variance due to the water-gas shift reaction, as explained in the previous section. Therefore, the results of A37.5H_2 are excluded from this analysis of the conversion degree.

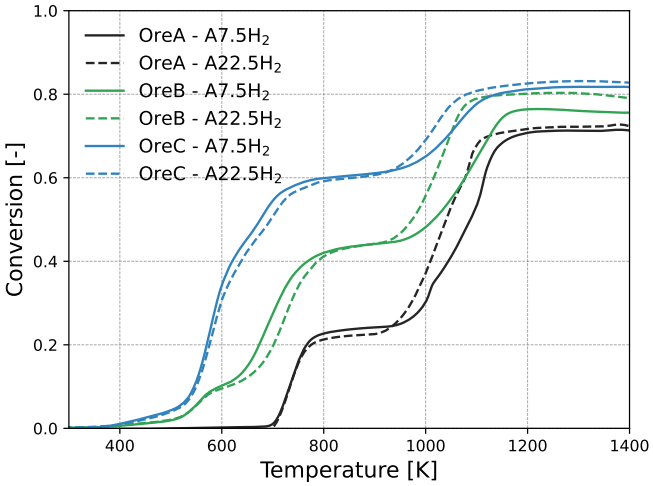


Figure 5.11: Conversion factors for OreA, OreB and OreC in the atmospheres A7.5H_2 and A22.5H_2.

Even though the initial conversion seems similar for all atmospheres of the same ores (OreA : $\alpha < 0.2$, OreB : $\alpha < 0.4$, OreC : $\alpha < 0.6$), higher conversion is achieved in the second conversion stage at lower temperatures with increasing hydrogen-levels. This phenomenon can be explained by the hematite reduction becoming the dominant conversion mechanism after the decomposition of other components, and this stage is more influenced by the enrichment of hydrogen in the reducing gas. For all three ores the influence of the increasing H_2-levels on the final conversion value is marginal. For OreA the conversion increases from approximately 71 to 72 %, for OreB from 76 to 80 % and for OreC from 82 to 83 %, for A7.5H_2 and A22.5H_2 respectively. Since for all ores it is expected that all possible thermal decomposition reactions are completed during the reduction and the only limiting reaction is the conversion from hematite to wüstite, the final conversion degrees of the ores are comparable. A clear difference in the final conversion between the three ores is visible. It seems that an increasing amount of goethite in the sample leads to an increase in total conversion, as lowest conversion is observed for

OreA (no crystal water) and highest for OreC (6.05-% crystal water). An explanation for this can be that the decomposition of goethite leads to a more fine-grained and porous structure and, therefore, to a more reactive hematite phase compared to the hematite in the virgin material. Li et al. [45] found that the heating and dehydration of goethite ores generate cracks and result in a more porous structure of the ore. Unfortunately, since this transformation occurs in the initial stages of the reduction in our experiments, it is not possible to verify this influence with microscopical analysis. In our previous study [12], as well as in other studies such as by Xing et al. [32] and Dilmaç [31], the Coats-Redfern Method [46] was applied to obtain kinetic parameters of hematite reduction and thermal decomposition in non-isothermal conditions at a single constant heating rate. However, the Coats-Redfern method is not applicable here due to the multiple simultaneous reactions that cannot be easily separated. Therefore, this study will not determine the kinetic parameters of the non-isothermal gas reduction of the different ores and will leave this to future studies, along with the morphological study of the previous proposed goethite thermal decomposition.

5.4. CONCLUSIONS

- In the isothermal experiments, an increase in H_2 in the reducing gas atmosphere enhances the conversion to wüstite within a temperature range of 1673–1773 K. Lowering the PCR from 60 % to 40 % and, therefore, increasing the H_2 level, further improves the conversion. A higher H_2 content not only increases the limit of conversion but also decreases the time after which the conversion saturates. In A7.5H_2 the conversion saturates between 502 and 794 s, in A22.5H_2 between 375 and 583 s and in A37.5H_2 between 206 and 297 s, depending on the temperature. Faster conversion is achieved at higher temperatures.

- Microscopical observations and model fitting based on the shrinking core model of the isothermal experiments indicate that the diffusion of the reacting gas through the developing product layer is the rate-determining mechanism. The activation energy decreases from 77.60 to 69.12 kJ/mol with an increase in H_2 in the same PCR, but increases to 79.91 kJ/mol with a decrease in PCR from 60 to 40 % in a temperature range of 1673–1773 K.

- Comparing the mass loss of the non-isothermal gas reduction to the isolated thermal decomposition, the initial reduction of hematite in OreA starts before the reduction proceeds simultaneously with dolomite decomposition. For OreB and OreC a first significant mass loss curve describes the simultaneous initial reduction of hematite together with goethite thermal decomposition, whereas only iron oxide reduction is observed at later stages.

- During the heating stage of the non-isothermal experiments, the water-gas shift reaction (WGSR) is clearly observable. The partial pressure of water-vapour in the gas atmosphere increases continuously, while that of H_2 decreases. During the later isotherm, the reactions of the WGSR lead to pressure changes in the system, influencing the mass loss data.

- In the non-isothermal experiments, the influence of ore mineralogy on the total conversion is stronger than the influence of H_2-enrichment in the atmosphere. Higher conversion is achieved with increasing goethite content in the ores: α_{OreA}(71–72 %) < α_{OreB}(76–80 %) < α_{OreC}(82–83 %). However, as in the isothermal experiments, the increase of H_2 in the atmosphere increases the speed of reduction and leads to conversion at lower temperatures. Overall, there is no significant difference on the final conversion achieved in the non-isothermal experiments (76–80 %) compared to the isothermal experiments (73–81 %) of OreB.

REFERENCES

[1] P. Leerhoff, J. C. Brouwer, C. Zeilstra, K. Meijer, J. van der Stel, S. T. Abrahami, N. Dogan, and Y. Yang. Impact of H_2-enrichment and ore mineralogy on the reduction of varying iron ores in suspension smelting ironmaking. **Powder Technology** 468 (2026). DOI: 10.1016/j.powtec.2025.121570.

[2] Worldsteel Association. Climate change and the production of iron and steel. 2021.

[3] Worldsteel Association. 2022 World Steel in Figures. 2022.

[4] M. Naito, K. Takeda, and Y. Matsui. Ironmaking Technology for the Last 100 Years: Deployment to Advanced Technologies from Introduction of Technological Know-how, and Evolution to Next-generation Process. **ISIJ International** 55 (2015), pp. 7–35. DOI: 10.2355/isijinternational.55.7.

[5] S. Seetharaman, R. Guthrie, A. McLean, S. Seetharaman, and H. Y. Sohn. Treatise on Process Metallurgy Volume 3: Industrial Processes. 2024. DOI: 10.1016/C2020-0-01069-8.

[6] K. Meijer, C. Guenther, and R. J. Dry. HIsarna Pilot Plant Project. METEC InSteelCon 2011, 2011.

[7] S. Santos, K. Meijer, J. V. D. Stel, P. Broersen, J. Monteiro, and P. V. Os. CO2 Capture in Combination with the HIsarna Process. June 2019.

[8] K. Meijer, C. Zeilstra, C. Teerhuis, M. Ouwehand, and J. van der Stel. Developments in Alternative Ironmaking. **Transactions of the Indian Institute of Metals** 66 (2013), pp. 475–481. DOI: 10.1007/s12666-013-0309-z.

[9] Z. Yan, T. T. Htet, J. Hage, K. Meijer, and Z. Li. HIsarna Process Simulation Model: Using FactSage with Macro Facility. **Metallurgical and Materials Transactions B** 54 (2023), pp. 868–879. DOI: 10.1007/s11663-023-02732-5.

[10] Y. Yang, K. Raipala, and L. Holappa. Treatise on Process Metallurgy. Vol. 3. Elsevier Ltd., 2014. Chap. Ironmaking, pp. 2–88. ISBN: 9780080969886. DOI: 10.1016/B978-0-08-096988-6.00017-1.

[11] A. K. Biwas. Principles of blast furnace ironmaking: theory and practice. Cootha Publishing House: Brisbane, 1981.

[12] P. Leerhoff, J. C. Brouwer, A. M. Armaki, C. Zeilstra, K. Meijer, J. van der Stel, S. T. Abrahami, N. Dogan, and Y. Yang. Characterisation of Varying Iron Ores and Their Thermal Decomposition Kinetics Under HIsarna Ironmaking Conditions. **Metals** 14, 1271 (2024). DOI: 10.3390/met14111271.

[13] Y. Qu, Y. Yang, Z. Zou, C. Zeilstra, K. Meijer, and R. Boom. Thermal decomposition behaviour of fine iron ore particles. **ISIJ International** 54 (2014), pp. 2196–2205. DOI: 10.2355/isijinternational.54.2196.

[14] Z. Chen, C. Zeilstra, J. van der Stel, J. Sietsma, and Y. Yang. Thermal Decomposition Reaction Kinetics of Hematite Ore. **ISIJ International** 60 (2020), pp. 65–72. DOI: 10.2355/isijinternational.ISIJINT-2019-129.

[15] P. C. Cavaliere. Hydrogen Assisted Direct Reduction of Iron Oxides. Springer International Publishing, 2022. ISBN: 9783030980566. DOI: 10.1007/978-3-030-98056-6.

[16] A. O. Zhang, B. J. Monaghan, R. J. Longbottom, M. Nusheh, and C. W. Bumby. Reduction Kinetics of Oxidized New Zealand Ironsand Pellets in H2 at Temperatures up to 1443 K. **Metallurgical and Materials Transactions B** 51 (2020). DOI: 10.1007/s11663-020-01790-3.

[17] I. Sohn and S. M. Jung. Effect of Metal Additions to the Reduction of Iron Oxide Composite Pellets with Hydrogen at Moderate Temperatures. **steel research international** 82 (2011), pp. 1345–1354. DOI: 10.1002/srin.201100144.

[18] H.-b. Zuo, C. Wang, J.-j. Dong, K.-x. Jiao, and R.-s. Xu. Reduction kinetics of iron oxide pellets with H_2 and CO mixtures. **International Journal of Minerals, Metallurgy, and Materials** 22 (2015), pp. 688–696. DOI: 10.1007/s12613-015-1123-x.

[19] I.-J. Moon, C.-H. Rhee, and D.-J. Min. Reduction of hematite compacts by H2-CO gas mixtures. **steel research** 69 (1998), pp. 302–306. DOI: 10.1002/srin.199805555.

[20] E. Kawasaki, J. Sanscrainte, and T. J. Walsh. Kinetics of Reduction of Iron Oxide With Carbon Monoxide and Hydrogen. **A.I.Ch.E. Journal** 8 (1962), pp. 48–52.

[21] M. Kazemi, M. S. Pour, and D. Sichen. Experimental and Modeling Study on Reduction of Hematite Pellets by Hydrogen Gas. **Metallurgical and Materials Transactions B** 48 (2017), pp. 1114–1122. DOI: 10.1007/s11663-016-0895-3.

[22] I. Sohn and R. J. Fruehan. The Reduction of Iron Oxides by Volatiles in a Rotary Hearth Furnace Process: Part I. The Role and Kinetics of Volatile Reduction. **Metallurgical and Materials Transactions B** 36B (2005), pp. 605–612.

[23] D. Spreitzer and J. Schenk. Iron Ore Reduction by Hydrogen Using a Laboratory Scale Fluidized Bed Reactor: Kinetic Investigation—Experimental Setup and Method for Determination. **Metallurgical and Materials Transactions B** 50 (2019), pp. 2471–2484. DOI: 10.1007/s11663-019-01650-9.

[24] K. Piotrowski, K. Mondal, H. Lorethova, L. Stonawski, T. Szymański, and T. Wiltowski. Effect of gas composition on the kinetics of iron oxide reduction in a hydrogen production process. **International Journal of Hydrogen Energy** 30 (2005), pp. 1543–1554. DOI: 10.1016/J.IJHYDENE.2004.10.013.

[25] D. Spreitzer and J. Schenk. Reduction of Iron Oxides with Hydrogen—A Review. **steel research international** 90, 1900108 (2019). DOI: 10.1002/srin.201900108.

[26] P. C. Beuria, S. K. Biswal, B. K. Mishra, and G. G. Roy. Study on kinetics of thermal decomposition of low LOI goethetic hematite iron ore. **International Journal of Mining Science and Technology** 27 (2017), pp. 1031–1036. DOI: 10.1016/j.ijmst.2017.06.018.

[27] P. Pourghahramani and E. Forssberg. Reduction kinetics of mechanically activated hematite concentrate with hydrogen gas using nonisothermal methods. **Thermochimica Acta** 454 (2007), pp. 69–77. DOI: 10.1016/j.tca.2006.12.023.

[28] B. Lyu, G. Wang, F. Yang, H. Zuo, Q. Xue, and J. Wang. Kinetic Analysis of Isothermal and Non-Isothermal Reduction of Iron Ore Fines in Hydrogen Atmosphere. **Metals** 12, 1754 (2022). DOI: 10.3390/met12101754.

[29] A. Hammam, Y. Li, H. Nie, L. Zan, W. Ding, Y. Ge, M. Li, M. Omran, and Y. Yu. Isothermal and Non-Isothermal Reduction Behaviors of Iron Ore Compacts in Pure Hydrogen Atmosphere and Kinetic Analysis. **Mining, Metallurgy & Exploration** 38 (2021), pp. 81–93. DOI: 10.1007/s42461-020-00317-3.

[30] Y. Sun, Y. Han, X. Wei, and P. Gao. Non-isothermal reduction kinetics of oolitic iron ore in ore/coal mixture. **Journal of Thermal Analysis and Calorimetry** 123 (2016), pp. 703–715. DOI: 10.1007/s10973-015-4863-y.

[31] N. Dilmaç. Isothermal and non-isothermal reduction kinetics of iron ore oxygen carrier by CO: Modelistic and model-free approaches. **Fuel** 296 (2021), p. 120707. DOI: 10.1016/j.fuel.2021.120707.

[32] L. Xing, Y. Qu, C. Wang, L. Shao, Z. Zou, and W. Song. Kinetic Study on Thermal Decomposition Behavior of Hematite Ore Fines at High Temperature. **Metallurgical and Materials Transactions B** 51 (2020), pp. 395–406. DOI: 10.1007/s11663-019-01747-1.

[33] A. Ammasi. Effect of Heating Rate on Decomposition Temperature of Goethite Ore. **Transactions of the Indian Institute of Metals** 73 (2020), pp. 93–98. DOI: 10.1007/s12666-019-01806-w.

[34] CRCT - ThermFact Inc. and GTT-Technologies. FactSage, Equilib Module. 2015. URL: https://factsage.com/.

[35] CRCT -ThermFact Inc. and GTT-Technologies. FactPS Database. 2015. URL: https://factsage.com/.

[36] O. Levenspiel. Fluid-Particle Reactions: Kinetics. 3rd ed. John Wiley & Sons, 1999.

[37] Y. Luo and Y. Wu. Comment on "Effects of particle size and coating on decomposition of alumina-extracted residue from high-alumina fly ash": Proposition of the shrinking cylinder model. **Journal of Hazardous Materials** 401 (2021). DOI: 10.1016/j.jhazmat.2020.123818.

[38] Y. H. Han, J. S. Wang, R. Z. Lan, L. T. Wang, X. J. Zuo, and Q. G. Xue. Kinetic analysis of iron oxide reduction in top gas recycling oxygen blast furnace. **Ironmaking & Steelmaking** 39 (2012), pp. 313–317. DOI: 10.1179/1743281211Y.0000000058.

[39] L. Y. Xing, Z. S. Zou, Y. X. Qu, L. Shao, and J. Q. Zou. Gas–Solid Reduction Behavior of In-flight Fine Hematite Ore Particles by Hydrogen. **Steel Research International** 90, 1800311 (2019). DOI: 10.1002/srin.201800311.

[40] Y. Qu, Y. Yang, Z. Zou, C. Zeilstra, K. Meijer, and R. Boom. Kinetic study on gas molten particle reduction of iron ore fines at high temperature. **Ironmaking and Steelmaking** 42 (2015), pp. 763–773. DOI: 10.1179/1743281215Y.0000000021.

[41] M. Bahgat and M. H. Khedr. Reduction kinetics, magnetic behavior and morphological changes during reduction of magnetite single crystal. **Materials Science and Engineering: B** 138 (2007), pp. 251–258. DOI: 10.1016/j.mseb.2007.01.029.

[42] H. Chen, Z. Zheng, and W. Shi. Investigation on the Kinetics of Iron Ore Fines Reduction by CO in a Micro-fluidized Bed. **Procedia Engineering** 102 (2015), pp. 1726–1735. DOI: 10.1016/j.proeng.2015.01.308.

[43] G. K. Reddy and P. G. Smirniotis. Introduction About WGS Reaction. Elsevier, 2015, pp. 1–20. DOI: 10.1016/B978-0-12-420154-5.00001-2.

[44] D. S. Newsome. The Water-Gas Shift Reaction. **Catalysis Reviews** 21 (1980), pp. 275–318. DOI: 10.1080/03602458008067535.

[45] H. Li, D. J. Pinson, P. Zulli, L. Lu, R. J. Longbottom, S. J. Chew, B. J. Monaghan, and G. Zhang. Interaction Between Mineral Phases in a Goethitic Iron Ore and Fluxing Materials During Sintering. **Metallurgical and Materials Transactions B** 52 (2021), pp. 996–1011. DOI: 10.1007/s11663-021-02072-2.

[46] A. W. Coats and J. P. Redfern. Kinetic Parameters from Thermogravimetric Data. **Nature** 201 (1964), pp. 68–69. DOI: 10.1038/201068a0.

6

IMPACT OF H_2-ENRICHMENT AND ORE MINERALOGY ON THE IN-FLIGHT REDUCTION OF IRON ORE FINES

This study investigates the in-flight flash reduction behavior of three fine iron ores with distinct mineralogies (OreA, OreB, and OreC) under high-temperature suspension smelting conditions. Combining morphological, mineralogical, and kinetic analyses, the study examines how particle properties, gas composition, and particle residence time influence pre-reduction behavior. In-flight reduction experiments were complemented by thermogravimetric analyses (TGA) to compare short and long residence time behavior. The results show that goethite-rich ores (OreB and OreC) exhibit higher porosity and internal cracking, indicating the possibility of nucleation and growth of magnetite as reaction mechanism, while the dense hematite ore (OreA) is reduced mainly by the surface-controlled reaction. The presence of goethite also enhances thermal decomposition and increases the overall pre-reduction degree under non-isothermal conditions. However, under isothermal conditions, once all ores are converted to magnetite, mineralogical differences become negligible. Even though reduction at long residence times shows significant higher reduction degrees, analyses of a formed slag phase reveals the formation of high amounts of Fe-silicates for the reduced goethite ores. Off-gas analyses reveals that the water-gas shift reaction significantly influences the present reducing atmosphere during suspension smelting conditions, decreasing the amount of H_2 and increasing water-vapor formation.

6.1. INTRODUCTION

Flash or suspension smelting ironmaking describe processes in which iron ore fines are reduced or pre-reduced within seconds at high temperatures [1]. Two prominent examples utilizing flash ironmaking are the Flash Iornmaking Technology (FIT) developed at the University of Utah [2–7], and HIsarna, developed by Tata Steel in IJmuiden as part of the ULCOS initiative [8, 9].

While the FIT can utilize almost pure hydrogen next to natural gas as reducing agents [1], HIsarna employs gas mixtures of $H_2 - CO - CO_2 - H_2O$ as the pre-reduction atmosphere before the final reduction by pulverized coal in a smelting vessel [9, 10]. The gas mixture originates from the the coal injection and final smelting reduction reactions in the smelting vessel [10]. In both processes, the ore particles are exposed to the reducing gas at very high temperatures (1473 - 1873 K)[1, 11]. Under these conditions, pre-reduction, particle heating, and partial melting occur within very short timescales, leading to a combination of gas-solid and gas-liquid reduction reactions [9]. Such reactions are often referred to as reduction in suspension [12].

Another process applying the flash ironmaking concept is the ZESTY process. In this case, the ore fines are reduced for slightly longer durations (order of 60 s) at temperatures more consistent with conventional DRI processes, yielding a flash-reduced DRI product [13, 14].

A major objective of the HIsarna process is the elimination of the pre-treatment steps required for the input materials [9]. By avoiding ore agglomeration and coke making, HIsarna achieves a significant reduction in CO_2-emissions compared to the traditional blast furnace process [15]. The FIT and ZESTY also utilize iron ores with very small particle sizes and, therefore, have similar advantages regarding the input material [1, 14, 16]. Earlier research in the framework of HIsarna also demonstrated a strong positive impact of small particle sizes on the reduction behavior [17, 18]. Especially at short particle residence times, the rapid heating of small particles facilitates gas reduction. Moreover, previous studies have highlighted the importance of thermal decomposition during the pre-reduction of iron ore fines [19], which is also enhanced by smaller particle sizes under flash ironmaking conditions [17].

Nevertheless, the goal of the HIsarna process is to enable fast and efficient reduction for a wide range of ores, including low- to mid-grade ore qualities, with varying particle size distributions [10, 20]. Therefore, the present study investigates the reduction behavior of three iron ores with different variation in goethite content, namely OreA, OreB and OreC, with larger particle size fractions of (63-125 μm) and (125-250 μm).

The reduction potential of the reducing gas in the upper section of HIsarna is described by the post-combustion ratio (PCR)Eq. (6.1) [10]:

$$\mathrm{PCR} = \frac{\%H_2O + \%CO_2}{\%H_2O + \%CO_2 + \%H_2 + \%CO} \times 100\% \tag{6.1}$$

A low PCR indicates a gas atmosphere rich in reducing gases (H_2, CO), whereas a high PCR reflects a higher concentration of oxidized gases (CO_2, H_2O). Across the gas pre-reduction stage of the HIsarna process, the reducing gases arising from the smelting reduction vessel (SRV) are gradually oxidized due to the reaction with the injected iron ores [11].

The in-flight flash reduction of the iron ores was previously studied under a PCR of approx. 95 % in Chapter 4. The present work (Chapter 6) extends the investigation to lower PCR values of down to around 60 %. Another preceding study ([21],Chapter 5) showed that in thermogravimetric analyses (TGA) and long particle residence times, nearly complete conversion to wüstite is achievable at a PCR of 60 %. Building on this research, the current study examines the influence of reduction time and ore mineralogy under isothermal PCR = 60 % conditions, comparing flash reduction in a drop-tube furnace with TGA reduction experiments to evaluate the reduction of larger particles under in-flight reduction conditions, compared to longer particle residence times.

6.2. METHODS

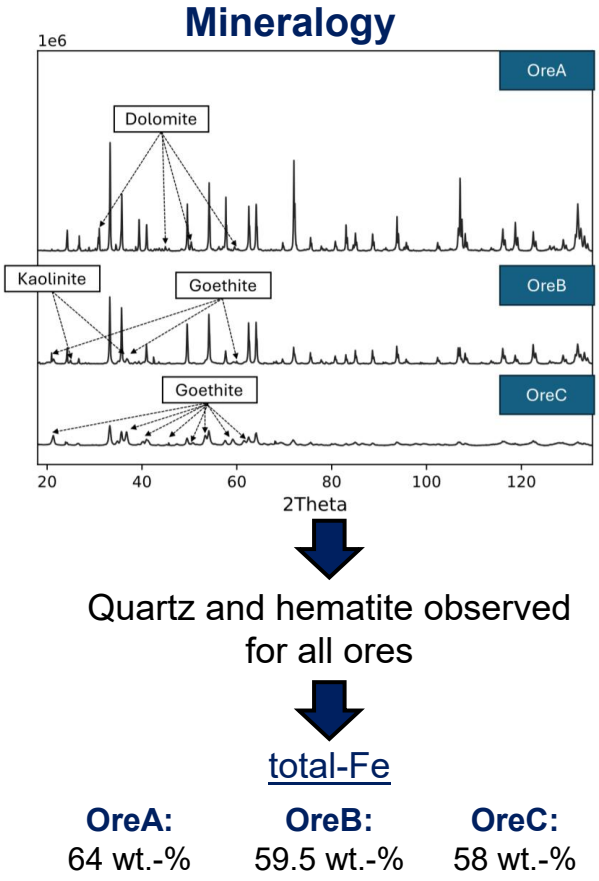
6.2.1. MATERIALS

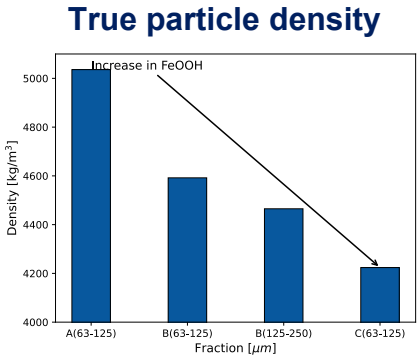
Three different iron ores are investigated in this study, namely OreA, OreB and OreC. For each ore a size fraction of (63-125 μm) is investigated. For OreB an additional larger size fraction of (125-250 μm) is also used to identify the impact of particle size under HIsarna gas reduction conditions. To obtain mineralogical differences between the three ores, x-ray fluorescence (XRF) (Panalytical AXIOS XRF, Netherlands) and loss of ignition analyses (LOI) (dissolution in nitric acid and TGA, LECO, Germany) were carried out. The resulting chemical compositions are presented in Table 6.1.

Table 6.1: Chemical composition of as-received ore materials obtained by XRF and LOI analyses.

	Ore A (63–125 µm)	Ore B (63–125 µm)	Ore B (125–250 µm)	Ore C (63–125 µm)
Fe_2O_3	91.50	85.07	84.07	82.92
total-Fe	64.00	59.50	58.80	58.00
SiO_2	2.96	5.83	6.17	5.30
Al_2O_3	1.44	4.78	5.10	3.00
MgO	0.41	0.04	0.03	0.11
CaO	1.23	0.05	0.04	0.07
TiO_2	0.92	0.35	0.32	0.16
MnO	0.60	0.03	0.03	1.24
total-C	0.23	0.07	0.07	0.14
H_2O (crystal)	–	3.26	3.63	6.39
Rest	0.21	0.31	1.01	0.26

In addition to the chemical analyses, the materials were analyzed in terms of their mineralogy via X-Ray diffraction (XRD) (Bruker D8 Advance diffractometer Bragg-Brentano geometry and Lynxeye position sensitive detector, Bruker, Germany)). Furthermore, their true particle density was determined with a helium pycnometer, specific surface area and porosity were obtained via BET surface analyses. The relationships among these parameters are illustrated in Figure 6.1.





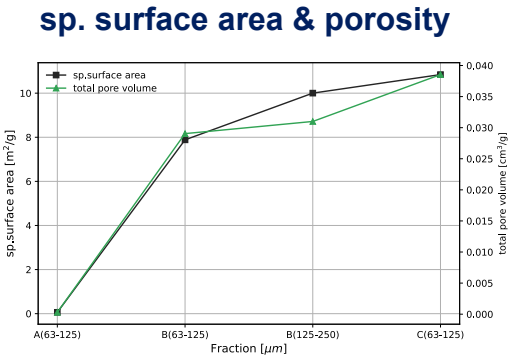


Figure 6.1: Overview of mineralogy and physical properties of as-received iron ore materials.

The main difference in mineralogy is the presence of the goethite phase in OreB and OreC, in contrast to OreA. The occurrence of goethite is indicated by both the XRD patterns and the crystal water content determined from the chemical analyses. The goethite fraction in OreC (68 mol.%) is higher than in OreB (34 mol.%). The presence of goethite leads to an overall lower iron ore grade. While OreA can still be classified as a medium-grade hematite ore, OreB and OreC are clearly low-grade ores, as their total Fe-content is lower than 60 %. Moreover, the presence of the goethite phase further decreases the true particle density and increases the specific surface area and porosity (Figure 6.1). A more detailed discussion of these effects is given in Chapter 4.

6.2.2. EXPERIMENTAL APPROACH

The main objective of this study is to investigate the influence of reduction time and ore mineralogy on the reduction behavior of different iron ores in H_2-enriched atmospheres relevant to suspension smelting ironmaking. For this purpose, experiments were performed using both a thermogravimetric analyzer (TGA) and a high-temperature drop tube furnace (HTDF).

The TGA experiments were used to determine the total achievable pre-reduction degree (PRD) at long particle residence times. Samples were heated to 1723 K at a rate of 5 K/min and then held at this temperature for 2 h to reach the limits of thermal decomposition before introducing the reducing gas mixtures, A7.5H_2 and A22.5H_2 for 1 h. After thermal decomposition, the oxide is expected to be fully converted to magnetite. Thus, the TGA experiments provide insight into the total conversion from magnetite to wüstite and the time required to achieve it.

In contrast, the HTDF set-up enables simultaneous thermal decomposition and gas reduction under short particle residence times (on the order of hundreds of milliseconds), typical for suspension smelting conditions. A schematic of the HTDF set-up is shown in Figure 6.2.

The HTDF allows to study in-flight pre-reduction of small quantities of iron ore particles under defined isothermal conditions and controlled residence times. After reduction, the samples are quenched in a water-cooled zone to immediately stop all ongoing reactions. The experimental parameters for both the TGA and HTDF set-ups are summarized in Table 6.2. For both the TGA and HTDF experiments, the A7.5H_2 atmosphere was applied to all three ores and both particle size fractions of OreB. The A22.5H_2 atmosphere was applied only to the (63-125 μm) size fraction of OreB. While the TGA experiments apply Ar as an insert gas, the HTDF experiments use N_2.

The main analytical parameter in this study is the pre-reduction degree, and its variation in regards to ore mineralogy and size, temperature, and particle residence time. PRD values were obtained using three complementary methods. These methods are the Rietveld refinement of XRD data, redox titration, and electron backscatter diffraction (EBSD). In general, the PRD is calculated according to Eq. (6.2) [19, 22] for the HTDF experiments and Eq. (6.3) for the TGA experiments:

$$PRD = 1 - \frac{3(Fe^{3+})_i + 2(Fe^{2+})_i}{3(Fe^{3+})_0 + 2(Fe^{2+})_0} = \frac{1}{3}\frac{Fe^{2+}}{TFe} \tag{6.2}$$

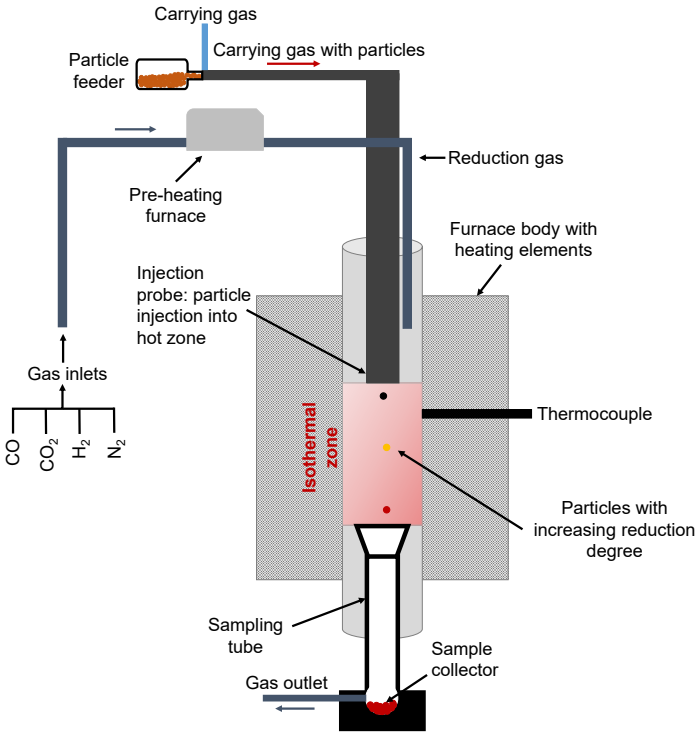


Figure 6.2: Schematic presentation of High-Temperature Drop Tube furnace (HTDF) used in this study.

$$PRD = \frac{m_0 - m_t}{m_0 - m_{Fe_2O_3 \rightarrow Fe}} \tag{6.3}$$

For Eq. (6.2), i represents the reduced state to metallic iron and 0 the initial state of hematite. The total iron (TFe) was determined with XRF, and the iron valency Fe^{3+} and Fe^{2+} state by chemical titration with potassium dichromate. For Eq. (6.3), m_0 is the initial mass, m_t is the mass at time t, and $m_{Fe_2O_3 \rightarrow Fe}$ is the theoretical mass after complete reduction to metallic iron.

Table 6.2: Experimental conditions for HTDF (flash) and TGA experiments.

Parameter	Condition (HTDF)	Condition (TGA)
Ore	A, B, C	
Particle size fraction [µm]	63–125, 125–250 (OreB)	
Temperature [K]	1600, 1650, 1700	1723
Atmosphere	A7.5H_2: 7.5% H_2/22.5% CO/45% CO_2/25% Ar (63–125 µm OreB) A22.5H_2: 22.5% H_2/7.5% CO/45% CO_2/25% N_2 or Ar	
Gas flow rate [L/min]	2	0.2
Heating rate [K/min]	–	5
Particle residence times [ms]	60–450	–
Holding time isotherm [h]	–	2 (Ar) + 1 (reducing gas)

6.3. RESULTS AND DISCUSSION

6.3.1. MORPHOLOGICAL ANALYSES

SEM images of the ores with a particle size fraction of (63-125 μm) in their as-received and reduced states (after reduction at 1700 K for 125 ms in A7.5H_2) are shown in Figure 6.3, together with the corresponding cross-section images. The results reveal distinct morphological changes after pre-reduction depending on the ore type.

OreA initially consists of angular, fine-grained particles. After reduction, both the iron oxides and gangue components undergo partial melting, changing to spherical particles with smoother surfaces. Some particles retain their angular morphology, exhibiting only minor or no cracking. The cross-section reveals a dense and compact structure with limited porosity.

In contrast, OreB exhibits a more irregular morphology. After reduction, the particles still display rough surfaces with visible porosity, while the cross-section shows alternating dense and porous regions. OreC also reveals a heterogeneous and porous structure. These observations are consistent with the pore generation and structural instability observed for goethite-type ores under flash reduction conditions, as discussed in Chapter 4.

To verify the distribution of gangue and iron oxides in the reduced samples, EDS mapping was performed (see appendix D). In OreA, the major gangue phases of SiO_2 and Al_2O_3 are primarily concentrated in distinct particles. For OreB and OreC more co-existince is observed with the iron phases. In OreB this is the case for SiO_2 and Al_2O_3, but for OreC only for SiO_2. This can be explained by the significant higher amounts of Al_2O_3 in OreB, compared to the other ores.

6.3.2. MINERALOGICAL ANALYSES

XRD analysis was carried out to identify the mineralogical phases of the fine ores after reduction. By applying Rietveld refinement to the XRD spectra, a semi-qualitative overview of the phase composition was obtained. A complete overview of the detected phases is given in Table D.1 in appendix D and selected results are presented in Figure 6.4 for the

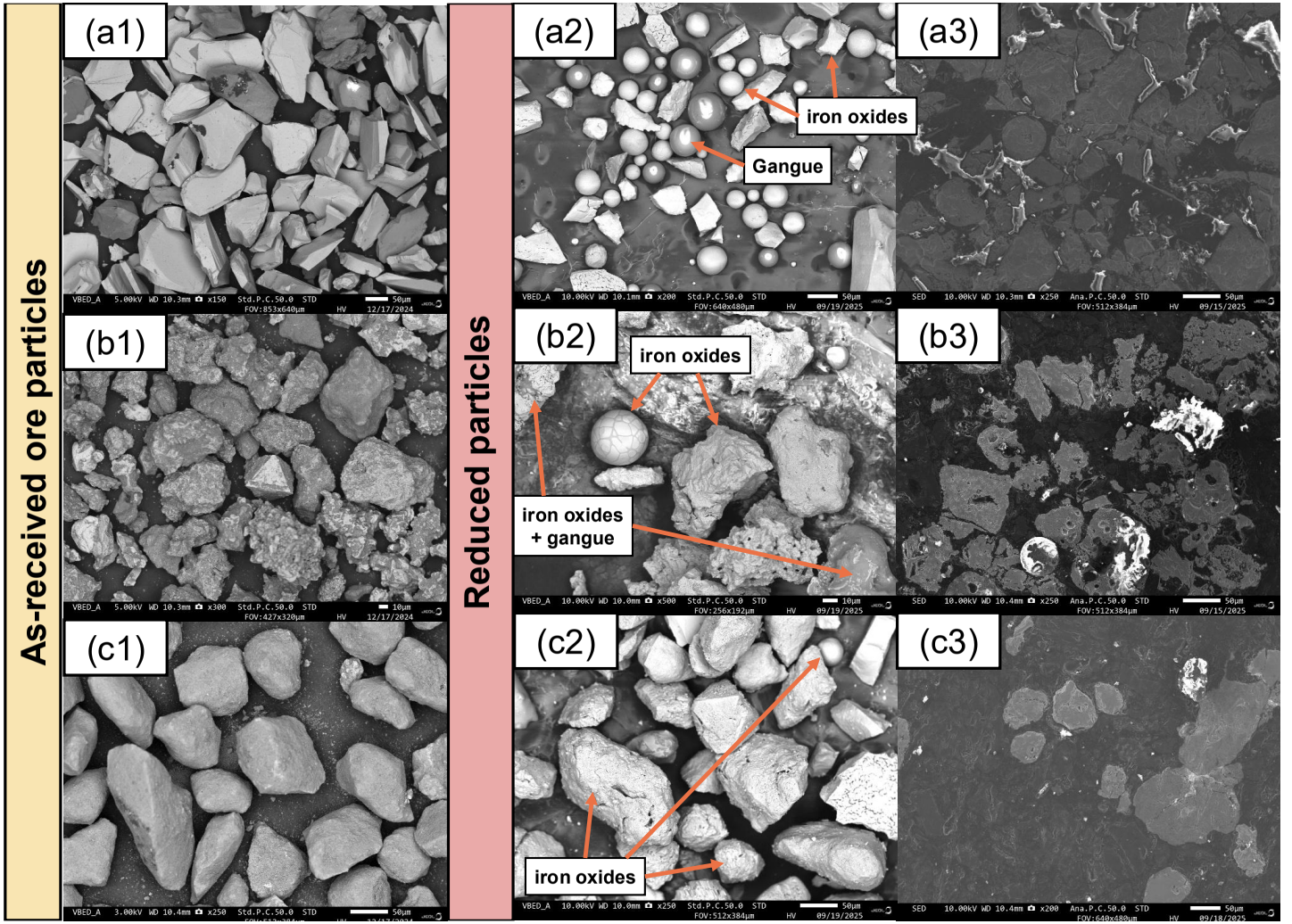


Figure 6.3: Morphological analyses of the reduced ore particles and their cross-section compared to their as-received state for (ai) OreA, (bi) OreB and (ci) OreC, i=1,2,3.

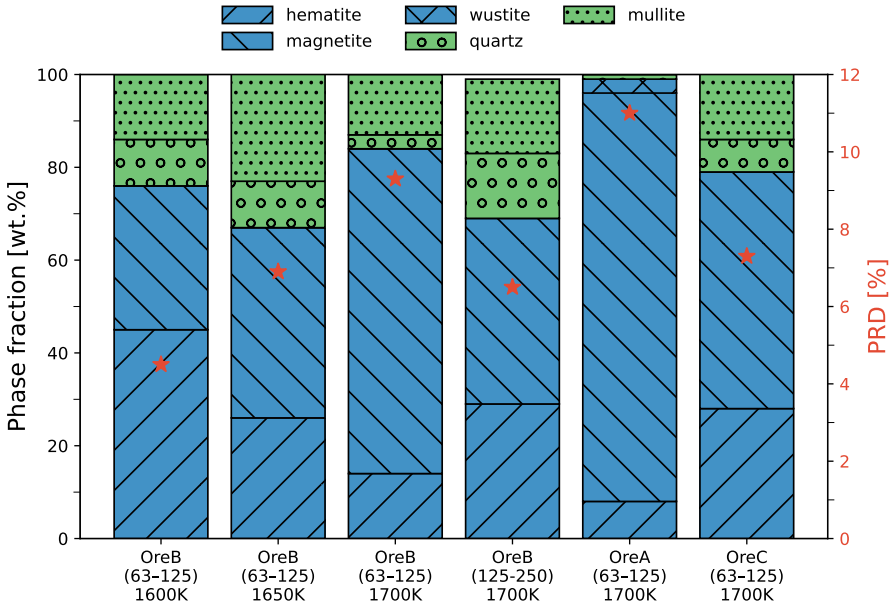


Figure 6.4: Mineralogical analysis of particulate products reduced in A7.5H_2 for 125 ms (exception OreB (125-250 μm) size fraction: 80 ms) (iron phases: blue; non-iron phases: green).

(63-125 μm) size fraction of OreA, OreB and OreC at particle residence times of approx. 125 ms. For OreB, examples are presented at 1600 K, 1650 K and 1700 K and for OreA and OreC at 1700 K. In addition, results for the larger size fraction of OreB (125-250 μm) are included for reduction at 1700 K and a residence time of 80 ms.

For all ores, the main iron-bearing phases detected were hematite and magnetite. Among them, OreA is the only ore where small amounts of wüstite formation could be observed. With increasing temperature, the hematite content after pre-reduction decreases while the magnetite content increases, demonstrating the positive impact of temperature on the reduction, even at very short residence times (125 ms). Clear differences in iron oxide phase evolution between the ores at 1700 K are also apparent. OreA exhibits the most advanced reduction, with the lowest hematite content, the highest magnetite fraction, and the presence of minor wüstite. OreB shows an intermediate reduction progress, while OreC remains least reduced. This is supported by the calculated PRDs. At 1700 K and 125 ms, OreA achieves a PRD of 11 % OreB of 9.3 % and OreC of 7.3 %. Comparing the larger size fraction of OreB to its finer counterpart, the coarser fraction reaches a PRD of 6.5 % at 1700 and 80 ms, similar to the fine fraction reduced at 1650 K for 125 ms (6.9 %). This similarity suggests that reduction of the larger particles is limited by their slower heating behavior at high-temperatures, as discussed in Chapter 4.

In addition to the iron oxides, two further phases are detected: a quartz phase (SiO_2) and a mullite phase ($Al_6Si_2O_113$). Quartz represents the primary gangue mineral and remains largely unreacted, though small portions react with alumina to form mullite. The mullite phase is found only in OreB and OreC, consistent with their higher Al_2O_3 contents

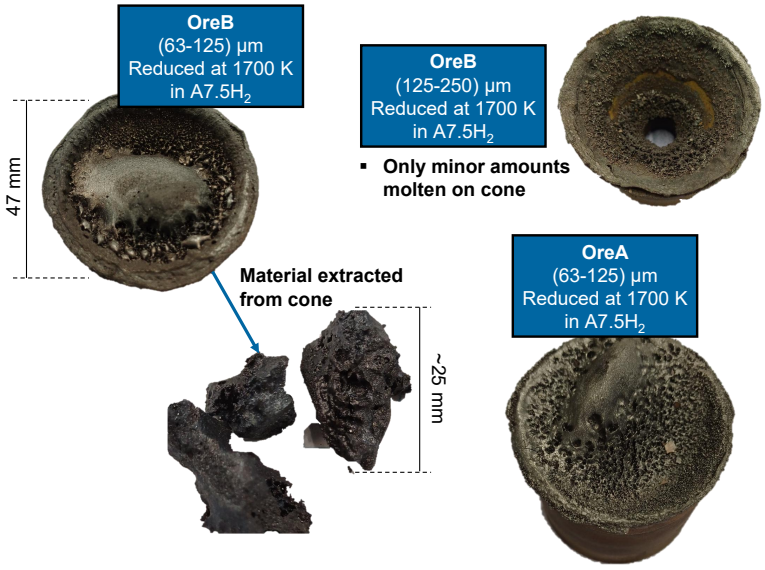


Figure 6.5: Cones with molten particle agglomeration after reduction of OreA and the two size fractions of OreB at 1700 K.

(5.30 - 6.17 wt.%) compared to OreA (2.96 wt.%). The overall lower gangue content of OreA likely contributes to its higher PRD, reflecting better reducibility under gas reduction conditions. Importantly, under in-flight conditions, no evidence of significant interaction between the iron oxides and gangue components is detected, implying minimal iron losses to silicate or alumina phases in the particulate samples.

During the experiments, some sample collection issues occurred, most likely due to particle melting. In the HTDF setup, particles fall through a collection cone before reaching the quenching zone, and substantial agglomeration of molten particles was observed on the cone after the experiments. Considering that the melting points of wüstite (≈ 1644 K [23]) and fayalite (≈ 1481 K [24, 25]) are considerably lower than that of magnetite (≈ 1869 K [23]), the formation of these phases increases the possibility of early melting. This behavior is consistent with the morphological analyses shown in Figure 6.3, where melting of both iron oxides and gangue materials is observed. Figure 6.5 shows some examples of the molten particle agglomeration on the collection cones. This phase is in the following termed "slag" phase.

While pronounced melting is observed for OreA and the smaller (63-125 μm) fraction of OreB, the larger (125-250 μm) fraction of OreB exhibited considerably less melting, likely due to slower particle heating, as discussed in Chapter 4. Because the particles are continuously collected during the experiment, a precise residence time for the molten fractions cannot be determined. Nevertheless, the resulting slag phases provide valuable insights into potential slag formation in liquid films that may occur and agglomerate during the pre-reduction stage of the HIsarna process. Therefore, XRD analysis and Rietveld fitting were also performed on the slag samples recovered at 1700 K. The complete

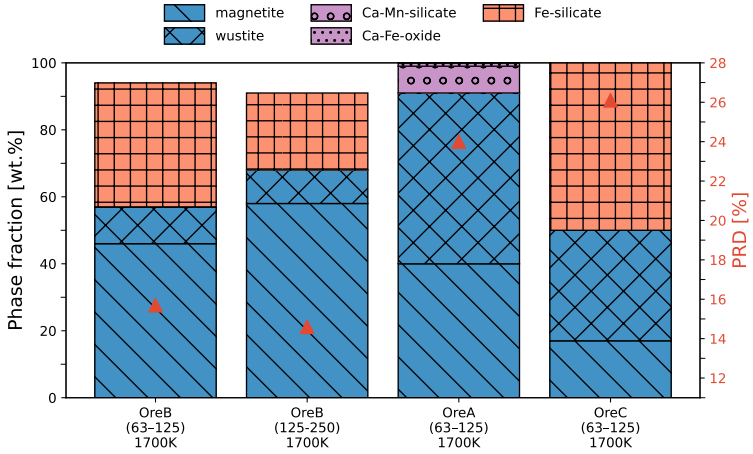


Figure 6.6: Mineralogical analysis of slag products reduced in A7.5H_2 (results of OreB don't add up to 100 % due to impurities from the reaction cone).

data is presented in Table D.1 and visualized in Figure 6.6.

As expected, the slag samples are more reduced than the particulate samples shown Figure 6.4. In all cases, hematite is no longer detected, indicating a complete conversion to, at least, magnetite. For both size fractions of OreB, magnetite remains the dominant phase, with only small amounts of wüstite present, corresponding to PRDs of 15.7 % (smaller fraction) and 14.6 % (larger fraction). The slag phases from OreA and OreC show higher wüstite contents, resulting in PRDs of 24.0 % and 26.1 %, respectively. These values should, however, be interpreted with caution, since the molten samples may not have experienced identical residence times. However, further insights can be drawn regarding reactions of the gangue and consequently slag formation. For OreA, little slag formation is observed, consistent with the particulate samples results. Only small amounts of iron are entrapped in a Ca-Fe-oxide phase (≈ 1 wt.%), along with ≈ 8 wt.% Ca-Mn-silicates. In contrast, OreB and OreC, which are both lower-grade ores, show significantly more slagging. For these samples, large amounts of Fe-silicate phases are identified, detected as fayalite (Fe_2SiO_4) or ahrensite (Fe_2SiO_4). The slag phase of OreC contains the highest Fe-silicate content (≈ 51 wt.%), followed by OreB (≈ 37 wt.% for the smaller and 23 wt.% for the larger fraction). Such extensive Fe-silicate formation can cause issues for ironmaking processes, as iron entrapped within silicate phases cannot be easily reduced to metallic iron in later process stages.

6.3.3. REDOX-TITRATION ANALYSES FOR PRD DETERMINATION

Another approach to determine the PRD from Eq. (6.2) is redox-titration, which quantifies the relative amounts of Fe^{2+} and Fe^{3+} in the reduced samples. In contrast to the Rietveld-based XRD fitting, where phase amounts are estimated from surface diffraction data, redox-titration measures the bulk reduction state by dissolving the entire sample. Therefore, the PRDs calculated via Redox-titration are expected to be more accurate

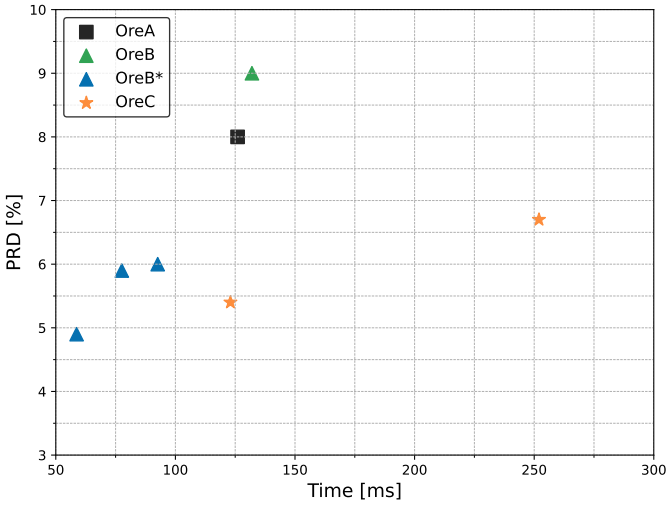


Figure 6.7: Influence of ore mineralogy on reduction in A7.5H_2 at 1700 K based on redox-titration (*corresponds to the larger size fraction of (125-250 μm).

compared to the PRDs calculated from the Rietveld fitting.

Figure 6.7 presents the PRDs obtained by redox-titration for OreA, both size fractions of OreB, and OreC, reduced under an A7.5H_2 atmosphere at 1700 K. The results clearly demonstrate the influence of both ore mineralogy and particle size on the reduction degree. Comparing the two size fractions of OreB, the larger particles show significantly lower PRDs, which can be attributed to their shorter residence times in the HTDF and slower heating rates. Nonetheless, even for the particles with a larger size fraction, a steady increase in PRD with only minor increase in residence time is observed, indicating ongoing reduction. Trends are evident between the different ores. OreB exhibits the highest PRDs, reaching approx. 9 %, followed by OreA with 8 % and OreC with notably lower values (5.4 %). However, OreC shows a pronounced increase in PRD (6.7 %) already by increasing the residence time from 125 ms to 250 ms , suggesting that the onset of reduction is more sensitive to time.

Next to the influence of ore mineralogy, a strong influence of the temperature on the PRD is observable. Figure 6.8 shows the effect of temperature on the PRD for OreB (63-125 μm) in A7.5H_2. At a residence time of approx. 125 ms, the PRD increases from 3.6 % at 1600 K to 9 % at 1700 K, highlighting strong temperature dependence of the reaction rate under flash conditions. Increasing the residence time leads to only marginal additional reduction. At 1600 K, the PRD rises from 3.6 % (125 ms) to 4.8 % (440 ms), and at 1650 K from 5.5 % (125 ms) to 5.7 % (450 ms). These values are still below the values reached at 1700 K within a much shorter reduction time.

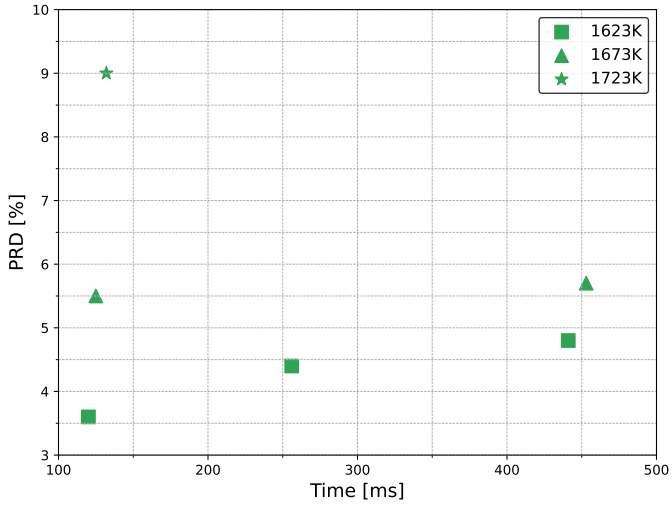


Figure 6.8: Effect of temperature and residence time on reduction in A7.5H_2 for the size fraction (63-125 μm) of OreB based on redox-titration.

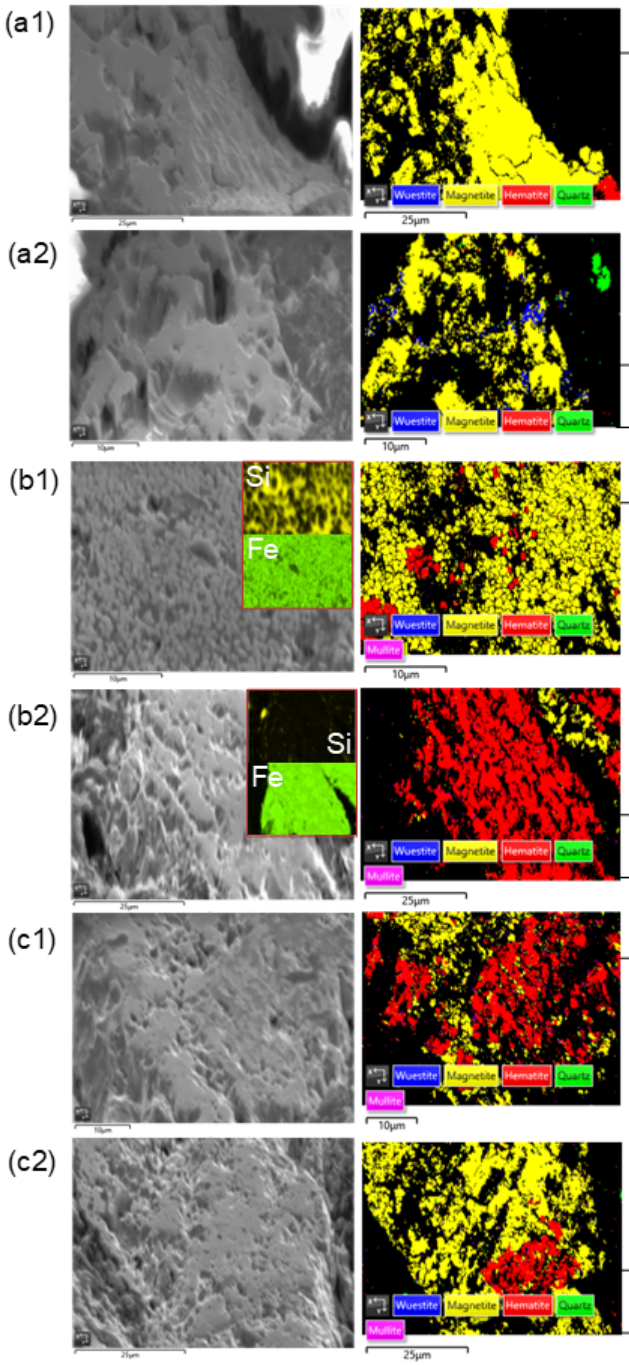
6.3.4. PHASE DISTRIBUTION

Figure 6.9 highlights differences in phase distribution among the various ores reduced at 1700 K for 125 ms in A7.5H_2, as determined by EBSD and EDS analyses. Although multiple particles were examined, the two particles showing the most representative and distinct reduction behavior for each ore are presented.

For OreA, magnetite is identified as the dominant phase, with hematite being almost completely reduced in both samples (a1) and (a2). In (a2), notable amounts of wüstite are also observed, which is absent for the other ores. Consistent with the XRD results, no mullite is detected in the EBSD maps of OreA.

In OreB, the reduced particles exhibit a more heterogeneous phase distribution. Certain regions show nearly complete conversion to magnetite, while others remain largely unreduced. Two characteristic particle types are identified. The first type features an island-like structure of magnetite grains surrounded by a distinct silica-rich matrix. The second particle type shows a more homogeneous distribution of iron phases. These contrasting morphologies may result from variations in gangue distribution within the ore or from the prior phase transformation of goethite to hematite.

Similar to OreB, OreC also demonstrates a wide variability in its reduction behavior. While (c2) contains 84.37 wt.% magnetite, (c1) exhibits only 33.65 wt.%. Despite OreC's higher goethite content compared to OreB, it does not display the same island-like morphology. The strong presence of hematite in both OreB and OreC indicates a less advanced reduction state compared to OreA.



	(a1)	(a2)
Hematite [wt.%]	3.1	0.91
Magnetite [wt.%]	95.95	87.95
Wustite [wt.%]	0.62	7.35
Quartz [wt.%]	0.32	3.79
Mullite [wt.%]	-	-
PRD [%]	10.87	12.22

	(b1)	(b2)
Hematite [wt.%]	9.53	92.84
Magnetite [wt.%]	89.04	6.2
Wustite [wt.%]	0.32	0.29
Quartz [wt.%]	0.61	0.23
Mullite [wt.%]	0.49	0.44
PRD [%]	10.0	0.78

	(c1)	(c2)
Hematite [wt.%]	62.17	13.46
Magnetite [wt.%]	33.65	84.37
Wustite [wt.%]	1.66	0.97
Quartz [wt.%]	1.29	0.74
Mullite [wt.%]	1.23	0.46
PRD [%]	4.29	9.7

Figure 6.9: Phase distribution based on EBSD analysis for two particles after reduction in A7.5H_2 at 1700 K and 125 ms of (a1)(a2) OreA, (b1)(b2) OreB and (c1)(c2) OreC, with the normalized phase statistics for the representative image and the corresponding pre-reduction degree and EDS elemental distribution of Fe and Si for both particles of OreB (b1)(b2) (wüstite: blue; magnetite: yellow; hematite: red; quartz: green).

6.3.5. THE WATER-GAS SHIFT REACTION

Considering the reducing gas composition in HIsarna, the water-gas shift reaction (WGSR) (Eq. (6.4) becomes relevant due to the coexistence of $CO - CO_2 - H_2O - H_2$ at high temperatures. This reaction can influence the effective gas atmosphere during reduction [26, 27], particularly under suspension smelting conditions, where equilibrium favors CO and H_2O formation.

$$H_2O(g) + CO(g) \leftrightarrow CO_2(g) + H_2(g) \tag{6.4}$$

To assess the WGSR behavior during reduction, the off-gas composition was analyzed using a HIDEN mass spectrometer. Since N_2 and CO cannot be distinguished by this method, CO concentrations were calculated assuming N_2 stays inert and therefore unreacted. The detailed results of the individual experiments are provided in the appendix D in Figs. D.2 to D.8. As observed in these measurements, the gas composition seems to approach a saturated state during the reduction experiment. To put these values in perspective, Figure 6.10 summarizes the saturated values of CO, CO_2, H_2O and H_2 for selected experiments and compares them to the amounts of the gases in the input gas stream before the gas phase reactions and thermodynamic equilibrium values calculated with FactSage 7.0 [28]. The FactSage values are derived from Figure 5.8 in Chapter 5, for the specific temperature (1600, 1650 or 1700 K) and atmosphere (A7.5H_2 or A22.5H_2).

The results of Figure 6.10 indicate strong deviations between the measured, equilibrium (bars) and supplied (red dotted line) gas compositions, confirming that the WGSR proceeds significantly in suspension smelting conditions. The equilibrium calculations indicate that for both atmospheres (A7.5H_2 and A22.5H_2) the concentration of CO_2 and H_2 should be lower and the concentration of CO and H_2O are higher, compared to the input amount.

Even though measured CO_2 values are higher compared to the input and thermodynamic values, H_2 levels are significantly lower, especially compared to the input levels. Only a small fraction of the injected H_2 remains in the gas phase. The injection of A7.5H_2 (7.5% H_2) results in just approx. 0.5 % measured H_2, while A22.5H_2 leads to a higher but still low H_2-content of 2 %. Even though H_2 participates in the reduction of the iron oxides, this impact on H_2 consumption is negligible, due to the much higher amounts of the gas phase compared to the solid material charge. This indicates that the introduced hydrogen does not fully participate in the reduction reaction under these conditions.

The concentration of CO and H_2O are both higher than in the inlet gas, which is consistent with the equilibrium shift toward the CO/H_2O side at high temperatures. However, considering the FactSage equilibrium calculations, the increase did not reach its limit during the experiments, especially for H_2O.

Overall, the off-gas measured values during the experiments reveal that the WGSR leads to strong deviations compared to the input gas streams and the gas phase reactions have not reached thermodynamic equilibrium.

To evaluate deviations from thermodynamic equilibrium in more detail, the experimentally derived equilibrium constants K_{eq} are compared with the thermodynamic values calculated using the reactions module of FactSage 7.0 [29](Figure 6.11).

The apparent K_{eq} values are substantially higher than predicted, implying that the partial pressure ratio $(p_{H2} * p_{CO_2})/(p_{H2O} * p_{CO})$ exceeds the equilibrium value. This devi-

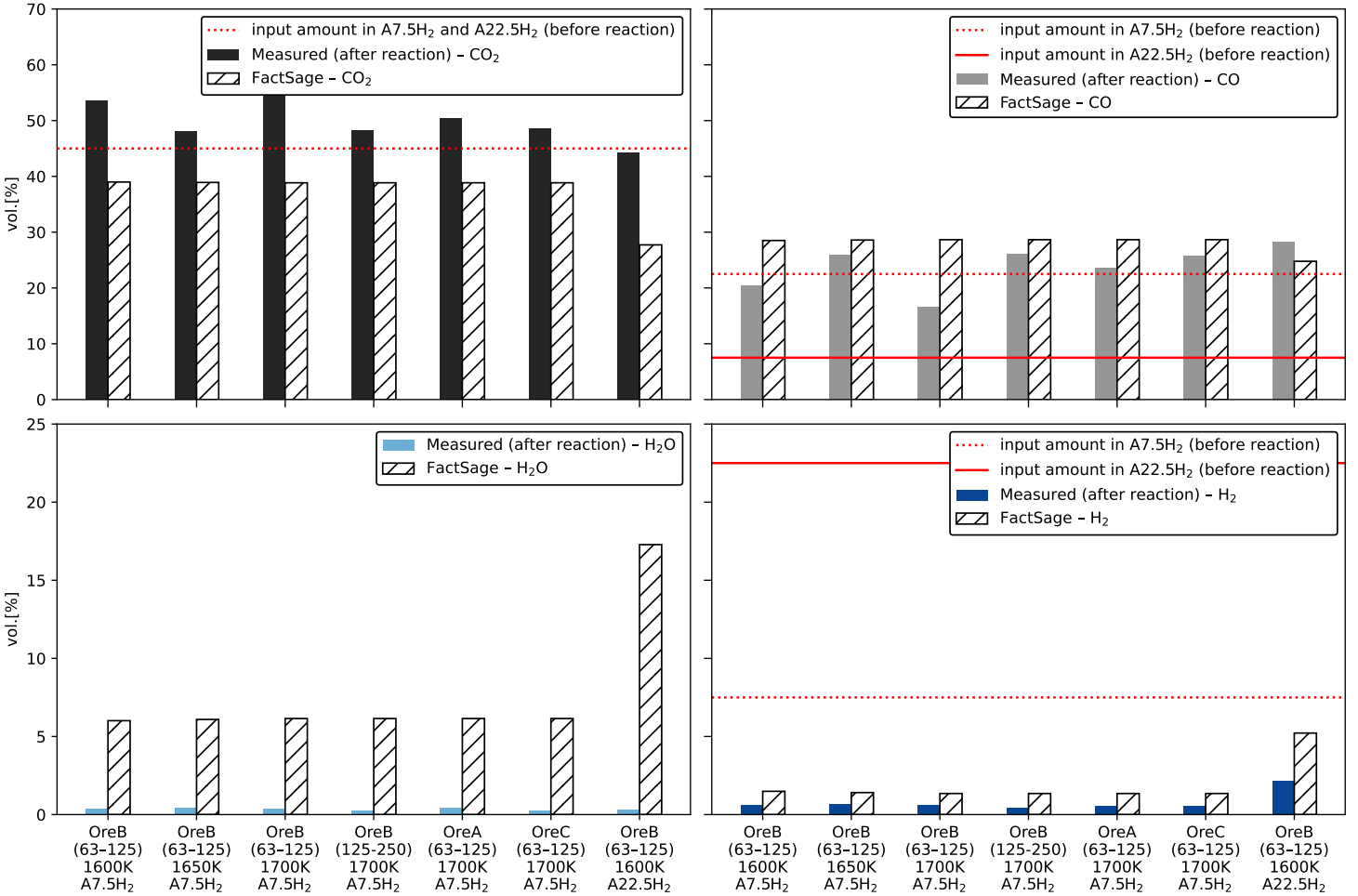


Figure 6.10: Comparison of online measured concentration of (a) CO_2, (b) CO, (c) H_2O and (d) H_2 before and after selected experiments with equilibrium values calculated by FactSage 7.0[28]. All values are in vol.%.

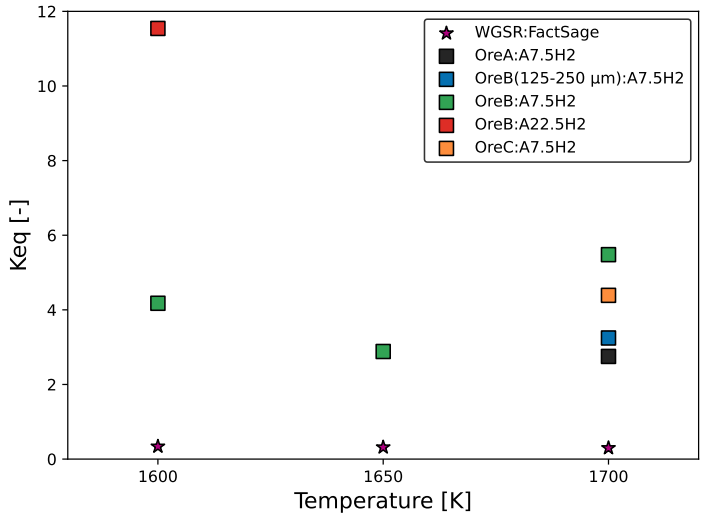


Figure 6.11: Comparison of experimentally and thermodynamically with FactSage 7.0 [29] calculated equilibrium constants for the WGSR.

ation does not reflect a true equilibrium shift but indicates that the WGSR does not reach equilibrium within the short gas residence times. The gas-phase kinetics are therefore too slow to reach equilibrium because of the too short residence time of the injected reducing gas and consequently limited gas utilization in flash conditions.

Because the gas flow is significantly higher compared to the amount of ore charged, the measured deviations mainly reflect kinetic limitations in the gas phase rather than changes induced by the ore reduction. A minor effect of water-release of the goethite phase is observed as K_{eq} is slightly higher for the goethite-containing ores (OreB and OreC) than for the purely hematite based ore (OreA). Overall, the results demonstrate that under flash conditions, the gas composition represents a non-equilibrium state, governed by gas-phase kinetics and gas residence time. The deviation from equilibrium increases with higher hydrogen levels, as shown by the significantly elevated K_{eq} values in A22.5H_2, compared to A7.5H_2. In contrast, temperature shows only a minor influence, since even the lowest tested temperature (1600 K) already exceeds the range where the WGSR equilibrium constant changes drastically [30, 31].

6.3.6. TGA GAS REDUCTION EXPERIMENTS

Since the flash reduction of the tested particle size fractions did not progress beyond magnetite formation, TGA experiments were performed to investigate the further reduction behavior of the ores under controlled conditions. This provides the possibility to investigate the impact of ore mineralogy on the gas reduction in later reduction stages and under longer particle residence times. As described in Table 6.2, the ores were first heated in Ar atmosphere to reach the limits of thermal decomposition before introducing the reducing gas mixtures to study the magnetite to wüstite reduction.

Figure 6.12(a) presents the whole range of the reduction degree, including both thermal decomposition and the following gas reduction. In alignment with the findings from Chapter 3, OreB and OreC exhibit higher thermal decomposition degrees than OreA during the thermal decomposition stage. After switching to reducing gas conditions, a distinct steep reduction occurs for all types of ores. Since the differences in total pre-reduction are small, Figure 6.12(b) provides a zoomed-in version of the plot focusing on the pre-reduction achieved after reducing gas injection.

Under A7.5H_2 atmosphere, the final pre-reduction for the (63-125 μm) size fraction are comparable. OreC reaches 24.8 %, OreA 24.6 %, and OreB 24.2 %. This indicates that mineralogical differences have only a minor effect once the ores have been thermally reduced to magnetite. Similarly, particle size shows limited influence, as the larger OreB fraction achieves a similar PRD ($\approx$ 24%). A slightly more pronounced effect is observed for the gas composition. An increase in hydrogen content from 7.5 % to 22.5 % raises the PRD of OreB from 24.2 % to 25.0 %. However, this also indicates that when the material is in contact with the reducing gas atmosphere for a long time (as in the TGA) the impact of higher H_2 levels decreases in significance.

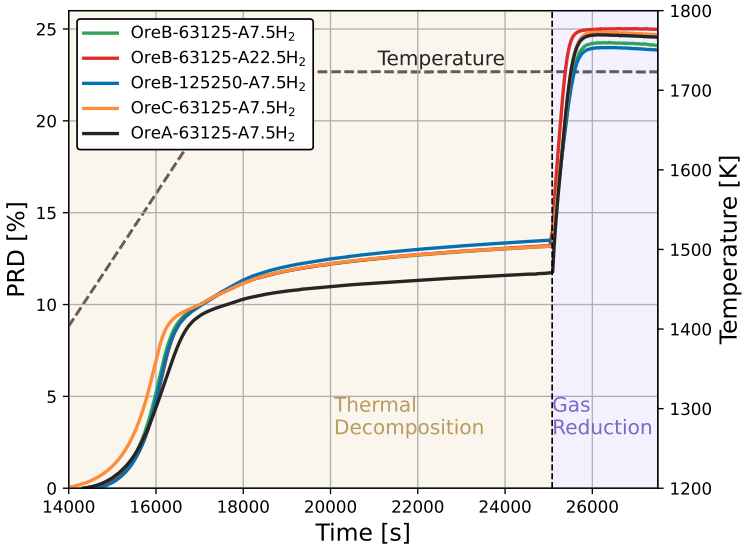
In contrast, both mineralogy and gas composition significantly affect the reaction rate. Figure 6.12(b) shows the time needed to increase the PRD from 13.65 to 23.5 %. Among the (63-125 μm) size fractions in A7.5H_2 atmosphere, OreA reduces the fastest (439 s), followed by OreC (472 s) and OreB(566 s). A larger particle size slows the reaction, shown by the OreB (125-250 μm) size fraction, requiring 614 s to reach the same PRD. The most pronounced effect is observed for the gas atmosphere, where increasing the H_2 content to 22.5 % shortens the required time to 344 s.

6.3.7. MECHANISMS OF PARTICULATE FRACTION REDUCTION

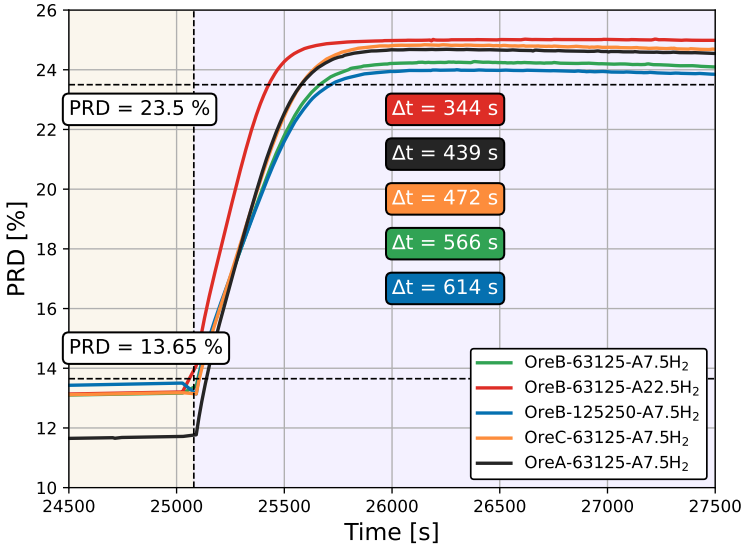
In this study, the pre-reduction degree (PRD) was determined using three analytical methods: chemical redox-titration, Rietveld fitting (XRD), and EBSD. Each method probes the sample differently, resulting in varying PRD values. Titration represents the total PRD, Rietveld fitting mainly reflects the particle surface reduction due to limited X-ray penetration depth, and EBSD highlights the maximum PRD within individual local particles. A comparison between the PRDs obtained by these three methods for the (63-125 μm) size fraction of OreA, OreB and OreC reduced at 1700 K for a residence time of 125 ms in A7.5H_2 is shown in Figure 6.13. For the EBSD measurement, the highest PRD observed in a particle is selected.

Overall, titration yields the lowest PRDs, while Rietveld fitting gives higher surface-based PRDs. A similar comparison has been made by Chen et al. [19], observing that the reduction degree measured by XRD is consistently higher compared to the reduction degree measured by chemical titration and this effect is stronger at higher reduction degrees. For OreA and OreC, the differences between bulk and surface PRDs are significant considering the investigated reduction range in this study (OreA: 8-11 %, OreC: 5.4-7.3 %), suggesting that reduction is concentrated near the surface. In contrast, OreB shows only a small difference (9-9.3 %), indicating a more uniform reduction through the particle.

Overall, morphology and mineralogy play key roles in the observed reduction behavior. SEM (Figure 6.3) and EBSD (Figure 6.9) analyses reveal that OreA has a compact, spherical structure and nearly complete conversion to magnetite. This is consistent with



(a)



(b)

Figure 6.12: Pre-reduction in the TGA with (a) presenting the whole reduction including thermal decomposition and gas reduction and (b) focusing on the pre-reduction achieved during gas reduction adding representative reduction times to increase the PRD from 13.65 to 23.5 % by gas reduction.

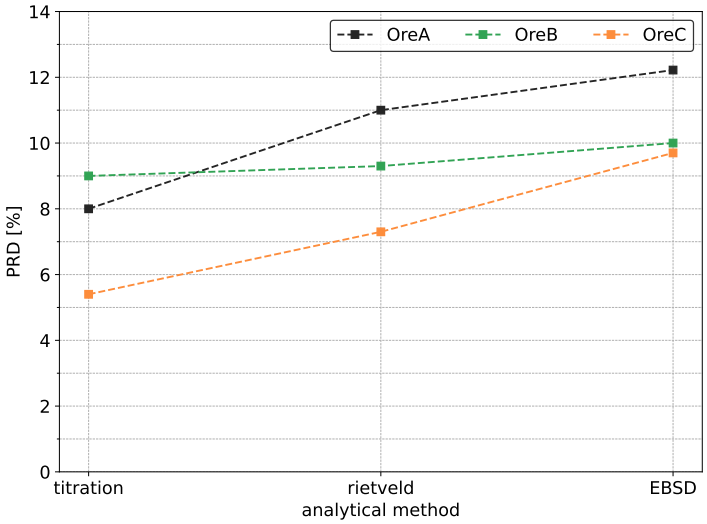


Figure 6.13: Overview of PRDs achieved based on analyses method for the size fraction (63-125 μm) of OreA, OreB and OreC reduced at 1700 K for a residence time of 125 ms under A7.5H_2 gas atmosphere.

a shrinking-core mechanisms, either limited by diffusion through the magnetite shell, the interfacial chemical reaction or a mixed mechanism of both [32–35]. Its low porosity prevents effective internal gas diffusion. In contrast, the mixed hematite-goethite ores (OreB and OreC) develop additional porosity and cracks from goethite decomposition which was also observed in Chapter 4 and agreed with studies by Ariyama et al. [36] and Strezov et al. [37]. This allows reducing gases to penetrate deeper, promoting internal nucleation of magnetite. However, EBSD still shows heterogeneity and residual hematite, reflecting incomplete reduction during the short residence time.

Comparing PRDs from the different methods supports these mechanistic interpretations. The surface-controlled reduction dominates for OreA (and partly for OreC), while pore-assisted internal nucleation is more relevant for OreB. Chen et al. [19] also interpreted that a higher deviation between reduction degrees calculated from chemical titration and XRD indicate a topo-chemical reaction control, as it is the case for OreA and OreC. Given the limited dataset, the calculated rate constants should be viewed as indicative, not definitive. Additional experiments with longer residence times and varying temperatures would be required for a more reliable activation energy determination.

However, first indications can be made based on this limited dataset. In order to obtain the reaction mechanism of OreB, the PRD over time is plotted and fitted with different kinetic models for the smaller size fraction of OreB at 1600 K and the larger size fraction at 1700 K. The chosen fitting models are the interface chemical reaction, internal diffusion based on the Ginstling-Brounsthein model and nucleation and growth based on the Avrami-Erofeev model. The mathematical formulations of the models are as following [38–41]:

$$\text{Interface chemical reaction: } 1-(1-PRD)^{\frac{1}{3}} = kt \tag{6.5}$$

$$\text{Internal diffusion: } 1-\frac{2}{3}PRD-(1-PRD)^{\frac{2}{3}} = kt \tag{6.6}$$

$$\text{Nucleation and growth: } \ln[-\ln(1-PRD)] = n\ln(t)+n\ln(k) \tag{6.7}$$

The rate constants of the interfacial chemical reaction and internal diffusion models are obtained from the slopes of the respective linear model plots vs. time. For the Avrami-Erofeev nucleation and growth model, the slope of the plot $\ln[-\ln(1-PRD)]$ vs. ln(t) gives the Avrami exponent n and k is obtained by the relationship "intercept = nln(k)". The model fits are shown in Figure 6.14. The fit is generally better for the (63-125 μm) size fraction, likely due to the broader range of residence times. For both data sets, the nucleation and growth model achieved the best fit, consistent with the microstructural analyses of magnetite nucleation within the ore particle.

All three models correlate reasonably well with the data, with R^2 values between 0.93 (chemical reaction controlled) and 0.98 (nucleation controlled) for the smaller, and 0.87 - 0.90 for the larger size fraction. The slightly higher R^2 for the Avrami-Erofeev model indicate that nucleation and growth kinetics describe the data best statistically. Because of the small dataset and similarity of the fits, it is difficult to confidently decide for the nucleation model, based only on the model fit. However, in combination with the EBSD phase distribution analysis in Figure 6.9 also pointing towards a nucleation mechanisms, the Avrami-Erofeev nucleation and growth model was chosen for further calculation of the activation energy. Figure 6.15 shows the Arrhenius fit for the Avrami-Erofeev model using a particle residence time of 125 ms at 1600, 1650 and 1700 K. For the fit an Avrami exponent n = 0.23 (from the 1600 K fit) was used. The resulting apparent activation energy is approx. 437 kJ/mol.

Various literature regarding flash ironmaking kinetics propose several reaction mechanisms and activation energies. Qu et al. [35, 42] found a dependency of temperature on the reaction mechanism in $CO-CO_2$ atmospheres for the hematite to wüstite reduction step. For a temperature range of 1550-1650 K the reaction is controlled by the interface chemical reaction (Ea = 270 kJ/mol), but shifts towards diffusion at temperatures of 1700 to 1750 K (Ea = 156 kJ/mol). Chen et al. [19, 22] proposed the hematite to wüstite conversion in $CO-CO_2-H_2-N_2$ atmospheres to be governed by nucleation and growth in a temperature range of 1710 to 1785 K with an apparent activation energy of 105.5 kJ/mol. They explained this significant lower activation energy, compared to the study of Qu et al., by the change in reaction mechanism due to temperature increase and lower-grade input material. However, they further mentioned a strong influence of the Avrami exponent on the activation energy, where a lower n, could lead to Ea > 250 kJ/mol. The complete reduction of hematite to metallic iron with either pure H_2 or CO atmosphere was studied at the University of Utah by Chen et al. [43, 44]. They also described the flash reduction process to be limited by a nucleation and growth mechanism and obtained an activation energy of 214 kJ/mol in H_2 and 231 kJ/mol in CO atmosphere.

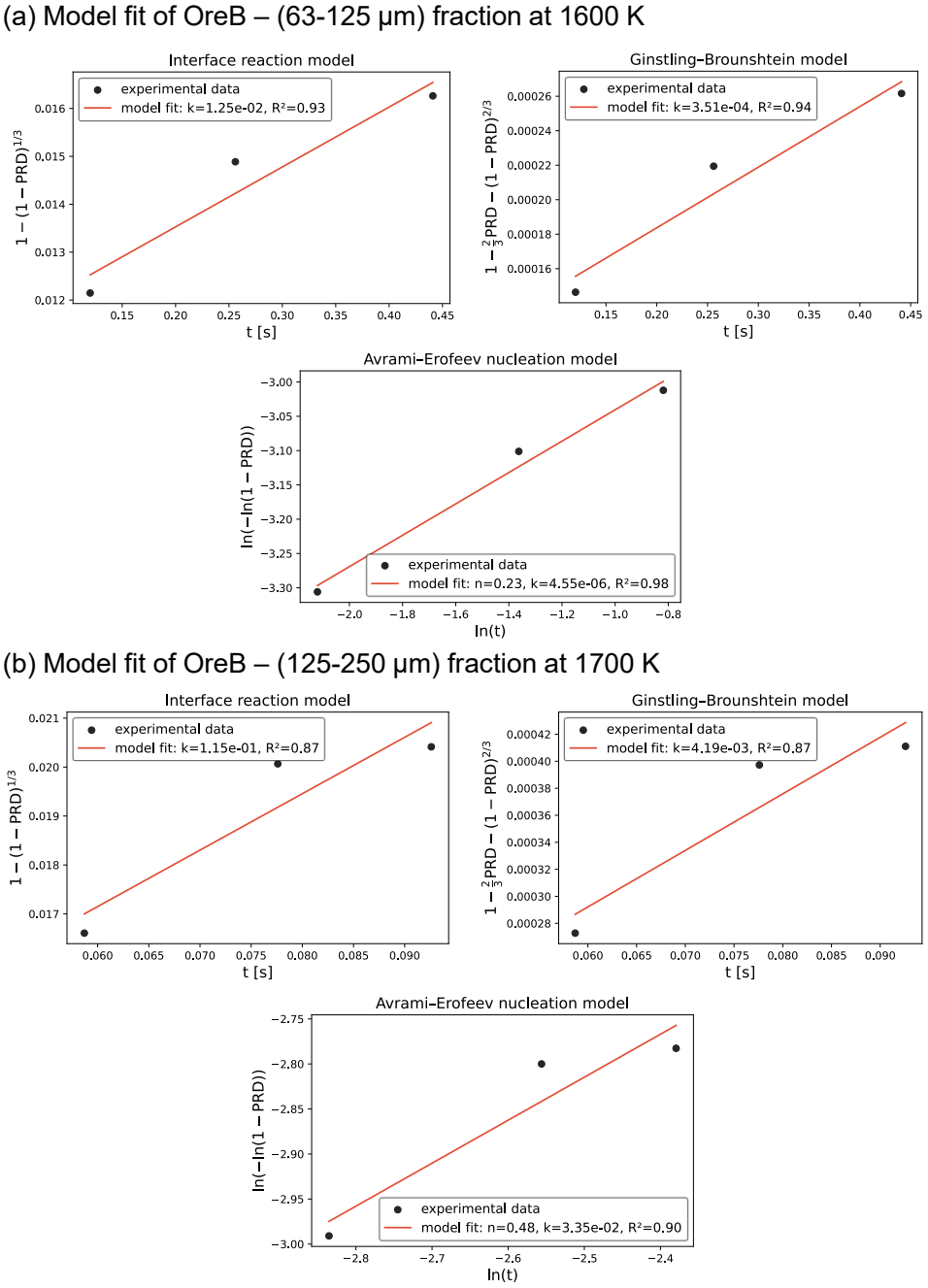


Figure 6.14: Model fitting for interface chemical reaction, diffusion (Ginstling-Brounshtein) and nucleation and growth (Avrami-Erofeev) for (a) OreB (63-125 μm) size fraction at 1600 K and OreB (125-250 μm) size fraction at 1700 K.

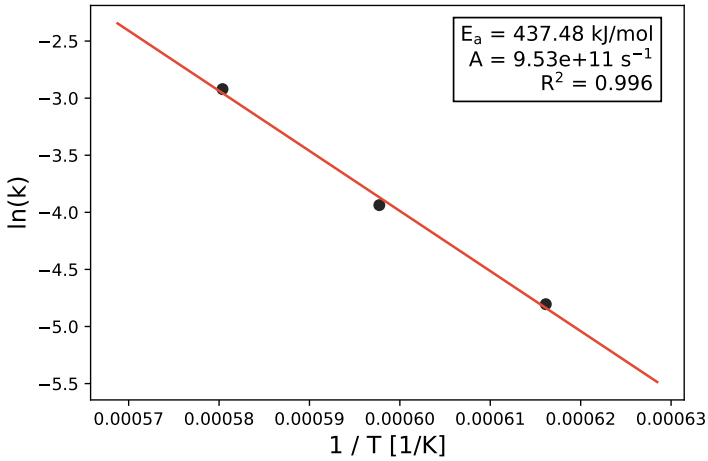


Figure 6.15: Arrhenius fitting of OreB (63-125 μm) size fraction for the nucleation and growth model at 1600, 1650 and 1700 K at a particle residence time of 125 ms.

6.3.8. INFLUENCE OF REDUCTION ATMOSPHERE

This chapter investigated the effect of a PCR = 60 % atmosphere under both flash and TGA conditions. Combining the findings from Chapter 4 (thermal decomposition and gas reduction in PCR = 95 %), this allows to differentiate between thermal decomposition and gas reduction contribution to the total reduction. Figure 6.16 summarizes the results of the thermal decomposition and gas reduction under PCR = 95 % from Chapter 4 and the gas reduction under PCR = 60 % from Chapter 6 for both flash and TGA reduction. For the specific condition of the flash reduction experiments, the experiment with the highest PRD was chosen.

In the TGA, particle size has no significant influence on either the total reduction or the relative contribution of the two mechanisms. The thermal decomposition contribution is only marginally higher for the larger fraction and the impact of gas reduction under PCR = 60 % and PCR = 95 % remains nearly identical for both size fraction. This can be explained by the liquid phase formation after thermal decomposition, decreasing the overall impact of particle size on the reduction.

In contrast, under flash conditions, reduction time becomes a crucial factor influencing the reduction mechanism. Thermal decomposition and gas–solid reduction occur simultaneously. A comparison between reduction by purely thermal decomposition (TD) and reduction in gas-enriched environments ($PCR95_{CO}$ and $A7.5H_2$) for the 63–125 μm size fraction shows that the PRD increases with increasing reducing gas content. However, the relatively small difference compared to reduction by thermal decomposition alone indicates that thermal decomposition still makes a major contribution to the overall reduction degree. For the larger fraction (125-250 μm), thermal decomposition was not measured but a similar behavior is expected, as the increase in PRD between PCR = 60 % and PCR = 95 % is small (approx. 2.3 %). Qu et al. [18] also made an estimation of the impact of gas reduction and thermal decomposition for a particle size fraction of 45-53

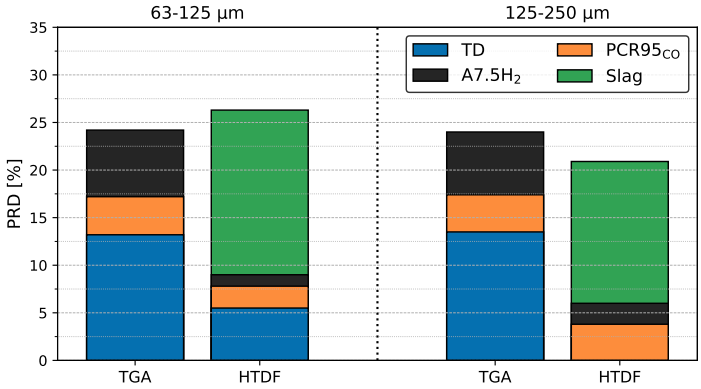


Figure 6.16: Impact of reaction atmosphere and particle size on the total (pre-)reduction degree of OreB in flash and TGA conditions (TD = thermal decomposition, $PCR95_{CO}$ = gas reduction in PCR = 95 %, $A7.5H_2$ = gas reduction in PCR = 60 %, Slag = agglomerated particles during flash reduction).

μm of almost pure hematite ore and a gas reduction atmosphere of 42.2%CO+57.8%CO_2. In the first 210 ms, the impact of thermal decomposition was much stronger than the impact of gas reduction. At 1600 K for example, thermal decomposition accounted for 4.3 % and gas reduction for 2.2 % of the reduction degree. Once thermal decomposition reaches its limits at the total conversion to magnetite, gas reduction accounts more to the further reduction to wüstite at increasing temperatures.

When comparing TGA and HTDF flash conditions, the PRDs under flash conditions are substantially lower due to the short reaction time. However, when the agglomerated particle fraction of the collection cone is also considered, which remains in contact with the reducing gases much longer than the suspended fine particles, comparable PRDs to the TGA can be achieved.

6.3.9. EXTENT OF REDUCTION UNDER ISOTHERMAL AND NON-ISOTHERMAL CONDITIONS

In this Chapter 6 the impact of ore mineralogy on the reduction in $A7.5H_2$ atmosphere under isothermal TGA conditions has been studied. To isolate the influence of gas reduction, the ores were first heated in Ar until thermal decomposition reaches equilibrium. As a result, the samples are already converted to magnetite, and some gangue components may have partially melted. This pre-treatment likely limits the beneficial effects of goethite in the ore.

In our previous study [45], we observed that after thermal decomposition all ores exhibit similar morphologies, supporting the conclusion that mineralogical effects are limited once hematite has fully transformed to magnetite. This likely explains the similar PRDs observed for all ores in isothermal $A7.5H_2$ conditions.

However, earlier work [21] (Chapter 5) showed that mineralogy influences the total pre-reduction in non-isothermal conditions. Figure 6.17 compares the total PRDs for OreA, OreB, and OreC under both isothermal and non-isothermal heating profiles in

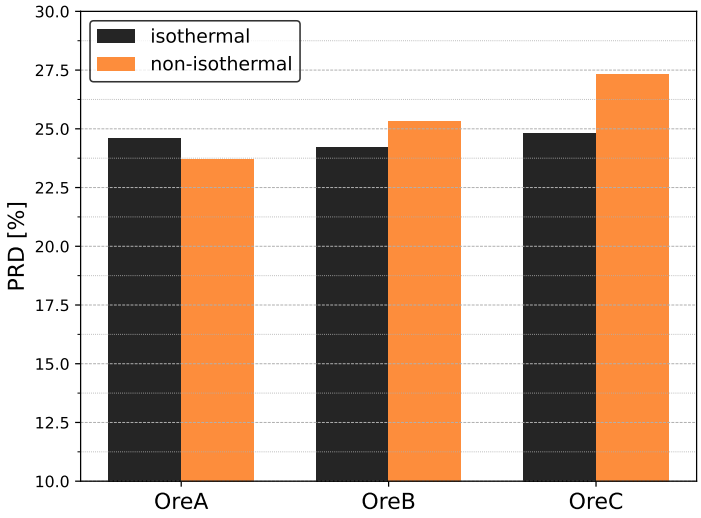


Figure 6.17: Extent of reduction under isothermal and non-isothermal conditions in A7.5H_2 atmosphere (non-isothermal data from Chapter 5[21].

A7.5H_2 atmosphere.

Under non-isothermal reduction conditions, a stronger mineralogical impact is observed and the total PRD increases with increasing goethite content (OreA → OreB → OreC). This finding highlights that during non-isothermal reduction, the ore's mineralogical and also physical properties, such as porosity, specific surface area, and true particle density, play a more significant role. Because the reducing gases are present from the beginning of heating, these structural differences can strongly affect the overall reduction achieved. Even though the flash reduction experiments are considered isothermal experiments, the impact of mineralogy and physical properties, as observed in the non-isothermal experiments in the TGA, are relevant. During flash reduction the particles are heated up in the isotherm in a short amount of time, while in contact with the reducing gases. Even though the experiment is set as isothermal, the heating behavior regarding a single particle could be considered non-isothermal, especially for larger particles.

6.4. CONCLUSIONS

This chapter provides a comprehensive investigation of the flash reduction behavior of three type of iron ores (OreA, OreB and OreC), combining morphological, mineralogical, and kinetic analyses. The results of (pre-)reduction studies under in-flight flash conditions are compared with thermogravimetric experiments (TGA), in which reduction times are significantly longer, allowing for investigation of the magnetite to wüstite reduction step after initial thermal decomposition. The main conclusions from the TGA and flash reduction experiments in the drop tube furnace are summarized below:

- **Reaction mechanisms:** The measured PRD values of the flash experiments vary

depending on the analytical technique. Chemical titration provides a bulk PRD, reflecting uniform particle reduction, whereas Rietveld fitting primarily captures surface reduction. At 1700 K and a particle residence time of 125 ms, higher PRDs are obtained by Rietveld fitting for OreA (11 %) and OreC (7.3 %) compared to chemical titration (OreA: 8 %, OreC: 5.5 %), while OreB shows similar values for both methods (titration: 9% and Rietveld: 9.3 %). SEM and EBSD analyses indicate that OreA forms compact, low-porosity particles after reduction, consistent with a surface-controlled reduction mechanism. In contrast, OreB and OreC exhibit higher initial porosity and develop additional cracking during reduction, promoting internal nucleation of magnetite in the goethite-containing ores. Consistently, kinetic analysis of OreB shows that the reduction under flash conditions follows a nucleation-and-growth mechanism, with an activation energy of 438 kJ/mol in the temperature range of 1600–1700 K.

- **Impact of atmosphere and particle size:** In the TGA experiments, a higher H_2 content in the reducing gas increases not only the total PRD, but also the reduction rate. An increase in particle size, however, has almost no influence on the total pre-reduction but slows the reduction rate. Thermal decomposition is a significant contributor for both the reduction in the TGA, but even more in the flash experiments in the HTDF.

- **Molten particle agglomeration:** A slag phase forms during the flash experiments, consisting of molten agglomerated particles. For the goethite-rich iron ores, high amounts of Fe-silicates are measured by XRD, which indicates the risk of iron loss in the slag phases at longer reduction times.

- **Isothermal vs. non-isothermal reduction in the TGA:** Under non-isothermal conditions, the ore mineralogy strongly influences the total (pre-)reduction, with goethite-rich ores achieving higher PRDs. In contrast, isothermal conditions after thermal decomposition limit the impact of mineralogy, as all ores are largely converted to magnetite prior to gas reduction. This shows that goethitic ores are favorable for the first reduction step of hematite to magnetite, provided that the particles remain unmolten. For the following molten magnetite to wüstite reduction, the impact of ore mineralogy is marginal and lower-grade ores could potentially even limit the conversion due to high amounts of gangue.

- **Impact of WGSR:** Off-gas analyses indicates that the water-gas shift reaction is kinetically limited under flash conditions, leading to non-equilibrium gas compositions. The presence of goethite slightly influences local gas composition, but overall, the reduction kinetics are predominantly controlled by solid-gas interaction and not the gas-phase equilibrium. Nevertheless, the WGSR reduces the effective hydrogen availability (measured 0.5 - 2 % vs. 7.5 - 22 % input value) and increases water-vapor and CO concentration, thereby influencing the overall reduction efficiency.

REFERENCES

[1] H. Y. Sohn. Energy consumption and CO_2 emissions in ironmaking and development of a novel flash technology. **Metals** 10, 54 (2020). DOI: 10.3390/met10010054.

[2] H. Y. Sohn. From Sulfide Flash Smelting to a Novel Flash Ironmaking Technology. Celebrating the Megascale. Cham: Springer International Publishing, 2014, pp. 69–76.

[3] H. Y. Sohn and Y. Mohassab. Development of a Novel Flash Ironmaking Technology with Greatly Reduced Energy Consumption and CO_2 Emissions. **Journal of Sustainable Metallurgy** 2 (2016), pp. 216–227. DOI: 10.1007/s40831-016-0054-8.

[4] H. K. Pinegar, M. S. Moats, and H. Y. Sohn. Process Simulation and Economic Feasibility Analysis for a Hydrogen-Based Novel Suspension Ironmaking Technology. **steel research international** 82 (2011), pp. 951–963. DOI: 10.1002/srin.201000288.

[5] H. K. Pinegar, M. S. Moats, and H. Y. Sohn. Flowsheet development, process simulation and economic feasibility analysis for novel suspension ironmaking technology based on natural gas: Part 1 – Flowsheet and simulation for ironmaking with reformerless natural gas. **Ironmaking & Steelmaking** 39 (2012), pp. 398–408. DOI: 10.1179/1743281211Y.0000000053.

[6] H. K. Pinegar, M. S. Moats, and H. Y. Sohn. Flowsheet development, process simulation and economic feasibility analysis for novel suspension ironmaking technology based on natural gas: Part 2 – Flowsheet and simulation for ironmaking combined with steam methane reforming. **Ironmaking & Steelmaking** 40 (2013), pp. 32–43. DOI: 10.1179/030192312X13345671456851.

[7] H. Y. Sohn. Suspension Hydrogen Reduction of Iron Ore Concentrate in AISI/DOE Technology Roadmap Program for the Steel Industry. Tech. rep. Utah: American Iron and Steel Institute, 2008.

[8] K. Meijer, M. Denys, J. Lasar, J.-P. Birat, G. Still, and B. Overmaat. ULCOS: ultra-low CO_2 steelmaking. **Ironmaking & Steelmaking** 36 (2009), pp. 249–251. DOI: 10.1179/174328109X439298.

[9] K. Meijer, C. Zeilstra, C. Teerhuis, M. Ouwehand, and J. van der Stel. Developments in Alternative Ironmaking. **Transactions of the Indian Institute of Metals** 66 (2013), pp. 475–481. DOI: 10.1007/s12666-013-0309-z.

[10] K. Meijer, C. Guenther, and R. J. Dry. HIsarna Pilot Plant Project. METEC InSteelCon 2011, 2011.

[11] Z. Yan, T. T. Htet, J. Hage, K. Meijer, and Z. Li. HIsarna Process Simulation Model: Using FactSage with Macro Facility. **Metallurgical and Materials Transactions B** 54 (2023), pp. 868–879. DOI: 10.1007/s11663-023-02732-5.

[12] P. C. Cavaliere. Hydrogen Assisted Direct Reduction of Iron Oxides. Springer International Publishing, 2022. ISBN: 9783030980566. DOI: 10.1007/978-3-030-98056-6.

[13] T. Dufty. Calix Zesty Tech – Zero Emissions Iron and Steel – KS5 Pilot Plant Study Report. 2023. URL: https://arena.gov.au/knowledge-bank/calix-zesty-tech-zero-emissions-iron-and-steel-ks5-pilot-plant-study-report/.

[14] B. Mokhtarani, M. Jafarian, S. Sabah, T. Dufty, G. Brooks, W. Saw, A. Chinnici, and G. J. Nathan. New Insights Into Hydrogen Reduction of Hematite in an Indirectly Heated Flash Reactor from Measurements and First-Order Modeling. **Metallurgical and Materials Transactions B** 56 (2025), pp. 1928–1941. DOI: 10.1007/s11663-025-03465-3.

[15] S. Seetharaman, R. Guthrie, A. McLean, S. Seetharaman, and H. Y. Sohn. Treatise on Process Metallurgy Volume 3: Industrial Processes. 2024. DOI: 10.1016/C2020-0-01069-8.

[16] C. Ormston, Y. Xia, T. Dufty, S. Sabah, S. Al-Assafi, A. Okely, J. Fu, S. V. Dorp, A. Rhamdhani, G. Brooks, M. Sceats, and M. Boot-Handford. Breakthrough Pilot Testing Results for the Hydrogen Direct Flash Reduced Iron Process. Association for Iron & Steel Technology, 2025, pp. 2251–2265. DOI: 10.33313/389/240.

[17] Y. Qu, Y. Yang, Z. Zou, C. Zeilstra, K. Meijer, and R. Boom. Thermal decomposition behaviour of fine iron ore particles. **ISIJ International** 54 (2014), pp. 2196–2205. DOI: 10.2355/isijinternational.54.2196.

[18] Y. Qu, Y. Yang, Z. Zou, C. Zeilstra, K. Meijer, and R. Boom. Melting and reduction behaviour of individual fine hematite ore particles. **ISIJ International** 55 (2015), pp. 149–157. DOI: 10.2355/isijinternational.55.149.

[19] Z. Chen, C. Zeilstra, J. van der Stel, J. Sietsma, and Y. Yang. Reduction Kinetics of Fine Hematite Ore Particles in Suspension. **Metallurgical and Materials Transactions B** 52 (2021), pp. 3393–3402. DOI: 10.1007/s11663-021-02269-5.

[20] J. Hage, C. Zeilstra, J. van Boggelen, K. Meijer, J. van der Stel, and T. Peeters. HIsarna: Benefits of an Innovative Smelting-Reduction Ironmaking Technology. AISTech 2021, 2021, pp. 1388–1399. DOI: 10.33313/382/143.

[21] P. Leerhoff, J. C. Brouwer, C. Zeilstra, K. Meijer, J. van der Stel, S. T. Abrahami, N. Dogan, and Y. Yang. Impact of H_2-enrichment and ore mineralogy on the reduction of varying iron ores in suspension smelting ironmaking. **Powder Technology** 468 (2026). DOI: 10.1016/j.powtec.2025.121570.

[22] Z. Chen, C. Zeilstra, J. van der Stel, J. Sietsma, and Y. Yang. Reduction Mechanism of Fine Hematite Ore Particles in Suspension. **Metallurgical and Materials Transactions B** 52 (2021), pp. 2239–2252. DOI: 10.1007/s11663-021-02173-y.

[23] C. W. Bale, E. Bélisle, P. Chartrand, S. A. Decterov, G. Eriksson, A. E. Gheribi, K. Hack, I. H. Jung, Y. B. Kang, J. Melançon, A. D. Pelton, S. Petersen, C. Robelin, J. Sangster, P. Spencer, and M.-A. V. Ende. FactSage Thermochemical Software and Databases – 2010 – 2016. **Calphad** 54 (2016), pp. 35–53.

[24] L. S. Darken. Melting Points of Iron Oxides on Silica; Phase Equilibria in the System Fe-Si-O as a Function of Gas Composition and Temperature. **Journal of the American Chemical Society** 70 (1948), pp. 2046–2053.

[25] H. Ren, X. Min, Y. Ke, Y. Wang, C. Peng, Y. Li, and C. Zhang. Mechanism study of lime decomposing fayalite melt: Thermodynamic basis for the sustainable and efficient recovery of iron resources from copper slag. **Journal of Cleaner Production** 462 (2024), p. 142678. DOI: 10.1016/j.jclepro.2024.142678.

[26] D. S. Newsome. The Water-Gas Shift Reaction. **Catalysis Reviews** 21 (1980), pp. 275–318. DOI: 10.1080/03602458008067535.

[27] G. K. Reddy and P. G. Smirniotis. Introduction About WGS Reaction. Elsevier, 2015, pp. 1–20. DOI: 10.1016/B978-0-12-420154-5.00001-2.

[28] CRCT -ThermFact Inc. and GTT-Technologies. FactSage, Equilib Module. 2015. URL: https://factsage.com/.

[29] CRCT - ThermFact Inc. and GTT - Technologies. FactSage, Reactions Module. 2015. URL: https://factsage.com.

[30] J. Li, P. Wang, L. Zhou, and M. Cheng. The Reduction of Wustite with High Oxygen Enrichment and High Injection of Hydrogenous Fuel. **ISIJ International** 47 (2007), pp. 1097–1101. DOI: 10.2355/isijinternational.47.1097.

[31] M. Bahgat, K. S. A. Halim, H. A. El-Kelesh, and M. I. Nasr. Fundamental Study of Water-Gas Shift Reaction in Ironmaking Process. 2012.

[32] O. Levenspiel. Fluid-Particle Reactions: Kinetics. 3rd ed. John Wiley & Sons, 1999.

[33] Y. H. Han, J. S. Wang, R. Z. Lan, L. T. Wang, X. J. Zuo, and Q. G. Xue. Kinetic analysis of iron oxide reduction in top gas recycling oxygen blast furnace. **Ironmaking & Steelmaking** 39 (2012), pp. 313–317. DOI: 10.1179/1743281211Y.0000000058.

[34] L. Y. Xing, Z. S. Zou, Y. X. Qu, L. Shao, and J. Q. Zou. Gas–Solid Reduction Behavior of In-flight Fine Hematite Ore Particles by Hydrogen. **Steel Research International** 90, 1800311 (2019). DOI: 10.1002/srin.201800311.

[35] Y. Qu, Y. Yang, Z. Zou, C. Zeilstra, K. Meijer, and R. Boom. Kinetic study on gas molten particle reduction of iron ore fines at high temperature. **Ironmaking and Steelmaking** 42 (2015), pp. 763–773. DOI: 10.1179/1743281215Y.0000000021.

[36] T. Ariyama, S. Isozaki, S. Matsubara, H. Kawata, and I. Kobayashi. Fluidization and Degradation Characteristics of Iron Ore Fines in Prereduction Fluidized Bed. **ISIJ International** 33 (1993), pp. 1220–1227. DOI: 10.2355/isijinternational.33.1220.

[37] V. Strezov, T. J. Evans, V. Zymla, and L. Strezov. Structural deterioration of iron ore particles during thermal processing. **International Journal of Mineral Processing** 100 (2011), pp. 27–32. DOI: 10.1016/j.minpro.2011.04.005.

[38] E. A. Giess. Equations and Tables for Analyzing Solid-state Reaction Kinetics. **Journal of the American Ceramic Society** 46 (1963), pp. 374–376. DOI: 10.1111/j.1151-2916.1963.tb11754.x.

[39] C. F. Dickinson and G. R. Heal. Solid–liquid diffusion controlled rate equations. **Thermochimica Acta** 340-341 (1999), pp. 89–103. DOI: 10.1016/S0040-6031(99)00256-7.

[40] P. Pourghahramani and E. Forssberg. Reduction kinetics of mechanically activated hematite concentrate with hydrogen gas using nonisothermal methods. **Thermochimica Acta** 454 (2007), pp. 69–77. DOI: 10.1016/j.tca.2006.12.023.

[41] J. Christian and J. Christian. The Theory of Transformations in Metals and Alloys. 3rd ed. Elsevier Science & Technology, 2002.

[42] Y. Qu, Y. Yang, Z. Zou, C. Zeilstra, K. Meijer, and R. Boom. Reduction kinetics of fine hematite ore particles with a high temperature drop tube furnace. **ISIJ International** 55 (2015), pp. 952–960. DOI: 10.2355/isijinternational.55.952.

[43] F. Chen, Y. Mohassab, T. Jiang, and H. Y. Sohn. Hydrogen Reduction Kinetics of Hematite Concentrate Particles Relevant to a Novel Flash Ironmaking Process. **Metallurgical and Materials Transactions B** 46 (2015), pp. 1133–1145. DOI: 10.1007/s11663-015-0332-z.

[44] F. Chen, Y. Mohassab, S. Zhang, and H. Y. Sohn. Kinetics of the Reduction of Hematite Concentrate Particles by Carbon Monoxide Relevant to a Novel Flash Ironmaking Process. **Metallurgical and Materials Transactions B** 46 (2015), pp. 1716–1728. DOI: 10.1007/s11663-015-0345-7.

[45] P. Leerhoff, J. C. Brouwer, A. M. Armaki, C. Zeilstra, K. Meijer, J. van der Stel, S. T. Abrahami, N. Dogan, and Y. Yang. Characterisation of Varying Iron Ores and Their Thermal Decomposition Kinetics Under HIsarna Ironmaking Conditions. **Metals** 14, 1271 (2024). DOI: 10.3390/met14111271.

7

CONCLUSIONS AND RECOMMENDATIONS

The main objective of this thesis project was to understand the influence of input material, with special focus on mineralogy, and how H_2-enrichment influences the reduction behaviour and kinetics of varying iron ores during suspension smelting ironmaking processes. The main parameter of evaluation in this regard was the pre-reduction degree of the ores, analysed under multiple experimental conditions with varying input ores and reducing atmospheres. The research was carried out in the framework of the HIsarna® process developments by Tata Steel in IJmuiden, helping to understand the fundamentals of the process and support up-scaling of this technology. To achieve this, the main experimental work discussed in Chapter 3-Chapter 6 focused on several important aspects for suspension smelting. In Chapter 3, multiple iron ores (OreA, OreB, and OreC) were characterized in detail, followed by an analysis of their thermal decomposition behavior in a TGA (Ar atmosphere). Building up on that, Chapter 4 discussed the thermal decomposition and pre-reduction with low reducing gas atmospheres of the same ores under flash conditions. In Chapter 5 and Chapter 6, in addition to the impact of ore mineralogy, the H_2-enrichment was investigated. While Chapter 5 utilized only a TGA, Chapter 6 used both TGA and the HTDF. This chapter summarizes main conclusions drawn from this thesis and provides recommendations for further research.

7.1. CONCLUSIONS

Figure 7.1 summarizes the main conclusions of this thesis and their relevance to the pre-reduction stage of the HIsarna process. Pre-reduction in HIsarna takes place in a highly complex environment in which multiple physical and chemical phenomena occur simultaneously. One of the key advantages of HIsarna is its ability to process a wide range of input materials, making it essential to understand how different ore properties and mineralogies influence the overall reduction behaviour.

After ore injection at the top of the HIsarna furnace, the fine ores are immediately exposed to very high temperatures. As a result, the particles undergo rapid flash thermal decomposition, which was investigated with the HTDF. In this stage, goethite rich ores (OreB and OreC) exhibited superior behaviour compared to the purely hematite-based ore (OreA), based on the findings obtained in Chapter 4. While the hematite-based ore showed no significant structural changes, the presence of goethite in the ores led to pronounced cracking and fragmentation. These changes were initiated by the rapid release of water-vapour from within the ore matrix. The resulting increase in surface area, exposing additional accessible reduction sites, led to improved reduction during the thermal decomposition stage for goethite rich ores.

At the top of the HIsarna furnace, the post-combustion ratio is high (approx. 95 %), meaning that the contribution of gas phase reduction is initially limited. However, the post-combustion ratio decreases towards the lower end of the pre-reduction stage (approx. 60 %), leading to higher reducing gas contents in the atmosphere. Therefore, the influence of gas reduction increases with increasing falling distance and higher particle residence times. Considering the gas reduction kinetics, goethite-rich ores (OreB and OreC) displayed fundamentally different behaviour compared to the purely hematite-based ore (OreA). The dense and compact structure of OreA resulted in surface-controlled gas reduction. In contrast, the cracked and fragmented structure of the goethite ores promoted a nucleation and growth-controlled mechanism due to improved penetration

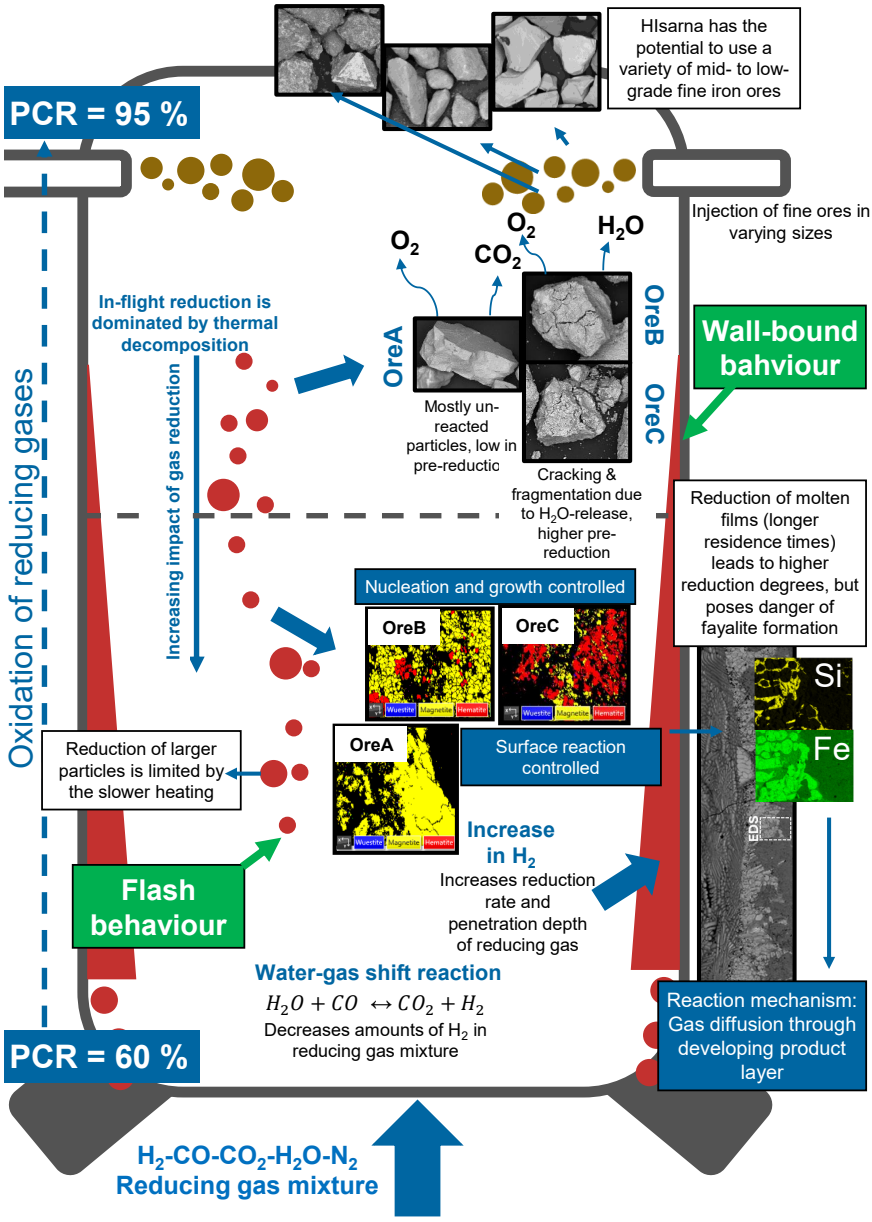


Figure 7.1: Summary on how the main conclusions of the study can be related to the pre-reduction in HIsarna ironmaking.

of the reducing gasses into the particle interior.

Particle size also affected the in-flight flash reduction. Larger particles (> 125 μm) experience delayed reduction under flash conditions as a result of slower particle heating rates and higher falling velocities. Nevertheless, with increasing residence time, and particle melting, the influence of particle size became less pronounced, indicating that residence time can partially compensate for potential particle size limitations.

In addition to the in-flight reduction, the HIsarna process also involves wall-bound reactions in the form of a molten agglomerated particle film. This behaviour was investigated in this thesis using the TGA (Chapter 3, Chapter 5, Chapter 6). The main conclusion from these experiments is the strong positive influence of H_2-enrichment on the reduction rate. Higher H_2-levels also increased the total pre-reduction degrees, which was attributed to deeper penetration of the reducing gas through the growing product layer, which also represented the rate limiting step of the reaction. Once the ores were fully molten, both particle size and ore-grade no longer had a significant influence on the pre-reduction degree. However, low-grade ores with high silica contents pose a risk of fayalite formation, which may reduce the amount of iron that remains accessible for the subsequent reduction stages.

While a strong effect of H_2 enrichment was observed in the TGA experiments, this effect was less pronounced during the flash reduction experiments conducted in the HTDF (Chapter 6). This discrepancy was caused by the water-gas shift reaction, which consumed H_2 and thereby reduced its availability for iron oxide reduction.

Overall, this thesis demonstrated that low-grade goethite-rich iron ore fines can be considered a valuable input material for HIsarna and suspension smelting ironmaking in general. This is primarily attributed to the improved physical properties, already initially present but also developed during in-flight flash reduction, which enhance gas accessibility, heating, and therefore reduction. Considering the formation of the molten particle film, no significant retardation of pre-reduction is expected with the use of lower-grade ores. However, the potential formation of fayalite must be carefully monitored and limited. Moreover, due to the occurrence of the water-gas shift reaction, H_2-enrichment in HIsarna must be applied with caution. Although higher H_2-levels were shown to increase reaction rates and the extent of reduction, the overall gas phase reactions of the water-gas shift reaction can significantly reduce the effective reduction potential. Therefore, the benefits of H_2-enrichment needs to be evaluated in the context of the complete reaction environment of the HIsarna process.

The following detailed conclusions are presented for the main parameters investigated in this thesis: material characterization, impact of ore mineralogy, H_2-enrichment, particle size and kinetic findings and reaction mechanisms.

MATERIAL CHARACTERIZATION

- The studied ores varied significantly in mineralogical and physical properties. Higher goethite content led to increased surface area and porosity, and lower true particle density.
- SEM analysis showed that the goethite-rich ores are more spherical in shape, whereas the purely hematite containing ores revealed a more angular and close-grained structure.

- The distribution of gangue varied between ores. OreA and OreC showed SiO_2 and Al_2O_3 either as inclusions on iron oxide particles or as distinct particles, whereas OreB's gangue overlapped more with iron phases.
- Goethite in OreB and OreC was heterogeneously distributed, with distinct particle types: nearly pure goethite, nearly pure hematite, or a mix of both.

IMPACT OF ORE MINERALOGY ON THERMAL DECOMPOSITION

- Higher goethite content enhanced reduction under non-isothermal TGA conditions, with OreC achieving highest reduction degrees (up to 13.8 %), followed by OreB (up to 12.9 %) and OreA (up to 10.8 %).
- Flash thermal decomposition of goethite to hematite caused particle cracking and fragmentation, affecting particle size and density (while cracking increase particle size and porosity, fragmentation decrease the size and increased the density).
- Under flash conditions, OreB showed higher early-stage reduction (80 ms at 1710 K), while OreC achieved higher overall reduction at longer residence times due to superior fragmentation.

IMPACT OF ORE MINERALOGY ON GAS REDUCTION

- Non-isothermal TGA results revealed that goethite-rich ores achieved higher pre-reduction, in the order, OreC (27.3 %) > OreB (25.3 %) > OreA (23.7 %).
- Flash reduction results in differences in particle morphology. OreA formed dense, low-porosity spheres, whereas OreB and OreC maintained higher porosity and cracking, promoting more uniform reduction throughout the particle.
- After gas reduction at longer particle residence times, Fe-silicate formation was observed in goethite-containing ores. This could potentially hinder further reduction.

IMPACT OF H_2-ENRICHMENT

- Under high PCR (95 %), H_2 had limited effect on the extend of reduction, likely due to the water-gas shift reaction significantly reducing available H_2.
- At lower PCRs (40-60 %), higher H_2 content increased both the reaction rate and the final reduction degree. For example, at 1773 K, increasing H_2 from 7.5 % to 22.5 % reduced the time to reach PRDs of 24-25 % from 502 s to 375 s. PCRs of 40 % further reduced the time to 206 s to reach a PRD of 27.1 %.
- In flash conditions, H_2 utilization was limited by the water-gas shift reaction, leading to lower measurable H_2 in the off-gas and technical challenges in quenching due to water condensation.

IMPACT OF PARTICLE SIZE

- In the TGA, particle size had a minor influence on the total reduction but significantly affected reaction rates. Smaller particles reduced faster than larger ones.

- In flash conditions, larger particles reduced more slowly due to slower heating and shorter in-flight residence time. However, typical HIsarna residence times are likely sufficient to pre-reduce even larger particles (> 125 μm).

KINETIC ANALYSIS IN THE TGA

- Goethite decomposed via a two-stage process. The first stage is controlled by chemical reaction, followed by a diffusion-controlled second decomposition stage. Higher goethite content increased the activation energy of the first step, but decreased the activation energy of the second stage.
- Hematite decomposition was chemical reaction controlled, with activation energies increasing in the order OreC < OreA < OreB .
- Isothermal gas reduction was limited by the diffusion of the reducing gas through the developing product layer. At high temperatures (1673 – 1773 K) and high amounts of H_2, the initial surface product layer likely formed very rapidly to be detected by the TGA and therefore could not act as a rate-limiting step. The activation energy within a given PCR decreased with increasing H_2 but increased as the PCR itself increased.

KINETIC ANALYSIS IN FLASH CONDITIONS

- Two distinct mechanisms were identified for flash thermal decomposition and reduction in PCR = 95 %: particle surface reactions forming a dense product layer, and reactions at the internal pore sites of some particles.
- Effective diffusion coefficients increased with goethite content, reflecting the morphological changes of thermally induced cracking and pore opening during thermal decomposition.
- Some calculated activation energies were unreasonably high, but overall, the activation energy for thermal decomposition is lower for OreC, probably due to enhanced reactivity by cracking and fragmentation.
- The activation energy for the reduction in $PCR95_{CO}$ was determined to by slightly higher compared to $PCR95_{H2}$ due to water-vapour formation by the water-gas shift reaction, increasing kinetic barriers.
- For a PCR of 60 %, reduction mechanisms differed among the ores. PRD analysis indicated that OreA shows a more surface-controlled reduction, while OreB displayed a more uniform reduction consistent with nucleation and growth behaviour.

7.2. RECOMMENDATIONS

This thesis presents an extensive investigation of the impact of ore mineralogy and hydrogen enrichment on the reduction behavior and kinetics under suspension smelting ironmaking conditions, specifically within the framework of the HIsarna process. Building upon these findings, several perspectives for future research are proposed. These

recommendations aim to enhance both experimental and analytical methodologies, as well as to extend the theoretical understanding of in-flight flash reduction mechanisms.

IMPROVEMENTS IN POST-ANALYSIS OF REACTED SAMPLES

The large range of particle sizes within the studied fractions results in differences in pre-reduction degrees and its kinetic mechanisms within particles of the same batch. A more accurate kinetic analysis requires a better control of a narrow particle size range with similar properties, while realistic conditions contain heterogeneous samples. To achieve this, more detailed post-analysis approaches are recommended. One approach is to create a narrower post-reduction size classification by sieving, thereby focusing on particles with comparable physical characteristics. However, this would neglect internal mineralogical heterogeneity, as it is common for low-grade iron ores. Therefore, a more comprehensive EBSD-based approach is advised. First, particles should be categorized according to their apparent reduction mechanisms. Then, a statistically significant number of representative particles should be analyzed by EBSD to quantify their reduction degree and phase evolution. Such an approach would enable a more reliable kinetic modeling, even within heterogeneous particle populations.

STEPWISE REDUCTION PROCESS

Results from both TGA and in-flight flash reduction experiments conducted in this thesis, along with previous studies [1, 2], confirm that thermal decomposition significantly affects the initial stages of reduction, particularly the hematite to magnetite conversion. All HIsarna-related studies carried out at Delft University of Technology [1–10] so far have employed hematite based raw materials under various partially reducing atmospheres, simulating multiple post-combustion conditions. However, due to the significant impact of thermal decomposition on the reduction, it is likely that finer particles have already transformed to magnetite before interacting with significant amounts of reducing gases. This aspect was partially explored in Chapter 5 and Chapter 6 through isothermal TGA experiments, where reducing gases were only introduced after thermal decomposition was completed, to isolate the magnetite to wustite reduction step. As discussed in Chapter 4 and previously reported by Strezov et al. [11] and Ariyama et al. [12], goethite particles undergo substantial structural changes upon thermal decomposition due to the release of water-vapor. In the current experimental approach in the HTDF, these changes occur simultaneously with the gas reduction in a short amount of time, similar to the HIsarna process. Future work should thus investigate the step-wise reduction sequence to evaluate reaction mechanisms and kinetics more precisely for each reaction. Particles could first undergo thermal decomposition under flash conditions, then be collected and re-introduced into the system for subsequent reduction under controlled atmospheres. This two-stage approach would disconnect the effects of thermal decomposition and reduction, allowing a more accurate assessment of the reduction behavior of particles in the early HIsarna pre-reduction zone and separate model assumption when studying the kinetic mechanism.

CFD-MODELLING OF PARTICLE HEATING

In Chapter 4, the heating of the fine ore particles was discussed in relation to the material properties. Results revealed a slower heating behavior of larger particles in the isothermal zone of the HTDF. This indicated that the reduction of larger particles in the HTDF does not necessarily proceeds isothermally due to the slow heating behavior. The co-existence of reduction and particle heating indicates a non-isothermal reduction behavior under extremely high particle heating rates. A CFD-simulation of the particle heating under reduction conditions in the HTDF could provide crucial information on the particle heating behavior and could potentially lead to a new approach in kinetic analysis of particles under flash reduction conditions using the drop-tube furnace.

REPETITION OF EXPERIMENTS

Obtaining reliable kinetic data in a drop-tube furnace requires a large number of experiments conducted at multiple temperatures and particle residence times. It is therefore recommended to increase the number of experimental repetitions and, where possible, to extend the ranges of temperatures and particle residence times in order to improve the statistical and practical reliability of the proposed reaction mechanisms, rate constants, and activation energies.

In this thesis, the positive effect of goethite in the ores on pre-reduction, attributed to cracking and fragmentation, is proposed. It is further recommended to broaden this investigation by systematically studying a wider temperature range in flash in-flight conditions, from the on-set of goethite thermal decomposition to temperatures exceeding 1773 K. By applying this approach to both ores, OreB and OreC, a more detailed overview can be established to identify the initiation of cracking and fragmentation, and to evaluate their dependence on temperature and particle residence time.

ADAPTATION OF WATER-VAPOR INJECTION

During this PhD project, the influence of hydrogen enrichment was studied. To better simulate gas atmospheres closer to the off-gases arising from the HIsarna smelting reduction vessel, which can contain substantial amounts of water-vapor, future work should consider controlled water-vapor injection into the drop-tube furnace.

A potential design is illustrated in Figure 7.2. Water from an external reservoir could be pumped via a roller pump to produce droplets at a defined feed rate. These droplets would be introduced into the reducing gas line stream before the pre-heater, where they would vaporize, forming a mixed gas-steam stream that enters the isothermal zone of the furnace.

Due to time constraints, this system was not implemented in the present work. However, its future application requires careful consideration of the water-gas shift reaction (WGSR), which becomes increasingly significant at the high temperature characteristic of suspension smelting. As observed in this thesis (Chapter 2,Chapter 4,Chapter 5,Chapter 6), the WGSR strongly favors water-vapor formation at these conditions. Thus, the amount of water-vapour addition should be adjusted to the real H_2O composition at the reaction temperatures, by considering the WGSR equilibrium. In the drop-tube furnace experiments, significant amounts of water-vapor were formed, particularly at hydrogen concentrations above 7.5 %. Increased condensation was observed in the quenching sec-

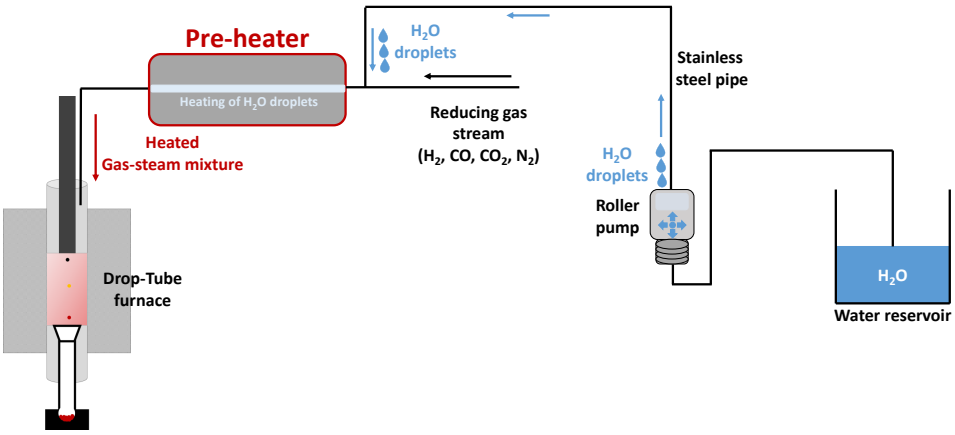


Figure 7.2: Water-vapor injection in the drop-tube furnace with a roller pump approach.

tion under such conditions, disrupting particle collection due to moisture accumulation (see Figure 7.3).

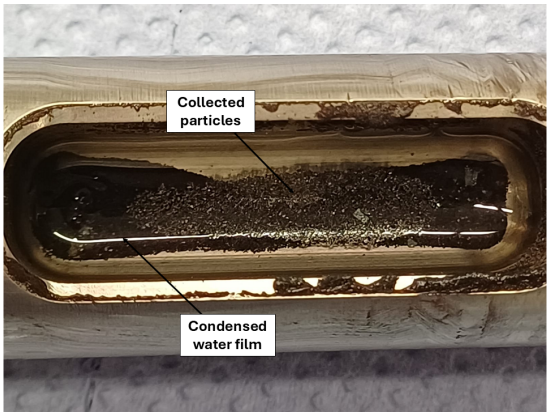


Figure 7.3: Agglomeration of condensed water-vapor in sample collector.

For future high hydrogen or steam-enriched experiments, the quenching system must be modified to handle larger water-vapor loads. Adjusting the cooling water temperature could mitigate condensation, but must be controlled carefully to prevent overheating and melting of water cooled components that extend into the isothermal zone of the furnace. However, achieving an optimal balance between preventing condensation and ensuring equipment safety will be essential.

Finally, it would be valuable to conduct a systematic kinetic study of the WGSR un-

der suspension smelting ironmaking conditions, particularly across varying hydrogen enrichment levels. This would provide insight into the dynamic gas-phase interactions that influence both reduction efficiency and gas composition during pre-reduction.

IMPACT OF FLUX MATERIAL ON SUSPENSION SMELTING IRONMAKING

Complementary research conducted within a master's thesis [13] in the framework of this PhD project examined the influence of flux addition (limestone and converter slag) on the thermal decomposition and pre-reduction behavior of OreA and OreB. The smaller size fraction (< 63 μm) was mixed with 5-50 wt.% of flux materials. The HIsarna pilot plant, which already operates with flux additions [14], could benefit from incorporating recycled steelmaking by-products such as converter slag, potentially enhancing process sustainability , circularity and minimizing landfilling. The objective of the thesis was to see how the converter slag performs compared to limestone as a fluxing agent. The impact of the fluxing agents is compared in terms of melting behavior, on-set temperature of hematite thermal decomposition, evolving mineralogy of iron and slag phases, and the difference in achieved pre-reduction degree.

Experiments were carried out using both a thermogravimetric analyzer (TGA, 25 mg samples) and a horizontal tube furnace (HTF, 6 g samples). The TGA experiments, conducted under Ar with a heating rate of 20 K/min to 1773 K, simulated rapid heating conditions, similar to HIsarna process, while the HTF experiments (3-5 K/min in N2, followed by 60 min isothermal at 1773 K) reflected slower reduction, trying to reach equilibrium behavior. The impact of the two flux materials on the pre-reduction for both the TGA and HTF experiments is presented in Figure 7.4.

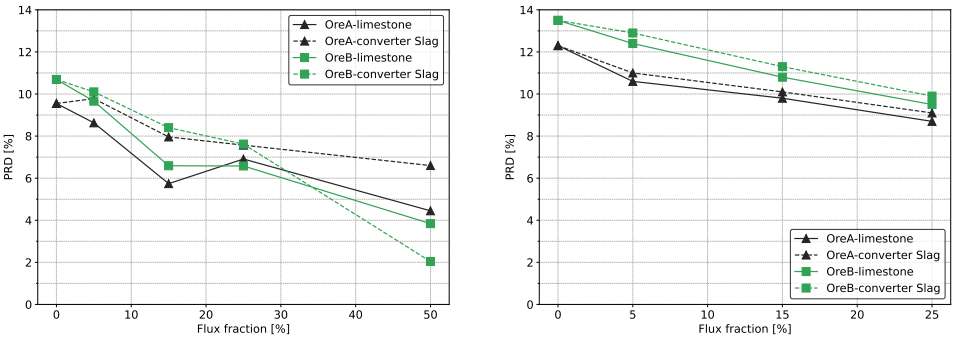


Figure 7.4: PRD results of (a) TGA and (b) HTF experiments at 1773 K for multiple flux mixtures of OreA and OreB, carried out in the framework of [13].

Both set-ups revealed a general decrease in pre-reduction degree with increasing flux content, though the effect was more pronounced under rapid heating. Importantly, converter slag exhibited less PRD retardation than limestone, suggesting its higher compatibility with fast reduction processes. However, liquid phase formation was found to occur more readily in limestone mixtures, lowering the onset temperature of hematite decomposition. Even though it is still unclear which influence is the more crucial factor for the HIsarna ironmaking process, the thesis already demonstrated the potential to

utilize converter slag during the pre-reduction of HIsarna ironmaking.

Further research is recommended to investigate ore/flux mixtures under in-flight (flash) conditions in the drop-tube furnace. In particular, insights into flux-ore particle behavior and interaction are needed, as flux and ore particles may not mix effectively at low feed rates. The creation of a particle swarm during injection could promote agglomeration under realistic melting behavior. Once optimized, similar experiments should be extended to hydrogen-enriched suspension smelting atmospheres to assess the combined effects of flux composition and atmosphere impact on the pre-reduction and melting phenomena under suspension smelting relevant conditions.

REFERENCES

[1] Z. Chen, C. Zeilstra, J. van der Stel, J. Sietsma, and Y. Yang. Reduction Kinetics of Fine Hematite Ore Particles in Suspension. **Metallurgical and Materials Transactions B** 52 (2021), pp. 3393–3402. DOI: 10.1007/s11663-021-02269-5.

[2] Y. Qu, Y. Yang, Z. Zou, C. Zeilstra, K. Meijer, and R. Boom. Melting and reduction behaviour of individual fine hematite ore particles. **ISIJ International** 55 (2015), pp. 149–157. DOI: 10.2355/isijinternational.55.149.

[3] Y. Qu, Y. Yang, Z. Zou, C. Zeilstra, K. Meijer, and R. Boom. Kinetic study on gas molten particle reduction of iron ore fines at high temperature. **Ironmaking and Steelmaking** 42 (2015), pp. 763–773. DOI: 10.1179/1743281215Y.0000000021.

[4] Z. Chen, C. Zeilstra, J. van der Stel, J. Sietsma, and Y. Yang. Reduction Mechanism of Fine Hematite Ore Particles in Suspension. **Metallurgical and Materials Transactions B** 52 (2021), pp. 2239–2252. DOI: 10.1007/s11663-021-02173-y.

[5] Y. Qu, Y. Yang, Z. Zou, C. Zeilstra, K. Meijer, and R. Boom. Reduction kinetics of fine hematite ore particles with a high temperature drop tube furnace. **ISIJ International** 55 (2015), pp. 952–960. DOI: 10.2355/isijinternational.55.952.

[6] Y. Qu, Y. Yang, Z. Zou, C. Zeilstra, K. Meijer, and R. Boom. Thermal decomposition behaviour of fine iron ore particles. **ISIJ International** 54 (2014), pp. 2196–2205. DOI: 10.2355/isijinternational.54.2196.

[7] Z. Chen, C. Zeilstra, J. van der Stel, J. Sietsma, and Y. Yang. Thermal Decomposition Reaction Kinetics of Hematite Ore. **ISIJ International** 60 (2020), pp. 65–72. DOI: 10.2355/isijinternational.ISIJINT-2019-129.

[8] Z.-y. Chen, Y.-x. Qu, C. Zeilstra, J. van der Stel, J. Sietsma, and Y.-x. Yang. Prediction of density and volume variation of hematite ore particles during in-flight melting and reduction. **Journal of Iron and Steel Research International** 26 (2019), pp. 1285–1294. DOI: 10.1007/s42243-019-00265-3.

[9] P. Leerhoff, J. C. Brouwer, A. M. Armaki, C. Zeilstra, K. Meijer, J. van der Stel, S. T. Abrahami, N. Dogan, and Y. Yang. Characterisation of Varying Iron Ores and Their Thermal Decomposition Kinetics Under HIsarna Ironmaking Conditions. **Metals** 14, 1271 (2024). DOI: 10.3390/met14111271.

[10] P. Leerhoff, J. C. Brouwer, C. Zeilstra, K. Meijer, J. van der Stel, S. T. Abrahami, N. Dogan, and Y. Yang. Impact of H_2-enrichment and ore mineralogy on the reduction of varying iron ores in suspension smelting ironmaking. **Powder Technology** 468 (2026). DOI: 10.1016/j.powtec.2025.121570.

[11] V. Strezov, T. J. Evans, V. Zymla, and L. Strezov. Structural deterioration of iron ore particles during thermal processing. **International Journal of Mineral Processing** 100 (2011), pp. 27–32. DOI: 10.1016/j.minpro.2011.04.005.

[12] T. Ariyama, S. Isozaki, S. Matsubara, H. Kawata, and I. Kobayashi. Fluidization and Degradation Characteristics of Iron Ore Fines in Prereduction Fluidized Bed. **ISIJ International** 33 (1993), pp. 1220–1227. DOI: 10.2355/isijinternational.33.1220.

[13] A. Bartolo. Use of Converter Slag as a Flux Material for HIsarna Ironmaking. MA thesis. Delft University of Technology, 2025.

[14] Z. Yan, T. T. Htet, J. Hage, K. Meijer, and Z. Li. HIsarna Process Simulation Model: Using FactSage with Macro Facility. **Metallurgical and Materials Transactions B** 54 (2023), pp. 868–879. DOI: 10.1007/s11663-023-02732-5.

ACKNOWLEDGEMENTS

As I mentioned in my prepositions, an experimental PhD is like a marathon, except you walk the first half and sprint the second. Even with training, you are still surprised by the strain it puts on you in the end. The journey of a PhD was certainly not an easy one, but many people made it significantly easier, and I am deeply grateful to all of them.

First of all, I would like to thank my supervisors: Yongxiang, Shoshan and Nes. Yongxiang and Shoshan, I still vividly remember the day when me and Joep joined you for our first visit to TU Delft. After completing both my Bachelor and Master at the same university, I was excited to experience a new academic environment, and you made this transition exceptionally easy for me. From the very beginning, I felt warmly welcomed, and I will always look back with appreciation on our discussions and shared time. When I started, the group was still small, which I valued at that time, as it allowed for close supervision and helped shape me into the PhD researcher I am today. I would further like to thank Nes, who joined halfway through my PhD as the group expanded. I am very grateful that you became part of my project, as your support significantly strengthened both the direction and quality of my work. Thank you all for your support and guidance throughout my PhD journey.

This project (CHIRON) was a small standalone project in cooperation with M2i and Tata Steel in IJmuiden. I would like to thank all project partners for their support throughout. Viktoria Savran, Jan van der Stel, and Koen Meijer, thank you for the many valuable discussions and continuous guidance. A special thank you goes to Christiaan Zeilstra, my direct contact at Tata Steel and a member of my defense committee. I greatly appreciate our long-standing collaboration and discussions over the years. These close interactions strongly supported my research development, and I am grateful to have contributed to the HIsarna development efforts.

A PhD journey is never a solitary one, and I have been fortunate to meet many wonderful colleagues along the way. As the list is long, I sincerely apologize to anyone I may have inadvertently missed. Many thanks to: Camila, Mohammed, Nirmal, Roberta, Frank, Jithin, Soroush, Vitória, Arash, Jaji, Eszter, Can, Aswin, Khatereh, Virginia, Jasper, Arjun, Alice, José, Keer, Gaojie, Jhon, Robert, Tobia, Marco, Yeli, Zhaorui, Jia-Ning, Saurabh, Pritish, Iftikhar, Radhey, Ehsan, Prakash, Jungwan, Konstantina, Ishank, and many more. Among them, a few people deserve special mention for the significant impact they had on my journey. Gautham, thank you for making the entire experience so much more enjoyable. Thank you for the laughs, the rants, and the endless sports discussions. Fabian, the best hugger at TU Delft and probably in the whole Netherlands. Joep, thank you for sharing this journey with me from day one. I could not have imagined a better companion for it. Tim, thank you for being the first person who truly made me feel at home at TU Delft. Luís, thank you for shaping my character. In a supportive way, of course. Amir, thank you for your support at work and the competition outside of it. I appreciated every moment. Daniel, thank you not only for being my only equal in beach volleyball, but

also for always supporting me in difficult times. Elsa, thank you for the excellent book recommendations. One day I will probably read them. And lastly, many thanks to Julia and Devi, without whom I would have shed many more tears in the lab.

It has been a pleasure to supervise one master student during my PhD. I would like to thank Alexandra for giving me the opportunity to take on this role so late in my PhD journey. It was an exciting experience, and I am very proud of the work we produced together in the challenging field of converter slag recycling within HIsarna ironmaking.

What is an experimental PhD without technical support? Most likely not a great experience. I would therefore like to thank all technicians who supported me along the way. Sean, thank you for starting in the lab with me during those challenging early days. Kees, Ruud, and Richard, thank you for your continuous help with analytical work supporting my PhD. I sincerely appreciate the time you invested in discussing my XRD results and helping me improve my complex microscopic analyses. Patrick, thank you for always being there when I needed help with anything. There are two people I would like to thank in particular. First, Hans, thank you for your support during a very difficult period of my PhD. You invested significant time and effort in designing experiments with me in your lab, and I am very happy that this collaboration led to two publications. Lastly, I would like to express my deepest gratitude to Julia. I know my lab setup was not the easiest to work with, nor were my experiments. Still, I am very grateful that we were able to overcome these challenges together, and without you not only my research output would have been lower, but also the enjoyment I had in the lab.

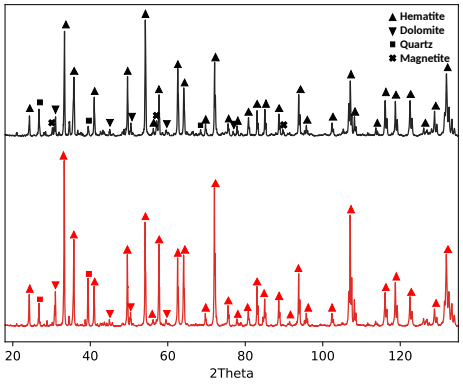
Einen besonders großen Dank möchte ich an meine Eltern aussprechen. Vielen Dank, dass ihr mir immer die Möglichkeit gegeben habt, mich frei zu entfalten, und mich in allem, was ich machen wollte, stets unterstützt habt. Dasselbe gilt natürlich auch für meine drei Schwestern. Danke, dass ihr immer für mich da seid und mir stets das Gefühl gebt, dass ich mich auf euch verlassen kann.

Lastly, I would like to thank the most important person in my life, my beautiful, thoughtful, and kind-hearted wife, Indra. I could thank you for always supporting me, but I feel that would not do our relationship justice. Ours has never been a relationship in which support needed to be asked for, it has always come naturally. Throughout the years, we have encouraged each other to pursue our own ambitions while growing together. Maybe some people may not know this yet, but it was you who first set us on this journey. Looking back, I could not be happier with the decision we made. Still, as this is an acknowledgments section, it only feels right to thank you for everything you have done for me throughout this academically challenging period of my life. I love you to the moon and back, and with great happiness I look forward to all the adventures and chapters that still lie ahead of us. A final shout-out goes to Hörnchen and Körnchen for their continuous emotional support, for keeping me humble, and for their rigorous workout routines.

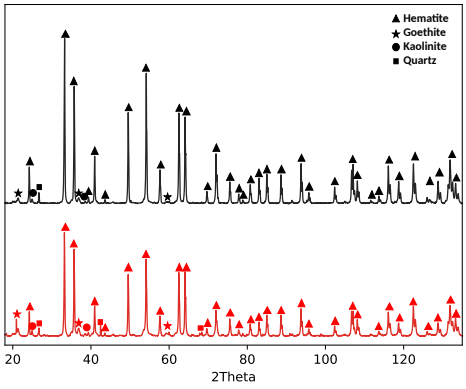
A

APPENDIX TO CHAPTER 3

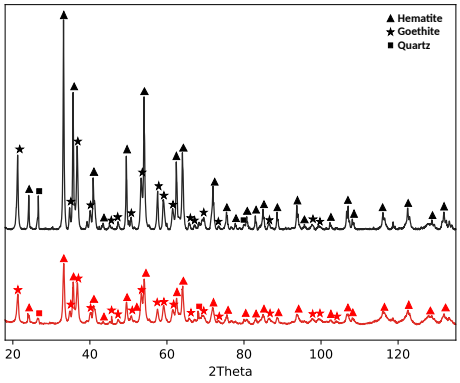
A



(a)



(b)



(c)

Figure A.1: XRD pattern of OreA (a), OreB (b) and OreC (c) with the particle size fraction < 63 μm portrait in black and the size fraction (63 – 125) μm in red.

Table A.1: Linear regression results of model fitting approach for thermal goethite decomposition (fraction < 63 μm).

	OreB						OreC					
	Heating rate [K/min]						Heating rate [K/min]					
	1		2		5		1		2		5	
Model	I	II	I	II	I	II	I	II	I	II	I	II
P1	0.5166	–	0.5607	–	0.6059	–	0.7082	–	0.6795	–	0.5169	–
P2	0.7538	–	0.7422	–	0.7650	–	0.8480	–	0.8110	–	0.6487	–
P3	0.8624	–	0.8397	–	0.8512	–	0.9112	–	0.8807	–	0.7408	–
P4	0.9272	0.8964	0.9068	0.9323	0.9117	0.9237	0.9504	–	0.9293	–	0.8214	–
A2	0.8973	0.8070	0.8791	0.8022	0.8884	0.7305	0.9476	0.3335	0.9498	0.6720	0.8647	0.5402
A3	0.8224	0.1671	0.8098	0.4053	0.8277	0.2221	0.9213	0.0092	0.9266	0.4947	0.8222	0.1183
A4	0.6573	0.6550	0.6800	0.1861	0.7155	0.3199	0.8699	0.4587	0.8855	0.2290	0.7604	0.1184
D1	0.9322	0.9332	0.9123	0.9536	0.9168	0.9478	0.9535	–	0.9334	–	0.8290	0.7092
D2	0.9374	0.9573	0.9191	0.9687	0.9234	0.9568	0.9604	0.7959	0.9465	0.9299	0.8544	0.9050
D3	0.9425	0.9606	0.9257	0.9613	0.9298	0.9430	0.9657	0.8330	0.9597	0.8798	0.8823	0.8746
R2	0.9260	0.9282	0.9069	0.9459	0.9125	0.9156	0.9565	0.1497	0.9454	0.7465	0.8520	0.5830
R3	0.9292	0.9350	0.9108	0.9408	0.9163	0.9104	0.9594	0.5858	0.9525	0.8042	0.8669	0.7436
F0	0.9157	0.6559	0.8942	0.8139	0.9002	0.7812	0.9433	–	0.9201	–	0.8047	–
F1	0.9351	0.9225	0.9185	0.9058	0.9237	0.8765	0.9627	0.6896	0.9640	0.7777	0.8947	0.7615
F2	0.9496	0.8561	0.9384	0.7832	0.9426	0.7606	0.9512	0.6528	0.9733	0.7064	0.9542	0.7083
F3	0.9592	0.8314	0.9537	0.7486	0.9569	0.7277	0.9184	0.6606	0.9541	0.7087	0.9777	0.7117

Table A.2: Linear regression results of model fitting approach for hematite thermal decomposition (fraction < 63 μm).

	OreA			OreB			OreC		
	Heating rate [K/min]			Heating rate [K/min]			Heating rate [K/min]		
Model	1	2	5	1	2	5	1	2	5
P1	0.7973	0.8438	0.8262	0.9054	0.8979	0.8902	0.8797	0.9289	0.8900
P2	0.8250	0.8597	0.8485	0.9158	0.9086	0.9010	0.8960	0.9401	0.9073
P3	0.8479	0.8735	0.8672	0.9246	0.9178	0.9104	0.9094	0.9490	0.9211
P4	0.8726	0.8892	0.8876	0.9345	0.9282	0.9211	0.9239	0.9582	0.9354
A2	0.9008	0.9154	0.9132	0.9657	0.9568	0.9522	0.9507	0.9800	0.9699
A3	0.8868	0.9066	0.9017	0.9620	0.9524	0.9476	0.9441	0.9769	0.9658
A4	0.8700	0.8966	0.8879	0.9578	0.9472	0.9424	0.9363	0.9732	0.9607
D1	0.8753	0.8910	0.8898	0.9356	0.9294	0.9223	0.9254	0.9592	0.9369
D2	0.8887	0.9027	0.9020	0.9469	0.9402	0.9342	0.9371	0.9680	0.9516
D3	0.9037	0.9151	0.9151	0.9596	0.9522	0.9470	0.9489	0.9768	0.9667
R2	0.8899	0.9048	0.9033	0.9515	0.9440	0.9384	0.9399	0.9709	0.9575
R3	0.8975	0.9110	0.9100	0.9576	0.9499	0.9446	0.9458	0.9752	0.9645
F0	0.8669	0.8855	0.8829	0.9322	0.9258	0.9186	0.9206	0.9561	0.9322
F1	0.9125	0.9230	0.9230	0.9689	0.9607	0.9562	0.9562	0.9825	0.9734
F2	0.9515	0.9535	0.9569	0.9860	0.9805	0.9786	0.9734	0.9930	0.9327
F3	0.9766	0.9735	0.9793	0.9747	0.9770	0.9790	0.9689	0.9878	0.8473

A

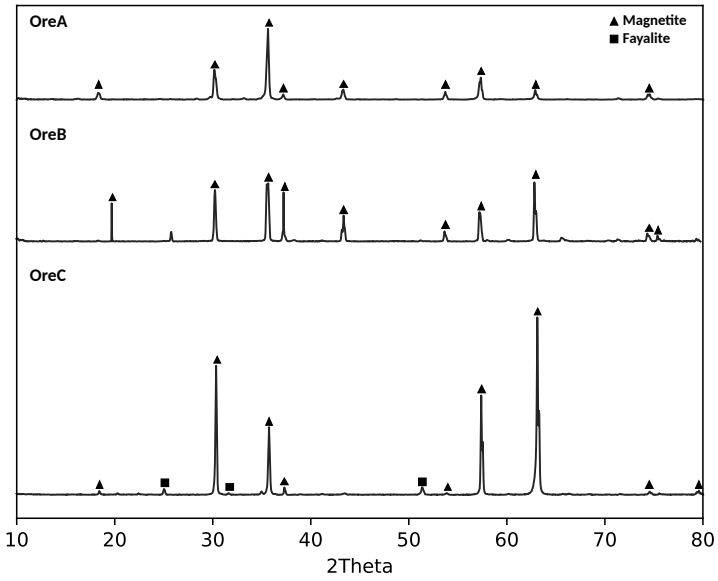


Figure A.2: XRD patterns of cross-section of OreA, < 63 μm, heating rate of 2 K/min, OreB, < 63 μm, heating rate of 2 K/min and OreC, < 63 μm, heating rate of 5 K/min.

B

APPENDIX TO CHAPTER 4

B

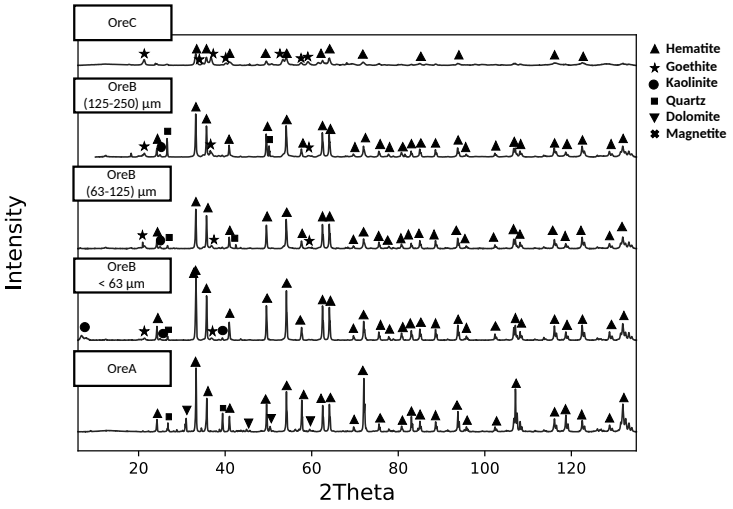


Figure B.1: XRD of virgin materials used in the study (related to Table 4.2 in the main chapter).

Calculation of particle residence time:

$$\frac{m_P\, du_P}{dt} = F_D + F_G - F_B \tag{B.1}$$

Where m_P is the particle mass $m_P = V_P * \rho$, u_P is the particle velocity and t the residence time.

$$F_D = C_D \cdot A_P \cdot \frac{1}{2} \cdot \rho_g \cdot (u_g - u_p)|u_g - u_p| \tag{B.2}$$

$$F_G - F_B = V_P \cdot g \cdot (\rho_P - \rho_g) \tag{B.3}$$

Where $C_D = \frac{24}{Re}$, Re is the Reynolds number ($Re = \rho * (u_g - u_p) * \frac{d_P}{\mu_g}$), d_P is the particle diameter, μ_g is the particle viscosity, A_P is the surface of the particle corss-section, ρ_g is the gas density, u_g is the gas velocity, $|u_g - u_p|$ represents the magnitude of the velocity, V_P is the volume of the particle and g is the gravitational force.

$$u_P = u_g + d_p^2 \frac{g}{18\mu_g}(\rho_P - \rho_g) - \left[(u_g - u_P^0) + d_p^2 \frac{g}{18\mu_g}(\rho_P - \rho_g)\right] \exp\left(-\frac{18\mu_g t}{dP p^2 \rho_P}\right) \tag{B.4}$$

$$L = \sum_{i=1}^{n} u_P \Delta t \tag{B.5}$$

$$L = u_g t + \frac{d_P^2 g}{18\mu_g}(\rho_P - \rho_g)t + \left[(u_g - u_P^0) + \frac{d_P^2 g}{18\mu_g}(\rho_P - \rho_g)\right] * \frac{d_P^2 \rho_P}{18\mu_g}\left[\exp\left(\frac{-18\mu_g t}{d_P^2 \rho_P}\right) - 1\right] \tag{B.6}$$

- Particle residence time is calculated by iterating the particle velocity for a specific time over the defined length of isothermal zone of the HTDF

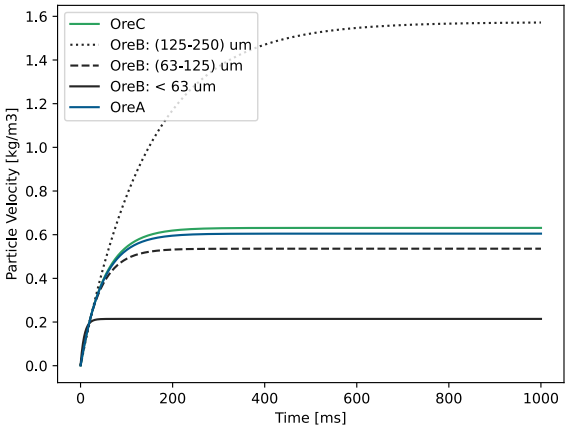


Figure B.2: Influence of material properties on particle velocity (OreC and OreA presented for size fraction of (63-125 μm).

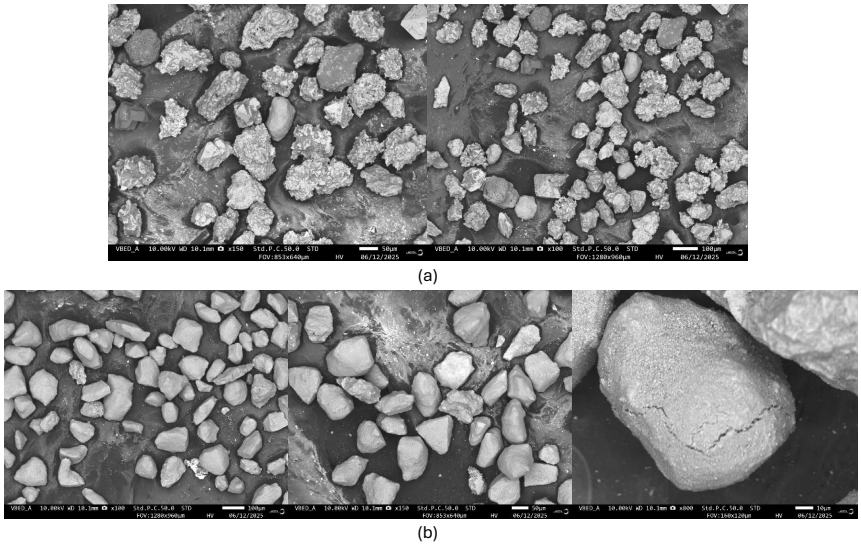


Figure B.3: SEM images of (a) OreB and (b) OreC particles, size fraction (63-125 μm) heated in a TGA until 973 K with a controlled heating and cooling rate of 10 K/min.

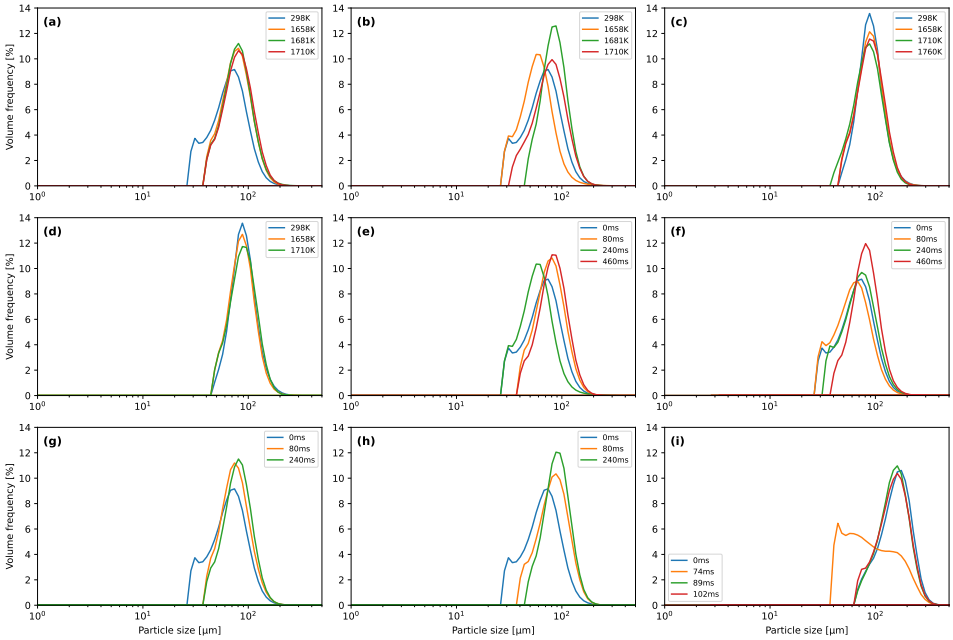


Figure B.4: Particle size distribution in relation to Figure 4.3 and Figure 4.4 for reduced particles of the medium size fraction (a) OreB in N_2 at 80 ms, (b) OreB in N_2 at 240 ms, (c) OreC in N_2 at 80 ms, (d) OreC in N_2 at 220 ms, (e) OreB in N_2 at 1658 K, (f) OreB in $PCR95_CO$ at 1658 K, (g) OreB in $PCR95_{H2}$ at 1658 K, (h) OreB in $PCR95_CO$ at 1710 K and the large size fraction (i) OreB in $PCR95_CO$ a 1710 K.

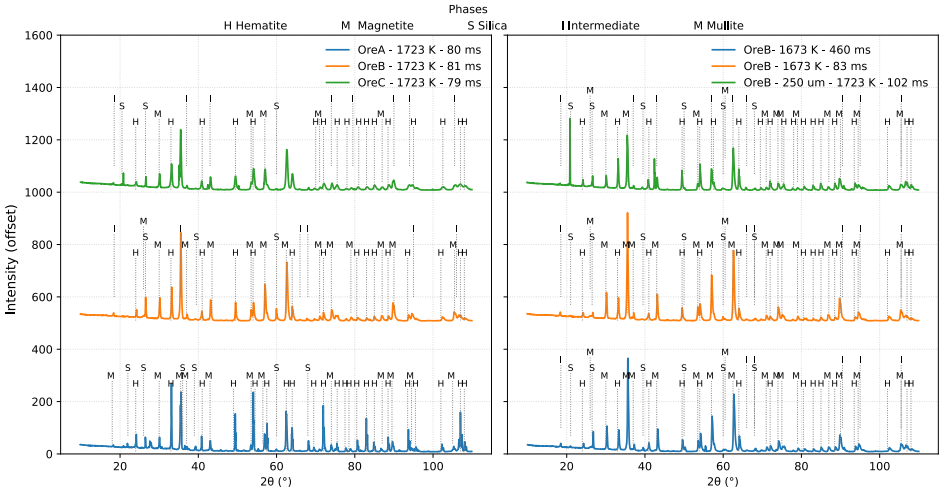


Figure B.5: XRD patterns of selected experiments.

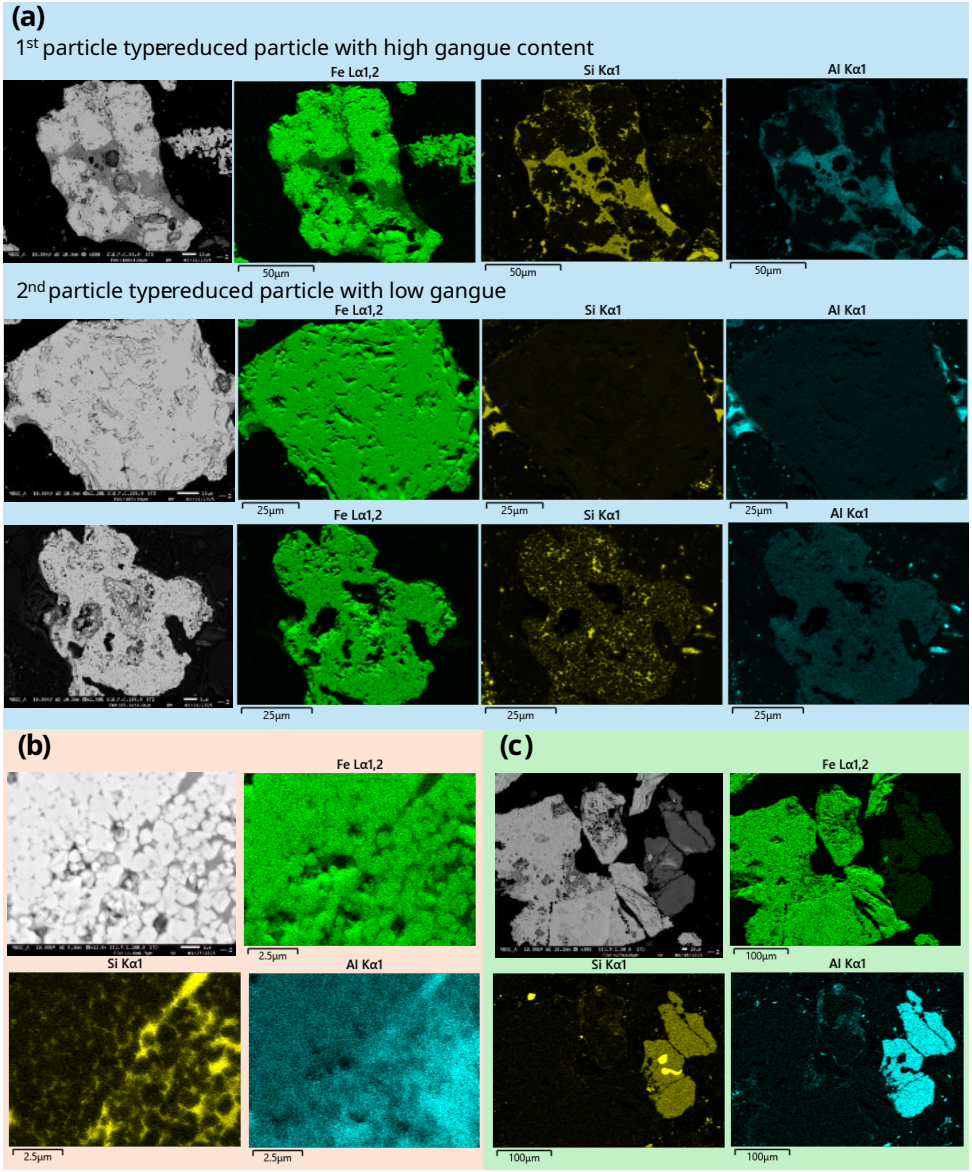


Figure B.6: SEM-EDS analysis of PCR3CO reduced particles of OreB particle size fraction (63-125 μm) at (a) 1710 K and 80 ms (b) 1681 K and 80 ms and OreB particle size fraction (125-250 μm) at (c) 1710 K and 74 ms.

B

Table B.1: PRDs of experiments carried out within this study.

Ore	Particle size [µm]	Atmosphere	Temperature [K]	Residence time [ms]	PRD [%]
B	63–125	N_2	1658	82	1.70
				242	3.90
				460	2.80
			1681	82	5.10
				241	4.40
				458	5.30
			1710	81	5.50
				243	6.10
				460	4.40
		CO	1658	83	5.8
				245	3.1
				460	5.5
			1681	85	7.2
				245	7.5
			1710	83	7.8
				247	8.6
		H_2	1658	83	4.8
				246	7.7
			1681	85	5.8
	125–250	CO	1710	74	1.4
				89	3.2
				102	3.8
C	63–125	N_2	1658	79	3.30
				221	2.70
			1710	79	2.50
				221	1.90
				433	6.30
			1760	80	5.70
A	<63	N_2	1710	1144	5.40
	63–125	N_2	1710	80	1.40
				398	1.60

Table B.2: Summary of diffusion coefficients based on the Jander and Ginstling-Brounshtein equation.

Atmosphere	Ore	Particle size [µm]	Temperature [K]	Time [ms]	Jander D_0 [$m^2/s \times 10^{-7}$]	Ginstling–Brounshtein D_0 [$m^2/s \times 10^{-7}$]
	OreA	(63–125)	1710	80	2.75	2.74
				400	0.72	0.72
	OreB	(63–125)	1658	80	3.96	3.95
				240	7.17	7.10
				460	1.93	1.92
			1681	80	36.49	36.07
				240	9.20	9.10
				460	7.07	6.98
N_2			1710	80	43.10	42.54
				240	17.74	17.50
				460	4.82	4.77
	OreC	(63–125)	1658	80	15.66	15.55
				220	3.73	3.71
			1710	80	46.91	46.31
				430	10.63	10.50
			1760	80	46.91	46.31
	OreB	(63–125)	1658	80	46.85	46.24
				245	4.45	4.42
				460	7.60	7.50
			1681	85	71.20	70.03
				245	26.86	26.40
PCR95CO			1710	80	85.93	84.40
				245	35.30	34.61
		(125–250)	1710	74	2.97	2.96
				82	13.06	12.96
				102	16.14	16.00
	OreB	(63–125)	1658	80	31.87	31.52
$PCR95H_2$				245	28.24	27.73
			1681	85	45.75	45.15

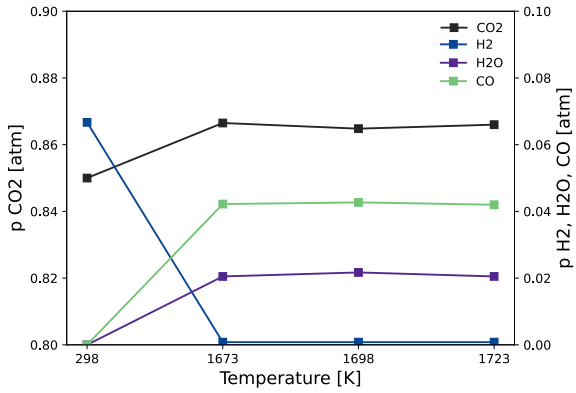


Figure B.7: HIDEN mass spectrometer analysis of the off-gas in $PCR95_{H_2}$ atmosphere, without material charging.

C

APPENDIX TO CHAPTER 5

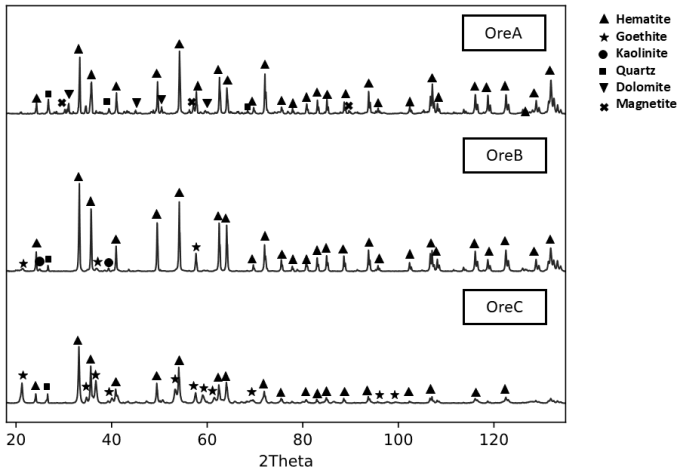


Figure C.1: XRD analysis of OreA, OreB and OreC in the as-received state (Instrument: Bruker D8 Advance diffractometer Bragg-Brentano geometry and Lynxeye position sensitive detector. Cu $K\alpha$ radiation. Divergence slit V12, 45 kV 40 mA. Detector settings LL 0.19 W 0.06, Software: Bruker software DiffracSuite.EVA vs 6.0 (or 5.2), Measurements: Coupled TwoTheta/Theta scan, step size 0.04 ° 2θ, counting time per step 2 s, Database: ICDD pdf4).

ICDD PDF database entries of the detected phases portrait in Figure C.1:
OreA: Hematite: PDF 00-013-0534, Quartz: PDF 01-070-8054, Magnetite: PDF 04-005-4307, Dolomite: PDF 01-081-8226
OreB: Hematite: PDF 01-089-0599, Quartz: PDF 01-085-0794, Goethite: PDF 04-015-8335, Kaolinite: PDF 01-078-2110
OreC: Hematite: PDF 01-089-0599, Goethite: PDF 04-014-5919, Quartz: PDF 00-001-0649

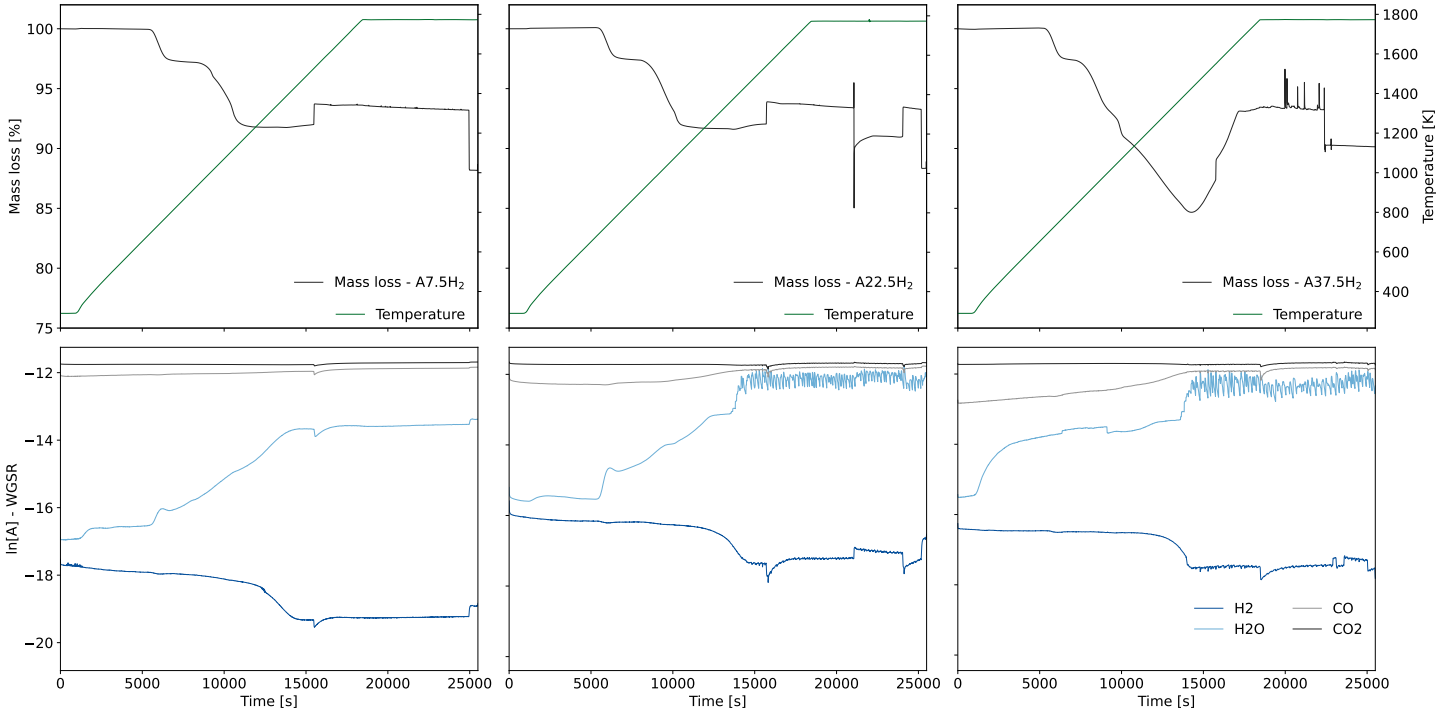


Figure C.2: Off-gas measured together with mass loss for $A7.5H_2$, $A22.5H_2$ and $A37.5H_2$ of OreA.

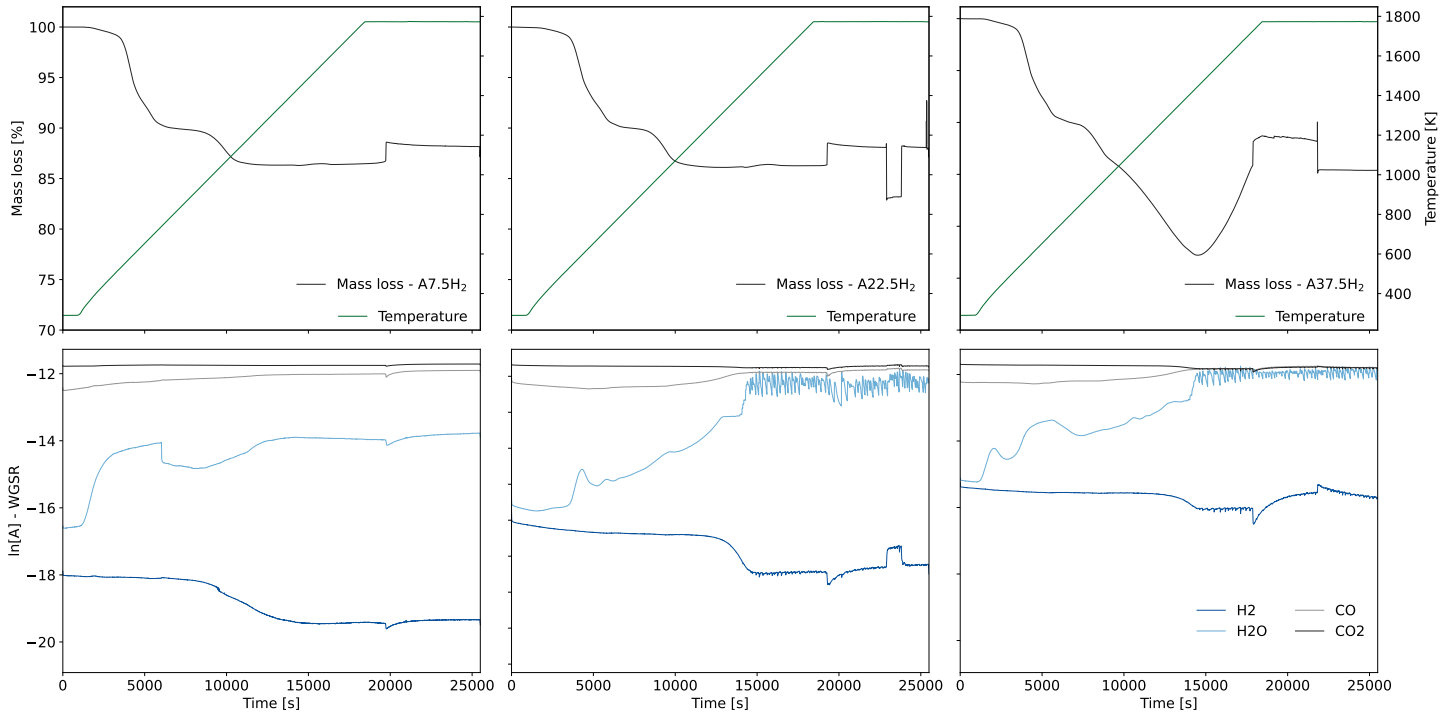
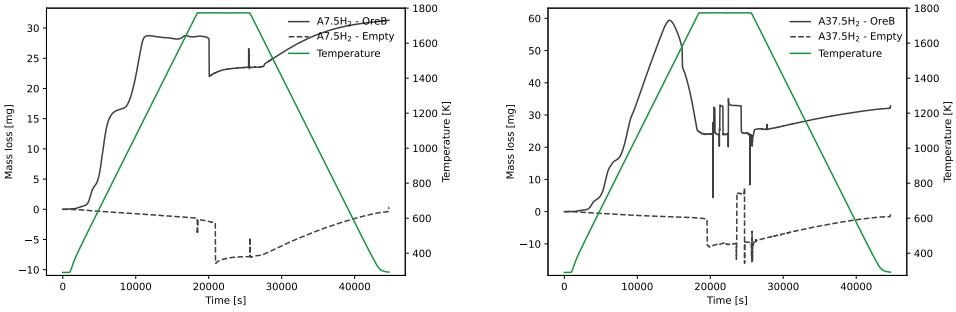


Figure C.3: Off-gas measured together with mass loss for $A7.5H_2$, $A22.5H_2$ and $A37.5H_2$ of OreC.



(a) (b)

Figure C.4: Runs in (a) A7.5H_2 for OreB and empty run without material and in (b) A37.5H_2 for OreB and empty run without material.

D

APPENDIX TO CHAPTER 6

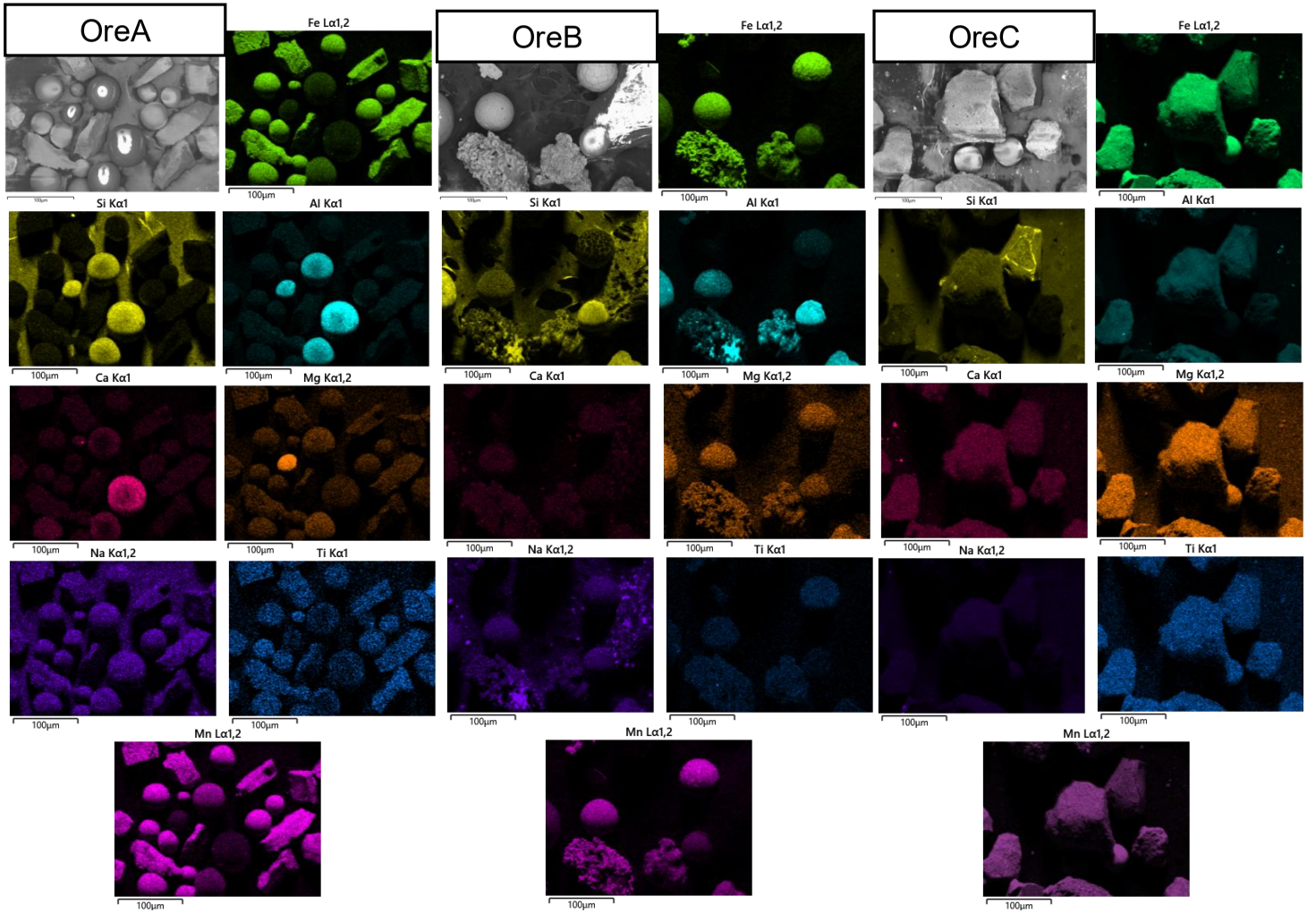


Figure D.1: EDS mapping of (63-125 μm size fraction of OreA, OreB and OreC reduced in A7.5H_2 atmosphere at 1700 K for 125 ms.

Table D.1: Phase composition of ores and slags under different PCR=60% conditions.

Ore	Particle size [μm]	Atmosphere	Temp. [K]	Residence time [ms]	Hematite [wt.%]	Magnetite [wt.%]	Wustite [wt.%]	Quartz [wt.%]	Mullite [wt.%]	Ca-Mn-silicate [wt.%]	Ca-Fe-oxide [wt.%]	Fayalite [wt.%]	Ahrensite [wt.%]	PRD [%]
Powder														
B	63–125	A7.5H_2	1623	120	45	31	–	10	14	–	–	–	–	4.5
B	63–125	A7.5H_2	1623	256	40	46	–	5	8	–	–	–	–	6.0
B	63–125	A7.5H_2	1673	125	26	41	–	10	24	–	–	–	–	6.9
B	63–125	A7.5H_2	1673	269	40	49	–	4	7	–	–	–	–	6.2
B	63–125	A7.5H_2	1723	132	14	70	–	3	13	–	–	–	–	9.3
B	63–125	A22.5H_2	1623	260	57	32	–	11	–	–	–	–	–	4.1
B	125–250	A7.5H_2	1723	58.7	33	37	–	11	19	–	–	–	–	6.0
B	125–250	A7.5H_2	1723	77.6	29	40	–	14	16	–	–	–	–	6.5
A	63–125	A7.5H_2	1723	126	8	88	3	1	–	–	–	–	–	11.0
C	63–125	A7.5H_2	1723	123	28	51	–	7	15	–	–	–	–	7.3
C	63–125	A7.5H_2	1723	252	15	79	–	3	2	–	–	–	–	9.4
Slag														
B	63–125	A7.5H_2	1723	–	–	46	11	–	–	–	–	37	–	15.7
B	125–250	A7.5H_2	1723	–	–	58	10	–	–	–	–	23	–	14.6
A	63–125	A7.5H_2	1723	–	–	40	51	–	–	8	1	–	–	24.0
C	63–125	A7.5H_2	1723	–	–	17	33	–	–	–	–	41	10	26.1

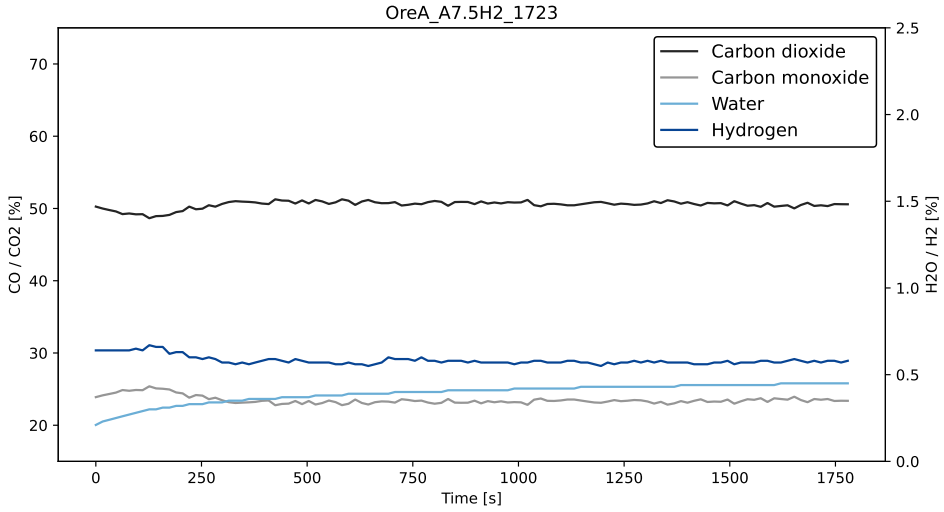


Figure D.2: Off-gas analysis of OreA, reduced at 1723 K in A7.5H2

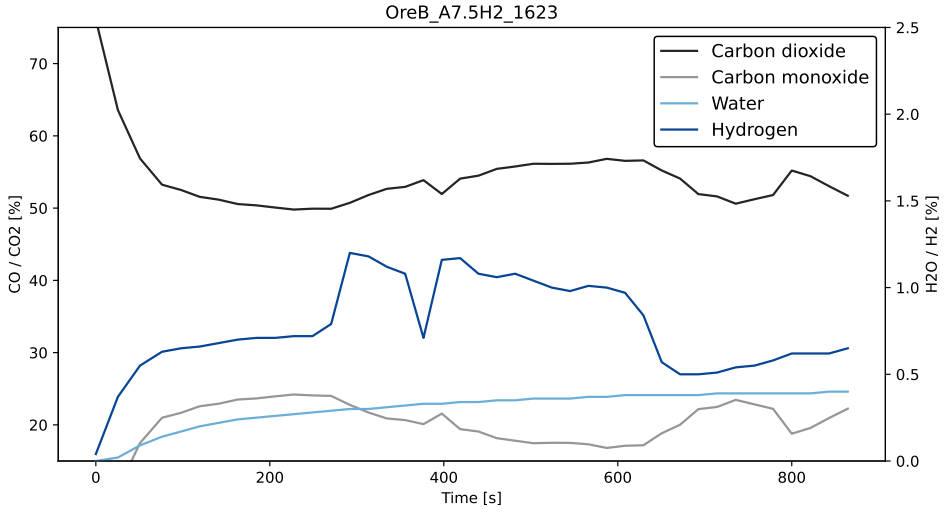


Figure D.3: Off-gas analysis of OreB, reduced at 1623 K in A7.5H2

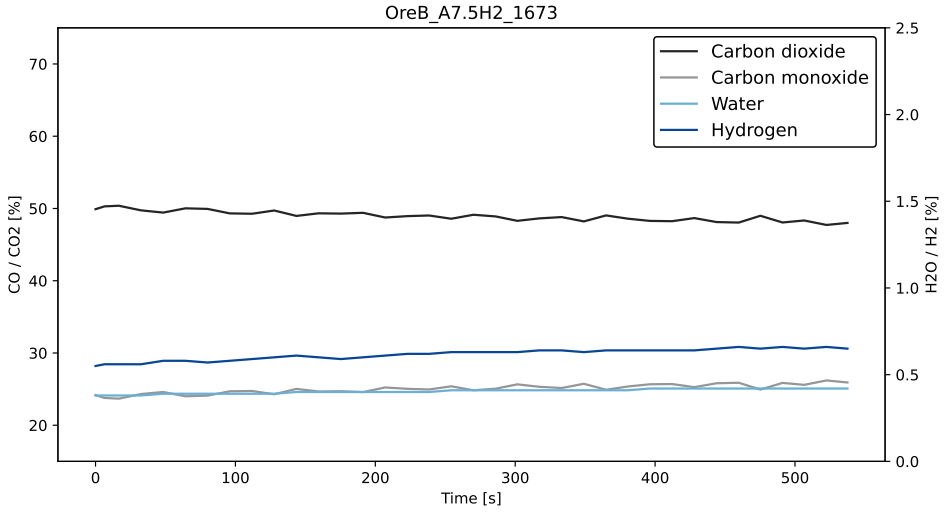


Figure D.4: Off-gas analysis of OreB, reduced at 1673 K in A7.5H2

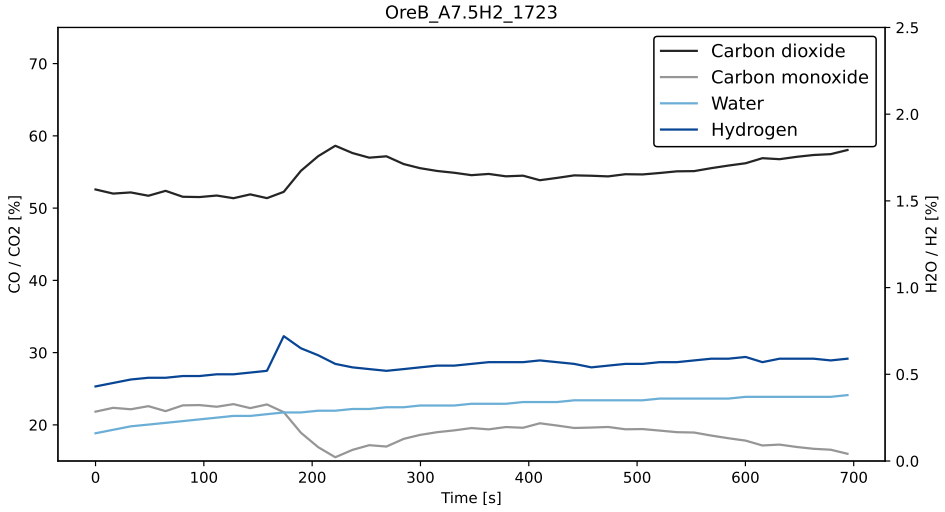


Figure D.5: Off-gas analysis of OreB, reduced at 1723 K in A7.5H2

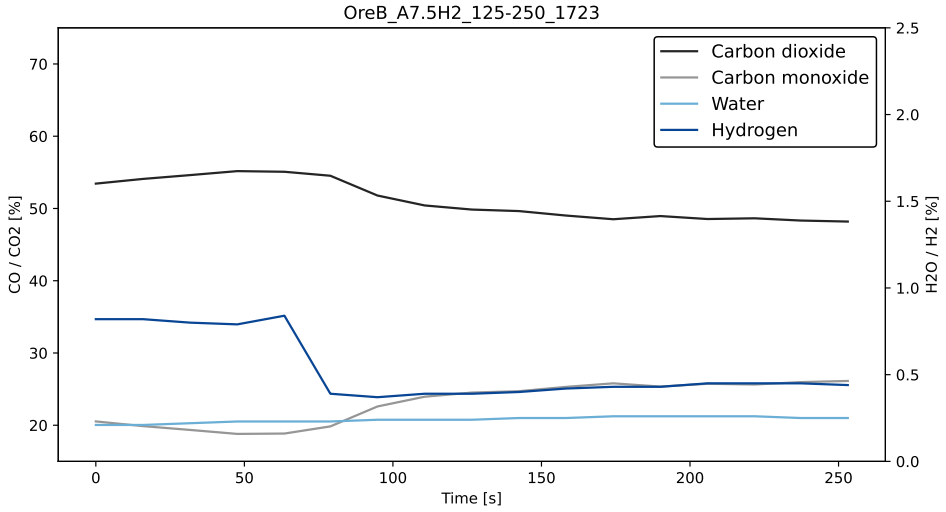


Figure D.6: Off-gas analysis of OreB large fraction of (125-250) um, reduced at 1723 K in A7.5H2

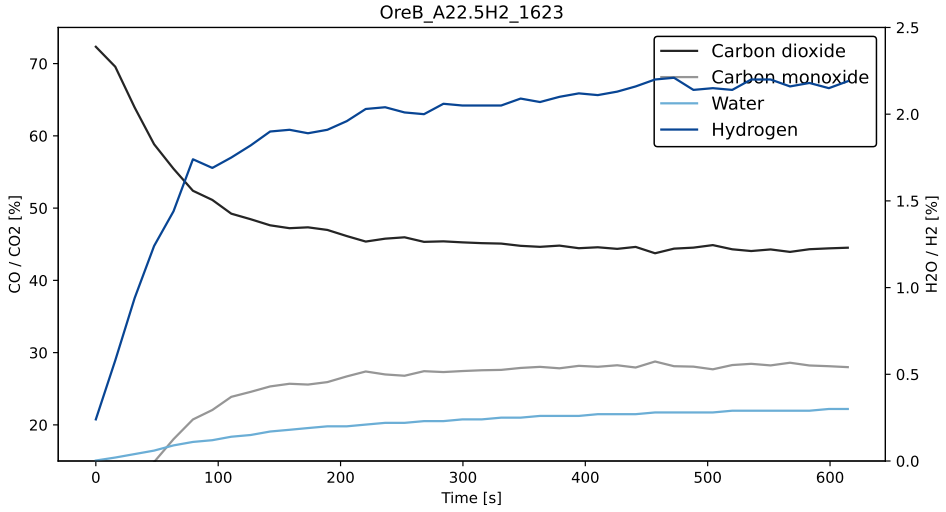


Figure D.7: Off-gas analysis of OreB, reduced at 1623 K in A22.5H2

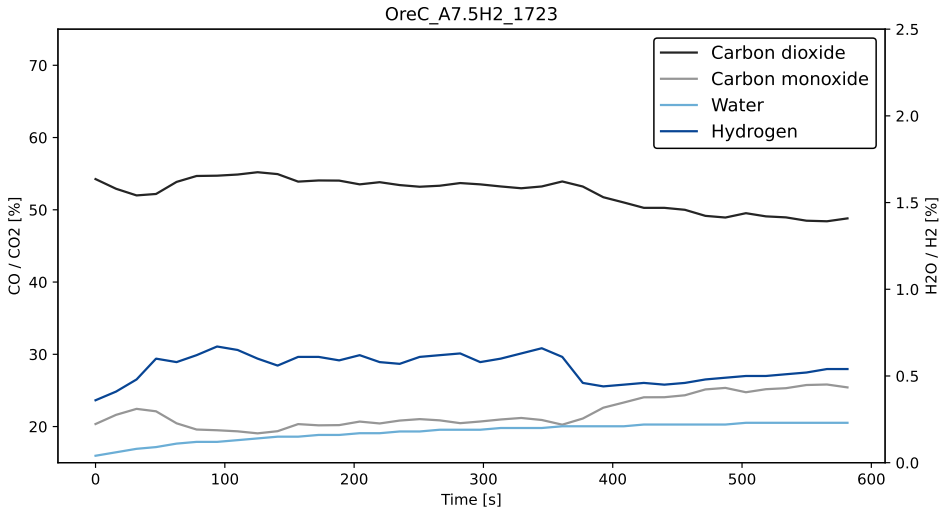


Figure D.8: Off-gas analysis of OreC, reduced at 1723 K in A7.5H2

Curriculum Vitæ

28-09-1995 Born in Aachen, Germany.

Education

2014–2018 Bachelor of Science
Business Administration and Engineering Materials and Process Engineering
RWTH Aachen University
Thesis: A comparative study of the influence of rutile and mechanically activated rutile on the aluminothermic production of titanium alloys
Promotor: Prof. Dr.-Ing. Dr. h. c. Dr. E. h. B. Friedrich

2018–2021 Master of Science
Business Administration and Engineering Materials and Process Engineering
RWTH Aachen University
Thesis: Comparative parameter study between static and rotary kiln pyrolysis in the field of lithium-ion battery recycling
Promotor: Prof. Dr.-Ing. Dr. h. c. Dr. E. h. B. Friedrich

2019 Semester Abroad
Pohang University of Science and Technology

2021–2026 PhD. Materials Science & Engineering
Delft University of Technology
Thesis: Reduction mechanisms of goethite-rich iron ore fines under suspension smelting conditions
Promotors: Dr. Y. Yang, Dr. ir S.T. Abrahami and Dr. N. Dogan

Professional Experience

2021–2025 PhD.Researcher
Delft University of Technology

List of Publications

1. **Leerhoff, P.**, Brouwer, J. C., Armaki, A. M., Zeilstra, C., Meijer, K., van der Stel, J., Abrahami, S. T., Dogan, N., Yang, Y. Characterisation of varying iron ores and their thermal decomposition kinetics under HIsarna ironmaking conditions. **Metals** 14, 1271 (2024). https://doi.org/10.3390/met14111271.

2. **Leerhoff, P.**, Brouwer, J. C., Zeilstra, C., Meijer, K., van der Stel, J., Abrahami, S. T., Dogan, N., Yang, Y. Impact of H_2-enrichment and ore mineralogy on the reduction of varying iron ores in suspension smelting ironmaking. **Powder Technology** 468, 121570 (2026). https://doi.org/10.1016/j.powtec.2025.121570.

3. **Leerhoff, P.**, Zeilstra, C., Meijer, K., van der Stel, J., Abrahami, S. T., Dogan, N., Yang, Y. H_2 adaptation in ironmaking: a review with focus on suspension smelting and its reaction mechanisms. **Mineral Processing and Extractive Metallurgy: Transactions of the Institutions of Mining and Metallurgy** (2026). https://doi.org/10.1177/25726641261463593

4. **Leerhoff, P.**, Zeilstra, C., Wilson, B.P., Meijer, K., van der Stel, J., Abrahami, S. T., Dogan, N., Yang, Y. Thermal decomposition and pre-reduction of goethitic iron ore fines and their effects on phase transformation and material properties. **Sci Rep** (2026). https://doi.org/10.1038/s41598-026-62756-0

